Measured and Simulated Prompt Fission Neutron and Photon Correlations

by

Matthew J. Marcath

A dissertation submitted in partial fulfillment
of the requirements for the degree of
Doctor of Philosophy
(Nuclear Engineering and Radiological Sciences)
in the University of Michigan
2018

Doctoral Committee:

Professor Sara A. Pozzi, Chair
Dr. Robert C. Haight, Los Alamos National Laboratory
Professor Edward W. Larsen
Professor Wolfgang Lorenzon

Matthew J. Marcath

mmarcath@umich.edu

ORCID ID: 0000-0002-0026-4394

Dedication

To my family old and new.

Acknowledgments

I would like to thank first and foremost my advisor Professor Sara Pozzi for giving me the opportunity to pursue my PhD. I would also like to thank her for the mentorship and for providing many opportunities to grow as a professional.

I would also like to thank everyone in the DNNG for their support since I joined as an undergrad in UROP. Along the way to my dissertation, you've provided immense professional support and offered great friendship.

I would not be here if it weren't for my parents encouragement to follow my interests early in my life and for my wife's encouragement to apply to graduate school. I am thankful for my whole family's support during my long stint as a student and for attempting to understand how I spent my time.

This research was performed under appointment to the Nuclear Nonproliferation International Safeguards Graduate Fellowship Program sponsored by the National Nuclear Security Administrations Next Generation Safeguards Initiative.

Table of Contents

List of Figures

List of Tables

List of Appendices

List of Abbreviations

CFD constant fraction discrimination. 54

DAFCA Data Acquisition For CAEN Apparatuses. 113

DNNG Detection for Nuclear Nonproliferation Group. 3, 54, 113, 127

FWHM full-width half maximum. xi, 23, 116

HFF heavy fission fragment. 15

IAEA International Atomic Energy Agency. 1, 2

LANL Los Alamos National Laboratory. 4, 77, 108, 110

LANSCE Los Alamos Neutron Science Center. 51, 77

LFF light fission fragment. 15

PFNS prompt fission neutron spectrum. 67

PMT photo-multiplier tube. vii, xi, 10, 11, 10, 11, 51, 108, 110, 111

PSD pulse shape discrimination. xi, 5, 7, 9, 10, 54, 55, 113, 116, 118

SNM special nuclear material. xvi, 2

TKE total kinetic energy. vii, 15, 17, 127

TOF time-of-flight. 11, 50, 51, 76, 126

TXE total excitation energy. 17

Abstract

An accurate understanding of fission is critical to characterization of special nuclear material (SNM) for nonproliferation and safeguards applications. Noninvasive and nondestructive techniques rely primarily on highly penetrating and relatively abundant fission emissions. Spontaneously and under particle interrogation, SNM emits neutrons and photons from fission, which are characteristic of the fissioning isotopes. Characteristic neutrons and photons are emitted from nuclear fission when a deformed, neutron-rich nucleus divides into two fragments that then de-excite. During de-excitation, neutrons are emitted first, followed by photons; this process gives rise to correlations. New, event-by-event, physics-based models, `CGMF` (Los Alamos National Laboratory) and `FREYA` (Lawrence Livermore National Laboratory), predict correlations in prompt fission emissions. Current safeguards and nonproliferation systems do not utilize angular or multiplicity correlations. Little data exist to validate these models; correlated quantities have been measured only for ^{252}Cf(sf). My work provides measured correlation data to validate models useful for future system design.

Previous correlation measurements have been limited by the acquisition challenges of a many-detector array and therefore have used simple detector systems. Additionally, few detection methods exist that are simultaneously efficient to neutrons and photons. In this work, I show a many-detector array of pulse-shape-discrimination-capable organic scintillators, sensitive to both fast neutrons and photons, to measure correlations in neutron energy, photon energy, multiplicity, and emission angle. This work is achieved through `MCNPX` − `PoliMi` simulations and through use of time-synchronized, high-throughput, multiple-digitizer acquisition systems. I performed experiments sensitive to correlations with a large array of organic scintillators. I performed measurements

of ^{252}Cf(sf) at both the University of Michigan and the Los Alamos National Laboratory; and of ^{240}Pu(sf) spontaneous fission at the Joint Research Centre in Ispra, Italy, and at the Los Alamos National Laboratory.

I measured the ^{240}Pu(sf) neutron-neutron angular distribution and found it to be less anisotropic than the ^{252}Cf(sf) neutrons. ^{240}Pu(sf) and ^{252}Cf(sf) neutron-neutron angular distribution simulation results indicate that fission models capture the general trend of neutron anisotropy. ^{252}Cf(sf) and ^{240}Pu(sf) experimental multiplicity results suggest weak neutron-photon competition during fragment de-excitation. The measured correlations were compared with `MCNPX – PoliMi` simulations using the built-in model and two new event-by-event fission models, `CGMF` and `FREYA`, which predict correlations in prompt emissions from fission. Simulation results from `CGMF` and `FREYA` predict a stronger negative correlation than the experiment result.

Chapter 1

Introduction

1.1 Motivation

The discovery of fission in 1938 by Hahn and Strassmann [1] and a first explanation by Meitner and Frisch [2] was followed by a rapid development of nuclear technology, both constructive and destructive. Scientists quickly understood the immense potential of fission due to two key features: a large energy release and the emission of multiple neutrons able to form fission chains. Despite 80 years of research, much remains unknown regarding the details of fission and of fission emissions and my work described here contributes to that body of knowledge.

Immediately after the discovery of fission and conception of a fission chain, physicists expressed concerns about proliferation of this new-found technology. Fears of technology abuse materialized as scientists hypothesized, and ultimately demonstrated, that fission chains could be maintained (in the case of a critical fission reactor) or made to grow exponentially (in the case of a fission bomb) [3]. Proliferation concerns were further justified as the world entered World War II and the United States, United Kingdom, Japan, Germany, and Soviet Union pursued fission-based weapons. As those in and out of the nuclear weapons states realized the potential threat of nuclear weapons proliferation, treaties and agreements were later enacted to limit the testing and use of nuclear weapons, while encouraging peaceful nuclear technology.

The first international treaty to indirectly limit nuclear proliferation was the Partial

Test Ban Treaty in 1963 [4]. The treaty's main goal was to limit fallout from atmospheric nuclear testing and did so by forcing nuclear testing underground. Proliferation of nuclear weapons was slowed because testing and diagnostics are more challenging in that environment. The next substantial, international step to prevent nuclear weapons proliferation was the Non-Proliferation Treaty in 1968 [5]. This treaty aimed to prevent the spread of nuclear weapons and technology, to promote cooperation in the peaceful uses of nuclear energy, and to further the goal of achieving nuclear disarmament and of general and complete disarmament. The treaty provided a framework for cooperation between weapons states and non-weapons states to pursue and access peaceful use of technology while preventing the further spread of weapons technology. The treaty established a safeguards system under the International Atomic Energy Agency (IAEA) to verify compliance with the treaty.

The IAEA safeguards intend to verify and to prevent diversion of declared nuclear material, as well as in some cases to identify undeclared nuclear material, within nuclear facilities. These goals are achieved through various means, including physical protection, tamper-proof seals, cameras, and radiation detection. Verification using radiation detection can rely on many different signatures from nuclear material, including emitted gamma rays and neutrons. These nuclear signatures are used to verify declared characteristics such as isotopic composition and mass.

Outside of nuclear facilities and of IAEA safeguards is the threat of illicit nuclear material moving illegally across a nation's borders; radiation detection systems exist to intercept those materials. These detection systems also rely on nuclear material radiations.

Safeguards and nonproliferation radiation detection systems are used to characterize or locate special nuclear material (SNM) which is defined as plutonium, uranium-233, or uranium enriched in isotopes 233 or 235 [6]. These materials emit radiation, particularly from fission, both passively and under active interrogation with particle beams. Fission is unique because it releases both neutrons and photons in multiplicity. Observed properties of fission neutrons and/or photons are used in safeguards and nonproliferation systems.

Most deployed safeguards and nonproliferation radiation detection systems rely on simple or average responses to fission emissions, such as spectra or multiplicity, and are not sensitive to complex correlations between emissions. Monte Carlo particle transport codes are often used to predict experimental outcomes and to design detection systems. These codes use fission models to produce neutron and photon emissions from SNM. Common fission models are limited in detail and do not capture the full physics of the fission fragment de-excitation process [7,8]. These models are based on evaluated neutron and photon energy and multiplicity spectra, but they ignore details of fission fragment de-excitation. New event-by-event, physics-based models capture interesting correlations not reflected in these commonly used models [9].

Both the destructive and constructive facets of fission-based technology continue to drive our pursuit of understanding fission and fission emissions. As radiation detector technology has progressed and as greater demands are put on nonproliferation and safeguards systems, increasingly complex detector systems are being developed to meet emerging challenges. Novel safeguards and nonproliferation systems that are inherently more sensitive to fission emissions are currently being developed without the insight of highly detailed fission models. There is, therefore, a need to provide correlated fission data to validate and improve models for the development and improvement of radiation detection systems.

1.2 Contributions and overview of this dissertation

In this dissertation, I measure event-by-event correlations in prompt fission emissions relevant to nuclear safeguards applications. Most of the correlations shown here have never been observed before; previous studies and gaps in those studies are detailed in each chapter. The newly-measured correlations are also compared to correlated fission models. The fission models are described in Chapter 3.

While not discussed in this dissertation, work by the Detection for Nuclear Nonproliferation Group (DNNG), including contributions from myself as a co-author, showed

^{252}Cf(sf) neutron-neutron angle and energy correlations [10]. This work evolved into the first detailed measurement of ^{240}Pu(sf) neutron-neutron angular and energy correlations, discussed here in Chapter 4.

Upon completion of the single particle neutron-neutron measurements, my work transitioned to measuring inter-particle correlations. Detailed in Chapter 5, a measurement was performed at the University of Michigan to explore neutron-photon energy correlations. This work was motivated in part by new event-by-event fission models `CGMF` [11] and `FREYA` [12], which exhibit inter-particle correlations, and also by the lack of data to validate these models.

Prompted by interesting results from the University of Michigan experiment and fission model predictions, I experimentally measured neutron-photon competition during fission fragment de-excitation, discussed in Chapter 6. To perform the experiment, I took an acquisition system that I assembled specifically for a summer-long experiment to use the organic scintillator Chi-Nu array at Los Alamos National Laboratory (LANL) [13]. I compared experimental results to `CGMF` and `FREYA` simulation results where I integrated fission events into `MCNPX` − `PoliMi`.

Once I had measured ^{252}Cf(sf) neutron-photon competition, I approached a more safeguards-relevant isotope, ^{240}Pu(sf), with a similar experiment in mind. Detailed in Chapter 7, I designed a stilbene detector array and acquisition system to measure a small amount of ^{240}Pu at LANL. Again, I compared experimental results to `FREYA` simulation results.

Finally in Chapter 8, I discuss conclusions from this dissertation work and suggest future work.

Chapter 2

Neutron and Photon Detection

Here I explain how I detect radiation, for relevant radiations and detector types, and how I characterize my detectors, specifically for fission experiments. I will restrict discussion to detection of neutrons and photons with energies typical for fission emissions, below approximately 10 MeV.

2.1 Organic Liquid Scintillators

Organic scintillators, including EJ-309 [14] and stilbene [15], are composed of organic molecules which create scintillation light when excited by charged particles. Scintillation light is produced after a recoiling charged particle excites molecular states. Organic scintillators are sensitive to photons and neutrons through charged particle recoils. Photons interact primarily through Compton scattering on an electron; photoelectric absorption is unlikely at relevant energies on these small nuclei, shown in Fig. 2.1. Above two times the electron rest-mass energy, pair production is energetically possible and creates an electron-positron pair. The positron will slow down in the surrounding material to subsequently annihilate producing two 511 keV photons. The pair production recoil electron and the annihilation photons can then be detected. Only partial photon energy is deposited in Compton interactions. Neutrons interact primarily via elastic scattering on hydrogen and carbon nuclei, shown in Fig. 2.2; inelastic scattering on carbon and capture on hydrogen are relatively rare. Some organic scintillators, including the EJ-309 and

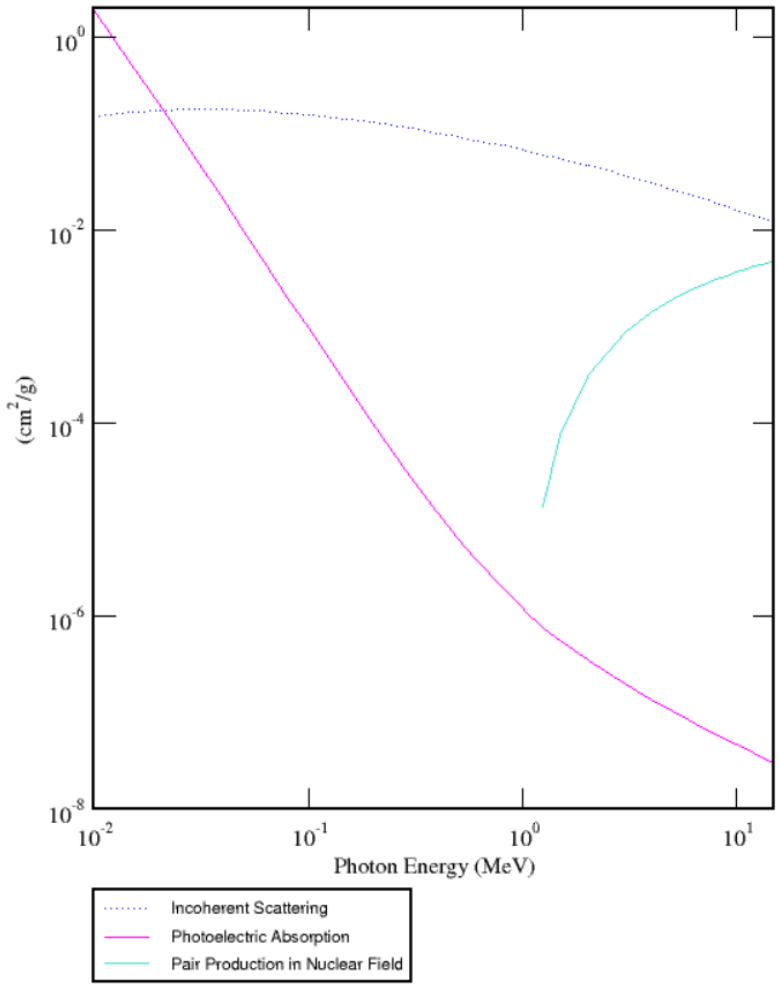

Figure 2.1: Photon reaction cross sections for stilbene [17]. Low probability reactions are omitted.

stilbene used here, are capable of discriminating between electron and proton recoils, a process known as PSD [16].

2.1.1 Reactions and energy deposition

Figure 2.1 shows that fission energy photons are most likely going to interact through Compton (incoherent) scattering. Very low energy photons could be photoelectrically absorbed, but are unlikely to be above acquisition thresholds. Pair production becomes likely as photon energy increases, however Compton scattering is still most common for fission energies. Compton scattering only deposits a fraction of the photon energy $h\nu$ to

the recoil electron,

$$hv' = \frac{hv}{1 + \frac{hv}{m_0c^2}(1 - \cos\theta)}, \tag{2.1}$$

where m_0c^2 is the electron rest mass energy. The maximum energy deposited occurs when the outgoing photon angle θ is π radians, giving a minimum outgoing photon energy hv'. Using Eqn. 2.1, a 662 keV ^{137}Cs characteristic gamma ray can deposit a maximum of 478 keV. Due to the likely interaction modes and energy deposited by photons in organic scintillators, they are not well suited for photon spectroscopy.

Figure 2.3 shows for an EJ-309 organic scintillator that the detection efficiency to incident photons peaks at low energies and decreases toward higher energies. The energy dependent efficiency is primarily a convolution of interaction cross sections and light production, but also includes other detector readout characteristics. The rising edge in efficiency is due to a lower energy threshold imposed due to acquisition and PSD limitations. The sharp drop in efficiency near 3.5 MeV is due to the upper dynamic range of the waveform digitizer.

Figure 2.2 demonstrates that neutrons primarily interact in organic scintillators through elastic scattering on hydrogen and carbon nuclei. Proton scatters are most likely, but at resonances above a few MeV carbon elastic scattering is more probable. In a nonrelativistic elastic scatter, the recoil nucleus with mass A and energy E_R at angle θ

$$E_R = \frac{4A}{(1 + A)^2}(\cos^2\theta)E_n \tag{2.2}$$

can only take the full energy of the neutron when $A = 1$ and $\theta = 0$. Neutrons can deposit their full energy in proton scatters, but a neutron can deposit only 28.4% of its energy on carbon nuclei.

Figure 2.3 shows for an EJ-309 organic scintillator that the detection efficiency to incident neutrons peaks at low energies and decreases toward higher energies, similar to photons. Again, neutron energy dependent efficiency is primarily a convolution of interaction cross sections and light production, but also includes detector readout characteristics. Small features in the efficiency distribution near 2.5, 4, 6, and 7.5 MeV are

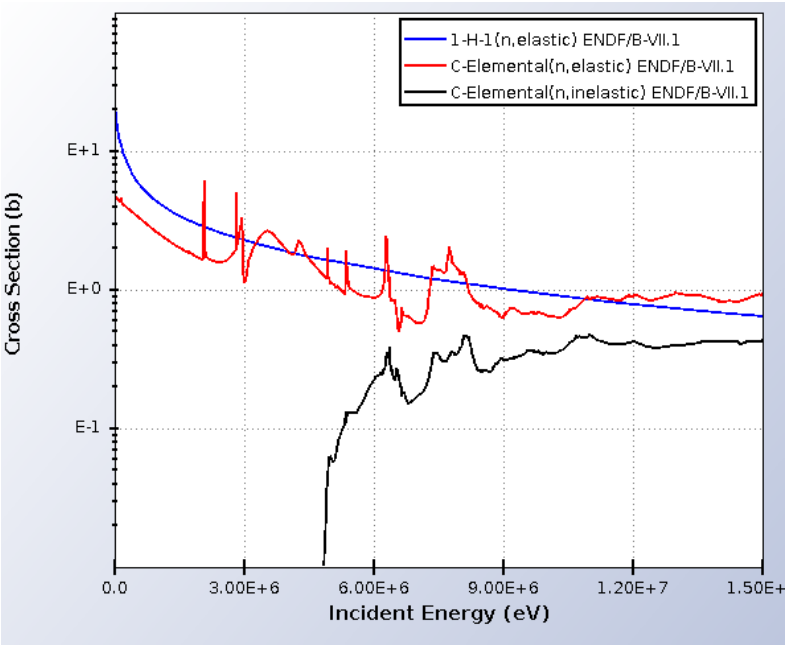

Figure 2.2: EJ-309 neutron interaction cross sections to neutrons of fission energies [18].

caused by the resonances in the carbon elastic scattering cross section.

Cross talk occurs when a particle incident on a detector scatters from one detector to another detector and causes a detection event in both. Organic scintillators are susceptible to cross talk because they are sensitive to particles primarily through scattering; further discussion can be found in Chapter 4.4.2.

2.1.2 Scintillation light production

The organic scintillator converts charged particle kinetic energy into scintillation light. Energy conversion is linear for electron recoils over fission photon energies, but energy conversion of proton recoils kinetic energy is non-linear, shown in Fig. 2.3. The relevant light emission processes are summarized here, but for a more detailed discussion see Ref. [19].

The fluorescence in organics comes from transitions in the energy level structure of a single molecule [20]. Kinetic energy of a recoiling charged particle can be absorbed by a molecule through exciting the molecule to π-electronic energy levels. A series of singlet (spin 0) and triplet (spin 1) electronic states can be created. Most excitations produce molecules in the first excited singlet or triplet states. Prompt fluorescence occurs in the

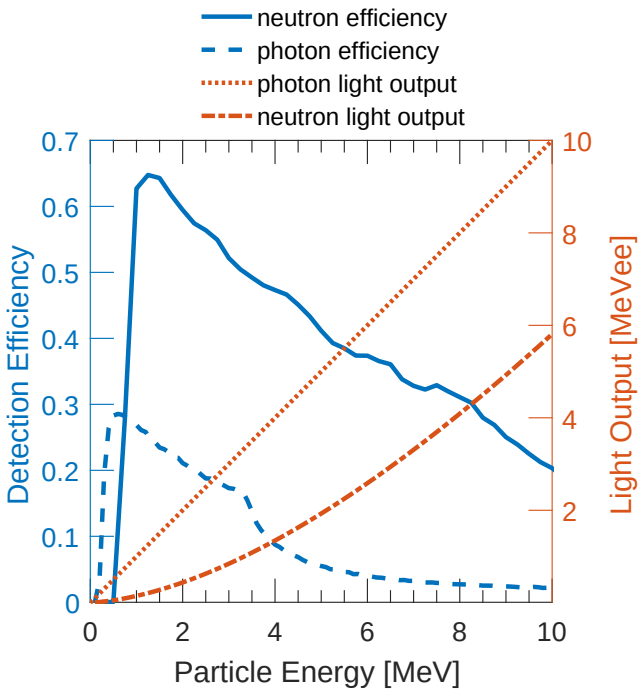

Figure 2.3: Calculated neutron and photon detection efficiency and light output distributions used in the detector response code for neutron scattering on a proton and for photon scattering on an electron in a 17.78 x5.08 cm EJ-309 detector.

transition from the first excited singlet state to a ground state. The singlet transition to a ground state has a decay time of 3.5 ns. The triplet state has a much longer decay time to a ground state; however, two triplet states in close proximity can annihilate to form one singlet excited state and one singlet ground state [21]; the new singlet excited state can then decay to ground state on a faster time scale. Excitation energy in the π-electronic states can transfer from molecule to molecule and not all energy from the excited states is converted to fluorescence.

PSD in organic scintillators arises from differences in scintillation when excited states are formed by electrons and protons. The proton has a higher stopping power than the electron; consequently, the proton creates higher density regions of excited molecules. The higher density regions enable higher rates of triplet-triplet annihilation and singlet state quenching. Therefore, the recoil proton produces relatively less prompt fluorescence and more slightly delayed fluorescence to a recoil electron of the same energy. A proton recoil will produce more total fluorescence than an electron recoil with the same peak intensity, as shown in Figure 2.4. These effects also cause proton recoil kinetic energy

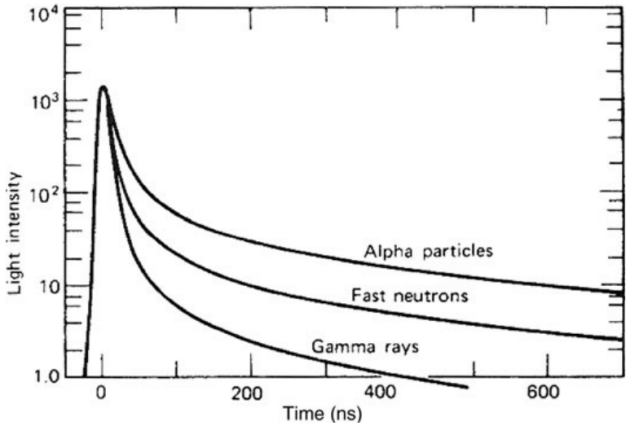

Figure 2.4: Light output intensity in arbitrary units as a function of time after a charged particle recoil in stilbene [23].

conversion to appear as non-linear, shown in Fig. 2.3.

Practically, PSD becomes challenging for small energy depositions. As a proton or electron waveform becomes small, so do the differences in the waveform tails. Here, I used charge integration PSD to discriminate between interaction types [22]. Charge integration PSD compares the waveform tail integral to the total waveform integral of each waveform to a discrimination function.

2.1.3 Light collection and readout

Scintillation light from a charged particle recoil must be collected, converted to an electrical signal, amplified, and then read out by a waveform digitizer or analogue electronics.

Scintillation light is emitted in the scintillator volume and must escape to a readout system. In this work, we used a photo-multiplier tube (PMT) to convert scintillation light to an electric signal and to amplify that signal. Each PMT was attached to one face of a right circular cylindrical scintillator. The scintillation light has a relatively long mean free path in the organic material and may scatter many times within the scintillator. To improve light collection in the PMT, a reflective coating is applied to the sides of the scintillator not connected to the PMT.

In Fig. 2.5, a PMT consists of a vacuum tube with a photocathode at one end and at the other end readout and high voltage probes. The face of the PMT, directly attached to the scintillator, contains a photocathode, which converts incident scintillation light

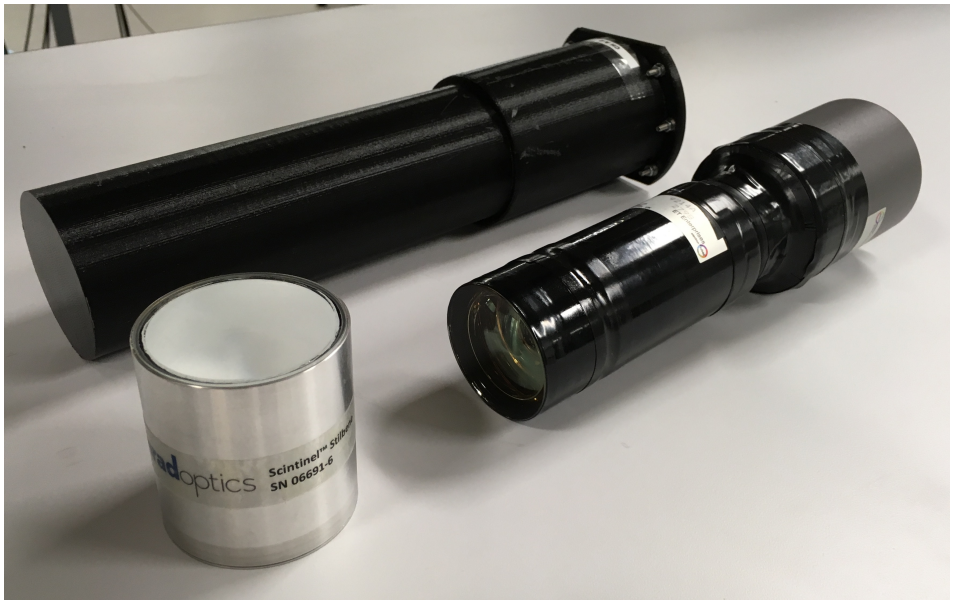

Figure 2.5: (Bottom left) InRad optics stilbene encased in aluminum, (bottom right) ET Enterprises 9214b PMT, and (top) 3D printed case for detector assembly. The PMT and stilbene scintillator are coupled with optical grease and secured with black electrical tape to make the system light tight.

to electrons in the PMT. A vacuum is necessary to allow the low-energy electrons to drift unimpeded through electric fields in the tube. Once electrons are created, they are focused and drifted to a series of dynodes. As an electron strikes a dynode, the energy deposited by the electron may liberate more than one electron, thereby creating a multiplying effect. Multiplication gain for the 9214b PMT from ET Enterprises is on the order of 10^6, depending on applied voltage.

Organic scintillator fluorescence decay times are on the order of nanoseconds and the PMT, given a reasonable choice of PMT and signal acquisition, preserves the fast timing of that signal. Thus, organic scintillators have nanosecond-order time resolution to particle interactions. Good time resolution is useful for neutron time-of-flight (TOF) spectroscopy and for accurate correlation of a fission particle detections with a fission trigger.

2.2 NaI(Tl) scintillators

For a small part of my thesis work, I used an inorganic scintillator, sodium iodide doped with thallium NaI(Tl). NaI(Tl) is notable for its high light yield of approximately 38,000 photons per MeV energy deposition compared to most inorganic scintillators [20]. While NaI(Tl)has a fast light decay time compared to most inorganic scintillators, it has a poor light decay time of 230 ns, and thus a poor time resolution relative to organic scintillators such as EJ-309 and stilbene.

Relative to an organic scintillator, NaI(Tl) is advantageous for photon spectroscopy and for its higher efficiency to photons. NaI(Tl) is a poor neutron detector, because only a small fraction of neutron energy may be deposited in neutron elastic scattering on sodium or iodine nuclei, respectively 16% and 3.1%, and the scattering cross sections are on the order of a few barns. Figure 2.6 shows that, due to the higher Z elements, NaI(Tl) has an appreciable photoelectric absorption cross section over fission photon energy ranges. In photoelectric absorption, the incoming photon is absorbed by the atom and an energetic electron is ejected from one of its bound shells. The ejected electron has kinetic energy equal to the difference of the incoming photon energy and the binding energy of the electron. The binding energy is small relative to fission photon energies; therefore it is assumed that the full photon energy is converted to kinetic energy of the ejected electron. Some photons will interact through Compton scattering. In a NaI(Tl) pulse height histogram from a monoenergetic photon source, a photopeak and Compton continuum are observed, while in contrast, organic scintillators only exhibit a Compton continuum. A photopeak or full-energy peak is narrow peak that is observed when photoelectrons produced by photoelectric absorption of monoenergetic photons deposit their full energy in the scintillator.

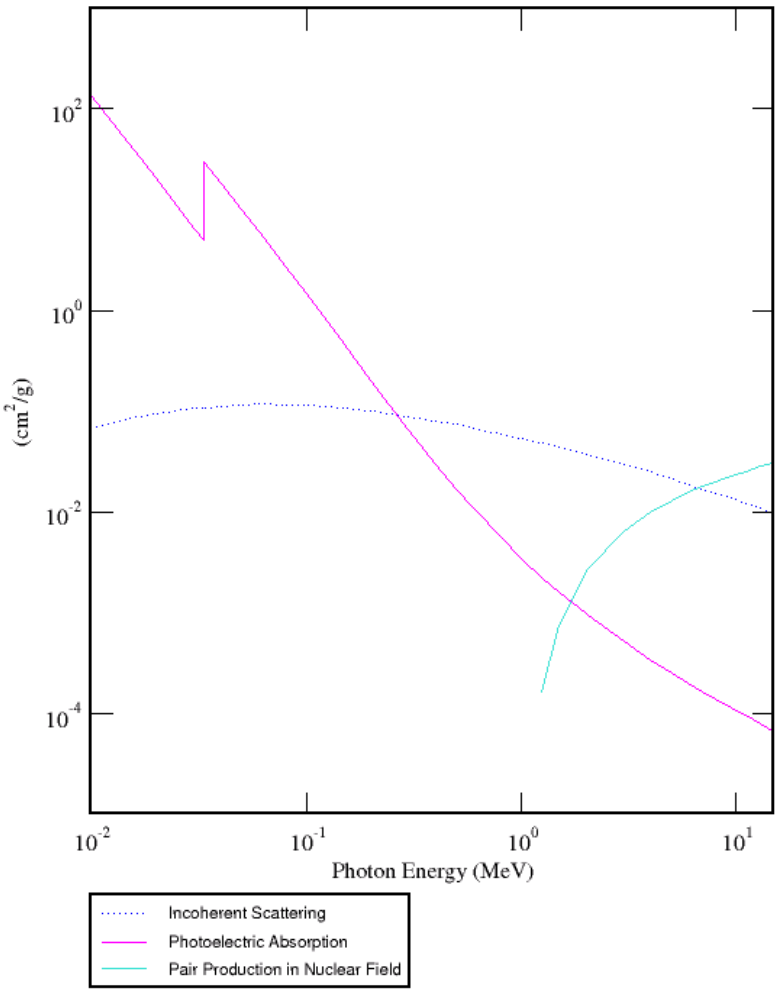

Figure 2.6: Photon reaction cross sections for NaI(Tl) [17]. Low probability reactions are omitted.

Chapter 3

Fission Experiment Modeling

Here, I describe the Monte Carlo particle transport code `MCNPX − PoliMi` used to model experiment environments and radiation sources, as well as the detector response code `MPPost` to analyze transport data. I also describe the fission event generators used by `MCNPX − PoliMi`, including its built-in event generator as well as `CGMF` and `FREYA`.

3.1 Nuclear fission

Large, neutron-rich nuclei can undergo fission, splitting into two or more fragments, spontaneously or through excitation by particle absorption [24]. Approximately 200 MeV energy is released in fission, the largest of that energy going to fragment kinetic energy (150-170 MeV) and a smaller fraction to various excitations. After scission, the instant

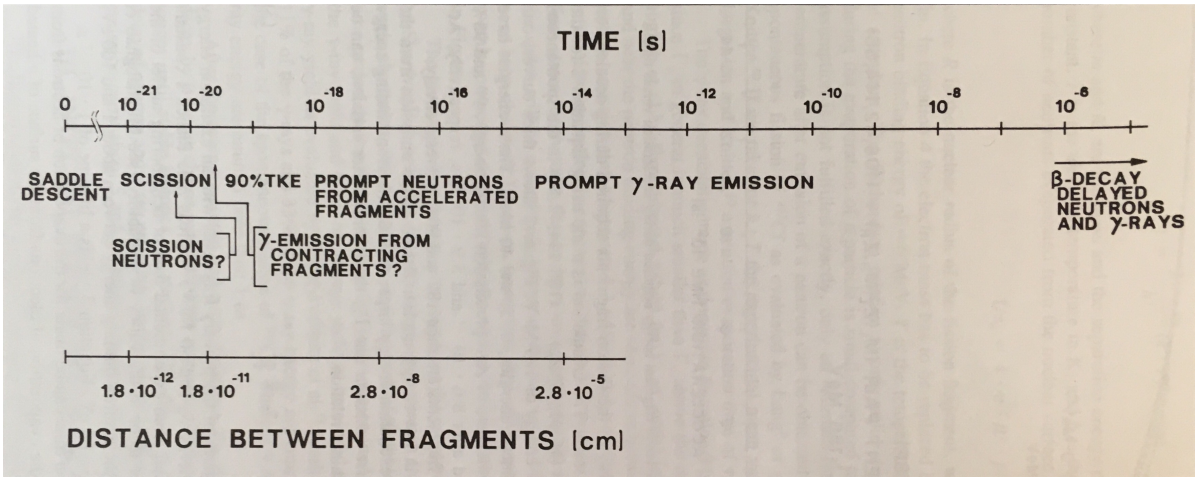

Figure 3.1: Time scale in fission [24].

when the two fragments separate, the fragments are left in an excited state as they are accelerated away from one another by Coulomb forces. The fragments then deexcite through neutron and photon emission where approximately 20 MeV goes to neutron emission and approximately 7 MeV goes to photon emission. First, neutrons are primarily emitted, then there is a transition to photon emission, shown in Figure 3.1. The discussion here is limited to prompt emissions, those from primary fragments, which are typically emitted on the order of nanoseconds after scission.

These large, neutron-rich nuclei are most stable when in an oblong shape as opposed to a sphere, shown by the local minimum at approximately a quadrupole moment of $q_2 = 1$ in Figure 3.2. The quadrupole moment describes elongation of the nucleus, where zero is a sphere. Large nuclei are most stable in oblong shapes because of competing attractive nuclear forces between both neutrons and protons and repulsive Coulomb forces primarily between protons.

The nucleus deformation can oscillate, over saddle points, between different oblong shapes and sometimes progress toward a dumbbell shape, as shown in Figure 3.2. The progression toward a dumbbell shape can occur spontaneously or through absorption. One or more potential energy barriers must be crossed when the oblong nucleus progresses toward a dumbbell shape and finally to scission at high quadrupole moments. Once the nucleus reaches a dumbbell shape, Coulomb forces can overcome nuclear forces and accelerate the two fragments away from one another. Scission occurs when the neck between the two fragments stretches and Coulomb forces begin to dominate. At the scission point, more than two fragments may form, but the most likely outcome is a binary fission.

Figure 3.2 shows a potential surface where the least resistive path to scission produces an asymmetric dumbbell – in other words, the dumbbell ends are unequal. In binary fission, fragment masses are typically asymmetric where there is one light fission fragment (LFF) and one heavy fission fragment (HFF), shown in Figure 3.3.

After scission, the fragments inhabit unique mass, charge, excitation, kinetic, and spin states which influence the neutron and photon emissions. Therefore understanding the

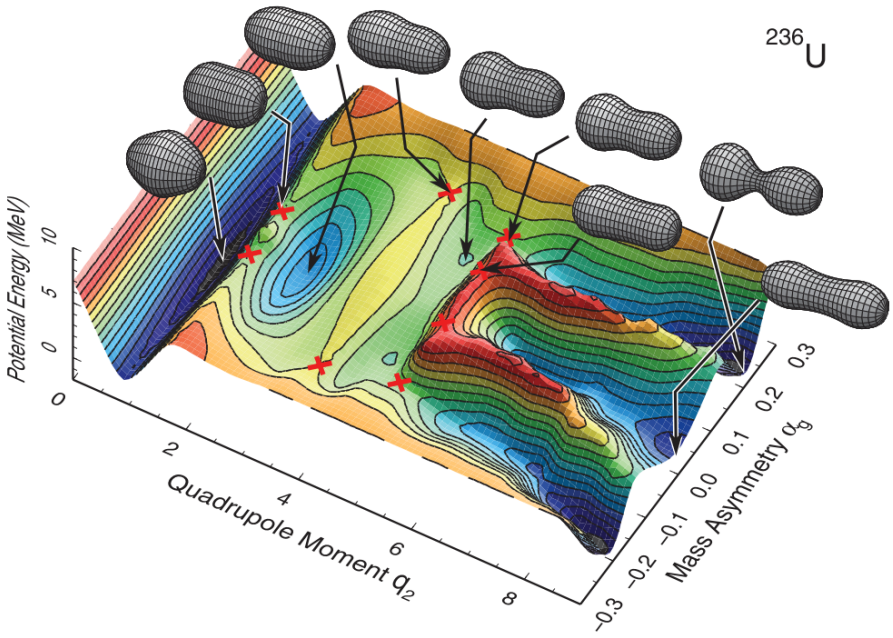

Figure 3.2: ^{236}U calculated potential energy surface as a function of quadrupole moment and a mass-asymmetry parameter [25].

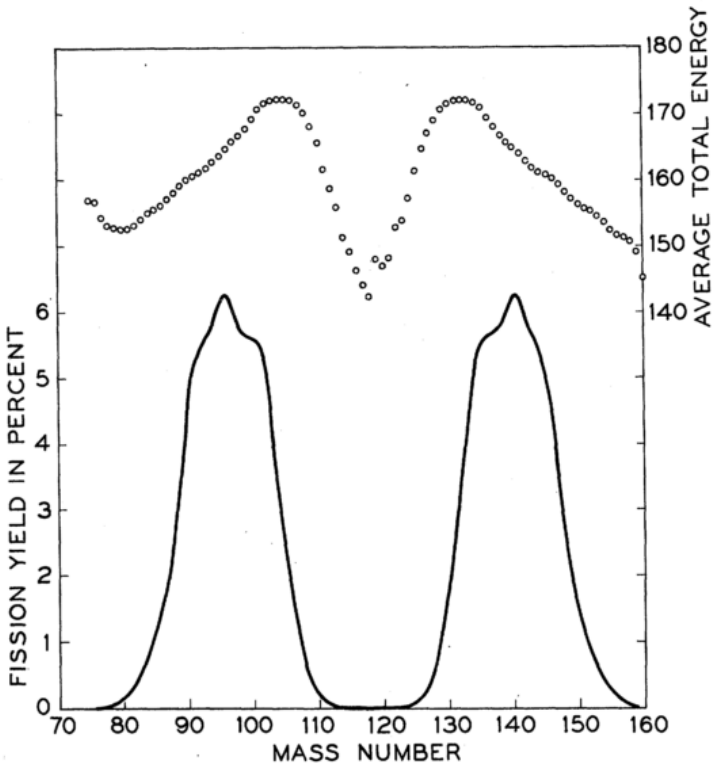

Figure 3.3: Experimental data of $^{235}U(n_{th}, f)$ fragment mass yields and average TKE as a function of mass number [26].

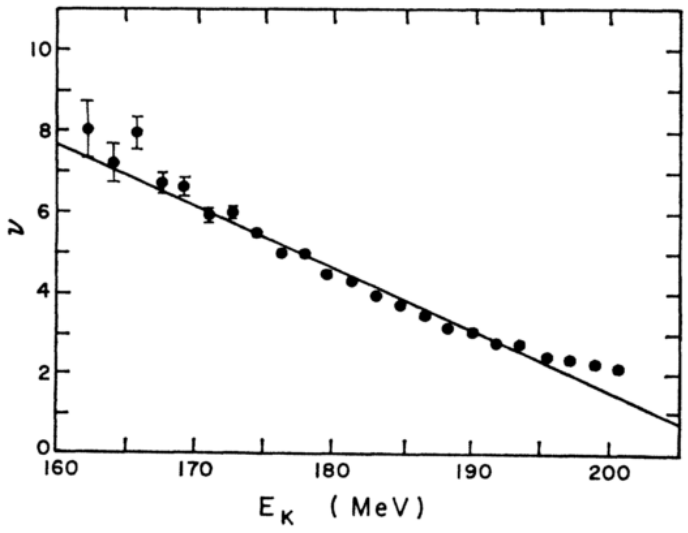

Figure 3.4: Experimental data of ^{252}Cf(sf) $\overline{\nu}$ versus TKE [27].

fragment properties just after scission is important to understanding fission emissions.

Prompt fission neutron properties are strongly correlated to fragment properties, particularly to fragment kinetic energy and mass. Energy is split between total kinetic energy (TKE) and total excitation energy (TXE), therefore we expect fragment TXE to be at a minimum where TKE is at a maximum. Neutron multiplicity decreases with increasing TKE because less excitation energy must be removed through neutron evaporation, shown in Figure 3.4. In Figure 3.5, neutron multiplicity increases with mass number up to a peak at 126 and then sharply decreases, rising again toward high masses. This behavior in neutron multiplicity indicates that larger amounts of excitation energy are present in fragments at and just below 126. Neutron energy is dependent on the nuclear temperature at the time of emission [24].

Prompt fission photon properties are also strongly correlated with fragment properties. Figure 3.6 shows that the total photon energy decreases from approximately 8.5 MeV to 5 MeV over the range of TKEs. Similar to neutron emission, as TKE increases TXE decreases and so less excitation energy must be dissipated through photon emission. Photons also dissipate remaining angular momentum from the fission fragments.

Since both neutrons and photons are removing excitation energy and angular momentum from fission fragments, we expect that on an event-by-event basis those emissions would be correlated. Initially, fragments deexcite most probably through neutron emis-

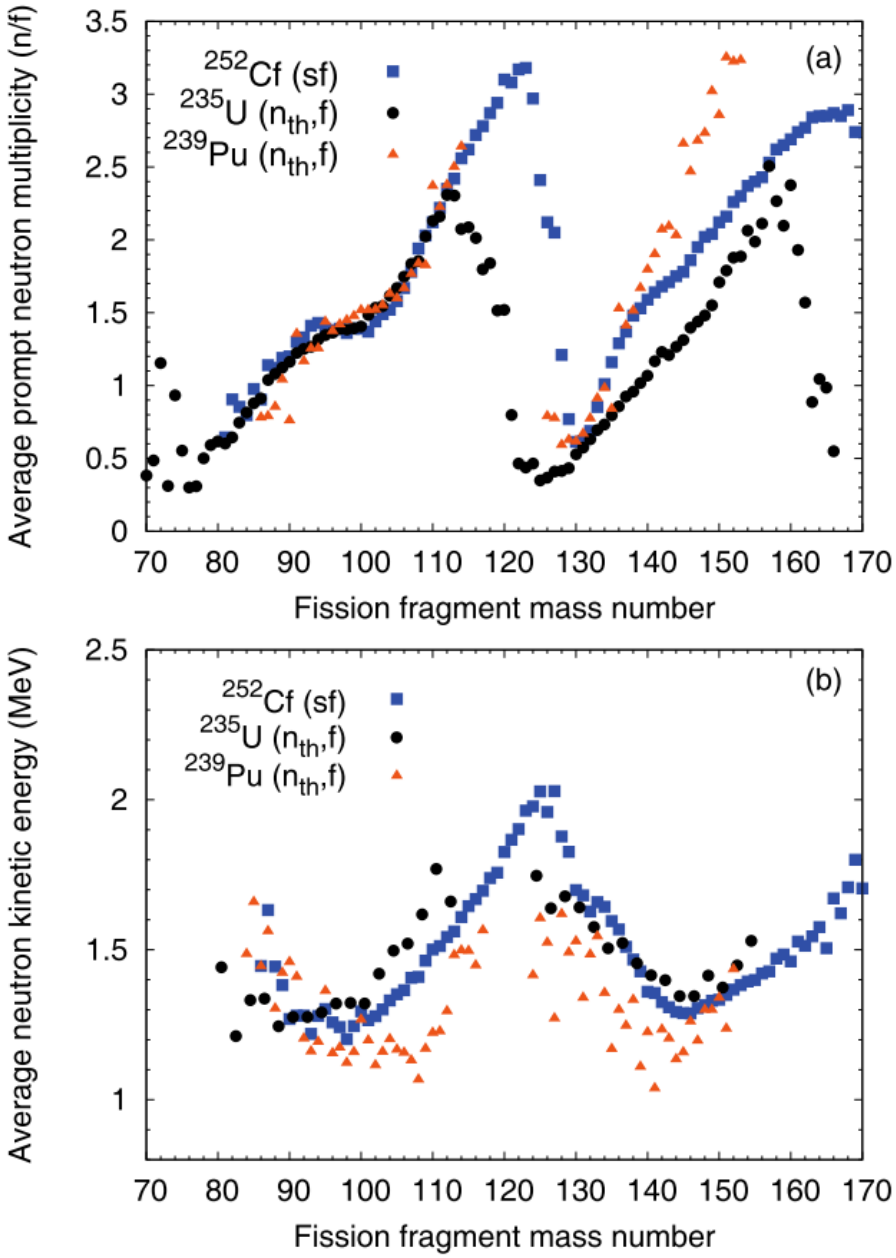

Figure 3.5: (a) Mean prompt fission neutron multiplicity and (b) mean prompt fission neutron energy in the center of mass frame as a function of fragment mass [9].

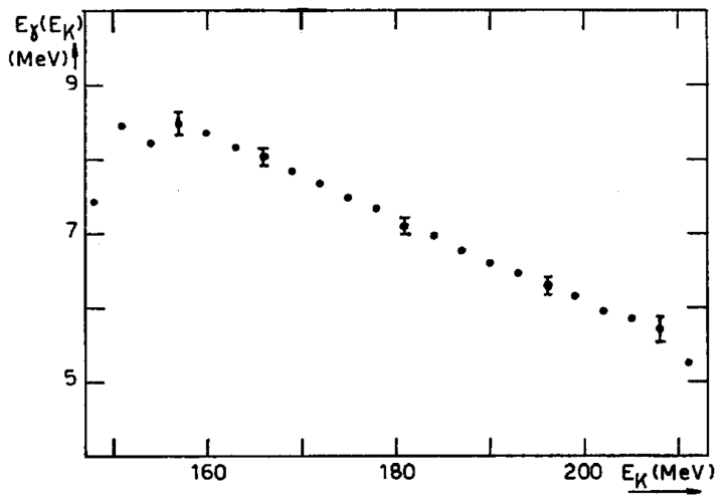

Figure 3.6: Experimental data of ^{252}Cf(sf) M_γ versus TKE [28].

sion because this process efficiently removes excitation energy. Some event-by-event fission models [12,29] emit neutrons from a fragment until the excitation energy decreases to approximately the neutron separation energy S_n, shown schematically in Figure 3.7. Following neutron emission, photons are emitted. Statistical photons are emitted until the excitation energy reaches the yrast line, then discrete photons are emitted [30, 31]. The exact mode of transition from primarily neutron emission to primarily photon emission, however, is not well understood [9].

Neutrons are emitted within a few femtoseconds after scission, but are also emitted from fully accelerated fission fragments, shown in Figure 3.1. Neutron emission angle relative to the fragment is approximately isotropic in the fragment frame of reference; given the momentum of the fragment, in the laboratory frame neutrons appear to be preferentially emitted in the directions of the fission fragments, shown in Figure 3.8. Also, the energy spectrum in the laboratory frame is slightly harder in the directions of the fragments.

Most photons are emitted from a few femtoseconds to a few nanoseconds after scission; a small fraction of photons are emitted after a few nanoseconds [33, 34]. With spin equal to 1, photons carry away not only excitation energy but also angular excitation. Photons are slightly anisotropic relative to the fragment direction [35, 36], however because the anisotropy is weak an experiment without knowledge of fragment characteristics or with

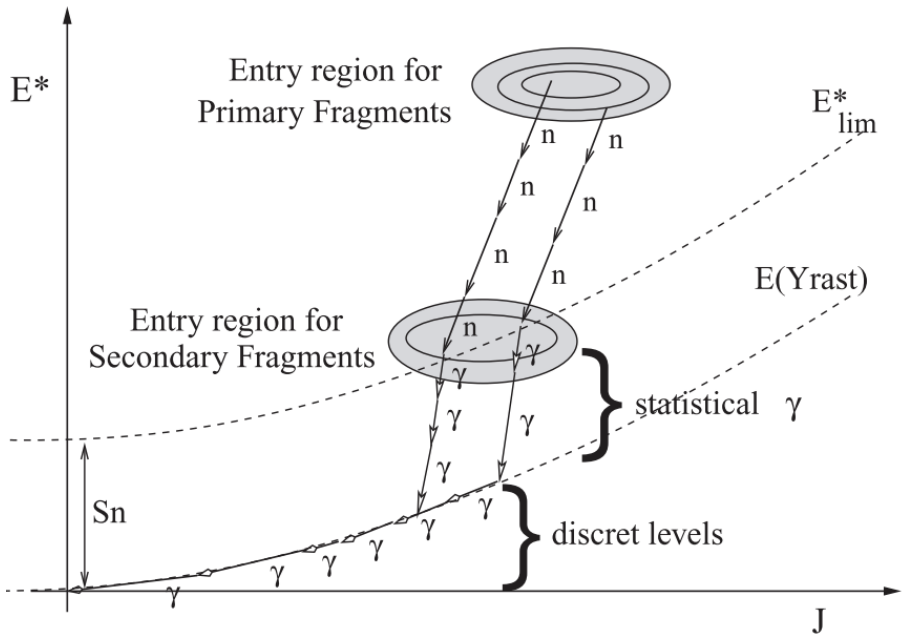

Figure 3.7: Fission fragment deexcitation through neutron and photon emission where neutrons remove excitation energy and photons remove angular momentum [31].

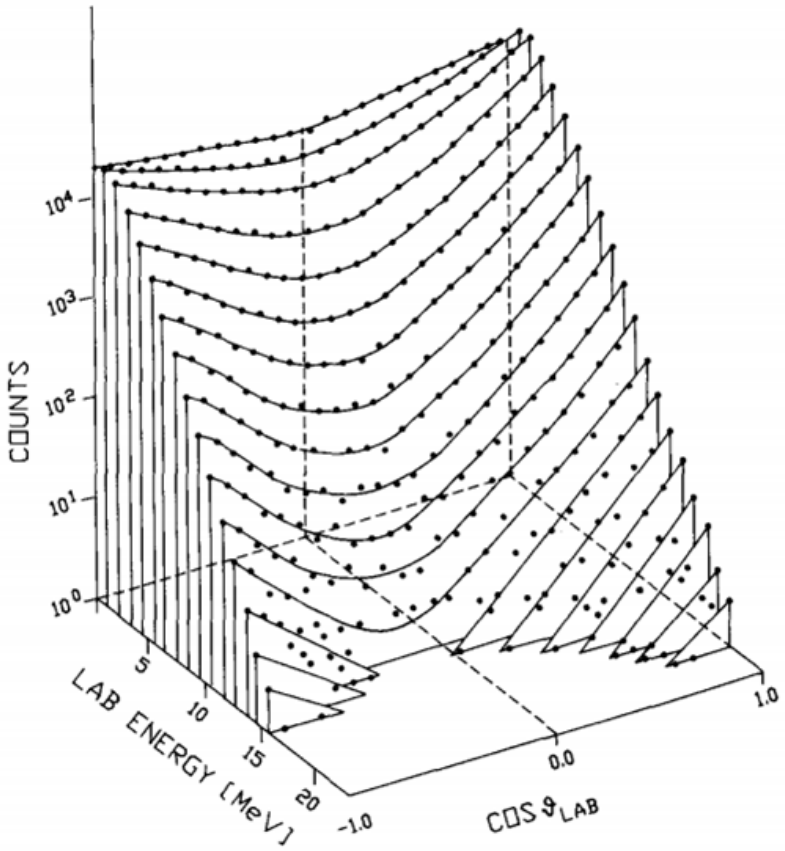

Figure 3.8: Fission neutron yield versus the laboratory neutron energy and versus the cosine of the angle between the direction of movement of the light fragment and the neutron [32].

energy spectroscopy would be insensitive.

3.2 MCNPX − PoliMi simulated fission experiments

Radiation detector response tools are used to directly connect radiation particle transport outputs from Monte Carlo N-Particle eXtended (MCNPX) code simulations to laboratory measurements [7]. MCNPX is a general-purpose code used for neutron, photon, electron, and coupled transport in arbitrary three-dimensional materials defined by geometric cells. MCNPX takes a user defined lab geometry, physics models, and source term, shown in Fig. 3.9. The MCNPX code is capable of reliably transporting radiation and recording important interactions in detectors, however MCNPX does not have the ability to translate those reactions to a laboratory-analogous detector signal for most detector types.

The PoliMi code extension to MCNPX was developed to better simulate coincidence measurements and subsequent time analyses by improved event-by-event tracking and conservation of energy and momentum on an event-by-event basis [8]. MCNPX − PoliMi has the option to track and record event information collision-by-collision in specified detector regions. For each collision, key information is recorded: history number, particle number, particle type, collision type, target nucleus, collision cell, and collision time. Recorded collision information can be used to accurately model non-linear detector responses on an event-by-event basis. Additionally, MCNPX − PoliMi samples photons produced in neutron interactions more realistically than MCNPX, because outgoing photons are sampled after the neutron interaction is sampled.

I modified MCNPX − PoliMi to read in arbitrary fission events from file, shown in Fig. 3.9. The fission event file needs to provide particle type, energy, direction, and time of emission. The MCNPX − PoliMi code also includes built-in correlations for key isotope spontaneous fissions (Cf-252, U-238, Pu-240, Pu-242, Cm-242, Cm-244, Pu-238) and (α, n) reactions.

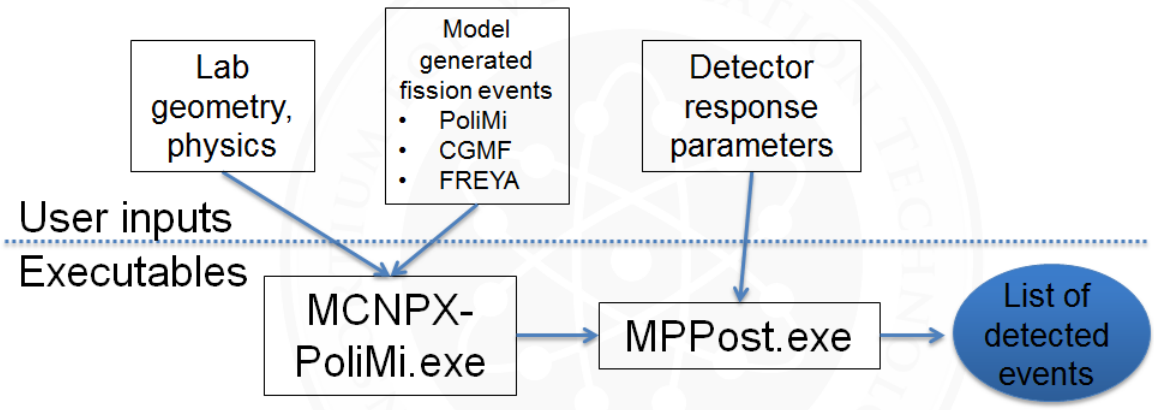

Figure 3.9: A block diagram describing the `MCNPX – PoliMi` and `MPPost` simulation tools and their inputs to reproduce detected events.

3.3 Detector response modeling and `MPPost`

`MPPost` is a detector response code used to convert `MCNPX – PoliMi` interaction file output to a laboratory-analogous detector signal, as illustrated in the Fig. 3.9 work-flow diagram. Depending on the detector being modeled, `MPPost` uses details recorded in the interaction file including interaction type, particle type, nucleus of interaction, energy deposited, and time of interaction. For scintillators, `MPPost` converts energy deposition to scintillation light, handles multiple interactions, applies resolutions, and applies thresholds to ultimately record a list of detected pulses. The list of detected pulses includes for each event: particle type, light output, and time of detection.

For scintillators, key detector dependent parameters in `MPPost`, which the user must input, include upper and lower light output thresholds, energy dependent resolution, light output on electron and proton recoils, and time resolution. The energy or light output resolution, $\Delta E/E$ where ΔE is the full-width half maximum (FWHM), is energy dependent and follows

$$(\frac{\Delta E}{E}) = \sqrt{\alpha^2 + \frac{\beta^2}{E} + \left(\frac{\gamma}{E}\right)^2} \tag{3.1}$$

[37]. The energy resolution is assumed to be Gaussian. The time resolution is sampled from a single Gaussian with user specified FWHM.

`MPPost` has a few models for light output on scatter events: linear, exponential [38], and Birks [39]. The linear model was used to approximate light output from electron

recoils, and the exponential and Birks models were used to approximate light output from proton recoils in the stilbene. The Birks model

$$L(E) = \int_E^0 \frac{S}{1 + k_B \frac{dE}{dx}} dE \tag{3.2}$$

takes two coefficients, the scintillation efficiency S and Birks material-dependent constant k_B with a material dependent stopping power dE/dx to give the light production L for a recoil energy E, shown in Fig. 2.3. The Birks model is a semi-empirical function to account for ionization quenching along the recoil particle's path. Quenching increases with ionization density which also follows stopping power. The exponential, however, takes up to five coefficients. Within a pulse generation window, `MPPost` converts each interaction that deposits energy to light then sums those light outputs to create a final light output. It is critical that energy is converted to light and then summed because the light output is not linear with energy deposited for proton recoils, shown in Fig. 7.5. Resolution broadening is applied after the light is summed.

`MPPost` accurately reproduces detector response under most conditions. The code does not treat pulse pile-up or dead time, however one can remove pile-up and dead time events manually from the produced pulse list. Additionally, `MPPost` assumes perfect pulse classification by particle type, whereas particle discrimination in experiment is typically not ideal and events may be misclassified.

3.4 Fission models

Three fission models were used in this work: the built-in `MCNPX` − `PoliMi` (referred to as `PoliMi`), `CGMF`, and `FREYA`. See Ref. [9] for more details and model comparisons. The discussion here is focused on event-by-event neutron and photon correlations.

The general purpose transport code `MCNPX` − `PoliMi` [8,40] was used to transport particles from all three fission models. The `PoliMi` spontaneous-fission source uses evaluated multiplicity distributions and energy spectra for prompt neutrons and photons [40]. Because neutrons and photons are sampled independently, no correlation between particle

types is predicted. However, neutrons are correlated with the sampled fission fragment direction in the laboratory frame because of the fragment momentum boost.

MCNPX − PoliMi built-in spontaneous fission sources use evaluated data for the integral energy and multiplicity spectra. The neutron energy spectrum is, however, multiplicity dependent. As multiplicity increases, the energy spectrum softens. MCNPX − PoliMi assumes that, in the fission fragment momentum frame, neutrons are emitted isotropically; therefore in the laboratory frame, with imparted momentum from the fission fragments, neutrons are anisotropic and have slightly higher energies. To impart momentum from the fission fragments, MCNPX − PoliMi assumes constant fragment masses and kinetic energies. The model samples the number of neutrons emitted from each fragment from a symmetric triangle distribution. The triangle distribution is centered around an equal number of neutrons being emitted from each fragment. Photons are emitted isotropically.

The CGMF code [11, 29, 41, 42], developed at Los Alamos National Laboratory, is a Monte Carlo implementation of the statistical Hauser-Feshbach nuclear reaction theory. As input, CGMF takes fragment mass, charge, and total kinetic energy (TKE) yields as well as ground-state masses to calculate excitation energies. The code follows the fission fragments immediately after scission through de-excitation by sequential neutron and photon emission. CGMF uses a mass-dependent parameter to better reproduce the experimental mass-dependent neutron multiplicity and uses a single parameter to fix the initial fragment spin distribution. Because Hauser-Feshbach nuclear reaction theory is used, both neutrons and photons could be emitted during any stage of the de-excitation process. However, as the fragment de-excites, photon emission becomes more likely. The calculated neutron-photon competition is strongly influenced by the spin distribution in each fragment produced. A higher spin leads to more photons being emitted, at the expense of emitted neutrons.

FREYA v2.0.2 (Fission Reaction Event Yield Algorithm), developed at Lawrence Berkeley and Lawrence Livermore National Laboratories, calculates emissions from complete fission events on an event-by-event basis [12,43,44,45,46,47,48]. Similar to CGMF, FREYA requires fragment mass and charge yields as inputs as well as tabulated ground-state masses.

FREYA also requires the fragment TKE as a function of heavy fragment mass rather than the yields as a function of TKE, as in CGMF. Similar to CGMF, FREYA uses a single parameter to modify the initial spin distribution. As opposed to CGMF, FREYA currently uses a single, fixed parameter to determine fragment excitation energy sharing. Neutron evaporation occurs until the nuclear excitation energy is at or below the neutron separation energy where photon emission takes over. FREYA produces negatively-correlated neutron and photon multiplicities, similar to CGMF.

In Figs. 3.10, 3.11, and 3.12, the calculated distributions for neutron and photon emission from ^{252}Cf(sf) are shown for PoliMi, CGMF, and FREYA. Shown in Fig. 3.10, there is no correlation between neutrons and photons with PoliMi. Both CGMF and FREYA exhibit negative correlations between the particle multiplicities on an event-by-event basis. The trends from these two calculations are the same but have different absolute scales.

Figure 3.11 compares the fission model neutron and photon energy spectra. PoliMi uses the Mannhart [49] ^{252}Cf(sf) neutron energy spectrum evaluation, shown in Fig. 3.11(a). The calculated CGMF ^{252}Cf(sf) neutron spectrum is softer than the evaluation spectrum, Mannhart [49], whereas the calculated FREYA spectrum is harder. Figure 3.11(b) compares the photon spectra to an experiment by Billnert *et al.* [50]. PoliMi uses the Valentine [51] ^{252}Cf(sf) photon evaluation, shown in Fig. 3.11(b). Above 1 MeV, all calculated photon spectra are harder than the Billnert *et al.* data. The PoliMi and FREYA photon spectra are in agreement with each other, but the CGMF spectrum is slightly higher between 1 and 3 MeV.

Figure 3.12 compares the fission model neutron and photon multiplicity distributions. PoliMi uses the Santi and Miller [52] evaluation for its ^{252}Cf(sf) neutron multiplicity distribution. Reflecting the mean neutron multiplicities shown in Fig. 3.10, the PoliMi and FREYA neutron multiplicity distributions are similar while CGMF shows a slightly higher distribution. PoliMi uses Valentine and Mihalczo [53] for its ^{252}Cf(sf) photon multiplicity distribution. While the PoliMi and FREYA mean photon multiplicities are similar, shown in Fig. 3.10, the FREYA distribution is narrower than the PoliMi distribution. The

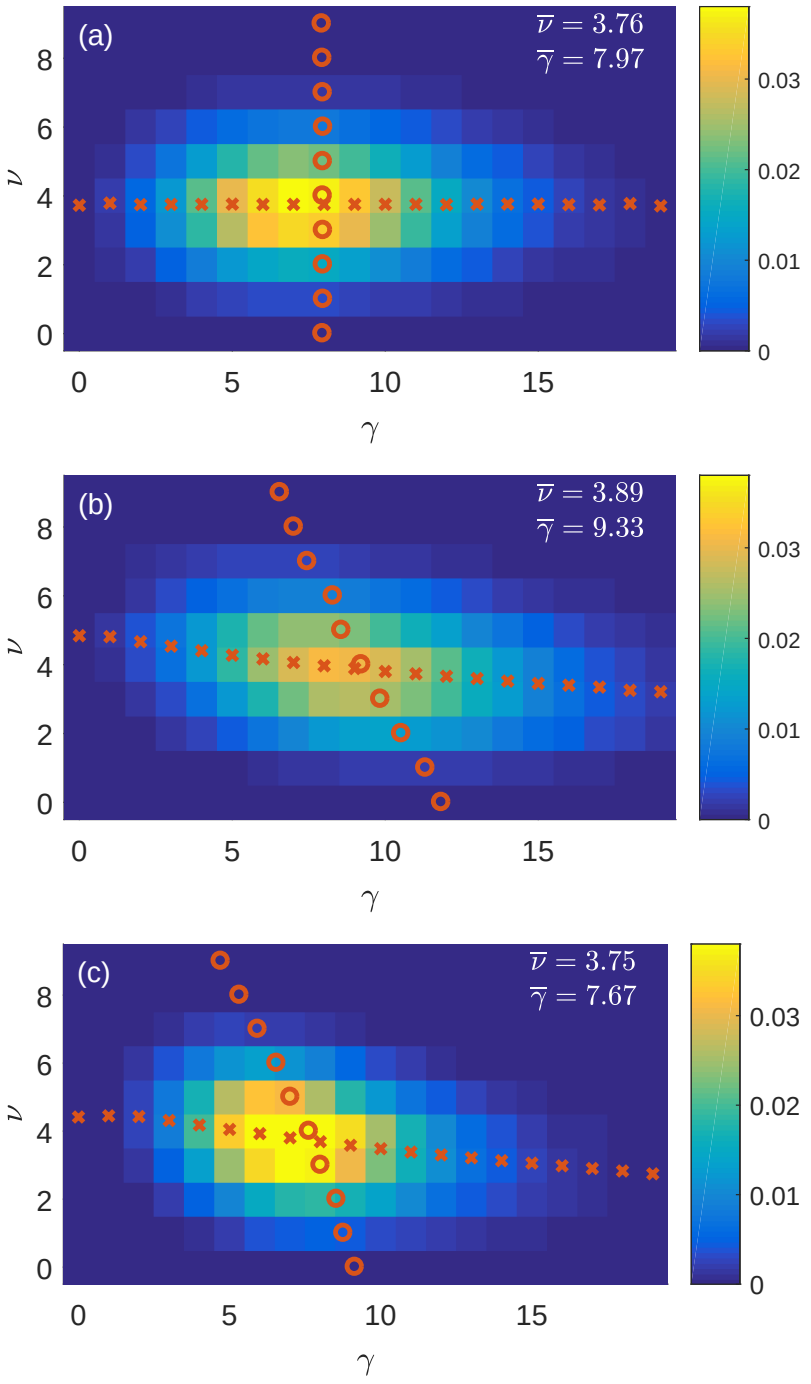

Figure 3.10: ^{252}Cf(sf) neutron (y-axis) and photon (x-axis) multiplicities with mean neutron, $\overline{\nu}$, and mean photon, $\overline{\gamma}$, multiplicities from `PoliMi` (a), `CGMF` (b), and `FREYA` (c) with $E[\nu|\gamma]$ (x) and $E[\gamma|\nu]$ (o) overlaid.

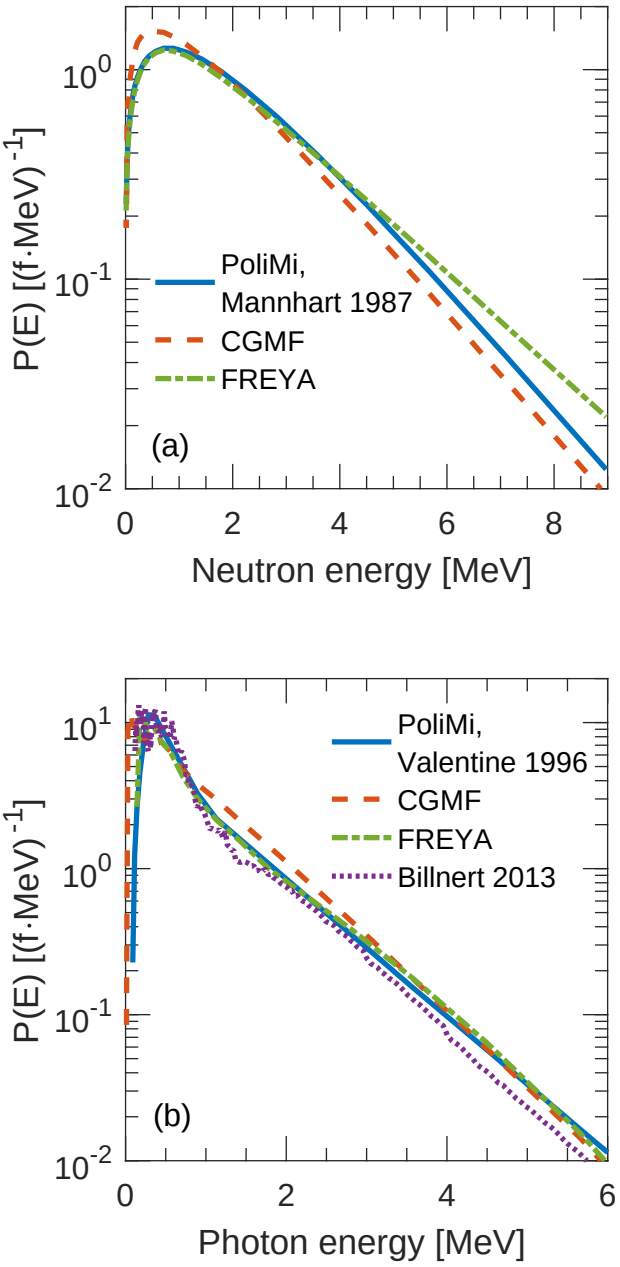

Figure 3.11: ^{252}Cf(sf) neutron (a) energy spectra from `PoliMi`(uses Mannhart [49]), `CGMF`, and `FREYA`. ^{252}Cf(sf) photon (b) energy spectra from `PoliMi`(uses Valentine *et al.* [51]), `CGMF`, `FREYA`, and Billnert *et al.* [50].

CGMF photon multiplicity distribution is significantly higher than the other data, which is caused by a lower photon threshold than PoliMi or FREYA.

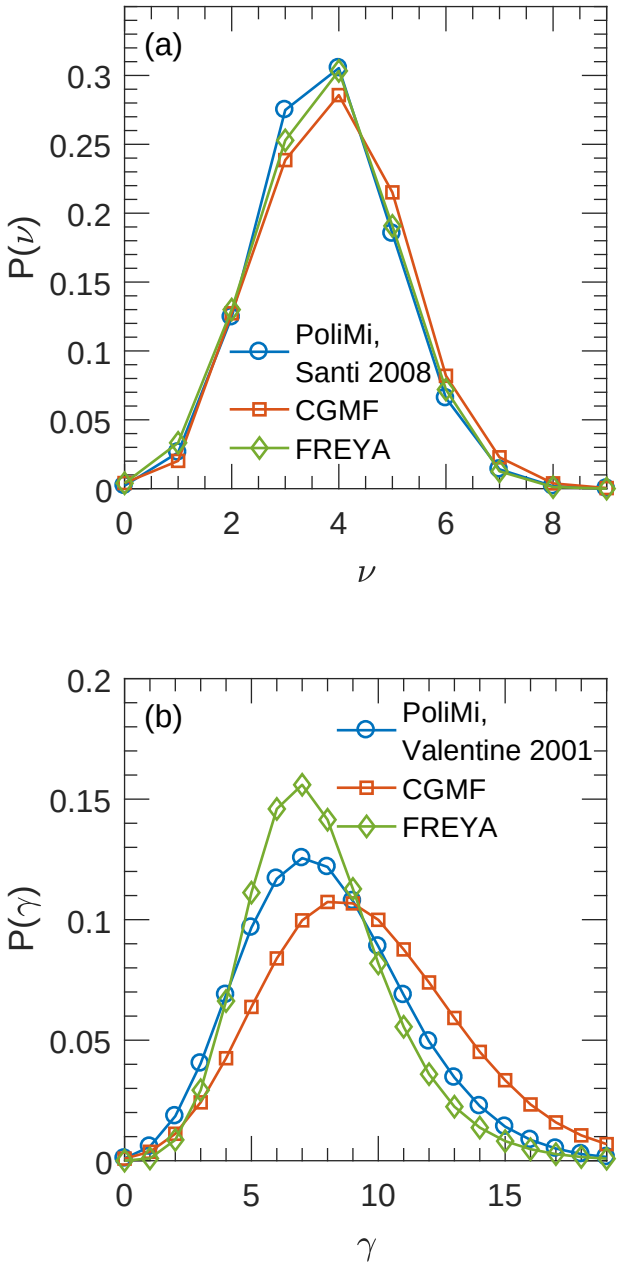

Figure 3.12: ^{252}Cf(sf) neutron (a) multiplicity distributions from `PoliMi` (uses Santi and Miller [52]), `CGMF`, and `FREYA`. ^{252}Cf(sf) photon (b) multiplicity distributions from `PoliMi`(uses Valentine *et al.* [53]), `CGMF`, and `FREYA`.

Chapter 4

Neutron Angular Distribution in ^{240}Pu(sf) from the Joint Research Centre Experiment in Ispra, Italy

This chapter describes work performed to quantify the anisotropy in neutron emission from ^{240}Pu(sf) and is taken from my publication on the work [54]. In this work, J. L. Dolan took measurements of plutonium fission neutrons using an organic scintillator array and acquisition system at the PERLA laboratory at the Joint Research Centre at Ispra, Italy [55]. I analyzed the raw waveform data for angular correlations and modeled the experiment with `MCNPX` − `PoliMi` and `MPPost` to produce the results shown here.

4.1 Introduction

Plutonium is a special nuclear material that can be used in the core of a nuclear weapon. The odd-numbered isotopes of plutonium, in particular ^{239}Pu, are used to sustain a fission-chain reaction. However, bulk plutonium always contains some percentage of ^{240}Pu, which has a relatively high spontaneous fission rate, approximately 40,000 times greater than ^{239}Pu. This feature makes plutonium detectable and quantifiable by passive means, and more specifically by counting neutron doubles [56]. In fact, fission generates multiple prompt neutrons emitted in coincidence. Over 70% of ^{240}Pu spontaneous fissions emit more than one neutron [52].

Detection and characterization of special nuclear material could rely on knowledge of fission neutron anisotropy [8,10,46,57]. In fission, an anisotropic neutron angular distribution is observed in the laboratory reference frame because neutrons emitted isotropically in the fission fragment frame of reference carry momentum from the fully accelerated fission fragment [24, 46]. Current nonproliferation and verification neutron measurement systems, however, rely on detecting thermalized neutrons; the neutron properties at the time of emission are obscured by down-scattering. When fast neutron detectors are used, the neutron-neutron correlation from fission can be used to characterize fissile samples. Neutron-neutron correlation can distinguish metal from oxide and can estimate the fission to (α, n) rate [58]. In metals, fission neutrons are dominant, while in oxides, fission and (α, n) neutrons are both present. Fission neutrons are emitted anisotropically; (α, n) reactions, present in oxides, emit single neutrons, therefore chance neutron-neutron coincidences from (α, n) reactions are observed isotropically. Only cross-talk neutron coincidences from (α, n) would be observed anisotropically, biased toward zero degree coincidences.

Many fission neutron angular correlation experiments have quantified anisotropy in fission neutron emission [10, 27, 59]; no published work exists, however, that investigates ^{240}Pu spontaneous fission neutrons. Previous experiments characterize neutron correlations in ^{239}Pu thermal neutron induced fission, for which an excited state of ^{240}Pu is formed prior to fission, but conclusions from this data are not directly applicable to ^{240}Pu spontaneous fission [60].

Experimental results are presented here on correlated ^{240}Pu spontaneous fission prompt neutrons, expanding on work performed by Dolan and colleagues [55]. Specifically, we present new results on the angular correlation of prompt neutrons from ^{240}Pu fission. These experimental results are compared to simulations performed with the `MCNPX − PoliMi` v2.0.0 Monte Carlo code. Cross-talk coincidence effects are estimated with `MCNPX − PoliMi` simulations and are removed from the experimental neutron-neutron angular distributions.

4.2 Experiment

The experiment consisted of two plutonium experiments, using a 0.84 g and 1.63 g $^{240}Pu_{eff}$ sample, hereby designated PM2 and PM3. The quantity $^{240}Pu_{eff}$ mass is a convenient mass definition for neutron coincidence counting [56] where $^{240}Pu_{eff}$ is the weighted sum of even plutonium isotope masses in the sample

$$^{240}Pu_{eff} = 2.52^{238}Pu + ^{240}Pu + 1.68^{242}Pu. \tag{4.1}$$

PM2 and PM3 were encased in aluminum right circular cylinders with inner cavity of 2.6 cm diameter and 3.3 cm height, wall thickness 0.3 mm, and top and bottom of 6.5 mm. The PM2 plutonium metal was 1 cm in diameter and 1.32 cm in height and was 2.23 cm from the bottom of the encasement and was placed 11 cm above the table surface at the center of the array. The PM3 plutonium material was 1.145 cm in diameter and 1.145 cm in height and was 2.23 cm from the bottom of the encasement and was placed 17.02 cm from the table surface at the center of the array. A ^{252}Cf sample was also used and was placed 17 cm above the table surface at the center of the array. At the time of the experiment, the plutonium metal samples had fission rates of 400 and 760 fissions/s for PM2 and PM3, respectively; the ^{252}Cf sample had a fission rate of 26,000 fissions/s. The experiment was performed at the PERLA laboratory at the Joint Research Centre at Ispra, Italy [55].

Shown in Fig. 4.1, $16 - 7.62\varnothing \times 7.62$ cm EJ-309 organic liquid scintillation detectors were used to measure neutron-neutron coincidences from the plutonium samples. Two concentric 8-detector rings were stacked; samples were placed along the central detector ring axis. The sample was shielded with a 1-cm thick lead cylinder 13 $cm\varnothing$ and 31.5 cm in height to reduce the gamma-ray count rate and acquisition dead time. Each detector was approximately 18 cm from the central axis; the top and bottom detector rings are separated by 10.6 cm from detector centers. Two time-synchronized CAEN V1720 digitizers were used to collect 120-sample pulses. Pulses above a 70-keVee threshold were recorded for offline processing. A 70-keVee acquisition threshold and a 2 V dynamic range

used in this experiment correspond to a range of 0.65 to 6.7 MeV proton recoils.

Pulse shape discrimination by digital charge integration was used to discern neutron detection events from gamma-ray detections [16, 20]. The pulse tail of a gamma-ray interaction decays faster than a pulse of the same height from a neutron interaction. Waveforms that exhibit pile-up are eliminated, and then a ratio of the pulse tail integral to the total pulse integral was used to distinguish gamma-ray and neutron detection events, shown in Fig. 4.2 for the PM2 sample. The PSD line was assigned using an algorithm described by Polack and colleagues that minimizes particle misclassification by analyzing segments of the tail-to-total integral points grouped by total integral [22]. The photon-to-neutron ratio for this sample was approximately 100:1 making PSD difficult at low pulse heights. The detection time differences of particles in a 60-ns coincidence window were used to create cross-correlation distributions with 2-ns bins for each detector pair.

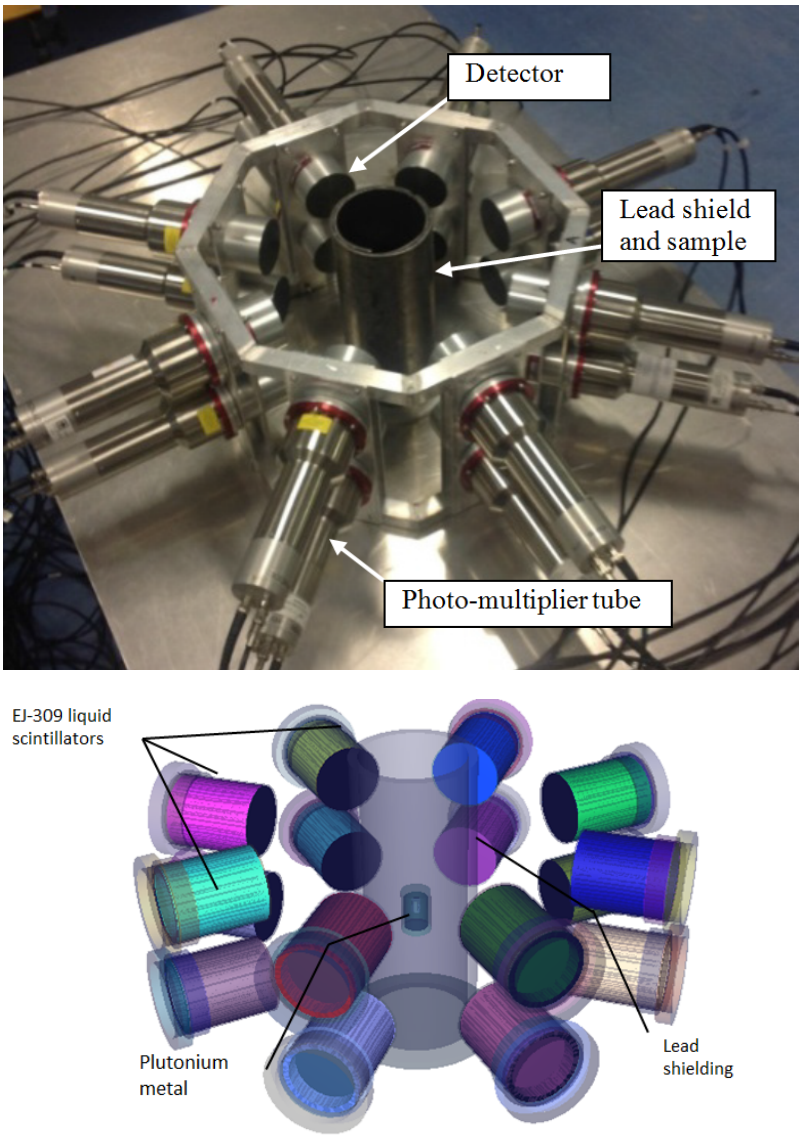

Figure 4.1: (a) A photograph of the experiment setup with a plutonium metal sample centered inside a lead shield and (b) the simulated plutonium metal experiment setup with EJ-309 7.62⌀ × 7.62 cm organic liquid scintillator detectors, plutonium metal, and lead shield are shown.

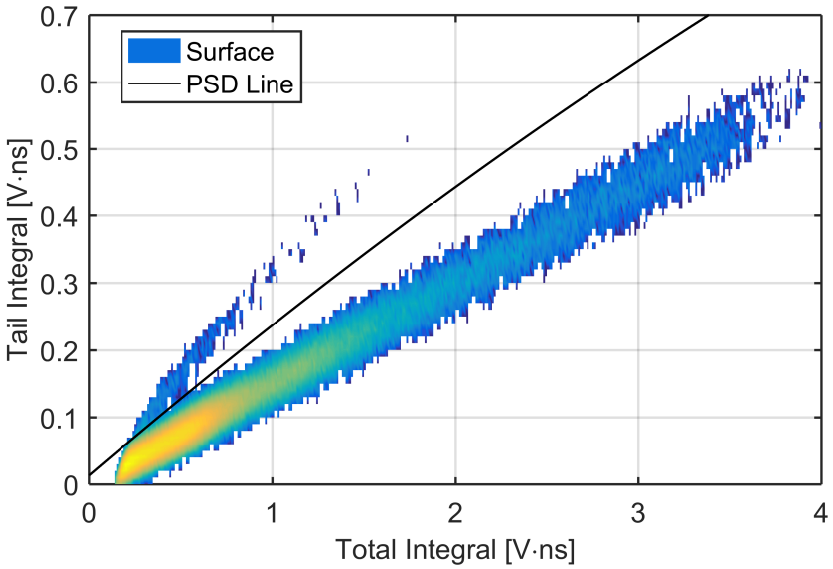

Figure 4.2: Experiment pulse shape discrimination plot of tail to total pulse integrals for 290,000 pulses from the PM2 sample. Color scaling is logarithmic ascending to yellow. Neutrons lie above the discrimination line.

4.3 Simulation with MCNPX – PoliMi

The MCNPX – PoliMi and MPPost codes were used to model the experiment geometry, the plutonium metal sample, and the detector response [8]. The experiment assembly is shown in Fig. 4.1(a) and the corresponding simulation model is shown in Fig. 4.1(b). The detector photomultiplier tubes, detector holder, aluminum table, and concrete floor were also modeled in simulation, but were omitted from the figure for clarity. The full MCNPX – PoliMi model input file for this experiment can be found in Appendix 1.

Each plutonium metal sample was modeled as a metal cylinder with composition described in Tables 4.1 and 4.2. The cylinder was topped by a void, and the void and cylinder were encased in aluminum.

The full isotopic composition of the samples was modeled in the material definition. Most fissions are from ^{240}Pu spontaneous fissions; only 0.5% and 0.9% of the spontaneous fissions are from ^{242}Pu for the PM2 and PM3 samples respectively. Less than 0.002 fissions per second are expected from ^{238}Pu spontaneous fission, therefore that contribution was ignored. The PoliMi mixed-source option, IPOL(1) = 99, was specified to sample from ^{240}Pu and ^{242}Pu built-in models. Using the plutonium metal sample MCNP model and the

Table 4.1: Plutonium metal sample isotopic composition.

Isotope	PM2 Weight Fraction	PM3 Weight Fraction
Ni	0.0504	0.0167
Cu	0.0319	0.0427
^{238}Pu	0.00004	0.00023
^{239}Pu	0.87367	0.85141
^{240}Pu	0.04076	0.07891
^{241}Pu	0.00028	0.00089
^{242}Pu	0.00013	0.00044

Table 4.2: Plutonium sample properties.

Sample property	PM2	PM3
Total Mass [g]	20.4	26.4
Density [g/cm^3]	19.7	22.4
240Pu Effective Mass [g]	0.84	1.63

spontaneous fission source term, it was estimated that approximately 8.4% and 10% of fissions are induced rather than spontaneous for PM2 and PM3. Also, approximately 88% and 79% of fission neutrons in the detectable range escaped the container and metal before interacting.

There are 120 possible detector pairings of 13 unique detector-sample-detector angles. Angles were calculated using the simulated mean neutron scatter position in the detectors for scatters above the minimum detectable energy. Unique angles within 2 degrees of another were combined for 9 unique angle groups for PM2 and 10 groups for both PM3 and ^{252}Cf, shown in Table III. Variable sample position along the detector array central

Table 4.3: Detector-sample-detector angles in degrees for each sample position.

$PM2$		$PM3$		^{252}Cf	
Angle [°]	Uncertainty [°]	Angle [°]	Uncertainty [°]	Angle [°]	Uncertainty [°]
28	10	27	11	28	8
42	12	41	11	44	15
45	12	45	11	53	11
52	12	51	12	87	14
83	13	80	12	93	11
91	13	91	13	127	14
120	11	114	9	136	13
135	11	132	10	149	12
166	13	158	9	154	14
		175	11	177	18

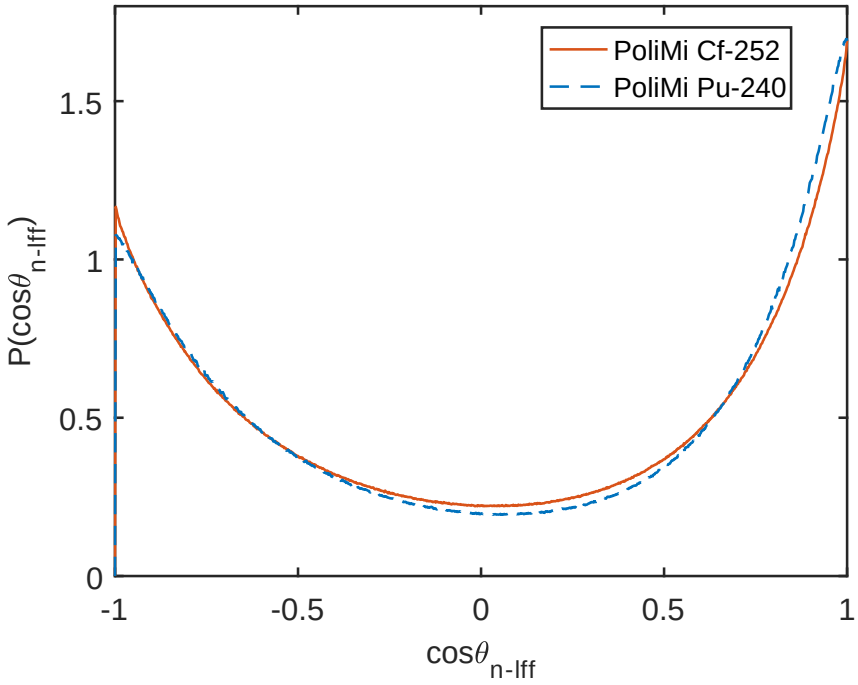

Figure 4.3: MCNPX – PoliMi neutron angular frequency relative to the light fission fragment direction for ^{252}Cf and ^{240}Pu spontaneous fission neutrons.

axis resulted in different angle groups for each sample. Estimated angular uncertainty was determined by the neutron scatter location variance, shown in Table 4.3. The uncertainty varied for each angle grouping with the largest uncertainty being 13 degrees for the PM2 and PM3 cases and 18 degrees for the ^{252}Cf case. The average uncertainty in angle for each sample was 12 degrees, 11 degrees, and 13 degrees for PM2, PM3, and ^{252}Cf respectively.

The MCNPX – PoliMi ^{240}Pu spontaneous fission neutron model includes a multiplicity-dependent energy spectrum, multiplicity from zero to six, and anisotropy. Neutron angular distributions relative to the light fission fragment direction for ^{252}Cf and ^{240}Pu are shown in Fig. 4.3.

4.4 Results and analysis

Experimental PM3 pulse height and time cross-correlation distributions are compared to simulated results to validate the MCNPX – PoliMi and detector response model. The neutron-neutron coincidence events versus detector pair angle for both experiment and

simulation were compared and are followed by subtraction of cross-talk coincidence events from the experiment results.

4.4.1 Simulation Model Validation

Simulated and experimental neutron pulse height distributions, shown in Fig. 4.4, for the top and bottom rings of detectors were binned. Two detectors in the array were removed from the results due to inconsistent pulse height responses. Differences between the integral counts for the top and bottom ring distributions are due to the samples placement slightly below the center plane of the detector array. The simulated pulse height distribution under-predicts the experiment result by approximately 20% point-by-point over the dynamic-range, with exception at the lowest pulse height bin. Gamma-ray misclassification increases toward lower pulse heights and is likely the source of larger disagreement at low pulse heights. Consistent under-prediction suggests that the aged fission rate used in the simulation is low. Improved agreement, with a single detector and lower gamma-ray to neutron ratio, was demonstrated in work by Pozzi and colleagues [61] when using a 3.3 cm lead shielded PM3 sample and a 7.62⌀5.1 cm EJ-309 detector.

Overall, the `MCNPX − PoliMi` and `MPPost` models adequately reproduce experimental pulse height distributions. Underestimation of the singles neutron rate does not impair the ability to model double coincidences including trends in neutron-neutron time or angular correlations.

The PM3 time cross-correlation distributions from simulation agree well with the experiment in shape for the 90-degree detector pair (Fig. 4.5(a)) and for the 175-degree detector pair (Fig. 4.5(b)). Results show that there are fewer counts in the 90-degree detector pair distribution than the 175-degree pair distribution because of the strong anisotropy in neutrons from spontaneous fission. The simulation result slightly underestimates the experiment count rate for the 175-degree case. Uncertainty in the plutonium sample position and incorrect neutron anisotropy models in simulation contribute to disagreement in Fig. 4.5(b). The distribution agreement in Fig. 4.5(a) and attributed disagreement in Fig. 4.5(b) validates the `MCNPX − PoliMi` and `MPPost` models used to rep-

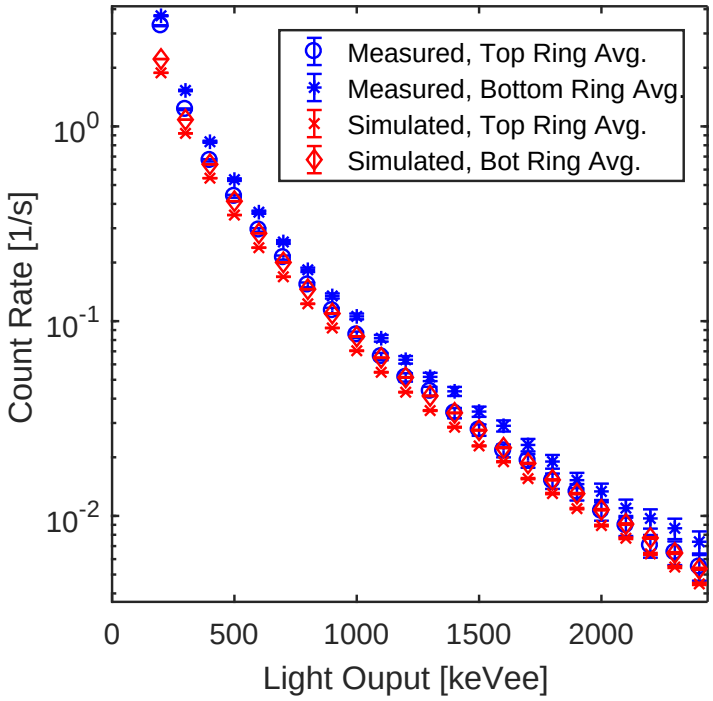

Figure 4.4: Experiment and simulated PM3 neutron pulse height distributions with a 100 keVee threshold for the average of the top ring and the bottom ring. One standard deviation statistical error bars are shown.

resent the laboratory environment and detector response. The accidental neutron-neutron coincidence rate was negligible relative to the true rate and was ignored in coincidence analysis. The accidental rate is shown in Figure 4.5 at large $\mid \Delta T \mid$.

For each unique angle, the neutron-neutron cross-correlation time distribution was integrated over a 60-ns window to give the total coincidence count rate, shown in Fig. 4.6. Each neutron-neutron coincidence point is normalized by solid angle, detector pairs, and fission rate. Figure 4.6 highlights that a neutron is more likely to be emitted at small angles or very large angles relative to another neutron than to be emitted at angles around 90 degrees.

The `MCNPX` − `PoliMi` distributions in Fig. 4.6 match general features of the experimental distribution. The simulation underestimates the experimental count rate at angles larger than approximately 50 degrees, while the simulation overestimates at angles smaller than 50 degrees. The `MCNPX` − `PoliMi` fission model has too many low angle coincidences relative to the experiment result. The simulation result with cross-talk removed shows better agreement over a larger range of angles with the experiment result; cross-talk events are easily identified and removed in simulation space. The cross-talk removed results show that many low angle coincidences are from cross-talk and the cross-talk fraction diminishes toward large angles.

4.4.2 Cross-talk Effect

Cross-talk occurs when a single neutron is detected by more than one detector, mimicking a true coincidence of two neutrons. The probability of cross-talk for a given neutron spectrum and detector array can be reduced by inter-detector geometric attenuation, by shielding, or by an increased detection threshold. Inter-detector geometric attenuation or increased thresholds are not feasible, because the true coincidence count rate would also be reduced. The cross-talk fraction is reduced as the light output threshold is increased because the once-or-more scattered, lower-energy neutron falls below threshold more often than a direct, unscattered source neutron. Shielding attenuation was avoided in this work to minimize in-scattering of neutrons.

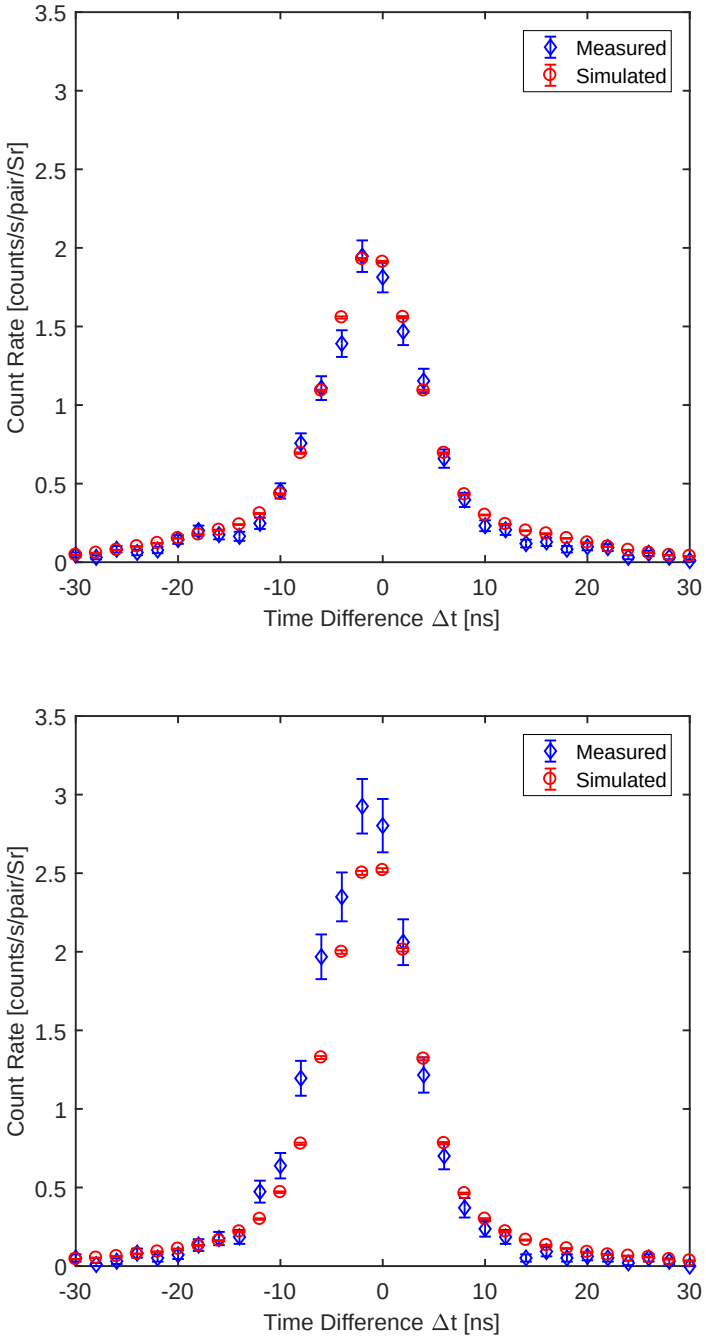

Figure 4.5: Experiment and simulated (`MCNPX – PoliMi`) PM3 neutron-neutron cross-correlation time distributions for 90-degree (a) and 175-degree (b) detector pairs with one standard deviation statistical uncertainty error bars.

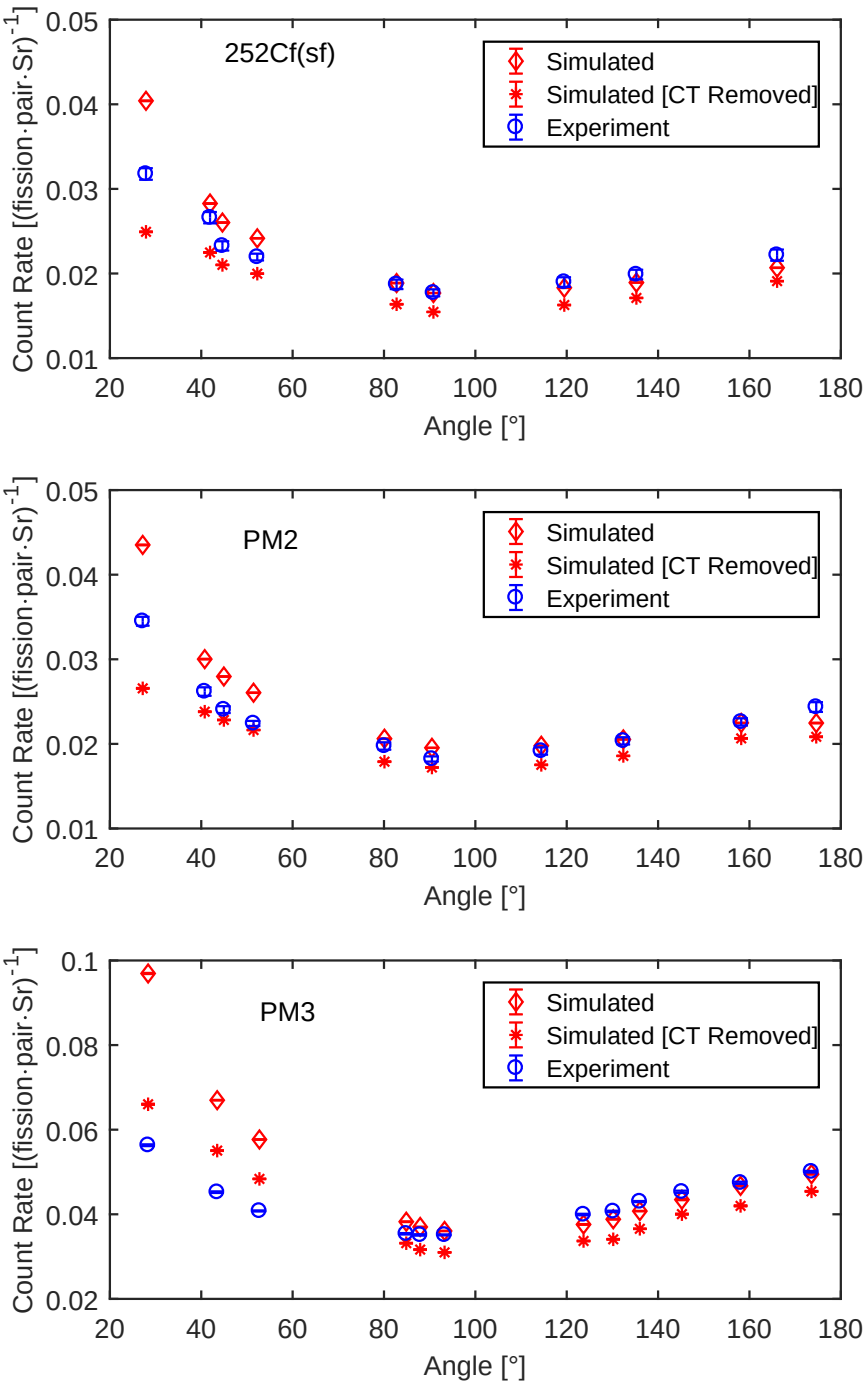

Figure 4.6: Simulated and experiment ^{252}Cf (top), PM2 (middle), and PM3 (bottom) neutron-neutron coincidence angular distributions with a 70 keVee threshold. Simulated results are shown with and without cross-talk. Vertical error bars represent one standard deviation statistical uncertainty; simulated vertical error bars are smaller than the symbols.

There is no reliable analysis for this experiment that could isolate cross-talk counts on an event-by-event basis, thus the simulated data were used to remove integral cross-talk counts from the experimental coincidences. The simulation collision history file allows the user to identify multiple detections that arise from a single neutron.

The simulation results in Fig. 4.7 show the number of cross-talk counts divided by the total number of coincidence counts. The 100, 150, and 200 keVee thresholds correspond approximately to 0.8, 1, and 1.2 MeV proton recoils, respectively. At the lowest angles for all thresholds, greater than 20% of coincidences are from cross-talk. Adjacent detectors share a large solid angle with each other and the cross-talk is correspondingly high, whereas opposing detector pairs near 180 degrees have cross-talk fractions under 10%.

4.4.3 Cross-talk corrected angular distributions

Figures 4.8, 4.9, and 4.10 show the experiment neutron-neutron angular coincidence distribution after cross-talk removal. Experiment geometry specific effects in the angular distributions are minimized when coincidences from cross-talk are removed. The simulated cross-talk fraction is reliable because it is primarily dependent on well-modeled factors, the detector array geometry and the incident neutron energy spectrum. The `MCNPX − PoliMi` cross-talk removed result in Fig. 4.6 has a higher count rate at low angles relative to those near 180 degrees, contrary to the trends observed in Figs. 4.8, 4.9, and 4.10. Therefore, the `MCNPX − PoliMi` model could be improved.

In Fig. 4.8, the ^{252}Cf coincidence distributions are compared to work by Petrov and colleagues [62]; the Petrov experiment had a $50\varnothing \times 50$ mm and a $40\varnothing \times 60$ mm stilbene crystal 50 cm from a ^{252}Cf source. This work compares well qualitatively with the Petrov data set. Differences between the two distributions are attributed to better angular resolution in the Petrov experiment.

For all samples, the neutron-neutron angular distributions with cross-talk coincidences removed show that low angle coincidences are less likely than those at higher angles. Also, the neutron-neutron angular distribution becomes more anisotropic as the pulse height threshold increases.

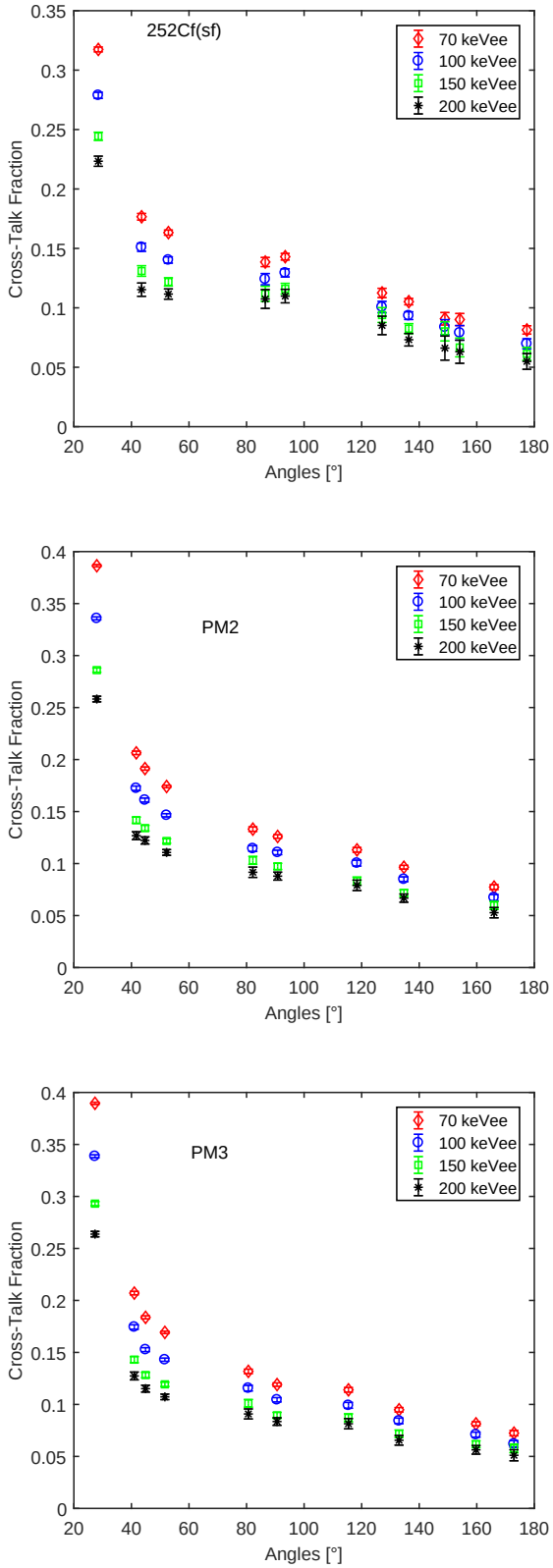

Figure 4.7: Simulated cross-talk fraction of total coincidences angular distributions for various light output thresholds at each detector angle for ^{252}Cf (top), PM2 (middle), and PM3 (bottom).

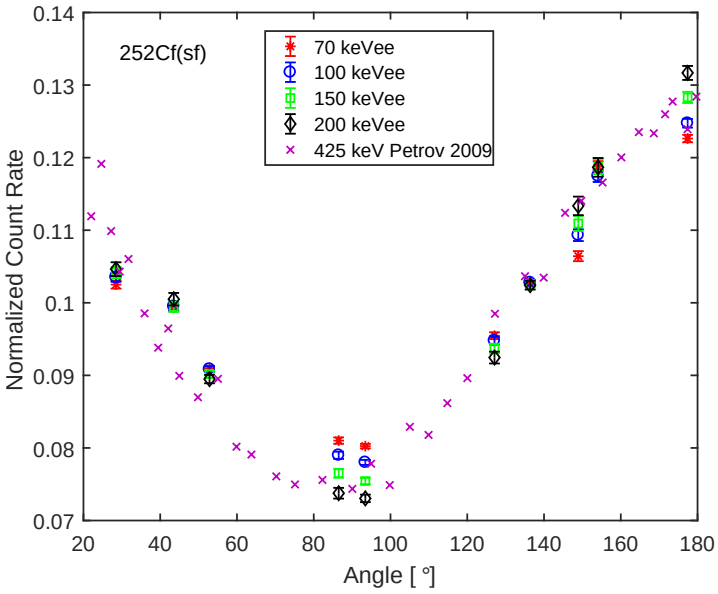

Figure 4.8: Experimental ^{252}Cf neutron-neutron cross-talk-corrected coincidence angular distributions with a light output threshold varied over 70 to 200 keVee; experiment data are compared to data normalized by integral and number of points from Petrov et al. (Xs) [62]. Vertical error bars represent one standard deviation statistical uncertainty.

The coincidence data point for PM2 in Fig. 4.9 at 42 degrees is higher than the point at 28 degrees likely because of sample position uncertainty, which affects the simulation estimated cross-talk. At low detector angles, the contribution of cross-talk is very sensitive to small changes in the sample position.

The neutron-neutron distributions for PM2 and PM3 show similar anisotropy, but the ^{252}Cf distribution is slightly more peaked toward 180 degrees. Slight differences in PM2 and PM3 size and isotopic composition do not manifest in the neutron-neutron angular coincidence distributions.

Figure 4.11 shows the ratio of 180 degree to 90 degree coincidences. As the light output threshold increases, the observed neutron-neutron coincidences become more anisotropic. More coincidences in the 90-degree pairs include low energy neutrons than in the 180-degree pairs; thus, as threshold increases so does anisotropy. Greater anisotropy is expected because more momentum is imparted to a neutron emitted near the fragment direction than to a neutron emitted perpendicular to the fragment direction. The ^{252}Cf data shows much stronger anisotropy than the ^{240}Pu data, but the slope of increasing anisotropy is similar. The data for the two ^{240}Pu samples, PM2 and PM3, agrees within

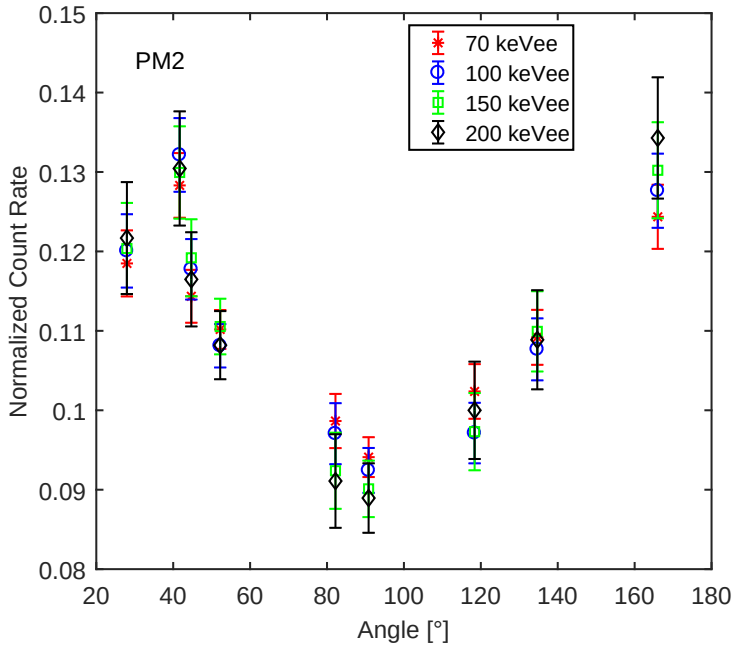

Figure 4.9: Experiment PM2 neutron-neutron cross-talk corrected coincidence angular distributions with a light output threshold varied over 70 to 200 keVee. Vertical error bars represent one standard deviation statistical uncertainty.

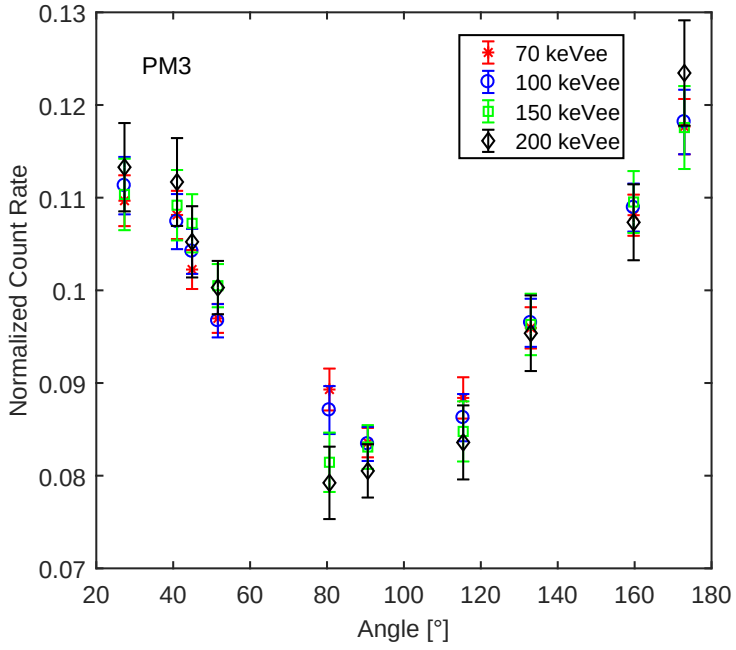

Figure 4.10: Experiment PM3 neutron-neutron cross-talk corrected coincidence angular distributions with a light output threshold varied over 70 to 200 keVee. Vertical error bars represent one standard deviation statistical uncertainty.

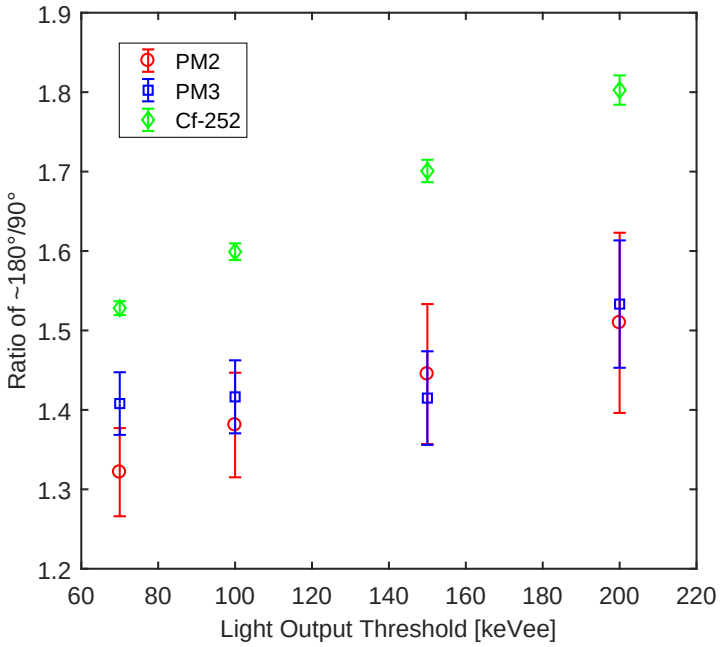

Figure 4.11: Experiment ratio of neutron-neutron coincidences at 180-degree to 90-degree detector pairs as a function of light output threshold.

the statistical uncertainty of this experiment.

4.5 Conclusions

Prompt neutron anisotropy from ^{240}Pu was observed and quantified in laboratory experiments for the first time. The experiments were performed using organic liquid scintillators with two plutonium metal samples; the results agreed within statistical uncertainties. ^{252}Cf spontaneous fission neutrons above 0.65 MeV were observed to be significantly more anisotropic than ^{240}Pu spontaneous fission neutrons above that same energy. These experiment results could be used to improve prompt fission neutron models used in Monte Carlo codes for nonproliferation and safeguards applications.

`MCNPX – PoliMi` simulation of the PM3 laboratory and detector system reproduced experiment pulse height and cross-correlation distributions for 90-degree and 175-degree detector pairs. `MCNPX – PoliMi` simulations were used to estimate the cross-talk fraction and then to remove that fraction from the neutron-neutron angular distributions. More than 20% of small angle coincidences were from cross talk because of large relative

detector-to-detector solid angles. ^{252}Cf neutrons were found to be more anisotropic than ^{240}Pu neutrons. The observed anisotropy increased with applied light output threshold for the plutonium metal and ^{252}Cf samples at a similar rate. The ratio of 180 to 90 degree neutron-neutron coincidences from the plutonium experiments varied from approximately 1.3 to 1.5 over a detection threshold of 70 to 200 keVee. Future experiments with reduced uncertainty, especially in detector pair angles, are necessary to further refine anisotropic neutron emission models for ^{240}Pu spontaneous fission.

Chapter 5

Neutron and Photon Correlations from the University of Michigan ^{252}Cf(sf) Experiment

In this work, I measured ^{252}Cf(sf) neutrons and photons using an array of EJ-309 organic and NaI(Tl) scintillators. I also modeled the experiment with `MCNPX − PoliMi` and `MPPost`. I modified `MCNPX − PoliMi` to read fission events from `CGMF` and `FREYA` into `MCNPX − PoliMi` and those results were compared to the experiment data. I analyzed both experiment and simulation data for pulse height, time cross-correlation, and multiplicity dependent neutron TOF energy. Portions of this work were published in a review publication of correlated fission data and modeling for transport simulations [9].

5.1 Introduction

New event-by-event fission models have prompt neutron and gamma-rays that are correlated in time, energy, and multiplicity, however there is limited measurement data available to validate these models. Measurement of high-order fission neutron and gamma-ray coincidences, those beyond triple coincidence events, is difficult and there has previously been little motivation to measure properties of both particle types simultaneously. A ^{252}Cf(sf) experiment was performed to collect correlated neutron and photon data. Prompt neutrons and photons were measured with an array of organic liquid and NaI(Tl) scintillator detectors.

High-order ^{252}Cf(sf) neutron and gamma-ray coincidences were measured with an

array of 24 liquid organic and eight sodium iodide scintillation detectors. Measured coincidence data including neutron time-of-flight energy and measured gamma-ray pulse height distributions are compared with MCNPX − PoliMi simulation results from built-in and event-by-event fission models.

5.2 Measurement setup

An array of 14 - 7.62⌀ × 7.62 cm EJ-309's, 8 - 7.62⌀ × 5.08 cm EJ-309's, and 8 - 7.62⌀ × 7.62 cm NaI(Tl) scintillators coupled to PMTs was used to measure neutrons and gamma-rays from ^{252}Cf(sf). The array in Figure 5.2 had a flightpath of 51 cm for all detectors with the spontaneous fission source at the center axis of the array between the detector planes.

5.2.1 Detector array

The detector array, shown in Figures 5.1 and 5.2, was re-purposed from a Los Alamos Neutron Science Center (LANSCE) WNR measurement using a U-235 parallel plate avalanche chamber. The detector holder was designed with a few key parameters in mind: to allow a beam to enter the center of the array; to have reasonable fission neutron time-of-flight with organic liquid scintillators; and to have detector adjustability in height. The array was not designed to be particularly neutron and photon efficient because neutron TOF spectroscopy was prioritized. The array used in LANSCE was completely EJ-309s, but in this measurement eight of the 7.62⌀ × 5.08 cm EJ-309's were replaced with NaI(Tl) to improve photon efficiency and to allow for spectroscopy.

The EJ-309 detectors have a chamber that contains the liquid active volume with a small nitrogen bubble to allow for expansion. There is a borosilicate glass window, BK-7, that protrudes in the active volume to prevent the nitrogen bubble from directly touching the active volume to PMT interface; light does not pass efficiently through the bubble to the PMT. The active volume is coupled to a PMT, a ET Enterprises 9821B on 7.62⌀×7.62 cm and 7.62⌀×5.08 cm EJ-309s. The EJ-309 energy resolution

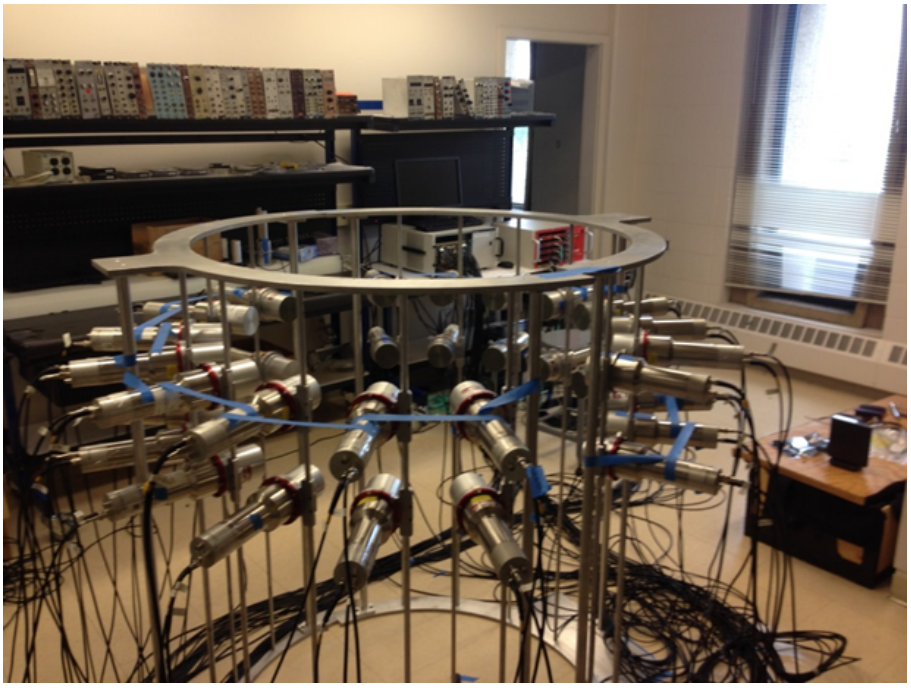

Figure 5.1: A photograph of the detector holder and 32 detectors, 14 - 7.62⌀ × 7.62 cm EJ-309's, 8 - 7.62⌀ × 5.08 cm EJ-309's, and 8 − 7.62⌀ × 7.62 cm NaI(Tl) scintillators.

is approximately 30% full-width half maximum at 662 keVee. Using constant fraction discrimination timing, timing resolution of approximately 1 ns full-width half maximum is observed, shown in Figure 5.15.

The detectors were aligned so that there were two horizontal planes of detectors separated by 20 cm from detector center axes. Detectors on a plane are in 20° increments with 40° openings for the beam that was used in a prior experiment. Great care was taken to adjust each detector to level and to point at the central system axis.

5.2.2 Acquisition

Pulses from the detectors were digitized using four CAEN V1720 waveform digitizers with 250 MHz sampling and 12 bit amplitude resolution over a 2 V range. The internal digitizer clock signals were synchronized so waveform global time stamps were also synchronized. Time synchronization was performed with CAEN provided software and phase lock loop files unique to each board were used.

All detectors output negative voltage, simplifying acquisition. The EJ-309 and NaI(Tl) photomultiplier tubes have negative signals, but the NaI(Tl) is often used with a pulse

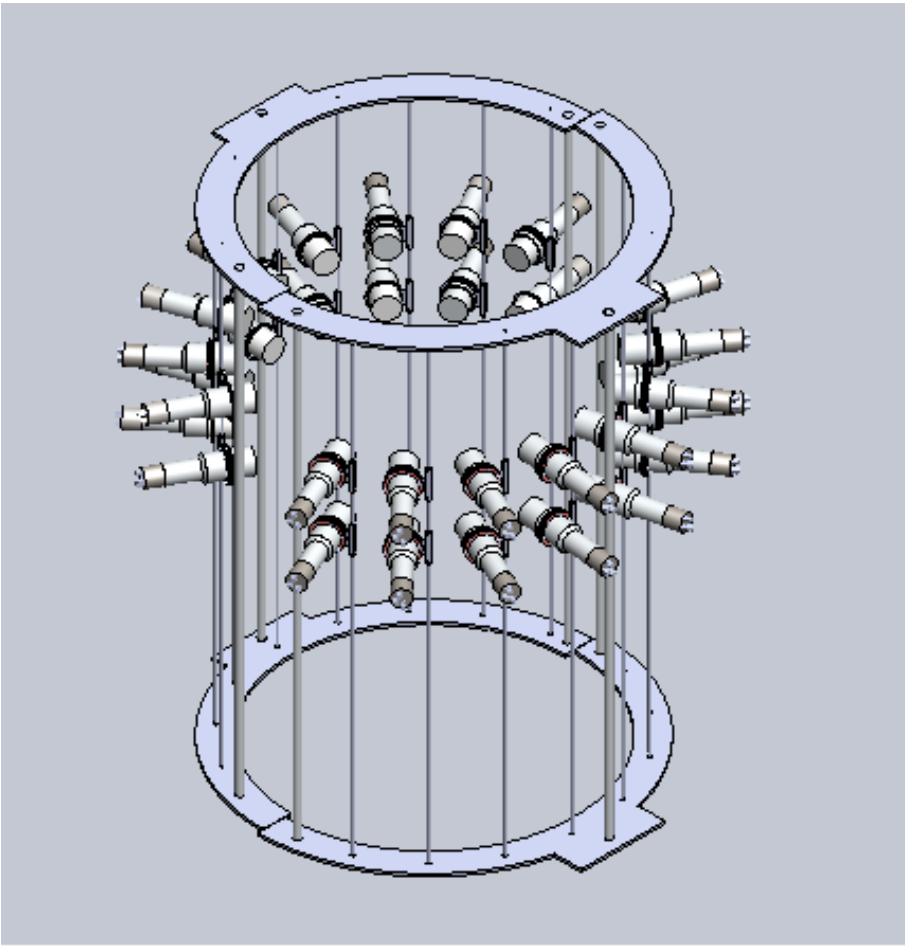

Figure 5.2: A model of the detector holder and 32 detectors, 14 - 7.62⌀×7.62 cm EJ-309's, 8 - 7.62⌀ × 5.08 cm EJ-309's, and 8 − 7.62⌀ × 7.62 cm NaI(Tl) scintillators.

shaper that inverts the signal polarity. This measurement does not use a pulse shaper for the NaI(Tl) detector signals because the pulse shaper lengthens the waveform and worsens timing resolution. Without a pulse shaper, energy resolution suffers.

Due to the source strength and NaI(Tl) high efficiency, data throughput limited the waveform size to a 400 ns window. A 400 ns window at 250 MHz sampling results in 100 samples, sufficient for pulse shape discrimination with an EJ-309, but not enough for full integration of a NaI(Tl) waveform. Each recorded waveform data packet included a global time stamp, channel, and 12-bit amplitude for each sample.

Acquisition is triggered by threshold crossing. The threshold was specified to approximately 40 keVee equivalent. At this level, background contribution is minimal in the NaI(Tl) detectors and PSD is possible in the EJ-309s. Each channel and board triggers independently; no triggering logic was used to enforce coincidences. Typically, a single channel triggering on a V1720 digitizer board passes a global trigger, acquiring data for all channels, however zero suppression was used.

The `Quacq` acquisition software, developed within DNNG was used on a Debian Linux desktop. `Quacq` was developed to partially parallelize acquisition when using multiple digitizers, however, great improvements have been made recently with other software developed within DNNG.

5.2.3 High voltage supply

High voltage was applied to each detector with a single supply from Wiener, EHS F 030n. The HV supply was controlled on a desktop via an Ethernet connection. The detectors were gain matched to 478 keVee at 0.3 V. Calibration was automated with a script that fits the Compton edge in pulse height distributions from a Cs-137 667 keVee characteristic gamma ray. Despite this calibration, pulse height regions far from 0.3 V could exhibit very different responses from detector to detector.

5.2.4 Waveform post-processing

All digitized waveforms were recorded for post-processing. Pulse shape discrimination was used to discriminate between neutron and gamma-ray events in the liquid organic scintillators [16]. Full digitized waveforms, of 100 samples at 250 MHz, were saved for post-processing. Only pulses above a specified threshold (70 keVee) were analyzed. Double pulses above a fraction of the triggering pulse height were removed, as PSD cannot be reliably performed on double pulses. The double pulse fractional height threshold is 10% for EJ-309s and 20% for the NaI(Tl)s. Pulse timing is determined through constant fraction discrimination (CFD). The CFD value for the EJ-309s is 50% and for the NaI(Tl)s is 10%.

EJ-309 waveforms were read into memory, cleaned, integrated for PSD, and then categorized by particle type. First, the maximum of the pulse is found and the baseline is subtracted. The pulse is kept if it is above the specified threshold. The time of the pulse is determined with a constant fraction discriminator, 50% is generally used. The waveforms were cleaned to remove any waveforms where PSD would be unreliable. Alignment within the window was checked; there must be enough samples to compute a baseline average and to integrate the tail of the pulse. The pulse must be free of double pulses; the tail is searched for peaks that exceed a specified fraction of the maximum pulse height.

After cleaning, the tail and total integrals were computed. The tail starts 11 samples (44 ns) after the maximum and ends 45 samples (180 ns) after the maximum. The total integral begins 5 samples before the maximum.

Figure 5.3 shows that the tail plotted against the total integral produces two bands, one for photons and one for neutrons. The two bands correspond to electron and proton recoils. Electrons fall below protons in tail integral for a given total integral because more singlet states are quenched and more triplet-triplet annihilations occur in the scintillator for the higher stopping power proton recoil. In practice a PSD line is assigned to discriminate between the two particle types. Significant overlap occurs at small integrals, therefore misclassification is most likely in this region. A quadratic line is used to discriminate particle type, as shown in Figure 5.3, and a unique PSD line was assigned for

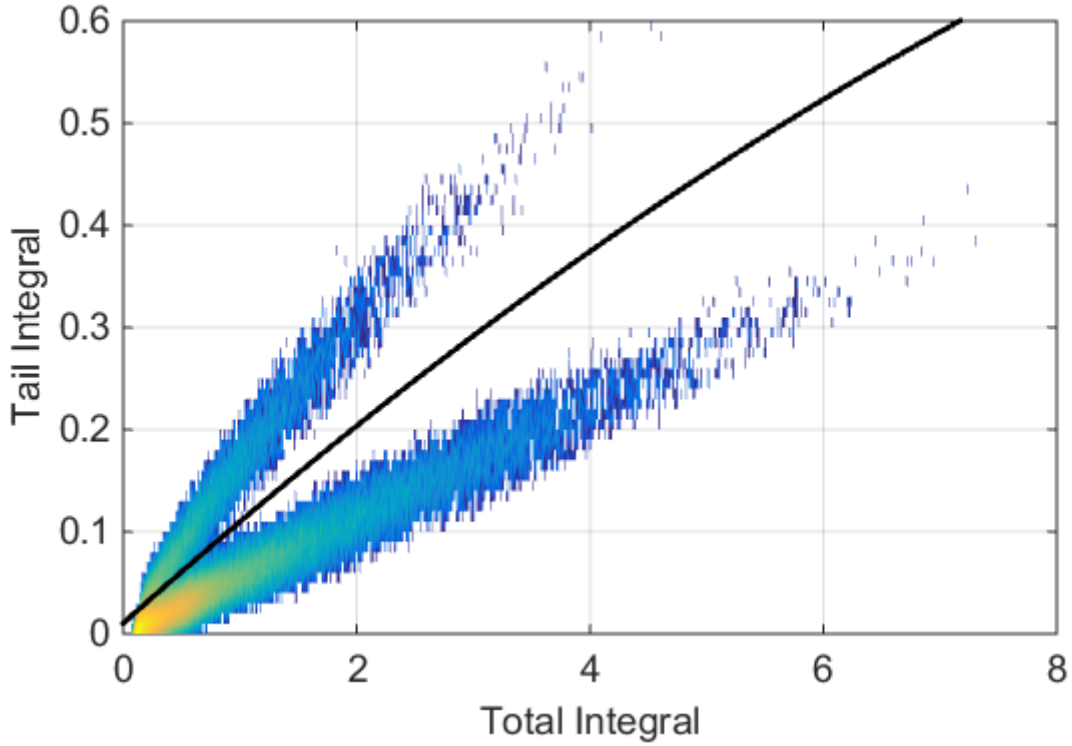

Figure 5.3: EJ-309 digitized waveform pulse tail integral to total pulse integral heat map with neutron-gamma-ray discrimination line where neutrons lie above the line and gamma rays lie below. Approximately 200,000 waveforms, after cleaning, are represented in the figure.

each detector to account for small differences in pulse shape due to readout.

After post-processing of waveforms including pulse shape discrimination, coincident events using a 200 ns window were collected. The coincident events were analyzed to produce pulse height, cross-correlation, multiplicity, and time-of-flight neutron energy distributions.

5.2.5 ^{252}Cf(sf) source

The Cf-252 source was 6001.2 μCi, recorded on 05-Aug-1994 and at the start of the measurement campaign was 31.07 μCi. Approximately 70 billion fissions were observed from the 35,500 fission/s ^{252}Cf(sf) source. The isotopic evaluation on that date is shown in Table 5.1. ^{250}Cf(sf) contributes 5.8% of the spontaneous fission events. The source was old relative to the creation date, therefore the relative strength of ^{250}Cf(sf) to ^{252}Cf(sf) is increased. The spontaneous fission fraction of ^{250}Cf is estimated to be approximately 6%

Table 5.1: Cf-252 source isotopic evaluation for fission decays, decayed from the 05-Aug-1994 evaluation, to the start of the measurement campaign, 05-Sep-2014.

Isotope	Fissions/s
Cf-252	35,500
Cf-250	2,200
Cm-248	137

at the time of measurement. This contribution is not modeled in the MCNPX − PoliMi simulations.

5.3 MCNPX − PoliMi model and simulation

MCNPX − PoliMi and MPPost were used to simulate the measurement. MCNPX − PoliMi was used to transport neutrons and photons in the laboratory space and MPPost was used to emulate detector response [8]. The full MCNPX − PoliMi model input file for this experiment can be found in Appendix 2. Simulated MCNPX − PoliMi results using the built-in ^{252}Cf(sf) model, the CGMF model [11,29,41,42], and the FREYA model [12,12,43,45,46,47,48] are compared to experimental results. For more details on the fission models see Chapter 3.

MPPost was used to emulate detector response. MCNPX − PoliMi collision histories are read and evaluated by MPPost to determine the outcome of the interaction and relevant information is recorded. The user provides detection thresholds and resolutions to be applied by MPPost.

Aside from the detector array, laboratory features were modeled. The laboratory has a concrete floor and tall concrete ceilings (3.5 m) that were included in the model. There were large polyethylene sheets near the detector array, approximately 2 m from the edge of the array that were also included in the model. The polyethylene sheets acted as the moderator in a He-3 detector portal monitor array; the He-3 detector material was not modeled.

5.4 Experiment and simulation analysis/comparisons

Experimental and simulation analysis were performed with analogous methods so that similar quantities could be directly compared. Experimental data analysis is described in Section 5.2.4.

Experimental and simulation results were compared. The `MCNPX − PoliMi` code was used to read fission histories from `CGMF`, `FREYA`, and its built-in ^{252}Cf(sf) models. After measurement post-processing and simulation collision file processing with `MPPost`, key experiment quantities were recorded and compared. Pulse height and cross-correlation distribution agreement help to demonstrate basic detector response and geometry accuracy, but higher order quantities were compared to investigate fission model differences.

5.4.1 Background considerations

A background experiment was performed to subtract chance events from the ^{252}Cf(sf) signals. Higher-order background coincidences were not as significant; for each increase in coincidence number the rate decreased approximately by an order of magnitude.

The pulse height distribution from each NaI(Tl) detector is shown in Figure 5.4. The distributions show characteristic background photon peaks. There is a significant difference between detector response at higher heights, away from 0.415 Vns where detectors were gain matched. The uppermost photopeak ranges from 1.2 to 1.5 Vns The different detectors deviate toward large pulse heights because signals were read from the pre-amplifier without further pulse shaping and the NaI(Tl) response is expected to be slightly non-linear. Pulses were not shaped because pulse shaping worsens time resolution.

Experiment cross-correlation data in Figure 5.5 show that neutron background is significantly less than photon background rates. The correlated background between approximately ±20 ns is primarily from environmental background neutron cross-talk, whereas outside of that range only uncorrelated chance coincidences are observed. The two peaks on either side of time zero are evidence that photon-photon coincidences arise

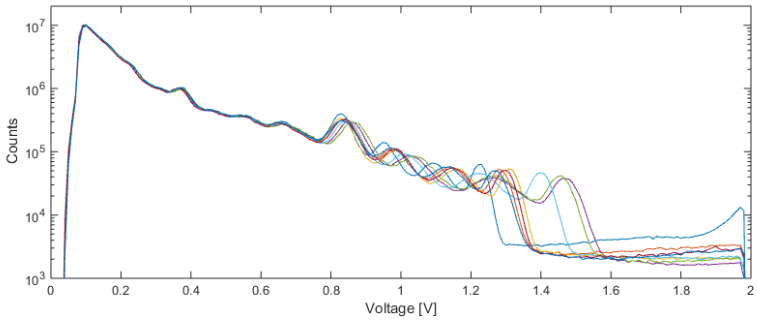

Figure 5.4: All eight NaI(Tl) detector background pulse height distributions over a 100 hour period over the full digital dynamic range.

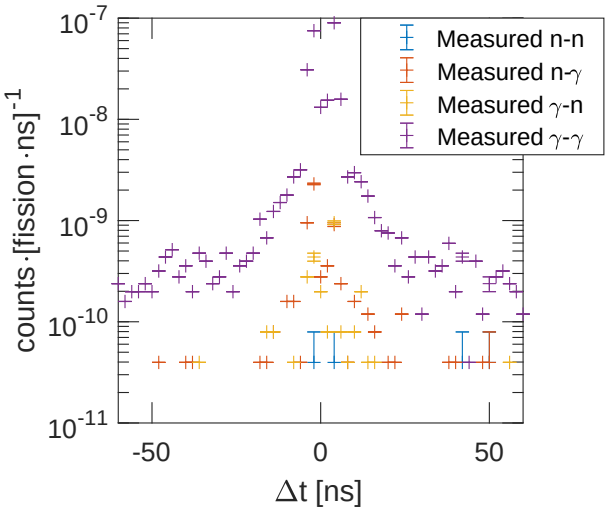

Figure 5.5: Background cross-correlation distribution between two 7.62×7.62 cm EJ-309 detectors with 134 degrees between the detectors.

primarily from cross-talk of background photons.

Figure 5.6 shows that the NaI(Tl) detector count rates are almost an order of magnitude higher than the pair of EJ-309 detectors in Figure 5.5. The double peak feature, indicative of photon cross-talk, is not as evident in Figure 5.6 because the timing resolution is poor.

5.4.2 Pulse height distributions

The singles pulse height distributions from the measurement and simulations are shown in Figures 5.7 through 5.11. The distributions are the average of each detector set. The distributions show the background-subtracted pulse height spectra, after PSD in the case of EJ-309s. Non-fission emissions from fission products built up in the Cf-252 sample

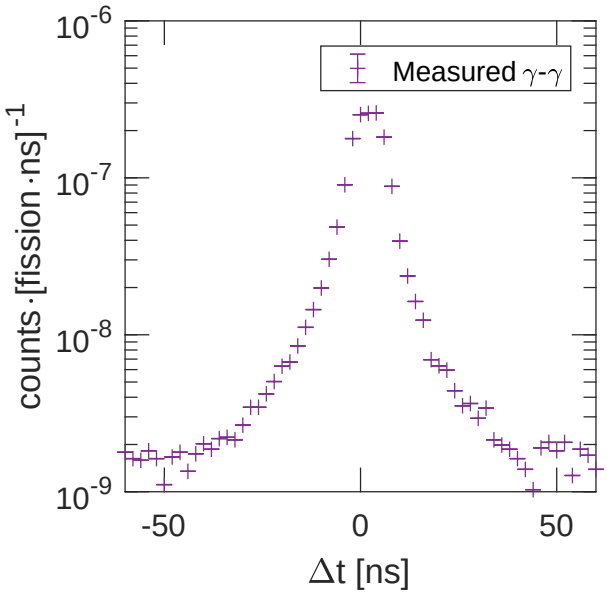

Figure 5.6: Cross-correlation distribution between two 7.62×7.62 cm NaI(Tl) detectors with 64 degrees between the detectors.

are included in these spectra; these emissions are primarily photons. A stricter triggering condition, such as higher order coincidences, could improve certainty that detection events are exclusively from fission events, however the best method to ensure detection events are correlated with fission is through the use of a source in an ionization chamber.

As shown in Figures 5.7 through 5.10, results from both EJ-309 detector sizes, 7.62×5.08 cm and 7.62×7.62 cm, are very similar for both particle types. The discrepancy at the lowest pulse heights is due to a mismatch in the detection threshold. The measured photon spectra agree in shape above 1,000 keVee to each of the models, but agreement with CGMF is best in magnitude. Below 1,000 keVee the models underpredict due to non-fission emissions. The neutron pulse height spectra show good agreement between all models, but above approximately 1,500 keVee the models overpredict the measured result. Above 1500 keVee, the codes diverge from the experimental data. Furthermore, the `FREYA` results over-predict the results from `CGMF` and `MCNPX − PoliMi`.

Figure 5.11 shows the NaI(Tl) pulse height distribution from measurement and simulation results. Agreement between the measurement and simulation results is poor below 1,000 keVee, primarily due to non-fission contributions. Agreement above 1,000 keVee is better, but it is not clear which fission model agrees best. There is significant difference

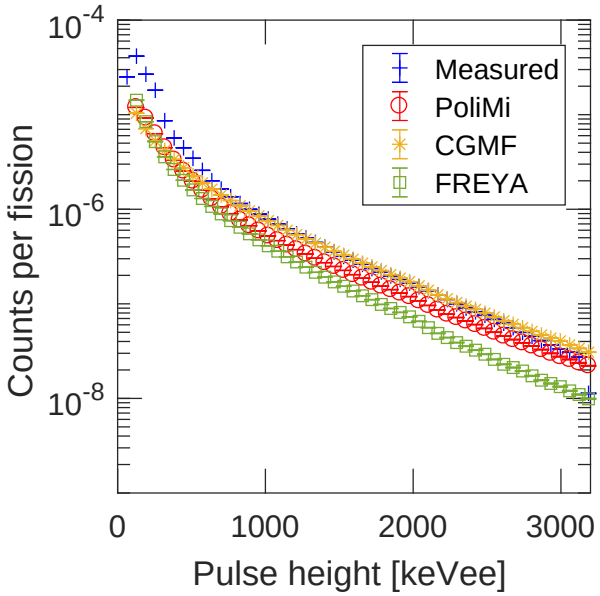

Figure 5.7: 7.62×5.08 cm EJ-309 photon pulse height distribution.

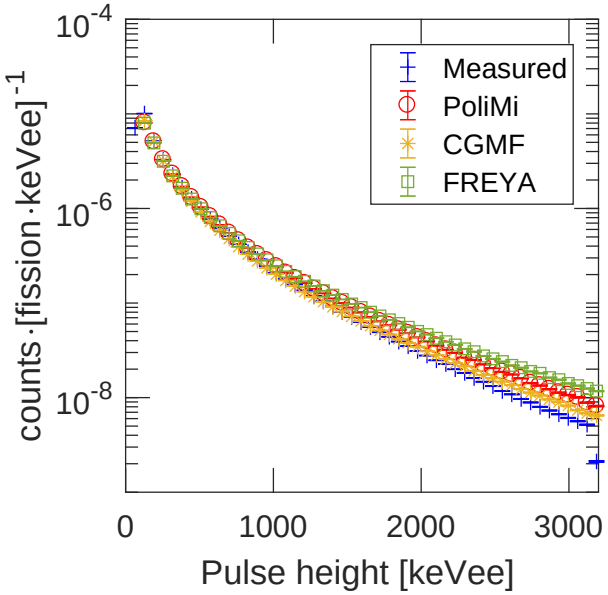

Figure 5.8: 7.62×5.08 cm EJ-309 neutron pulse height distribution.

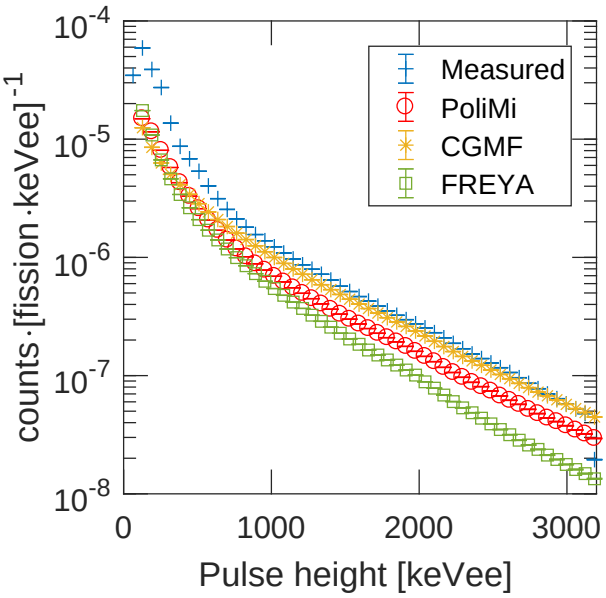

Figure 5.9: 7.62×7.62 cm EJ-309 photon pulse height distribution.

between each fission model prediction, however `PoliMi`and `FREYA`models are most similar.

5.4.3 Photon spectra with coincident neutron detection

Conditioning photon pulse height distributions on a coincident neutron detection improves measurement-simulation pulse height distribution agreement, shown in Figures 5.12, 5.13, and 5.14. The coincidence condition does not impact the shape of the simulation distributions significantly, whereas the measurement distributions are changed. Change in the measurement distribution shape indicates that non-fission emissions from the source are contributing to the distribution.

`PoliMi` fission model results agree best with the measured result for both EJ-309 detectors, however `FREYA` agrees best in the NaI(Tl) distribution. An ionization chamber with a fission foil would further provide better certainty in identifying emissions from fission events.

5.4.4 Time cross-correlation distributions

Comparison of time cross-correlation distributions after background subtraction show good agreement between measured and `MCNPX` − `PoliMi` simulated results. Figure 5.15 shows a cross-correlation time distribution for neutron-neutron, neutron-photon, photon-

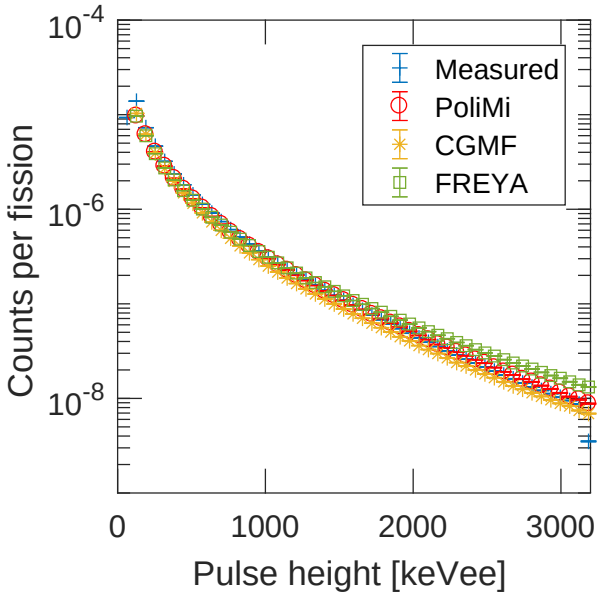

Figure 5.10: 7.62×7.62 cm EJ-309 neutron pulse height distribution.

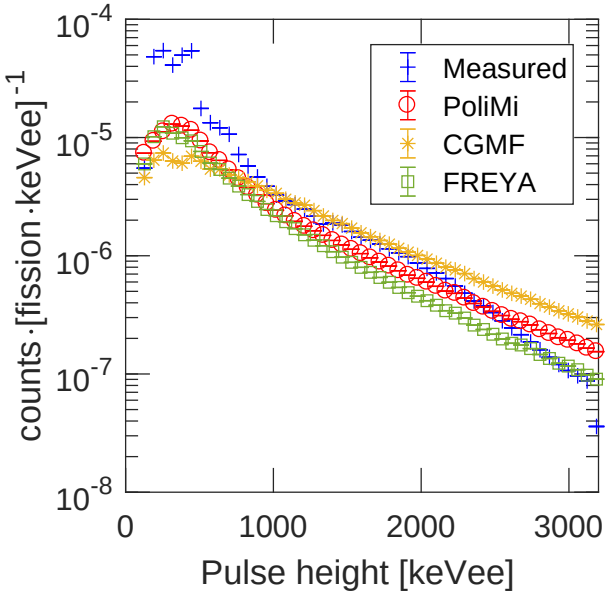

Figure 5.11: 7.62×7.62 cm NaI(Tl) pulse height distribution.

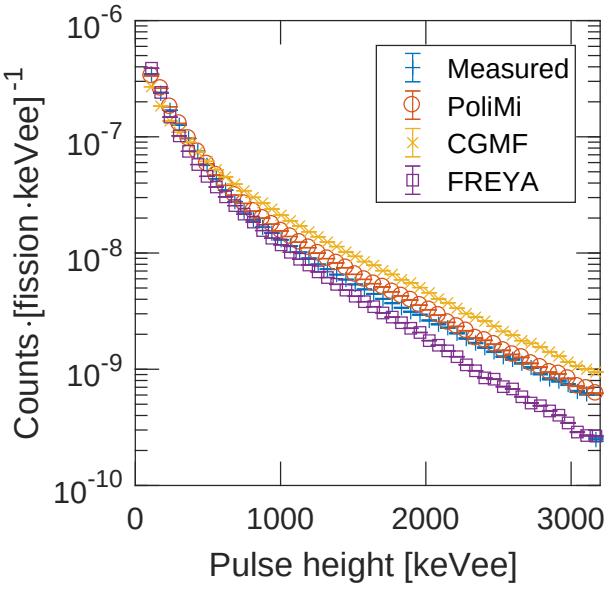

Figure 5.12: 7.62×5.08 cm EJ-309 photon pulse height distribution with a neutron coincidence required 5 to 75 ns after the photon detection.

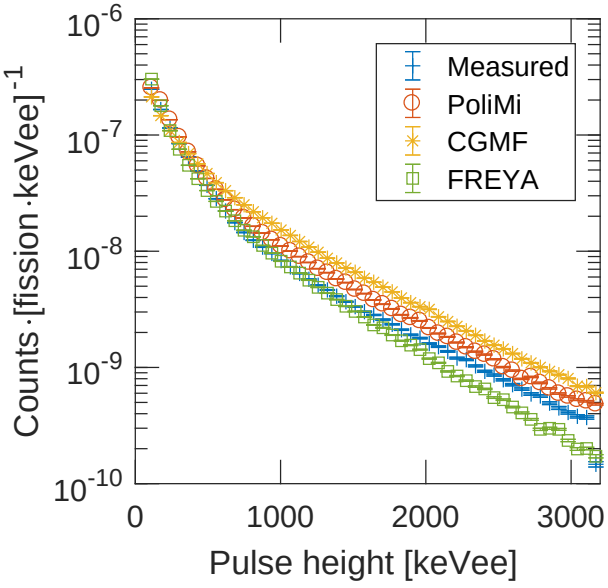

Figure 5.13: 7.62×7.62 cm EJ-309 photon pulse height distribution with a neutron coincidence required 5 to 75 ns after the photon detection.

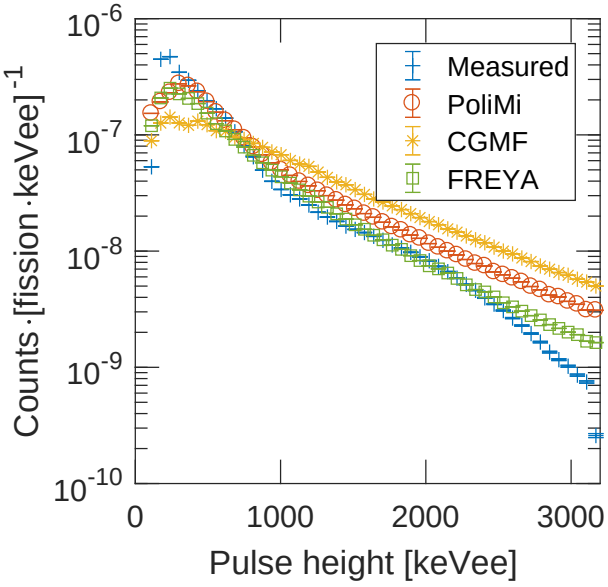

Figure 5.14: 7.62×7.62 cm NaI(Tl) pulse height distribution with a neutron coincidence required 5 to 75 ns after the photon detection.

neutron, and photon-photon coincidences for both measured and simulated results. The photon-photon distributions disagree outside of approximately +/-5 ns due to non-fission, un-modeled photon emissions from the source material, which are not entirely removed through simple background subtraction.

In Figure 5.15, all fission models slightly underpredict neutron-neutron coincidences, but `FREYA` agrees best. The `PoliMi` model has good neutron-photon, photon-neutron agreement over the full time range. `CGMF` has too many low energy neutrons and too few high energy neutrons.

Figure 5.16 shows better fission model agreement to neutron-neutron measurement distributions than in Figure 5.15. The only difference between the two detector sets is the angle between the detectors used to construct the coincidences. The total number of neutron-neutron coincidences was slightly higher at 134 degrees than at 59 degrees because of neutron anisotropy. The higher angle set of 134 degrees should also have a relatively higher energy neutron spectrum because more coincidences arise from fragment-boosted neutrons emitted along the fission fragment axes than in the 59 degree case.

Neutron-photon, photon-neutron, and photon-photon distributions should not be impacted by the difference in detector angle due to fission model features. Neutron-photon and photon-photon angles are isotropic in the fission models. Minor geometry asymme-

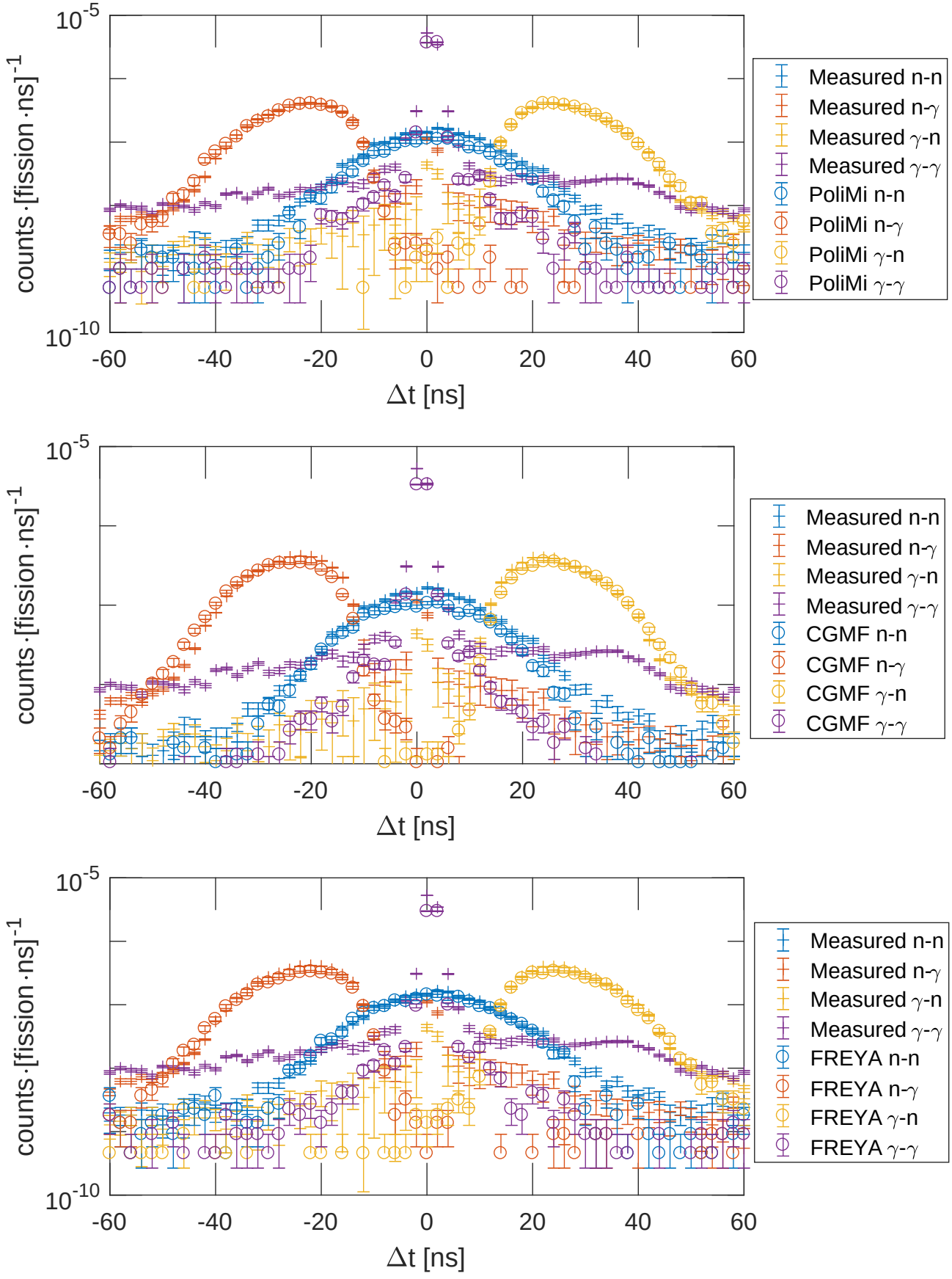

Figure 5.15: Cross-correlation distribution between two 7.62×7.62 cm EJ-309 detectors with 134 degrees between the detectors.

tries could change the distributions slightly.

Time cross-correlation distributions from a 7.62×7.62 cm EJ-309 and a 7.62×7.62 cm NaI(Tl) detector, in Figure 5.17, show similar neutron-photon agreement as previous results. Photon-photon distribution agreement is similar for all models. The photon-photon peak in simulation is broader than the measured result. Again, simulation underpredicts at time differences +/-10 ns due to non-fission, un-modeled photon emissions from the source material, which are not entirely removed through simple background subtraction. In the neutron-photon experiment data, a small peak at time zero indicates photon misclassification as neutrons.

Figure 5.18 shows cross-correlation distributions between two 7.62×7.62 cm NaI(Tl) detectors. Agreement is poor between the simulation result and measured result because the NaI(Tl) response is not well emulated by `MPPost`.

5.4.5 Coincidences

A custom script was written to tally coincidences in an 80 ns window for each simulation model and for the measured data. Events were tallied when two or more channels trigger within an 80 ns window. The coincidences were binned by the number of neutrons detected within the coincidence window in Fig. 5.19, with the C/E result, the ratio of the simulation result to the experimental result, shown as well. Simulation results for all models over-predict the number of coincidences for all neutron coincidences except zero. There can be zero neutron coincidences when there is a photon coincidence instead. Despite a basic background subtraction, the number of coincidences is underpredicted at zero because background photon coincidences contribute disproportionately. The observed discrepancy does not necessarily indicate a problem with neutron-photon correlation, but may indicate discrepancy in prompt fission neutron spectrum (PFNS). The likely case is a real ^{252}Cf(sf) photon is detected in coincidence with a background photon.

The ratio of the simulated result to the measured result shows that `CGMF` agrees best over the range of coincidences, but no model agrees well at high neutron coincidences.

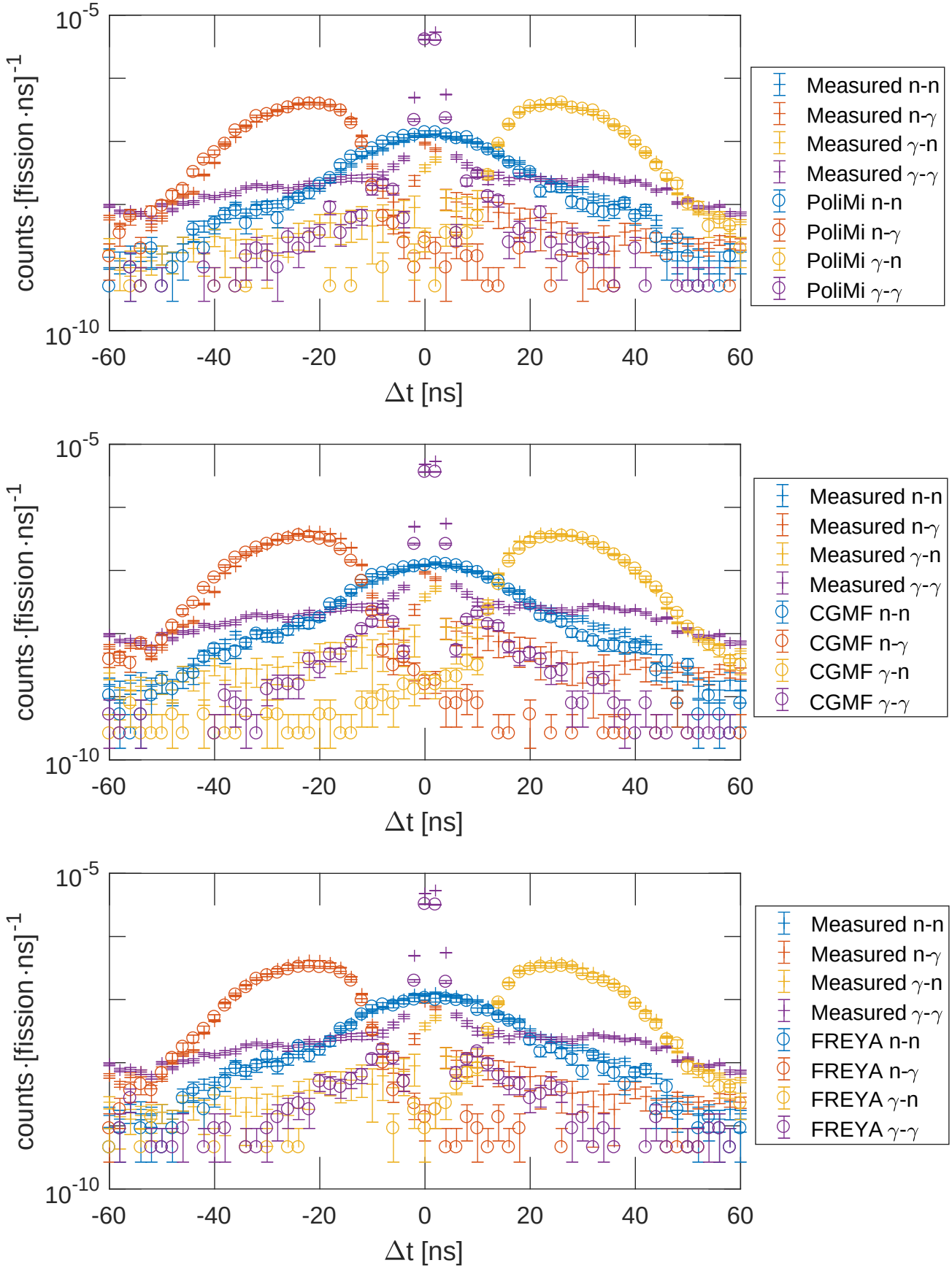

Figure 5.16: Cross-correlation distribution between two 7.62×7.62 cm EJ-309 detectors with 59 degrees between the detectors.

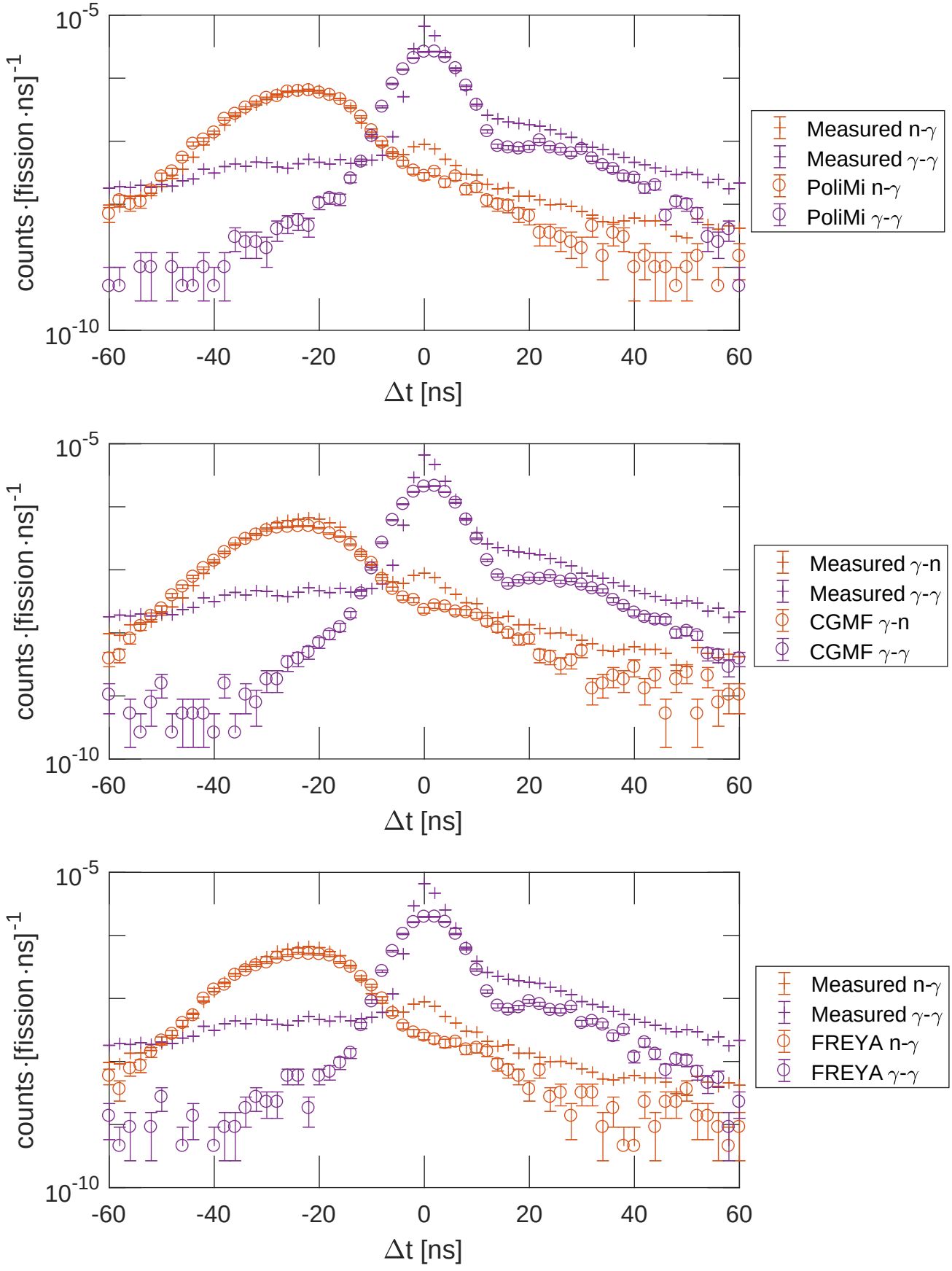

Figure 5.17: Cross-correlation distribution between a 7.62×7.62 cm EJ-309 and a 7.62×7.62 cm NaI(Tl) detector with 74 degrees between the detectors.

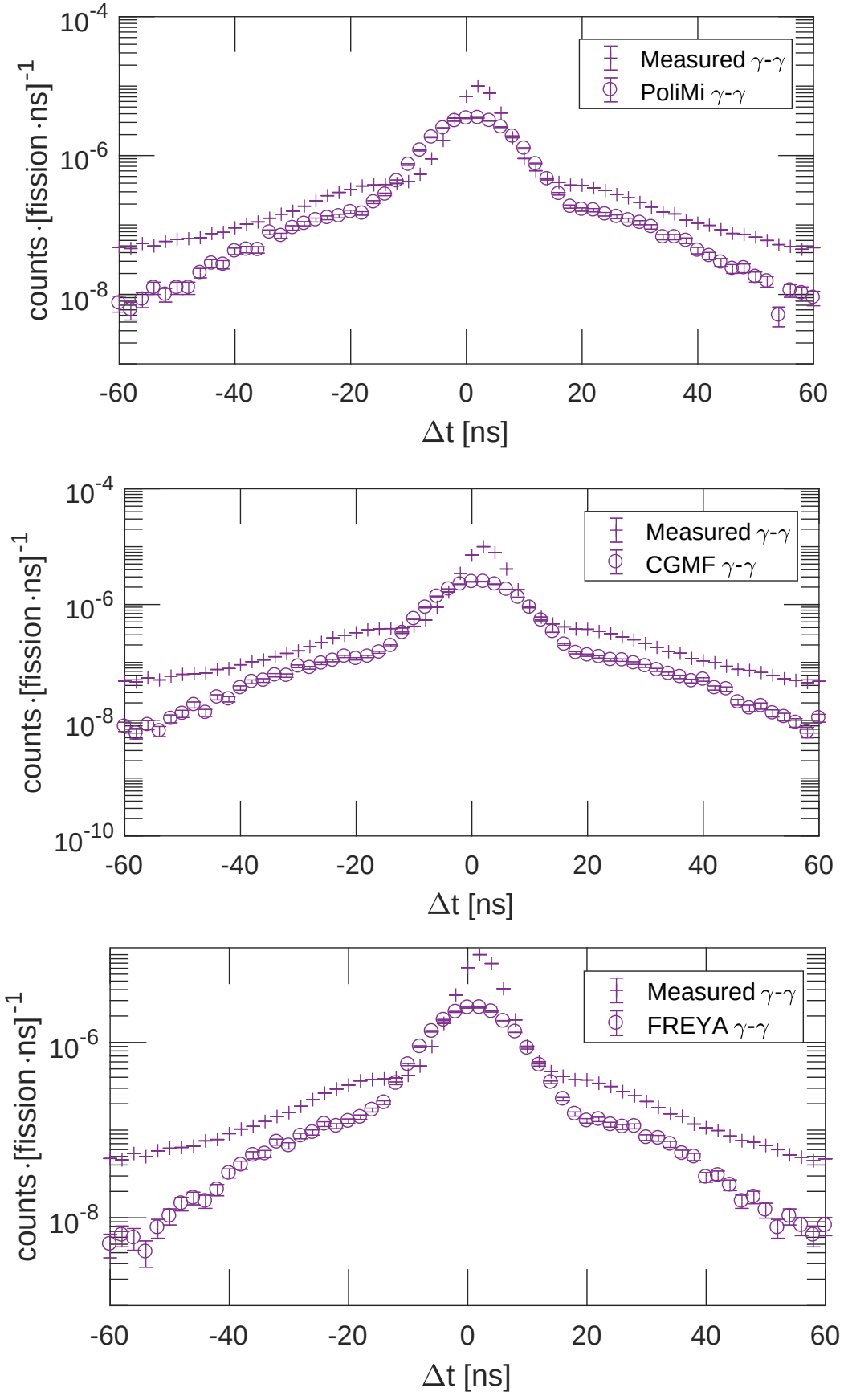

Figure 5.18: Cross-correlation distribution between two 7.62×7.62 cm NaI(Tl) detectors with 64 degrees between the detectors.

Agreement becomes progressively worse as order of coincidence increases.

The number of photon coincidences from CGMF agrees best with the measured number of coincidences in Figure 5.20. Two photons detected in coincidence is most likely because the number of zero and one photons in a coincidence event is artificially reduced by the overall coincidence condition and the low neutron detection rate.

In Fig. 5.21, the mean number of photons relative to neutron coincidences agrees well, where C/E is approximately 1, for zero and one counts. The agreement is within 10% up to three neutron counts. Also, the uncorrelated neutron-photon multiplicity model (PoliMi) overpredicts the number of photons toward high neutron coincidences, whereas the negatively correlated models slightly underpredict the number of photons. This result indicates that the true correlation is likely negatively correlated, but weaker than that represented by CGMF and FREYA.

5.4.6 Neutron time-of-flight

A script was written to estimate neutron energy spectra through photon tagged time-of-flight, which were binned by coincidence multiplicity. The time difference of a photon detection in an EJ-309 and neutron detection in a different EJ-309 was converted to neutron energy assuming the neutron flight path distance, 52.5 cm, from the source to the mean interaction depth in each detector. It is also assumed that the photon originated from the same fission event. Timing resolution is the largest contributor to uncertainty in the estimate of neutron energy, especially for high energy neutrons. This method does not consider late photon emission [34], therefore delayed and scattered photons also contribute to uncertainty in the neutron energy. Ideally, an ionization chamber with a fission foil would be used in this type of measurement. The energy spectra are divided by energy-dependent detector efficiency to estimate the incident neutron spectra.

Figure 5.22 shows the estimated neutron energy spectra from time-of-flight for both measurement and simulation results. The FREYA fission model results agree best with the reference Watt spectrum for Cf-252.

Tables 5.2 and 5.3 show mean neutron energy as a function of coincident detections

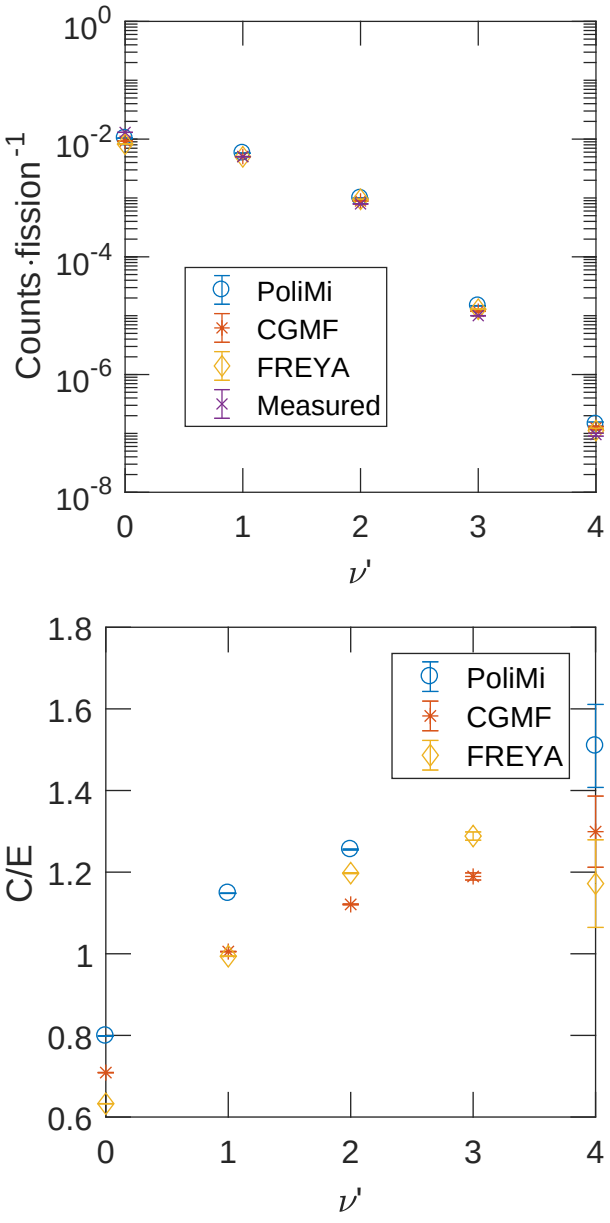

Figure 5.19: Neutron coincidences and the ratio of the simulation result to the experimental result, C/E, for neutron coincidences.

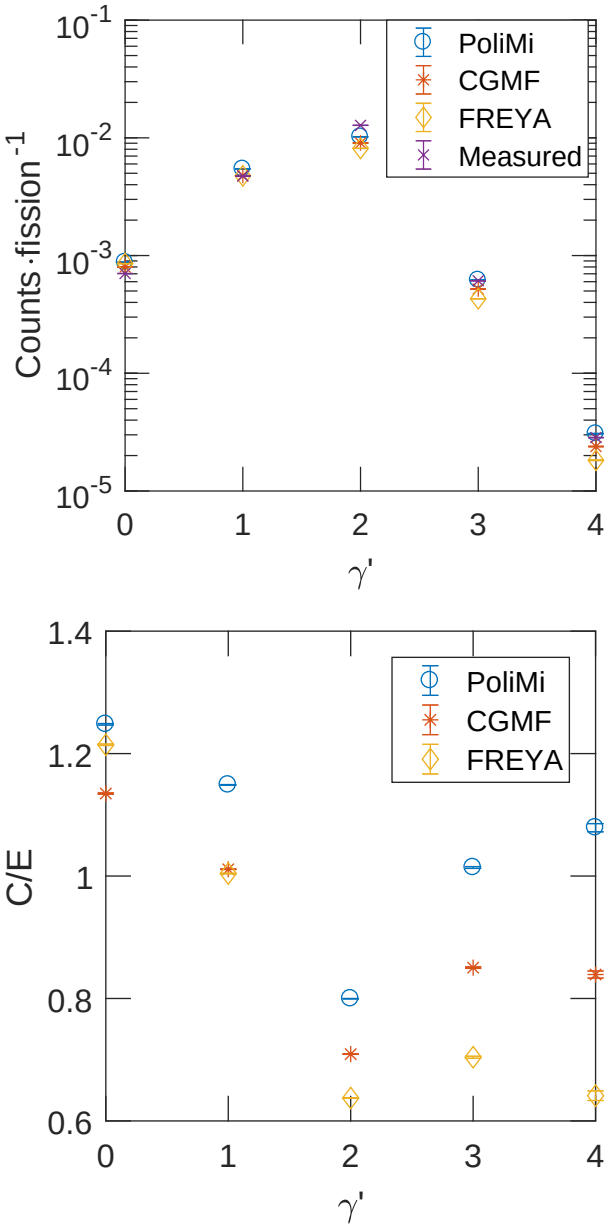

Figure 5.20: Photon coincidences and the ratio of the simulation result to the experimental result, C/E, for photon coincidences.

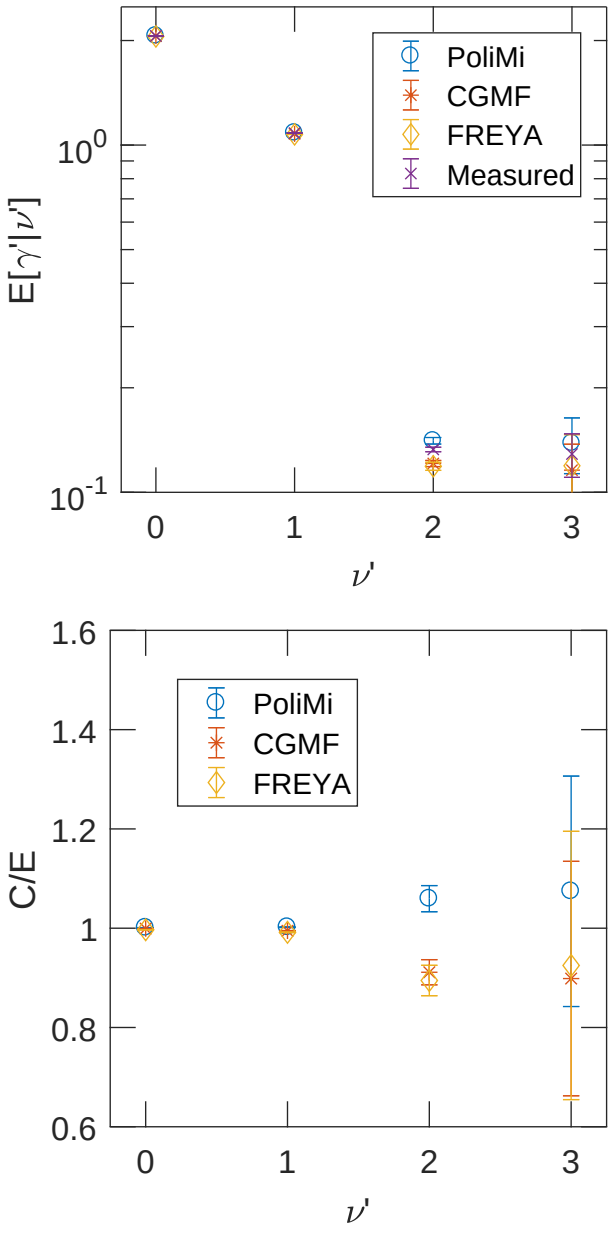

Figure 5.21: Average number of photon coincidences as a function of neutron coincidences and the ratio of the simulation result to the experimental result, C/E.

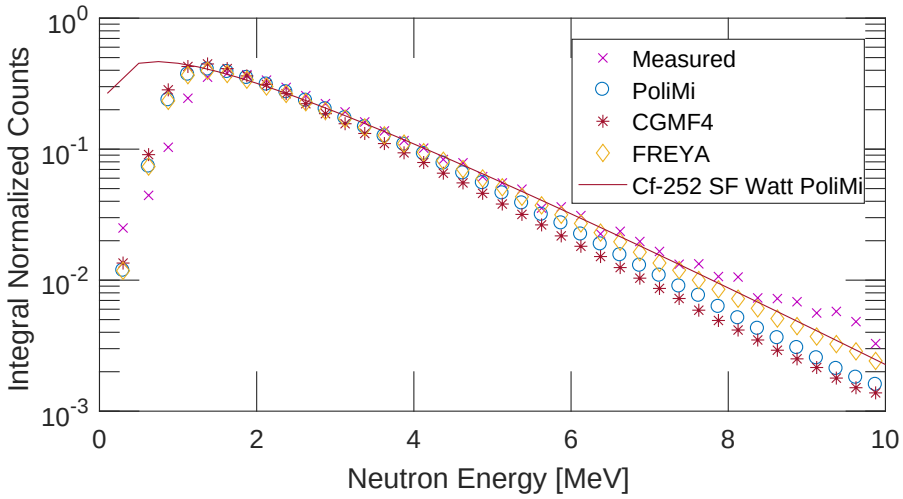

Figure 5.22: Neutron energy spectra from measurement and simulation obtained through time-of-flight techniques.

Table 5.2: Average detected neutron energy by time-of-flight over the sensitive range of the detectors, 1.1-8.1 MeV, as a function of neutron coincidences. Omitted entries had insufficient data.

Number of detected neutrons	Fission model			
	PoliMi	CGMF	FREYA	Experiment
1	2.492(2)	2.359(1)	2.563(2)	2.668(2)
2	2.51(1)	2.422(8)	2.61(1)	2.72(1)
3	2.49(6)	2.49(6)	2.63(8)	2.7(1)
4	2.5(6)	2.3(5)	3.2(9)	-

for measured and simulated data. A slight increase in neutron energy is observed with the number of coincident detections in table 5.2 and 5.3. More data is required to resolve any trend in the neutron energy; the upward trend is small relative to the statistical uncertainties.

Table 5.3: Average detected neutron energy by time-of-flight over the sensitive range of the detectors, 1.1-8.1 MeV, as a function of photon coincidences. Omitted entries had insufficient data.

Number of detected photons	Fission model			
	PoliMi	CGMF	FREYA	Experiment
1	2.489(2)	2.358(2)	2.561(2)	2.669(2)
2	2.57(1)	2.435(7)	2.66(1)	2.68(1)
3	2.62(5)	2.49(4)	2.70(6)	2.67(7)
4	2.8(3)	2.6(2)	3.0(5)	2.9(5)

5.5 Conclusions and future work

Fission models PoliMi, CGMF, and FREYA captured some key observed features from this experiment. These experimental results indicate that all fission models require improvements to refine neutron and photon energy and multiplicity distributions. PoliMi, however, had the best neutron and photon spectra agreement with experiment data, because it uses evaluated data for its model.

For experimental coincidence distributions, no model result agreed well. Future work should be performed to resolve potential spectral-multiplicity effects in this result. Additionally, future work would benefit from using a fission chamber to better condition coincidence counting. The neutron-photon correlated coincidence result indicates negative correlation, between the uncorrelated PoliMi model and the negatively, but more strongly correlated, CGMF and FREYA models.

The neutron TOF energy data relative to the number of neutron coincidences do not indicate a correlation in mean energy for experiment or simulation results. There is, however, a weak positive trend in mean neutron energy relative to the number of photons in coincidence. This result could be biased because the mean neutron energy is estimated using a photon trigger time. Again, future work would benefit from using a fission chamber to better condition coincidence counting.

Chapter 6

^{252}Cf(sf) Neutron-Photon Competition Experiment at LANL

This chapter describes work that I performed to quantify ^{252}Cf(sf)neutron-photon multiplicity correlation on an event-by-event basis. This work is taken from my publication on the work [63]. I designed an acquisition system, consisting of CAEN digitizers, and custom software to take to LANL's LANSCE facility where I employed the Chi-Nu organic scintillator array to measure ^{252}Cf(sf)neutrons and photons. I also modeled the experiment with `MCNPX – PoliMi` and `MPPost`. I modified `MCNPX – PoliMi` to read fission events from `CGMF` and `FREYA` into `PoliMi` , and those results were compared to the experiment data.

6.1 Introduction

In nuclear fission, neutrons are primarily emitted first [59] followed by photon emission [64]. However, the details of the transition from neutron to photon emission are poorly understood. This work seeks to observe and quantify the competition between neutron and photon emission in ^{252}Cf(sf). Many studies of prompt emissions, exclusive to one particle type, such as neutrons alone, have been done for key fissioning isotopes [50, 52, 65, 66, 67, 68, 69, 70, 71], but only a few experiments [28, 72, 73, 74] have measured neutrons and photons simultaneously. In previous work, experiments were performed to correlate both neutron and photon emission with fragment properties. One [28] shows a

positive correlation, another [72] observes a complex fragment-dependent correlation, a third [73] reports a negative correlation, while a fourth [74] found no evidence of correlated emission from specific fragment pairs. The fission event models CGMF [11, 29, 41, 42] and FREYA [12, 12, 43, 45, 46, 47, 48], however, predict a negative correlation. Additionally, only one previous experiment [73] commented on event-by-event correlations; the neutron and photon multiplicity from each fission event was measured and a correlation between the neutron and photon multiplicities was observed. Given the contradictory experimental results, it is clear that the transition from neutron emission to photon emission in fission fragment de-excitation is not well understood or measured.

After fission occurs, during fragment de-excitation, neutrons are primarily emitted until the fragment excitation energy nears the neutron separation energy [24]. Neutrons remove much of the excitation energy, but do little to change the angular momentum. Photons are emitted primarily after neutron emission and, in general, decrease the fragment angular momentum [75]. The transition between neutron and photon dominance could give rise to correlations between them, as were previously measured [28, 72, 73, 74].

Recently, physics-based event-by-event models, capable of calculating neutron and photon correlations, were developed to move beyond empirical models [8, 40, 51] and models limited to single particle distributions [53, 76]. These models include CGMF [11, 29, 41, 42], FREYA [12, 43, 44, 45, 46, 47, 48], FIFRELIN [77], and GEF [78]. These event-by-event models follow pairs of fission fragments from scission through the complete de-excitation process, capturing correlations between emitted neutrons, photons, and fragments. Many measured data sets are available to validate single-particle distributions from these event-by-event models but few correlated neutron-photon data sets exist and are currently limited to ^{252}Cf(sf) [28, 72, 73, 74]. Correlated data are particularly useful to validate the event-by-event treatment of the transition from neutron emission to photon emission.

This work presents measured neutron-photon correlations event-by-event. Neutrons and photons from ^{252}Cf(sf) were measured with an organic scintillator array. The measured neutron-photon correlations are compared to simulations employing the CGMF [11, 29, 41, 42], FREYA [12, 43, 44, 45, 46, 47, 48], and MCNPX − PoliMi [8, 40] fission generators.

Here, the built-in MCNPX − PoliMi fission model source card option IPOL(1) = 1 is referred to as PoliMi in the following. MCNPX − PoliMi was used to model the laboratory geometry and to transport fission neutrons and photons provided by three fission event generators. This work is the first dedicated measurement of neutron-photon correlations from all fragments on a fission-by-fission basis and provides new insight into neutron-photon competition.

6.2 Previous measurements of neutron-photon correlations

The four previous experiments measuring ^{252}Cf(sf) neutron-photon correlations discussed in the introduction [28, 72, 73, 74] are described in more detail in this section. Nifenecker *et al.* explored the correlation as a function of fragment mass [28]. Wang *et al.* studied the correlation in fragment mass and in kinetic energy bins [72]. Glässel *et al.* determined the correlation as a function of fragment kinetic energy as well as on an event-by-event basis [73]. Bleuel *et al.* isolated event-by-event multiplicities for two sets of fragment pairs [74].

Nifenecker *et al.* [28] averaged photon and neutron measurements over fragment properties. Therefore this experiment cannot comment on the event-by-event nature of neutron and photon competition. They concluded, however, that there was a linear relationship between the average total photon energy, $\overline{E}_\gamma$, and the average number of neutrons emitted for a given fragment, $\overline{\nu}$, in a ^{252}Cf(sf) event $\overline{E}_\gamma(A, \mathrm{KE}) = [0.75\overline{\nu}(\mathrm{A}, \mathrm{KE}) + 2]$ MeV, where A is the fragment mass number and KE is the fragment kinetic energy. When averaged over a pair of complementary fragments, they reported a relationship between total photon energy and neutron multiplicity of $\overline{E}_\gamma^{\mathrm{tot}} = [0.75\overline{\nu} + 4]$ MeV. They further determine a relationship between photon and neutron multiplicity emitted per fragment of $M_\gamma = 1.13\overline{\nu} + 3$ assuming a proportionality of 1.55 photons per MeV based on the measurements of prompt [33] and delayed [34] photons, $M_\gamma(A)$, summed by John *et al.* [79]. They suggested that their positive correlation is evidence of an increase in the mean spin

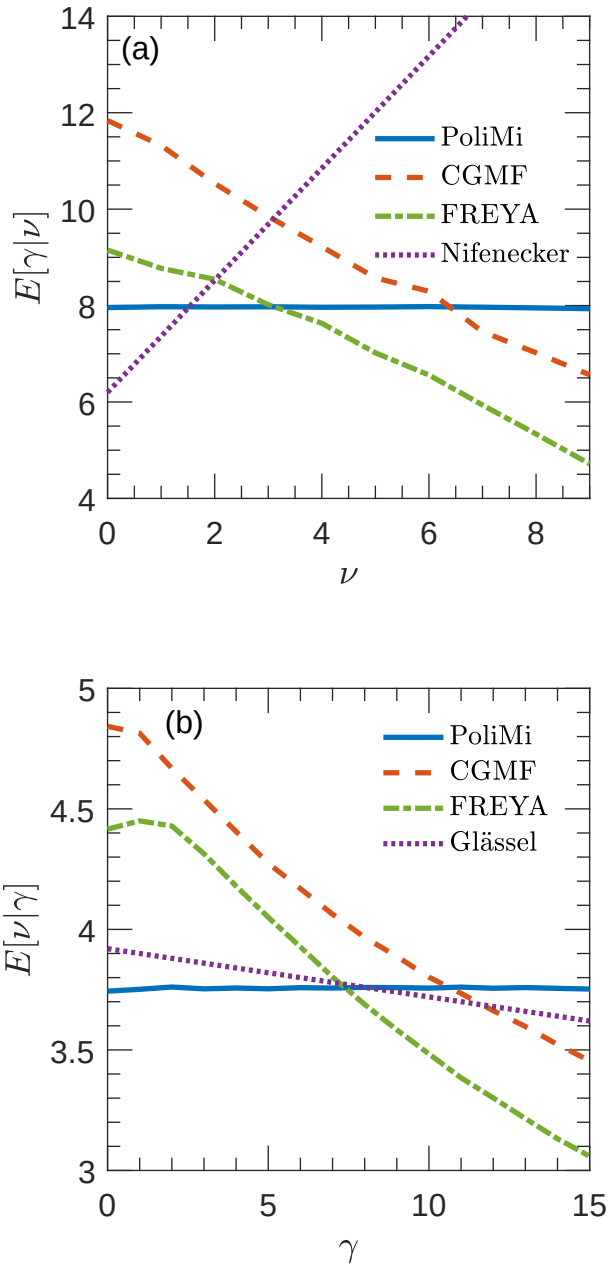

Figure 6.1: The average number of photons emitted given neutron number, $E[\gamma|\nu]$ (a), and average number of neutrons emitted given photon number, $E[\nu|\gamma]$ (b), for ^{252}Cf(sf). Results from fission models are compared to data from Nifenecker *et al.* [28] (a) and from Glässel *et al.* [73] (b).

of the fragments with excitation energy while the excitation energy is determined from measured fragment masses and total kinetic energy. Other modes of fragment excitation are ignored in their discussion.

The Nifenecker *et al.* correlation is shown in Fig. 6.1(a) where $E[\gamma|\nu]$ is the expected number of photons emitted given the number of neutrons emitted. If the neutron and photon multiplicity probability matrix is $P(\nu,\gamma)$, then $E[\gamma|\nu]$ is the row average while $E[\nu]$ is the average ν over the entire $P(\nu,\gamma)$ matrix.

Wang *et al.* [72] expanded upon the study in Ref. [28] by correlating photon and neutron multiplicities with total kinetic energy over three fragment mass regions of interest: light ($85 < A < 123$); symmetric ($124 < A < 131$); and heavy ($132 < A < 167$). The light and symmetric mass regions exhibit a linear trend with a positive slope, qualitatively consistent with Ref. [28], whereas the heavy region is nonlinear with an overall positive trend. Wang *et al.* also showed that the `FREYA` results followed general trends of the measured neutron-γ correlation binned in fragment mass and TKE, but the overall agreement was poor. While `FREYA` shows a fragment-dependent, positive correlation following the experimental binning, this result is not indicative of the ability of `FREYA` to reproduce observed neutron and photon competition on a fission-by-fission basis.

On the other hand, Glässel *et al.* [73] studied correlations between neutron and photon multiplicities on a fission-by-fission basis as well as based on averages such as studied by Nifenecker *et al.*. When studying averages, they determined that the photon multiplicity distribution as a function of fragment mass, $M_\gamma(A)$, was rather independent of mass, in contradiction to the earlier results of John *et al.* [79]. Thus, rather than the 1.13 photons per neutron obtained by Nifenecker [28], given above, they found ~ 0.16 photons emitted per neutron, a much smaller result. In addition, in event-by-event mode, they determined a decrease in $\overline{\nu}$ of 0.02 per emitted photon, suggesting that neutron multiplicity and photon energy are anticorrelated. While they also suggest, like Nifenecker, that a positive correlation with respect to excitation energy is evidence of an increase in the mean fragment spin with excitation energy, they add the qualification that this conclusion does not have any bearing on neutron-photon competition.

The Glässel *et al.* correlation is shown in Fig. 6.1(b) where $E[\nu|\gamma]$ is the expected number of neutrons emitted given the number of emitted photons. For the probability matrix $P(\nu,\gamma)$, $E[\nu|\gamma]$ is the column average while $E[\gamma]$ is the average γ over the entire $P(\nu,\gamma)$ matrix.

Bleuel *et al.* [74] found no significant correlation between neutron and photon multiplicity. Using a high-efficiency photon detector and known gamma-ray energy transitions, they isolated the photon multiplicity distributions for two post-neutron emission fragment pairings: two-neutron ^{106}Mo+^{144}Ba and four-neutron ^{106}Mo+^{142}Ba. The two-neutron distribution yielded 9.9 ± 0.7 photons on average while the four-neutron distribution yielded an average of 9.9 ± 0.5 photons. In contrast, Nifenecker *et al.*would predict an increase of ~ 1.3 photons for the four-neutron distribution relative to that of two-neutrons, an effect which should have been detectable. The Bleuel *et al.* conclusion was, however, based on specific fragment pairs with prominent photon lines rather than averages. It was also limited statistically, giving large uncertainties in the measured multiplicities.

The work presented here focuses on observing neutron-photon correlations on an event-by-event basis rather than averaged over fragment mass or energy to investigate event-by-event competition. We seek to determine if the number of photons detected, γ', in a given fission event has any implication on the number of neutrons detected, ν'.

In Figs. 6.1 and 3.10, the calculated distributions for neutron and photon emission from ^{252}Cf(sf) are shown for `PoliMi`, `CGMF`, and `FREYA`. There is no correlation between neutrons and photons with `PoliMi`. Both `CGMF` and `FREYA`, however, exhibit similar negative correlations between the particle multiplicities on a event-by-event basis, as shown in Fig. 6.1. The trends from these two calculations are the same, even though the absolute scales are different.

6.3 Experimental method and analysis

We measure correlations between neutrons and photons emitted during spontaneous fission of ^{252}Cf. First we describe the experiment and the data acquisition. Then we discuss

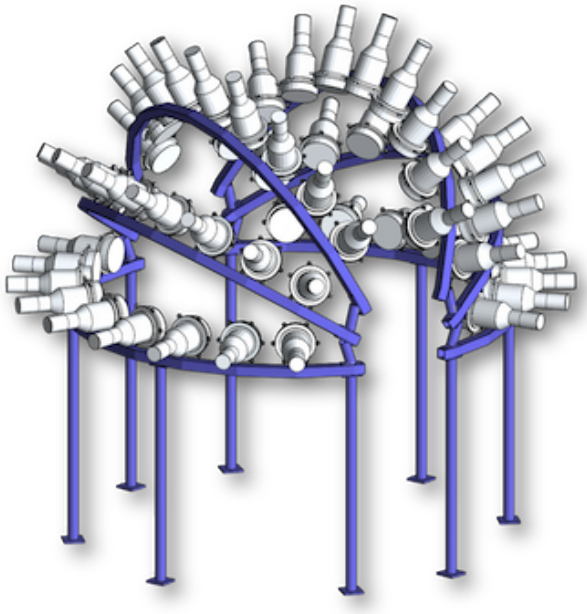

Figure 6.2: A model of the Chi-Nu detector holder and the 45 17.78 x5.08 cm EJ-309 detectors. Fifty-four detectors are pictured. One of the topmost arcs was in place but its signals were not read out. The fission chamber was placed at the center of the hemisphere for the measurement.

correlated background subtraction. Finally, we present simulations of the experiment.

6.3.1 Experiment

The Los Alamos National Laboratory Chi-Nu array [13], consisting of 54 17.78 cm diameter by 5.08 cm thick cylindrical EJ-309 scintillators coupled to 12.7 cm diameter photomultiplier tubes (Hamamatsu R4144), was used to measure neutrons and photons from ^{252}Cf(sf). In this work, because of the number of data channels available in the electronics, only 45 of the detectors were used. The array, shown in Fig. 6.2, has a flight path of 100 cm from each detector to the fission chamber, located at the center of the hemispherical array.

This experiment used an ionization chamber designed and fabricated in 2010 at Oak Ridge National Laboratory (ORNL) [80]. The californium source, with the composition shown in Table 6.1, was deposited over a hemispherical surface in the chamber. In a fission event, one or two fragments escape the surface and deposit energy through ionization, producing a pulse above a fixed threshold set to exclude alpha particle interactions [81].

Table 6.1: The californium source composition and the fission rates from the sources on the date of assay, November 2010, and the date of the experiment, July 2015.

Isotope	Nov. 2010 Assay (μg)	Nov. 2010 Fiss. Rate (f/s)	July 2015 Fiss. Rate (f/s)
^{252}Cf	1.641	9.705×10^5	2.986×10^5
^{250}Cf	0.265	8.19×10^2	6.45×10^2
^{248}Cm	0.173	3.06	17.5

The chamber was positioned in the center of the array on the end of a metal tube. The ionization chamber signal was used as the fission time trigger.

The experiment was performed shortly after the production of the Californium fission chamber relative to the 2.6 year ^{252}Cf half life. Therefore the ^{252}Cf(sf) rate was high relative to spontaneously fissioning impurities in the sample, as we now describe. The fission rate at the time of measurement was 2.98×10^5 spontaneous fissions per second. The majority of those fissions are ^{252}Cf [82] with small contributions from ^{250}Cf(sf) (0.2%) and ^{248}Cm(sf) (6×10^{-5}%). The different decay rates result in a growing fraction of ^{250}Cf and ^{248}Cm relative to ^{252}Cf. However, the fission contributions from ^{250}Cf(sf) and ^{248}Cm(sf) are negligible and are thus ignored in further analysis.

The fission rate in the ionization chamber was low enough that the fission events and their emissions are assumed to be well separated in time. The pile-up of fission events was approximately 3.5%, given the source rate and a 150 ns window, long enough to acquire neutrons at and below the detector threshold energy. The fission chamber pulse height trigger threshold, however, was set for zero digitizer dead time, resulting in a trigger rate of 65% of the expected fission rate. There were 3.21×10^9 fission triggers above threshold during the experiment.

Pulses from the detectors and fission chamber were digitized using three CAEN V1730 waveform digitizers with 500 MHz sampling and 14-bit amplitude resolution over a 2 V range. The detectors were gain-matched to 478 keVee at 0.3 V with a lower threshold of 40 keVee (a 0.62 MeV proton recoil equivalent threshold) and an upper threshold of 3,180 keVee (an 8.1 MeV proton recoil equivalent threshold) determined by the upper limit of the 2 V range. All digitized waveforms were recorded for post-processing. Pulse

shape discrimination (PSD) was used to discriminate between neutron and photon events in the liquid organic scintillators [16, 23].

For the organic scintillators, only pulses above a 100 keVee lower threshold (the 0.80 MeV proton recoil equivalent threshold) were analyzed. Double-pulse fractional cleaning [83] was used to remove pile-up events. Pulse pile up is removed because the PSD algorithm does not handle that case; pile-up pulses are usually classified as a neutron regardless of the contributing particle types. After cleaning, charge integration PSD [22] was performed. In charge integration PSD, two integrals are computed: one over the whole waveform and one over the tail of the waveform. The tail integral starts 24 ns after the peak. A quadratic PSD line was assigned to discriminate between the two particle types using an algorithm described by Polack *et al.* [22]. Figure 6.3 shows the tail integral plotted against the total integral. Two bands are produced, one for photons (below the discrimination line) and one for neutrons (above the discrimination line). Significant overlap occurs at small total integrals (below ~ 0.5 V ns) and pulse heights (below ~ 0.1 MeVee). Therefore, misclassification is most likely in this region. Misclassification of photons as neutrons was estimated to be $\sim 1\%$ using time-of-flight. After background is subtracted in the time region from fission to 10 ns after the fission, only photon detections are expected and all neutron detections in that region were considered misclassified photons.

The organic scintillators, in this configuration, were sensitive to neutrons above 0.8 MeV, given a 100 keVee threshold, and had limited sensitivity to neutrons above 8.1 MeV. The detectors are sensitive to approximately 77% of the neutron spectrum with an intrinsic efficiency of $\sim 32\%$ for the full spectrum. The detectors are sensitive to the full prompt photon spectrum. The intrinsic efficiency to the full photon spectrum is approximately 23%. Obtaining the correlation between the emitted neutron and photon multiplicities using experimental data was not possible because the inverse problem is poorly posed given the low neutron and photon efficiencies. While organic scintillators are sensitive to most of the photon and neutron spectra, these detectors are not uniformly sensitive to the entire spectral energy distribution. Consequently, correlations in regions

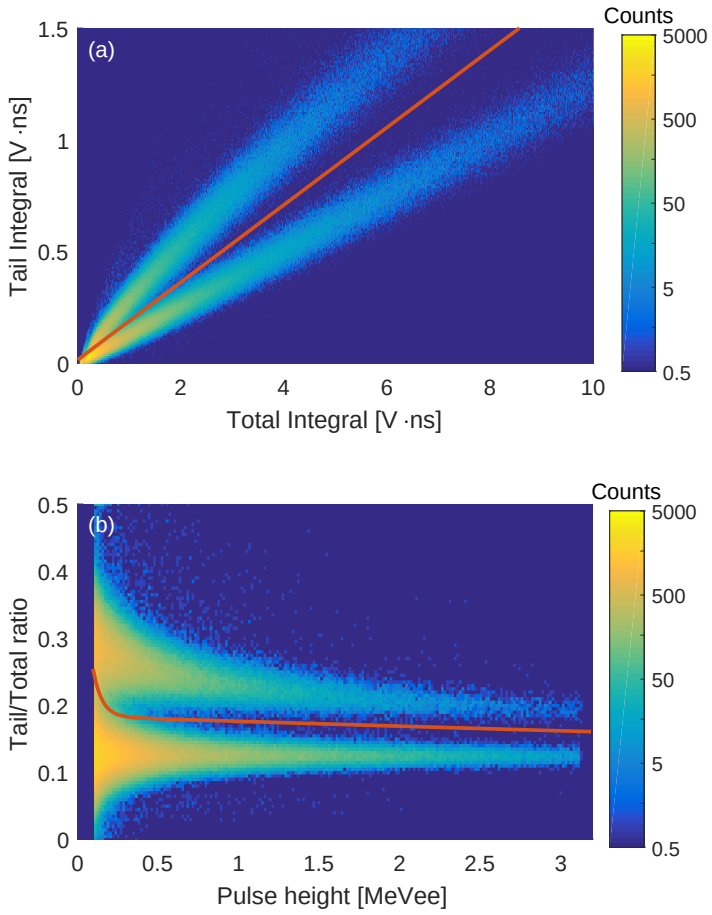

Figure 6.3: (a) The tail integral as a function of the total waveform integral. (b) The tail-to-total ratio as a function of pulse height. Two features are apparent: the upper bands in each panel primarily includes neutron detections while the lower bands indicate photon detections, separated by the discrimination line, in red. More than 730,000 detections are shown.

where the detectors are less sensitive may be unobserved or less proportionately observed.

After post-processing of the waveforms, which includes particle identification based on PSD, neutron and photon events in a 400 ns coincidence window were collected. The coincident events were analyzed to produce pulse height, cross-correlation, multiplicity, and time-of-flight distributions. The experimental distributions were then compared to simulated results from the fission models employed.

6.3.2 Correlated background subtraction

The simple assumption in a single bin experiment, such as the neutron multiplicity as a function of fragment mass, that the measured signal is a simple sum of real and accidental

counts, does not hold for these data. Instead, we have a two-dimensional histogram of measured events, M, with each element of the histogram, $m_{i,j}$, having two indices: i for the number of detected neutrons and j for the number of detected photons in each event. Each element $m_{i,j}$ is a sum of contributions from a combination of the real, R, and the accidental, A, histograms with elements $r_{k,l}$ and $a_{i-k,j-l}$ respectively,

$$m_{i,j} = \sum_{k=0}^{i} \sum_{l=0}^{j} r_{k,l} a_{i-k,j-l} \tag{6.1}$$

The one-dimensional background subtraction method used by Diven *et al.* [84] is extended here to two dimensions (neutrons and photons) to account for the accidental contributions to $m_{i,j}$.

Given $m_{i,j}$, it is possible to solve for the elements of unknown reals histogram $r_{i,j}$, with $(k,l) \neq (i,j)$:

$$r_{i,j} = \frac{m_{i,j} - \sum_{k=0}^{i} \sum_{l=0}^{j} r_{k,l} a_{i-k,j-l}}{a_{0,0}} \tag{6.2}$$

Due to the coincidence logic imposed at data acquisition (only events with one or more triggered detections were saved), the $m_{0,0}$ element could not be measured directly. However, $a_{0,0}$ was directly measurable. Thus, $m_{0,0}$ and $r_{0,0}$ were estimated from the simulation of the experiment. Section 6.4.1 discusses the fidelity of the simulation compared to experiment.

6.3.3 Simulation

The `PoliMi` code was used to model the laboratory geometry and particle transport. `PoliMi` models the detector system and surrounding laboratory in great detail. The detectors are modeled to almost full detail; the photomultiplier tube electronics are partially homogenized. Ignoring small hardware such as bolts and nuts, the Chi-Nu array structure is fully modeled. The concrete floor was modeled to replicate room-return effects. One topmost detector arc was not used for data acquisition. However, it was left in place during the measurement and therefore was included in the model of the experiment.

The ORNL fission chamber is modeled in detail with the source term sampled over the 1 cm diameter spot on a 304L alloy stainless steel hemispherical surface. A partial MCNPX − PoliMi model input file for this experiment can be found in Appendix 3.

The waveform processing and classification is assumed to be ideal in simulation; particle misclassification is not modeled. Misclassification is most prevalent at low pulse heights. Therefore, a conservative pulse height threshold of 100 keVee was used.

Other fission event generators were also utilized to generate events for transport. The fission event generators (CGMF, FREYA, and PoliMi) were used to produce a history file of fission events which were passed to the full PoliMi model for particle transport. Initial energy, initial direction, and particle type for each particle generated in each individual fission event was passed to PoliMi. The PoliMi code samples a new random fission event when using PoliMi and FREYA. A history file of 1.92×10^6 fission events generated by CGMF were resampled with new, randomly sampled, fission fragment directions.

Following transport, PoliMi records a file detailing interactions within specified detector cells. Details recorded in the interaction file include but are not limited to interaction type, particle type, nucleus of interaction, energy deposited, and time of interaction. This interaction file was passed to a code emulating detector response. The detector response code converts energy deposition to scintillation light, handles multiple interactions, and applies thresholds to ultimately record particle type, light output, and time for each detection. The light output distributions in MeV electron equivalent (MeVee) for energy deposited in MeV from neutron scattering on a proton and from a photon scattering on an electron are shown in Fig. 2.3. The Birks model, a semi-empirical relationship described by Norsworthy et al. [39], was implemented in the detector response code to convert neutron energy deposited on protons to light output in the EJ-309 scintillator. The light output response from photon scattering on electrons was one-to-one. Using PoliMi and the detector response code, the simulated intrinsic efficiency was calculated as a function of incident particle energy and is shown in Fig. 2.3 for neutrons and photons. After detector response is applied, PoliMi simulation results from each ^{252}Cf(sf) event generator were compared to measurement.

6.4 Results

We recall that three fission event generators (`CGMF`, `FREYA`, and `PoliMi`) were used to produce a history file of fission events which were passed to the full `PoliMi` model for particle transport. Initial energy, initial direction, and particle type for each particle generated in each individual fission event was passed to `PoliMi` for all fission event generators. Experimental and simulated detector results are compared for independent and dependent multiplicities of photons detected, γ', and neutrons detected, ν', following a fission event.

6.4.1 Simulation fidelity

To validate the `PoliMi` model and the detector response model, EJ-309 detector pulse height and time-of-flight distributions are compared to experiment results in Figs. 6.4-6.7 using `PoliMi`. `PoliMi` was used to transport emitted fragments, neutrons and photons from fission events generated by the three models (`PoliMi`, `CGMF`, and `FREYA`). Because evaluated spectra are used in the `PoliMi` fission source, Mannhart [49] for neutrons and Valentine [51] for photons, we expect agreement with experiment when the geometrical and detector response models are accurate.

The experimental count rates and pulse heights include only events in a specified time range after the fission start signal. A time window of 15 to 150 ns (energy equivalent of 22 to 0.2 MeV) after the fission events was used for neutrons while, for photons, a time window of 1 to 20 ns after fission was employed. The time regions from -150 to -15 ns and from -20 to -1 ns before the fission start signal were subtracted as background for neutrons and photons respectively since only accidental detections are expected before the fission start signal.

In Figs. 6.4(a) and 6.5(a), simulated and experimental pulse height distributions are compared and are shown to agree well over most of the pulse height range. The `PoliMi` result is within 15% of the experimental result over the entire range for both neutrons and photons. The ratios between the `PoliMi` and experiment results, C/E,

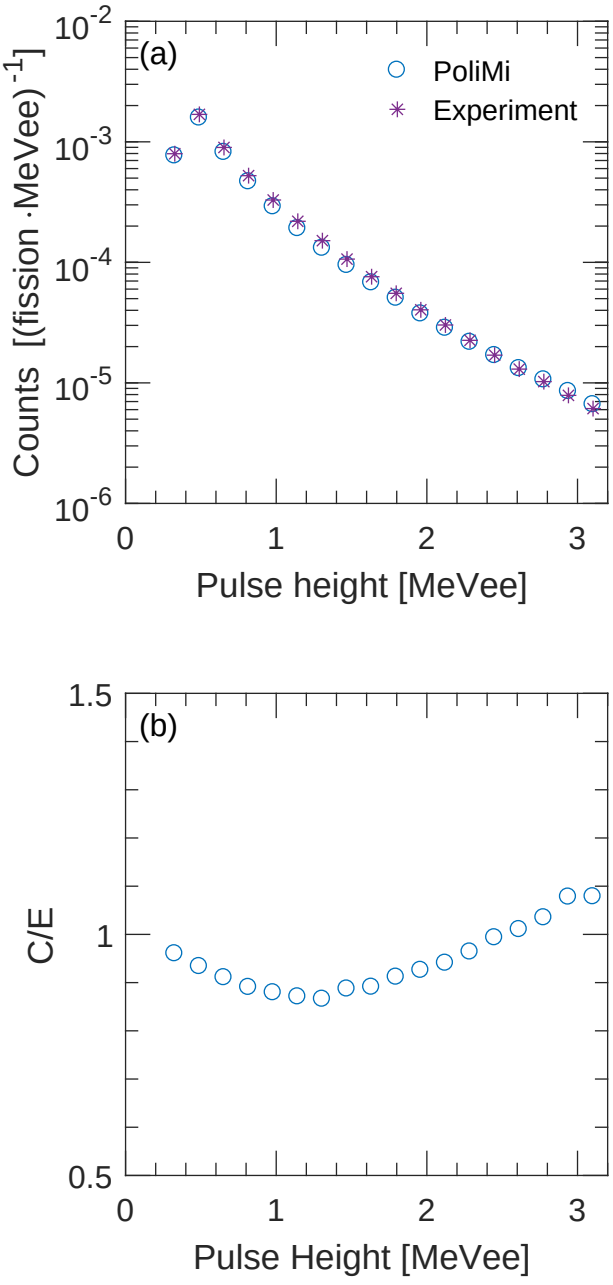

Figure 6.4: Calculated and experimental mean pulse height neutron distributions (a) and the ratio of the calculation results to the measurement, C/E (b) are shown. The results are averaged over all detectors. The statistical uncertainties are smaller than the points. Approximately 6.1×10^6 detections are shown for the experimental results.

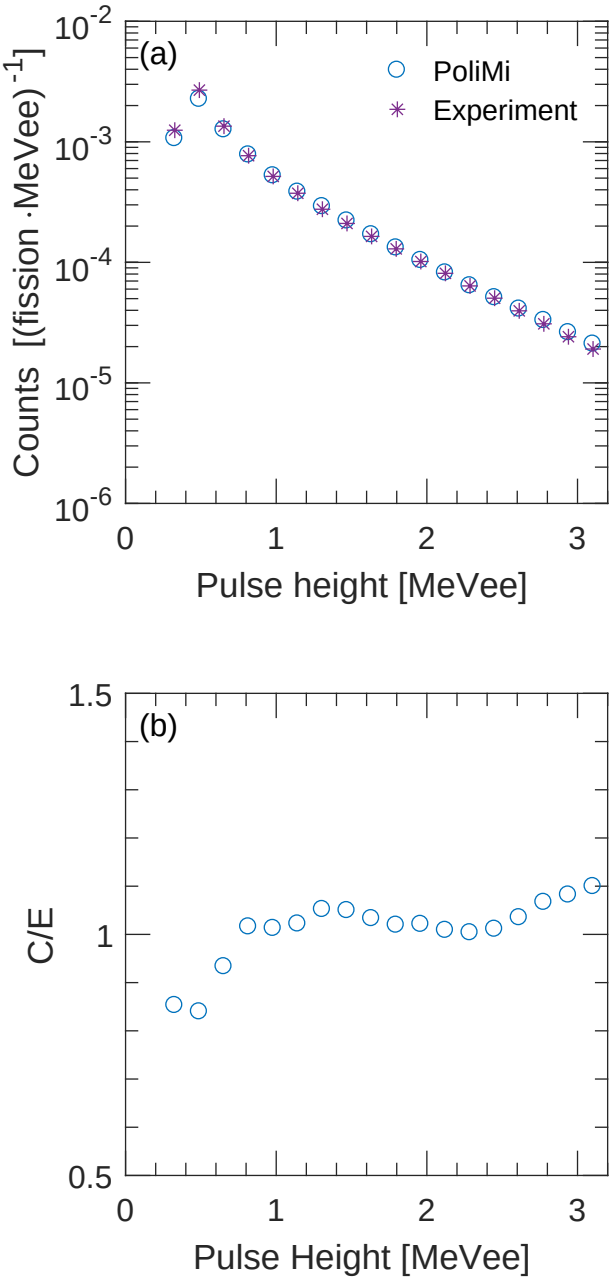

Figure 6.5: Calculated and experimental mean pulse height photon distributions (a) and the ratio of the calculation results to the measurement, C/E (b) are shown. The results are averaged over all detectors. The statistical uncertainties are smaller than the points. Approximately 1×10^7 detections are shown for the experimental results.

shown in Figs. 6.4(b) and 6.5(b), better quantify the agreement. In the neutron pulse height histogram, disagreement above 0.8 MeV is attributed to error in the function to convert proton recoil energy to light output used in the detector response emulator [39]. For photon pulse heights below 0.8 MeV, the simulation overpredicts the count rate. Because low pulse height detections are susceptible to PSD misclassification, some photon events are misclassified as neutron events or vice versa. However, the photon simulations agree within 5% over most of the range. The mean pulse height distributions in Figs. 6.4(a) and 6.5(a) show that the `PoliMi` model, including detector response, accurately replicates the experiment.

In Fig. 6.6, the simulated neutron time-of-flight distributions agree well with experiment over most of the time range, with the exception of the region below 20 ns. Given the upper (3,180 keVee or 8,100 keV proton recoil) and the lower (100 keVee or 800 keV proton recoil) pulse height thresholds, most neutron time-of-flight counts are expected between 25 and 80 ns for a fission neutron spectrum. The experiment is susceptible to particle misclassification, particularly evident below 20 ns whereas the simulated particle identification is perfect. For $30 < \Delta t < 75$ ns, `PoliMi` agrees with experiment within 10%. A small peak is seen in Fig. 6.6(b) in C/E in this region because fast neutrons arriving at the detector induce photons in the active volume of the detector and some neutrons may be misclassified as photons. Above 75 ns, room return becomes significant and C/E increases. In Fig. 6.7, the simulated and measured photon time-of-flight distributions agree well over most of the time range except for $\Delta t > 75$ ns where the model overestimates room return.

Agreement within 10% is considered sufficient confidence that the measurement and simulation agree and further analysis on higher-order coincidence and correlation results using simulations may be performed with confidence. The `PoliMi` simulation agrees with experiment, as is expected, because the built-in model uses evaluated multiplicity and energy spectra. The close agreement between the simulated and measurement for the pulse height and time-of-flight distributions provide confidence in the model of the laboratory and the detector response.

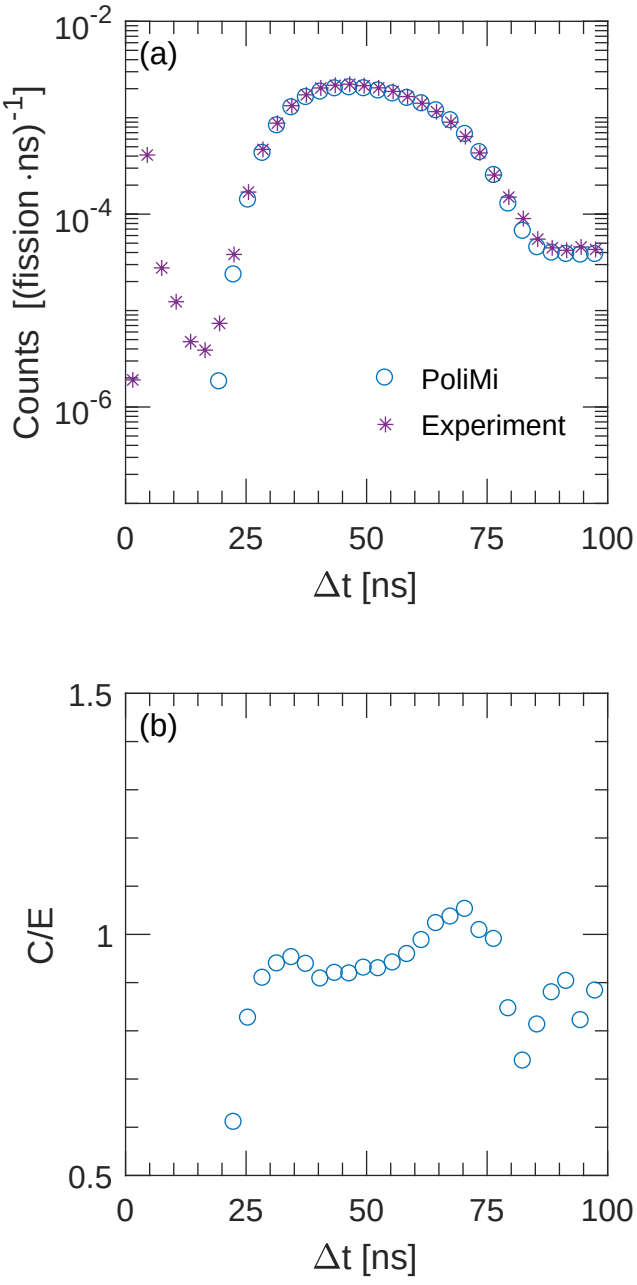

Figure 6.6: (a) The calculated and experimental neutron time-of-flight distributions. (b) The ratio of the calculation to the measurement, C/E. The results are averaged over all detectors. Time zero was the time of the fission start signal. The uncertainties are smaller than the points: 3.6×10^6 detections are shown for the experimental result.

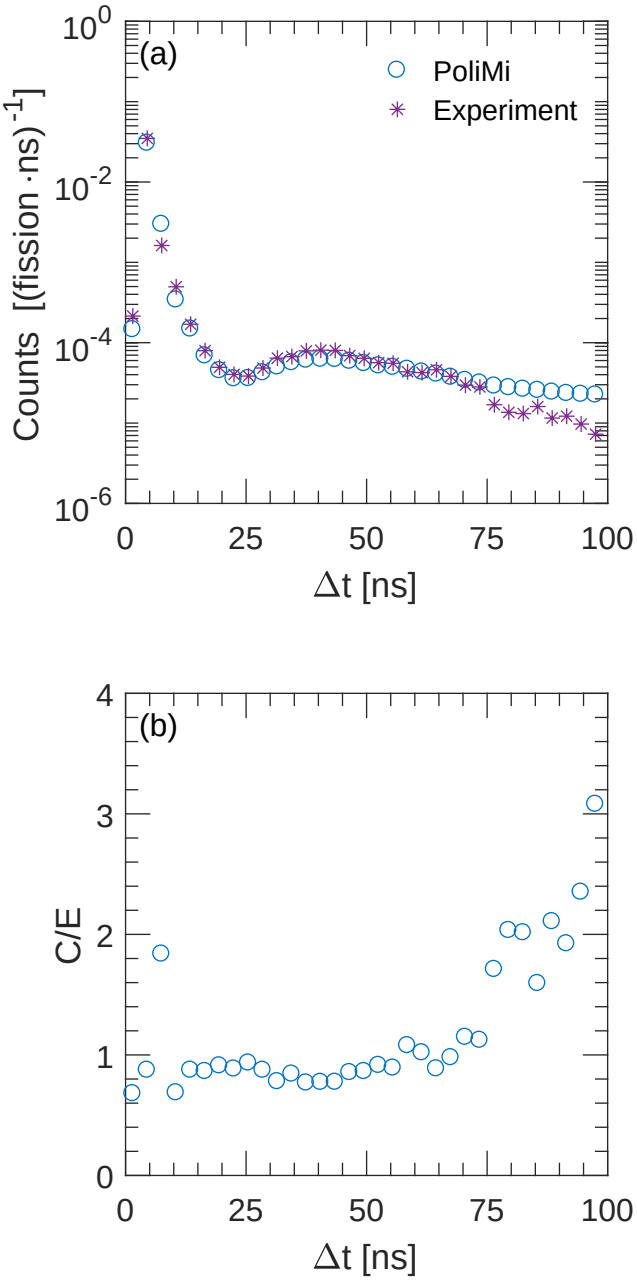

Figure 6.7: (a) The calculated and experimental photon time-of-flight distributions. (b) The ratio of the calculation to the measurement, C/E. The results are averaged over all detectors. Time zero was the time of the fission start signal. The uncertainties are smaller than the points: 6.2×10^6 detections are shown for the experimental result.

6.4.2 Correlated fission model comparisons

Comparison of the simulated and experimental pulse height, time-of-flight, and coincidence distributions are shown for each fission model to demonstrate the effect of detector response on each model and to highlight the differences between the models. Joint-particle distributions are then compared to evaluate the correlation and the effect of neutron and photon competition during fragment de-excitation in experiment and simulation. Differences between the models may be expected in both single and inter-particle distributions.

The CGMF and the FREYA photon and neutron pulse height histograms do not agree well with experiment, as shown in Figs. 6.8 and 6.9. CGMF underestimates neutron pulse heights over the sensitive range and FREYA overestimates over most of the range, especially at high pulse heights. This indicates that the CGMF neutron spectrum is too soft while the FREYA prompt fission neutron spectrum is too hard in the measured energy range. These calculation results are consistent with the emission data in Fig. 3.11(a) where the CGMF result is softer than the evaluation and FREYA is harder than the evaluation. The good agreement with PoliMi is because the model uses the evaluated spectrum.

The photon pulse height histograms, however, show that the CGMF distribution is uniformly too high above 1 MeVee and FREYA, while lower than CGMF, increasingly overestimates toward higher pulse heights. This indicates that both CGMF and FREYA produce too many high energy photons. Both the CGMF and the FREYA photon energy spectra are higher than the PoliMi spectrum toward higher energies in Fig. 3.11(b). Again, the PoliMi model, using evaluated spectra, shows expected good agreement.

The CGMF and FREYA neutron time-of-flight distributions in Fig. 6.10 exhibit poorer agreement than the PoliMi built-in model. FREYA produces too many fast neutrons while CGMF has too few fast neutrons and too many slower neutrons. This result is consistent with the harder FREYA neutron spectrum and with the softer CGMF neutron spectrum relative to the evaluation, shown in Fig. 3.11(a).

The PoliMi, CGMF, and FREYA photon time-of-flight distributions in Fig. 6.11 show similar agreement below 10 ns while CGMF and FREYA show poorer agreement above 18

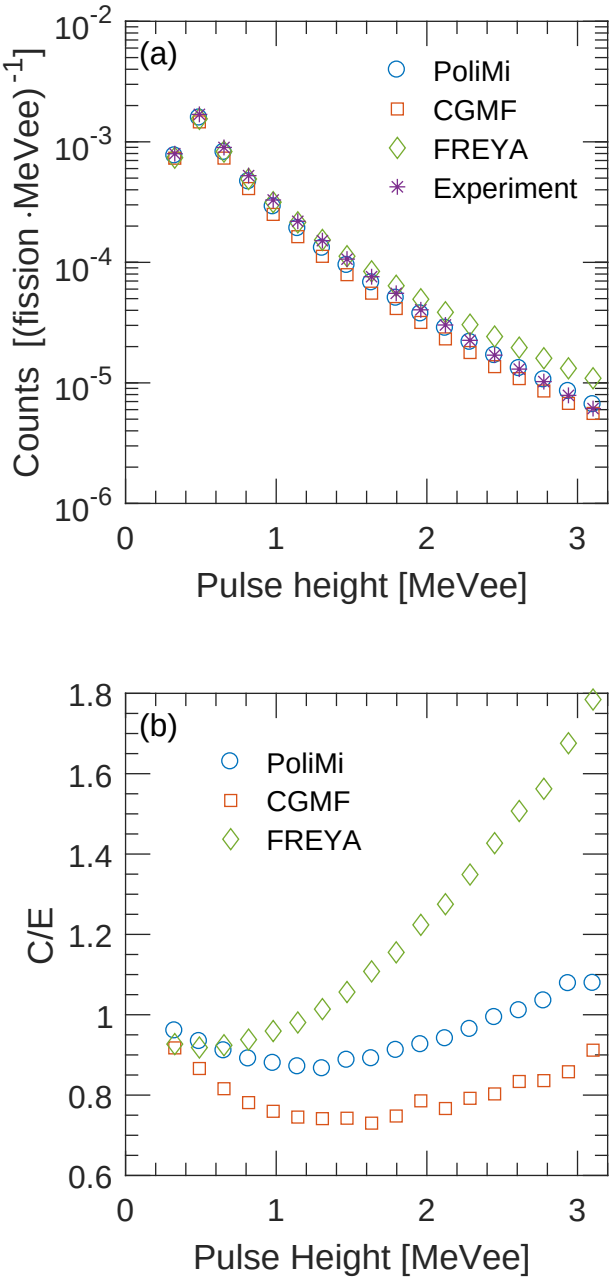

Figure 6.8: (a) The calculated and experimental neutron pulse height distributions. (b) The ratio of the calculation to the measurement, C/E. The results are averaged over all detectors. The uncertainties are smaller than the points: 6.1×10^6 detections are shown for the experimental result.

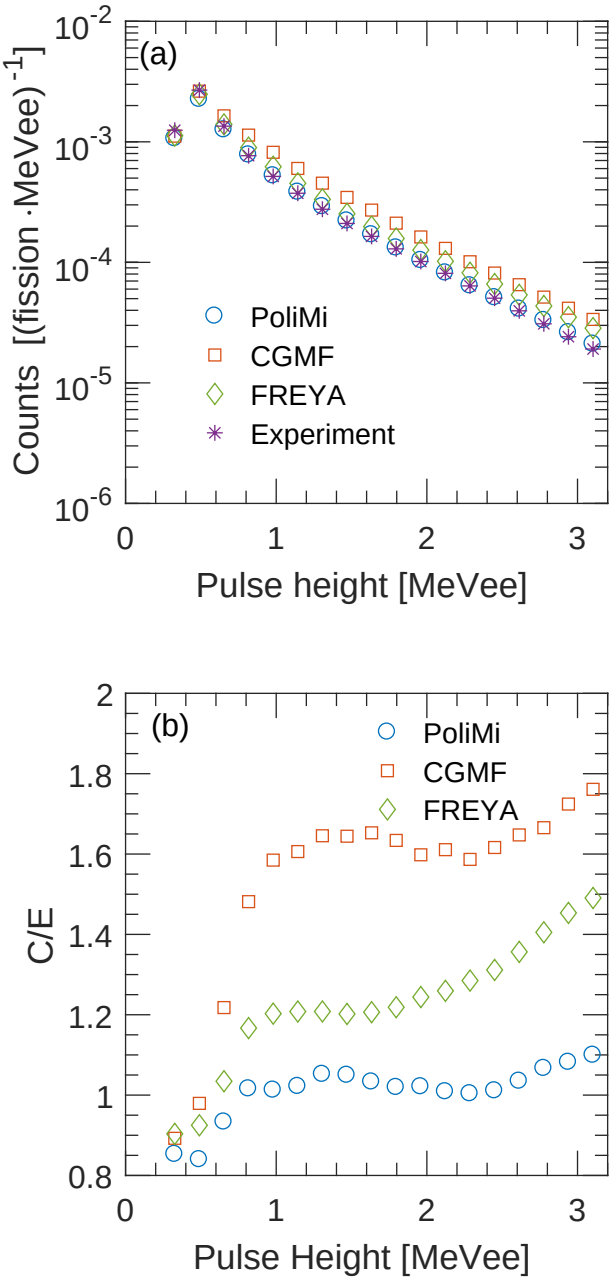

Figure 6.9: (a) The calculated and experimental photon pulse height distributions. (b) The ratio of the calculation to the measurement, C/E. The results are averaged over all detectors. The uncertainties are smaller than the points: 1×10^7 detections are shown for the experimental result.

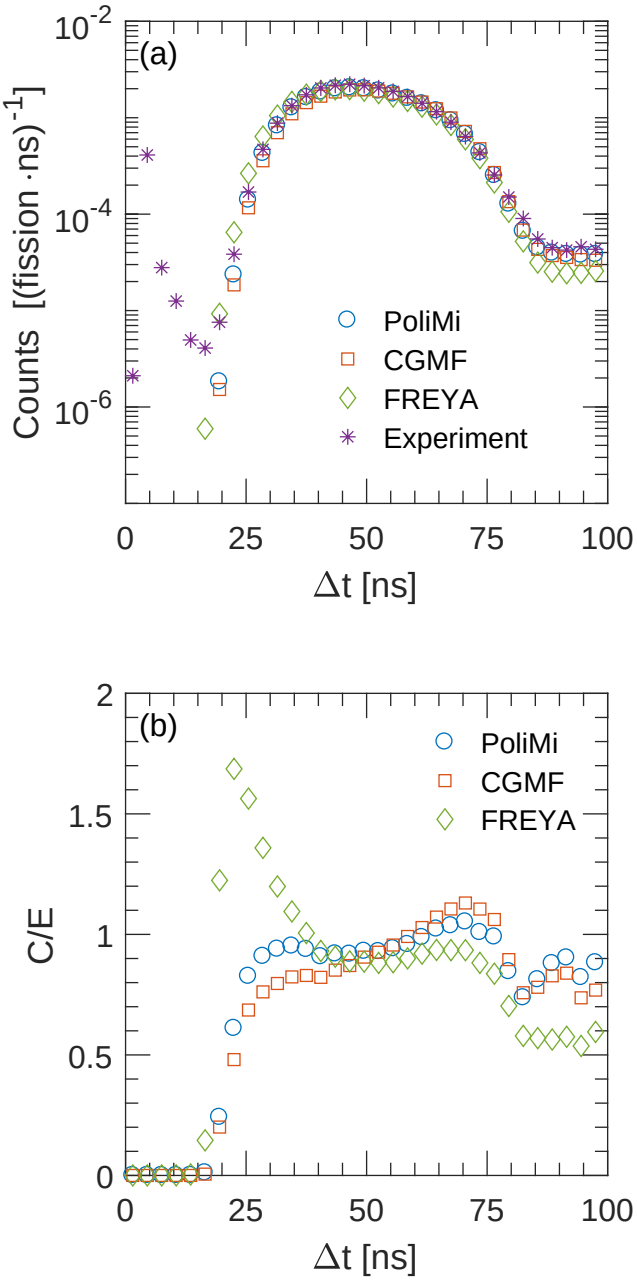

Figure 6.10: (a) The calculated and experimental neutron time-of-flight distributions. (b) The ratio of the calculation to the measurement, C/E. The results are averaged over all detectors. The uncertainties are smaller than the points: 3.6×10^6 detections are shown for the experimental result.

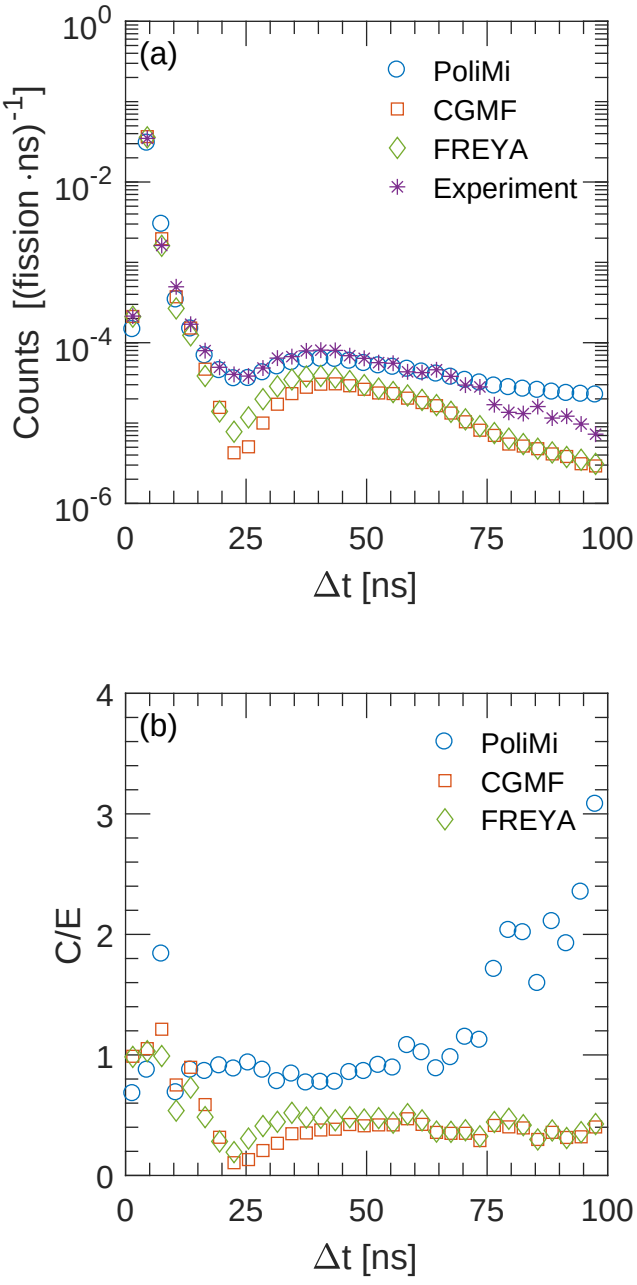

Figure 6.11: (a) The calculated and experimental photon time-of-flight distributions. (b) The ratio of the calculation to measurement, C/E. The results are averaged over all detectors. The uncertainties are smaller than the points: 6.2×10^6 detections are shown for the experimental result.

ns than PoliMi. Above 18 ns, delayed, scattered, and fast-neutron induced photons contribute to the signal. The PoliMi model produces time-distributed photons where a small fraction of photons are delayed according to Maier-Leibnitz *et al.* [85], whereas the CGMF and FREYA photon emissions only include prompt emission. The PoliMi result agrees between 18 and 75 ns because of a small contribution of delayed photons but beyond 75 ns PoliMi produces too many delayed photons. The region between 18 and 75 ns could also include a small contribution from neutrons misclassified as photons.

On a event-by-event basis, neutron coincidence distributions are shown in Fig. 6.12. The coincidence distribution is a convolution of the emitted multiplicity and the detector system response. Therefore, given the efficiency of the detection system, $\overline{\nu'}$, the mean number of detected neutrons, is expected to be much less than $\overline{\nu}$, and $\overline{\gamma'}$, the mean number of detected photons, is also expected to be much less than $\overline{\gamma}$. The neutron coincidences in FREYA agree well with experiment, as shown by the C/E for all ν' close to unity. Agreement of CGMF and PoliMi are similarly poor, overestimating C/E for more than two neutrons in coincidence, despite the CGMF $\overline{\nu}$ being higher than that for PoliMi.

The photon coincidence distributions are shown in Fig. 6.13. Photon coincidences from PoliMi agree well with experiment. Here CGMF overestimates the number of photon coincidences over the whole range while FREYA underestimates $P(\gamma')$ for $\gamma' > 2$. While PoliMi and FREYA have similar $\overline{\gamma}$, shown in Fig. 3.12(b), the impact of the narrower full photon multiplicity of FREYA shows at higher coincidences.

6.4.3 Correlations between neutrons and photons

Figure 6.14 compares the calculated $E[\gamma'|\nu']$, the expected number of photons detected given the number of neutrons detected, as a function of ν' to the experimental result. $E[\gamma'|\nu']$ and $E[\nu'|\gamma']$, the number of neutrons detected given the number of photons detected and shown in Fig. 6.15, are corrected for detector dead time as more particles are detected.

Figure 6.14 indicates little to no correlation for PoliMi and negative correlation for the other results. The PoliMi model is uncorrelated, therefore the result is expected to

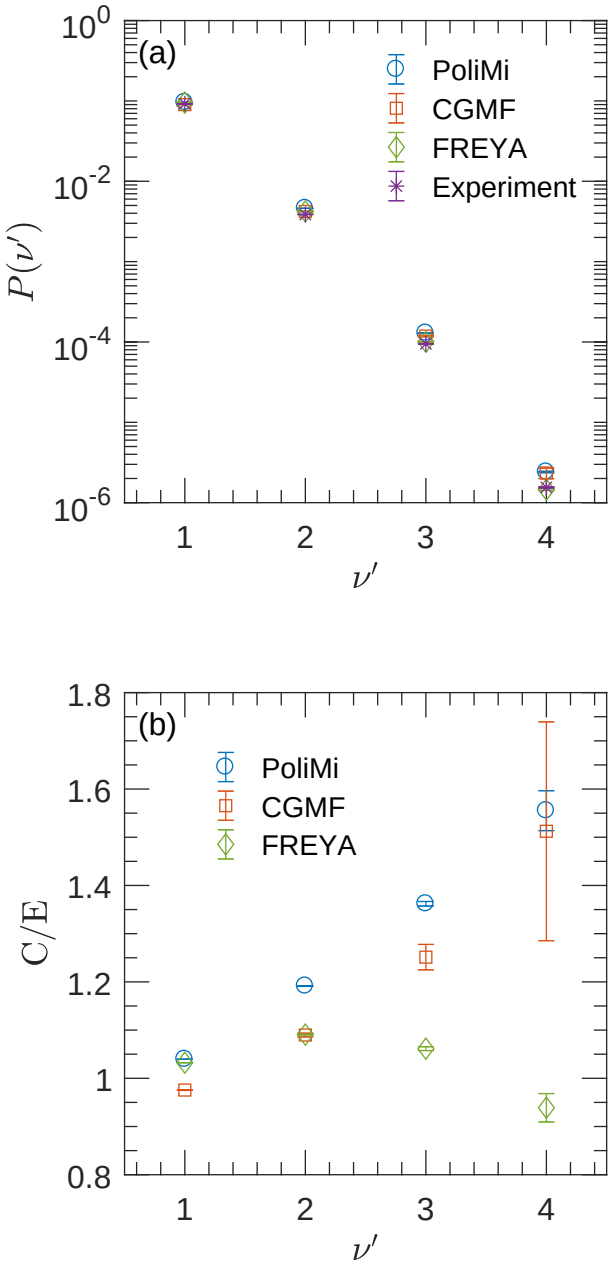

Figure 6.12: (a) Detected neutron multiplicity distribution, $P(\nu')$, after fission. (b) Calculated results relative to experiment. There are 3.3×10^8 neutron detections in the experimental result. Error bars represent statistical uncertainty only.

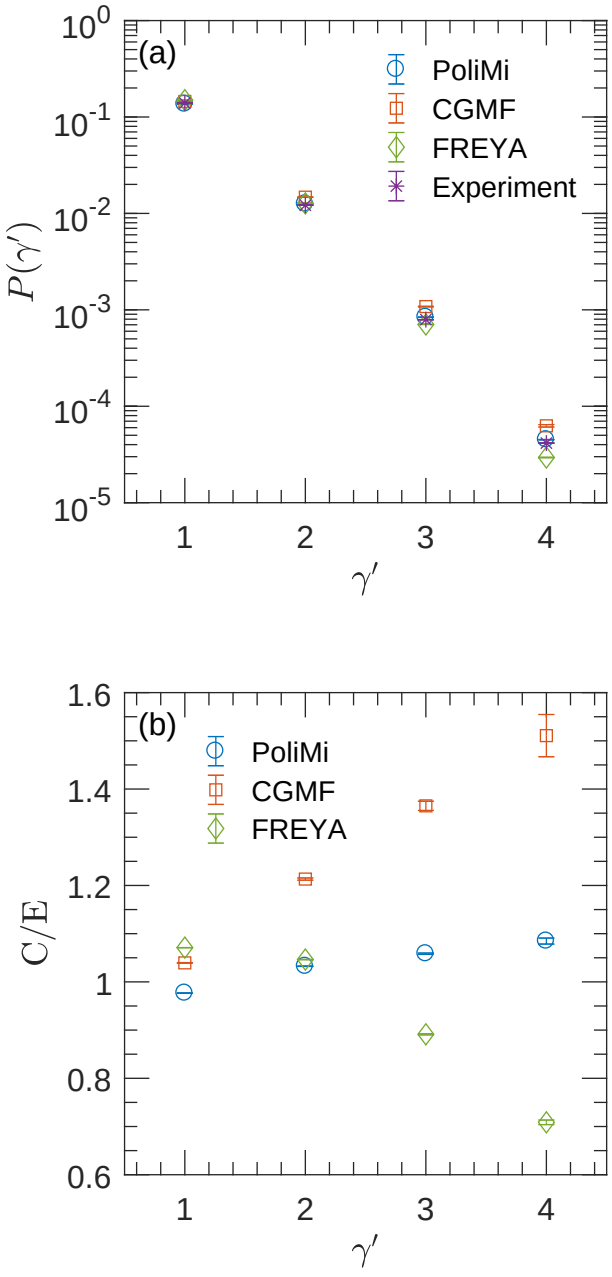

Figure 6.13: (a) Detected photon multiplicity distribution, $P(\gamma')$, after fission. (b) Calculated results relative to experiment. There are 5.6×10^8 photon detections in the experimental result. Error bars represent statistical uncertainty only.

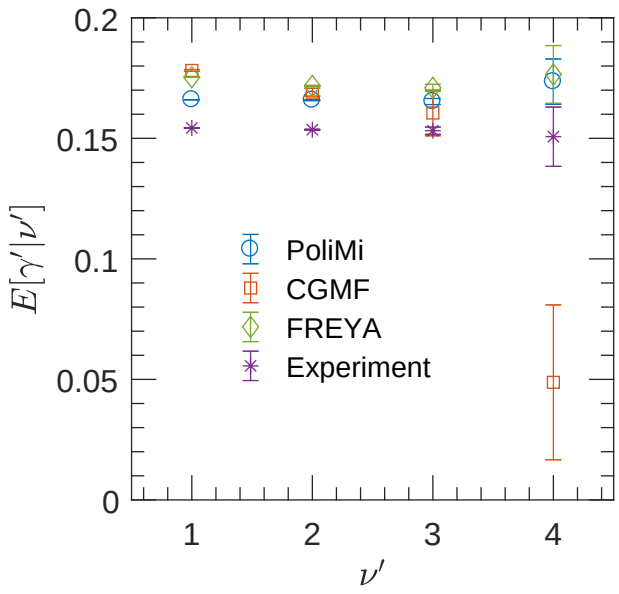

Figure 6.14: Expected number of detected photons given ν' neutrons detected in coincidence, $E[\gamma'|\nu']$. The experimental data include 7.8×10^8 detected fission events. Error bars represent statistical uncertainty only.

be invariant with neutron coincidences. The negative multiplicity correlation in `CGMF` and `FREYA` gives the expected result of decreased $E[\gamma'|\nu']$ for increasing ν'. This trend, however, is weak. In particular, since $\nu' = 4$ is greater than the measured $\overline{\nu}$ for ^{252}Cf(sf), ~ 3.76, the uncertainty on the model calculations, combined with the detector efficiencies, leads to large uncertainties on $E[\gamma'|\nu']$ for this value of ν'.

Figure 6.15 shows the relationship between $E[\nu'|\gamma']$ and γ' for the experiment and the simulations. Little to no correlation in `PoliMi` was observed while a negative correlation is seen for `CGMF` and `FREYA`, similar to the result in Fig. 6.14, albeit with a clearer trend in the zoom of $E[\nu'|\gamma']$ in Fig. 6.15(b), as expected. Here $\gamma' = 4$ is less than the measured average photon multiplicity for ^{252}Cf(sf), ~ 7.98 [53]. Thus one might expect the simulations to have smaller uncertainties for this value of γ', as shown in Fig. 6.15. The larger `CGMF` uncertainty on both $\nu' = 4$ and $\gamma' = 4$ in Figs. 6.14 and 6.15 due to the reuse of events from the history file.

We now discuss how the results compare to those of previous experiments. Recall that Glässel *et al.* found a negative neutron and photon multiplicity correlation of 0.02 neutrons per photon [73] on an event-by-event basis while Nifenecker *et al.* [28] suggested

a positive correlation of 0.89 neutrons per photon. To place these results on Fig. 6.15, a simple forward model was employed to propagate them through an analytic correlation model including detector response.

The analytic model assumed that both the neutron and the photon energy spectra were invariant with multiplicity, a binomial neutron multiplicity distribution [84], a double Poisson photon multiplicity distribution [53], and linear correlation between neutron and photon multiplicity. The photon spectrum is known to soften as photon multiplicity increases [86]. Assuming an invariant photon spectrum would only result in a small bias because the organic scintillators are sensitive to the full photon spectrum.

The photon multiplicity distribution $\Pi(G)$ for G prompt photons emitted was assumed to be a double Poisson distribution [53],

$$\Pi(G) = C_1 \frac{(C_2)^G e^{-C_2}}{G!} + (1 - C_1) \frac{(C_3)^G e^{-C_3}}{G!}, \tag{6.3}$$

where $C_1 = 0.675, C_2 = 6.78$, and $C_3 = 9.92$ [53]. The neutron and photon multiplicities were assumed to be linearly correlated. In the forward model, the photon distribution, Eq. (6.3), was assumed to be unchanged while the neutron multiplicity was adjusted by linearly varying the average number of neutrons emitted, $\overline{\nu}$, for a fixed photon multiplicity G. The neutron multiplicity distribution was assumed to be binomial [84] with emission of up to $m = 9$ neutrons allowed,

$$P(\nu) = \frac{m!}{\nu!(m-\nu)!} \left(\frac{\overline{\nu}}{m}\right)^{\nu} \left(1 - \frac{\overline{\nu}}{m}\right)^{m-\nu}. \tag{6.4}$$

The neutron and photon efficiencies simulated by `PoliMi` were applied to the emitted photon and neutron distributions to produce $E[\nu'|\gamma']$ as a function of γ' for the Nifenecker and Glässel correlations, +0.89 and -0.02 $\overline{\nu}$ per emitted photon, respectively. The agreement between the experimental result and Nifenecker *et al.* in Fig. 6.15 is poor. Nifenecker *et al.* lies above the experiment data and all simulations with the discrepancy increasing with γ'. This poor agreement suggests that the positive multiplicity correlation binned with fragment properties observed by Nifenecker does not predict neutron-photon

competition on an event-by-event basis. Thus the strong positive correlation suggested by Nifenecker is excluded by our result. Figure 6.15(b) omits the Nifenecker result to show low $E[\nu'|\gamma']$ to separate other results.

The Glässel correlation, however, shows a slightly negative trend in $E[\nu'|\gamma']$, smaller than the trends of `CGMF`, `FREYA`, and our experimental result.

Using a linear fit to the $E[\nu'|\gamma']$ data and the correlation model outlined in Eqs. (6.3) and (6.4), the experimental result shows a weak negative correlation of -0.0016 $\pm$ 0.0096 $\overline{\nu}$ per emitted photon that is small relative to the uncertainty. This result indicates a weaker neutron-photon correlation than the Glässel result, also weaker than the `CGMF` and `FREYA` results. The Bleuel *et al.* data [74], based on measurements of the photon multiplicity distribution with two and four neutrons emitted from Mo/Ba fragment pairs, indicated little to no correlation. However, the Bleuel *et al.* experiment may have been insensitive to the weak correlation measured here. Additionally, it is not clear how selecting fragments with specific neutron multiplicities might bias the result of Ref. [74].

Calculated relative to experiment data, C/E, shown in Figs. 6.8,6.9,6.10, and 6.11, demonstrate some uncertainty in the detector response, both in calculations and in experiment. We expect the uncertainty in detector response to manifest as a discrepancy in the expected magnitude of the calculated $E[\nu'|\gamma']$ or $E[\gamma'|\nu']$ data, but we do not expect uncertainty to affect in the overall trend or correlation of the data. Therefore, the comparison of experiment and calculated trends in $E[\nu'|\gamma']$ or $E[\gamma'|\nu']$ are reliable. If, however, there were energy-multiplicity correlations that produced strong spectral shifts outside of the sensitive range of the detectors, then the trends in $E[\nu'|\gamma']$ and $E[\gamma'|\nu']$ could be unreliable. However, the detectors should be sensitive to most energy-multiplicity correlations; as stated before, the detectors are estimated to be sensitive to 77% of the ^{252}Cf(sf) neutron spectrum and to the full photon spectrum.

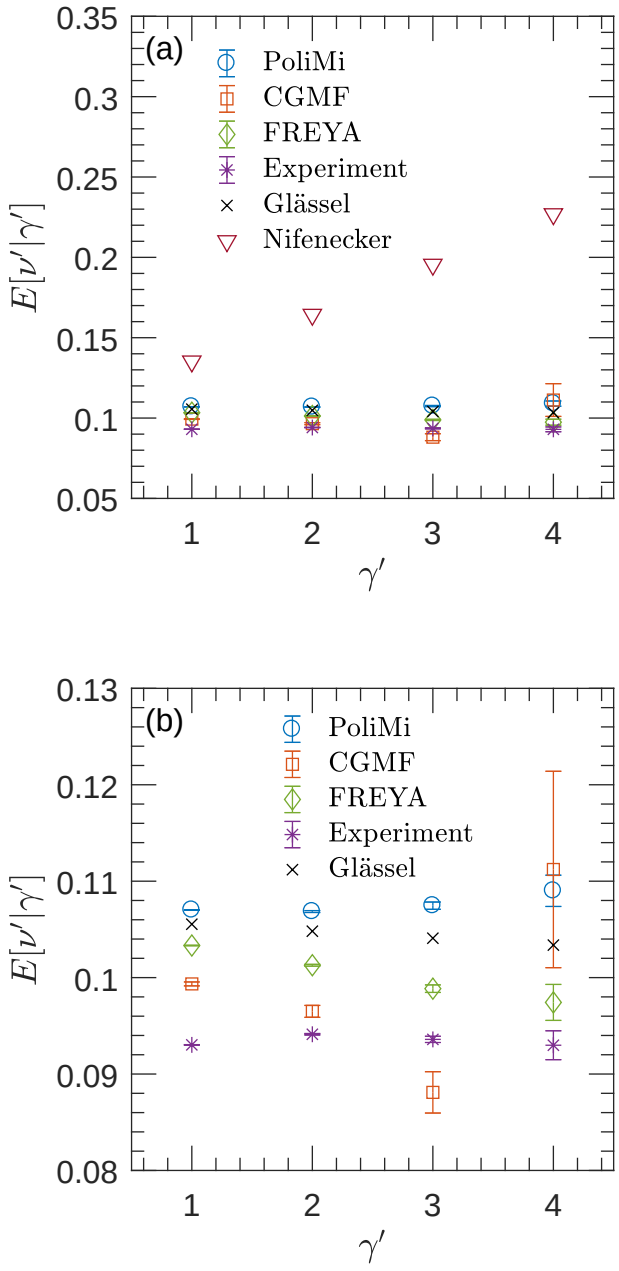

Figure 6.15: Expected number of detected neutrons given γ' photons detected in coincidence (a), $E[\nu'|\gamma']$, and zoomed in to separate the results at low $E[\nu'|\gamma']$ (b). The experimental data include 7.8×10^8 detected fission events. Error bars represent statistical uncertainty only.

6.5 Conclusions

A dedicated experiment to observe neutron-photon multiplicity correlations in ^{252}Cf(sf) was performed and compared to simulations using correlated emission fission models. Using an analytic correlation model, the experiment showed a weak negative neutron-photon multiplicity correlation on an event-by-event basis of -0.0016 ± 0.0096 $\overline{\nu}$ per emitted photon for ^{252}Cf(sf)that is small relative to the uncertainty. While the estimated correlation has large uncertainty, the result suggests possible weak competition between neutron and photon emission.

The simulated results for all employed models agree qualitatively with the pulse height and the time-of-flight distributions, but `PoliMi` results agree best. Comparison of the experiment and the `PoliMi` simulation results show that `MCNPX` − `PoliMi` with `CGMF` and `FREYA` generated events best explain the neutron-photon multiplicity correlation because of their inherent negative correlation. The correlation in the `CGMF` and `FREYA` models, however, is stronger than observed in the experiment.

Future work should include experiments that simultaneously measure fragment properties and emissions with high efficiency. Higher neutron and photon efficiency would allow for a more sensitive measurement of the multiplicity correlation. Event-by-event correlations measured with respect to TKE would help to understand how excitation and spin impact emission competition. Additionally, experiments should include measurements of event-by-event energy correlations.

Chapter 7

Measured and Simulated ^{240}Pu(sf) Prompt Neutron-Photon Competition Experiment at LANL

Previous work that I performed, shown in Chapter 6, found weak neutron-photon competition during fragment deexcitation in ^{252}Cf(sf). In the case of ^{240}Pu(sf), there are no published experimental data on neutron-photon correlations or competition. Here, I applied similar experimental methods from the ^{252}Cf(sf) work in Chapter 5 and 6 to a new experiment to measure ^{240}Pu(sf) neutrons and photons with a stilbene scintillator array at LANL. The goal of this work was observe neutron-photon multiplicity correlation in ^{240}Pu(sf) through experiments to measure event-by-event neutron and photon multiplicity and then to compare data to simulation results from correlated and uncorrelated fission models. By reading fission-model-generated events into `MCNPX − PoliMi` and using the same detector response, I was able to reliably compare simulation data from each fission model to experiment data.

In this work, I designed a stilbene-PMT based scintillator array, pictured in Figure 7.1, to measure neutron-photon multiplicity on a fission-by-fission basis. I also assembled a CAEN-based acquisition system and software package to collect waveform data. I took that array and acquisition system to LANL to measure emissions from a 0.695 g, 94% ^{240}Pu sample. I then wrote analysis scripts to process acquired data for pulse integral and correlated distributions.

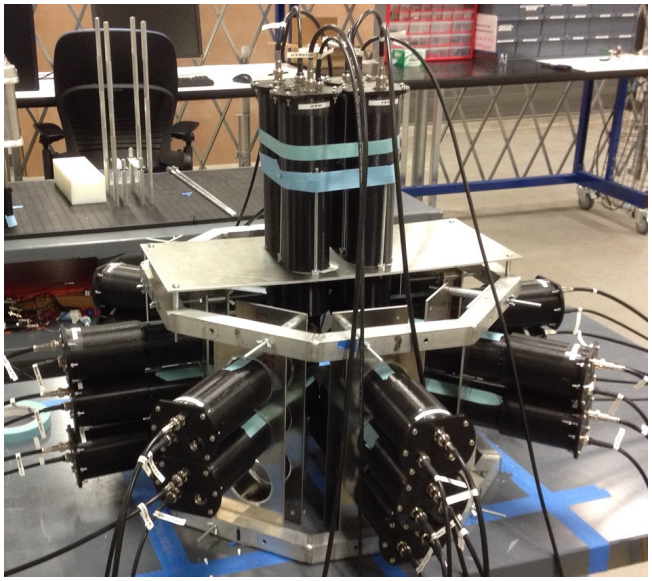

Figure 7.1: A photograph of the 24 stilbene detector array. Stilbene scintillators are coupled to ET Enterprises 9214b PMTs with readout bases and are then encased in 3D printed plastic cases. Two rings of eight detectors are arranged around a central axis; four detectors are pointed downward on top of a cavity for the source material; and four detectors are underneath the source cavity.

7.1 Introduction

Similar to published work on ^{252}Cf(sf), both neutron and photon emissions from ^{240}Pu(sf) are well studied independently. Multiplicity and energy distributions are well known. However, there are no prior experiments to measure neutrons and photons simultaneously on an event-by-event basis. Many measurements of bulk plutonium material have been performed with organic scintillators, but none focused exclusively on ^{240}Pu(sf) and neutron-photon correlations.

^{240}Pu(sf) is particularly challenging to measure because ^{240}Pu has a small spontaneous fission branching ratio (5×10^{-6}%), is difficult to find enriched, and is often contaminated with (α, n) emissions. The plutonium sample used here, described in Ref. [87], is almost ideal for neutron-photon correlation measurements because it is large enough at 0.695 g to be measured in a reasonable time-frame, but is not too large as to have significant contribution from induced fissions or as to self-shield low energy photons. Additionally, the sample is enriched to 94 Wt% ^{240}Pu and has a small (α, n) contribution with α = 0.142, where α is defined as the (α, n) rate divided by the spontaneous fission neutron

rate.

A high α-decay photon rate is of concern when measuring plutonium samples with organic scintillators. Plutonium isotopes in the sample primarily α decay or produce daughters that also α decay. The α particle, however, will not escape the sample. Many characteristic photons are emitted from the α decays in the sample, however one is of particular concern, a 59.5 keV photon from ^{241}Am. Most α decays produce low energy photons that are self-shielded, but the 59.5 keV photon from ^{241}Am is highly probable and can escape the sample.

7.2 Experimental Method and Analysis

An array of 24 stilbene scintillators, each coupled to a PMT, were arranged around a 0.695 g plutonium sample enriched in ^{240}Pu to 94 Wt%.

7.2.1 Plutonium source description

Bulk plutonium sample emissions are complex relative to those from ^{252}Cf samples. For freshly fabricated ^{252}Cf samples, all emissions are typically assumed to be from ^{252}Cf(sf), whereas emissions from bulk plutonium samples include spontaneous fission from all isotopes, induced fission on all isotopes, α decay, and (α, n)in widely varying fractions.

The plutonium sample (LANL identification FCZ-158 [87]) contains plutonium isotopes and a small amount of ^{241}Am, described in Table 7.1. The sample mass was decayed to show the masses at the time of the experiment. A significant increase in ^{241}Am occurs because ^{241}Pu β^- decays into ^{241}Am with a 14.3 year half-life. The other plutonium isotopes have relatively long half-lives and have changed insignificantly in weight fraction.

In this experiment analysis, results are focused on coincident detections therefore only sources of coincident emissions were considered. Most of the sample material is ^{240}Pu, but the emission rates must be considered. Ideally for this experiment, the sample would only produce ^{240}Pu(sf) neutrons and photons, however it is also a source of (α, n) and α decay photons. Table 7.3 shows the primary correlated emissions from the plutonium sample,

Table 7.1: The FCZ-158 0.695 g plutonium source composition on the assay date and at the time of the experiment. The composition values at the date of the experiment were obtained through decaying the August 1991 values.

Isotope	Aug. 1991 (Wt%)	Apr. 2018 (Wt%)
^{238}Pu	0.016	0.013
^{239}Pu	0.955	0.954
^{240}Pu	93.77	93.51
^{241}Pu	0.699	0.193
^{242}Pu	4.56	4.56
^{241}Am	0.001	0.4862

Table 7.2: The α-decay rates from the FCZ-158 plutonium sample at the time of the experiment. The decay rates were obtained through decaying the plutonium sample composition from the August 1991 assay.

Isotope	α/s
^{238}Pu	5.7×10^{7}
^{239}Pu	232
^{240}Pu	1.1×10^{4}
^{241}Am	3.4×10^{7}

where fortunately, most of the emissions were from ^{240}Pu(sf). Using a `PoliMi` model of the source material, an estimated 3% of emitted neutrons were from induced fissions. Further simulations include fissions and (α, n), but analysis does consider induced fissions. Simulations include ^{239}Pu(sf). The full `MCNPX` − `PoliMi` model input file for this experiment can be found in Appendix 4.

Characteristic α-decay gamma rays are a significant source of sample emissions, but most are of low energy relative to detector thresholds. Table 7.2 shows the α-decay rates at the time of the experiment, and one α decay can produce multiple coincident gamma rays. α-decay gamma ray is unlikely to deposit enough energy to trigger waveform acquisition in the detector. These gamma rays are still problematic because they can contribute to pile up and noise in fission signals.

A radiograph of the sample and three layers of stainless steel casing are shown in Figure 7.2, where the outermost casing is 3.11 cm in height and 5.66 cm in diameter. The second layer of casing moves within the outer case, therefore it is difficult to accurately know the sample location.

Table 7.3: Correlated emission rates from the FCZ-158 plutonium sample at the time of the experiment. The emission rates were obtained through decaying the plutonium sample composition from the August 1991 assay.

Reaction	n/s	γ/s	*reactions/s*
^{240}Pu(sf)	600	1780	278
^{239}Pu(sf)	1.5×10^{-4}	4.6×10^{-4}	6.6×10^{-5}
(α, n)	85	57	85

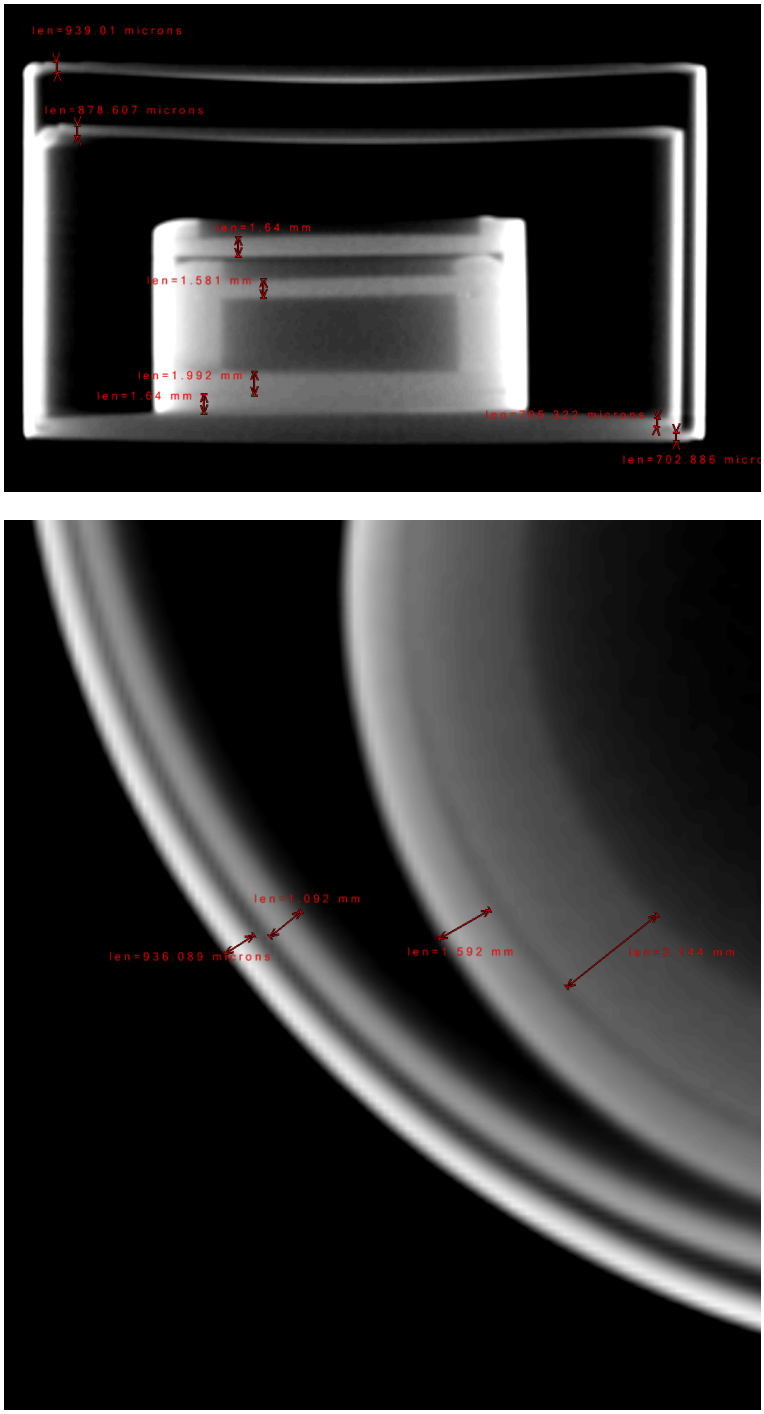

Figure 7.2: Radiograph image of the plutonium metal sample and casing with dimensions of the casing. The inner cannisters float freely within the outermost cannister.

7.2.2 Detector array and acquisition

An array of stilbene scintillators was designed, shown in Fig. 7.1, to efficiently measure high-order neutron and photon multiplets. The stilbene cells measure 5.08 cm diameter by 5.08 cm thick, pictured in the bottom left of Figure 2.5. The cells were wrapped in polytetrafluoroethylene and then cased in aluminum. Each cell was coupled to a 5.08 cm diameter ET Enterprises 9214b PMT, pictured with a readout base in Figure 2.5.

Two rings of eight detectors were arranged 7.25 cm radius from a central axis; four detectors were pointed downward on top of a cavity for the source material, 26.7 cm from the table top; and four detectors were underneath the source cavity. Each detector was held in place with 1/8" aluminum plates. Two plates held the side detectors and one plate held the top four detectors. The aluminum plates were bolted to two hexagons of 1" square box tubing, one at the top of the plate and one at the bottom.

Two CAEN V1730 16-channel waveform digitizers and four CAEN V6533 VME 6-channel high voltage supplies in a CAEN VME8008B 8-slot crate and a desktop acquisition system were used to collect waveform data. The high voltage supplies and digitizers were controlled via USB with the desktop, but acquired data was transmitted via two optical links. The digitizers had DPP-PSD firmware which allows for onboard PSD, zero suppression, and constant fraction discrimination timing. The DNNG acquisition code Data Acquisition For CAEN Apparatuses (DAFCA) was used to communicate with the digitizers and save data to the desktop.

The digitized waveforms for channels 2, 4, 6, and 8 on both boards showed large baseline drift between acquisition folders and were not included in the final analysis. Waveforms from these channels could not be used for PSD because the baseline drifted outside of the dynamic range.

The FCZ-158 sample was measured for 88.5 hrs over five days, and a ^{137}Cs calibration source was measured each morning. The ^{137}Cs source was used to gain-match the Compton edge from each detectors pulse integral distribution.

7.2.3 Modeling

Similar to previous experiments, the MCNPX − PoliMi code was used to model the laboratory geometry and particle transport in great detail, shown in Figure 7.3. PoliMi models both the detector system and the surrounding laboratory. MPPost was used to model the detector response.

Fission events from FREYA and PoliMi (IPOL(1)=3) were used in PoliMi particle transport to produce the detector collision event file; CGMF fission events were not used. CGMF ^{240}Pu(sf) histories were not available at the time of writing, but this and other isotopes are currently being added to the code. With $\alpha = 0.142$, the PoliMifission and (α, n)sources were mixed such that there are 0.142 (α, n)neutrons per fission neutron. The (α, n)reactions were modeled, as an approximation, as PoliMibuilt-in sources with 63% $^{238}PuO_2$ (IPOL(1)=-38) and 37% $^{241}AmO_2$ (IPOL(1)=-41). When the (α, n) PoliMi sources are negative, the full α-decay gamma-ray chain is ignored and one (α, n) occurs per nps. An 1 Wt% oxygen mass contamination was estimated in the plutonium sample.

The aluminum table with a cadmium sheet and a concrete floor were modeled. The detectors were modeled to almost full detail, but the photomultiplier tube electronics were partially homogenized. The plutonium FCZ-158 sample was modeled according to specifications in Tables 7.1 and 7.3 (ignoring ^{239}Pu(sf)) and sizes from the radiograph in Figure 7.2.

In simulation, waveform classification is ideal. A 50 keVee pulse integral threshold was used, and is a conservative threshold for stilbene. A conservative threshold was used to account for the high photon-to-neutron ratio and to make a reliable comparison to simulation results.

To properly model the detector system, we need to quantify the system energy resolution and to understand the Compton edge location. The true Compton edge location allows us to convert pulse integrals in Vns to MeVee.

A ^{137}Cs source was measured with a single stilbene scintillator to obtain a pulse integral histogram, which shows a single Compton continuum from the 662 keV photon, shown in Fig. 7.4. The experiment was modeled in MCNPX − PoliMi, including the

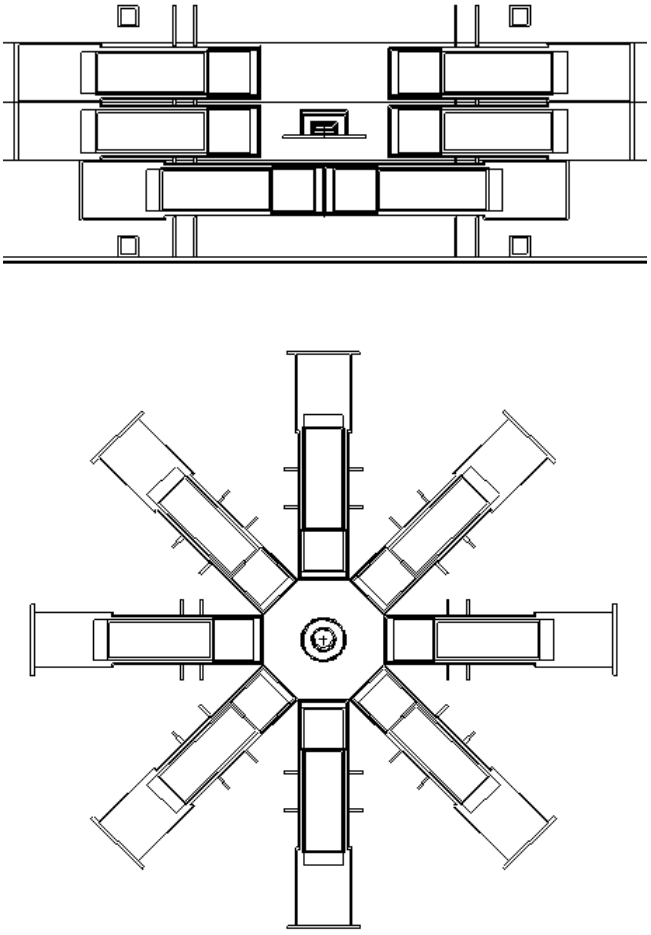

Figure 7.3: The MCNPX − PoliMi model of the 24 stilbene detector array with aluminum 1/8" plates and 1" square box tubing to hold the detectors in place. The source was placed in the detector cavity (15.5 cm in diameter) and in plane with the center ring of detectors. These cross-sections do not show the top four detectors pictured in Figure 7.1.

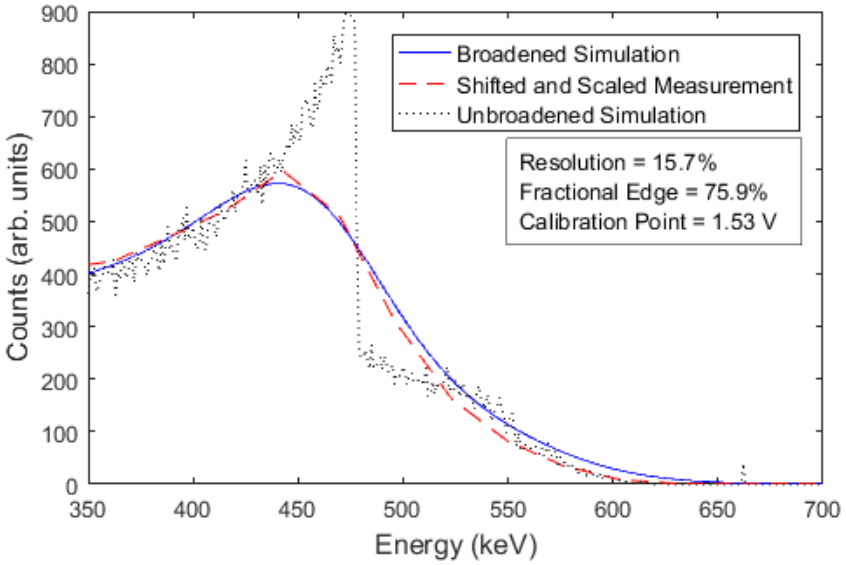

Figure 7.4: Experimental and an unbroadened and broadened ^{137}Cs simulation pulse integral histogram result showing the Compton edge at 478 keV and portion of the continuum. The counts above 478 keV are multiple scatter events. The broadening indicates 15.7% resolution at FWHM and a calibration of 1.53 Vns at 478 keVee.

single detector and ^{137}Cs 662 keV source, to tally photon energy deposited in the detector cell. The simulated energy deposited histogram shows an unbroadened Compton continuum, however the observed result is broadened due to photoelectron statistics, variable scintillation efficiency, electronic noise from readout, and drift in time of the response [20]. The unbroadened Compton continuum is then Gaussian iteratively broadened to match the experiment histogram. The final broadened result indicates 16% resolution at 478 keVee and is shown in Fig. 7.4. For this detection system, we found $\alpha = 0.0075$, $\beta = 0.026$, and $\gamma = 26.96$ in MeVee for Eqn. 3.1. We also found a calibration constant of 3.2 Vns/MeVee. This calibration and the dynamic range of the digitizer gives an upper threshold of 2.52 MeVee.

A ^{252}Cf(sf) source was measured with a single stilbene scintillator to obtain a pulse integral histogram for neutrons, after PSD. The experiment was modeled in `MCNPX − PoliMi`, including the single detector and ^{252}Cf(sf) source, to tally neutron energy deposited in the detector cell. The Birks model [39] was used to estimate light output from proton recoils in the stilbene with coefficients $S = 1.63$ and $kB = 11.83$, shown in Fig. 7.5. Electron recoil light output was treated as linear. The simulation and experimental pulse integral

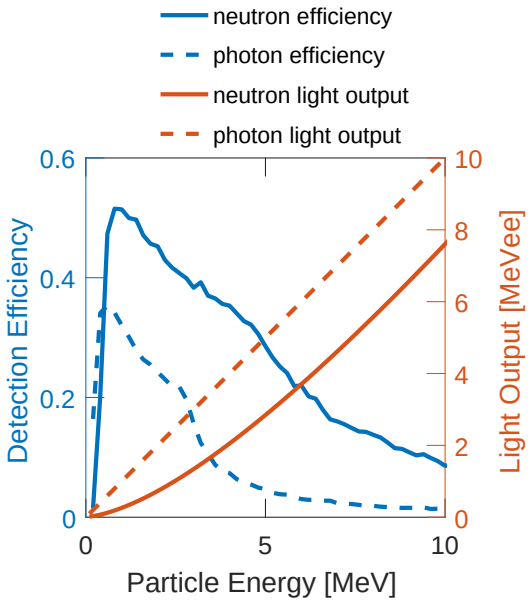

Figure 7.5: Calculated neutron and photon detection efficiency and light output distributions used in the detector response code for neutron scattering on a proton and for photon scattering on an electron in a 5.08⌀x5.08 cm stilbene detector. Proton recoil light output uses coefficients $S = 1.63$ and $kB = 11.83$ from the Birks model [39].

histograms are compared in Fig. 7.6. Experiment and calculation agreement is good with most points differing by less than 10%, but there is larger scatter above 1.5 MeVee due to limited statistics. The good agreement in pulse integral distributions indicates a valid light output response in `MPPost`.

Figure 7.5 also shows the `MCNPX` − `PoliMi`and `MPPost`calculated intrinsic efficiency as a function of incident particle energy for neutrons and photons. The neutron efficiency peaks at approximately 50% near 1 MeV and decreases toward higher energies. The photon efficiency peaks at approximately 35% just below 1 MeV and decreases to a sharp drop just above 2.5 MeV. The sharp drop in photon efficiency above 2.5 MeV occurs because waveforms were clipped by the upper range of the 2 V digitizer.

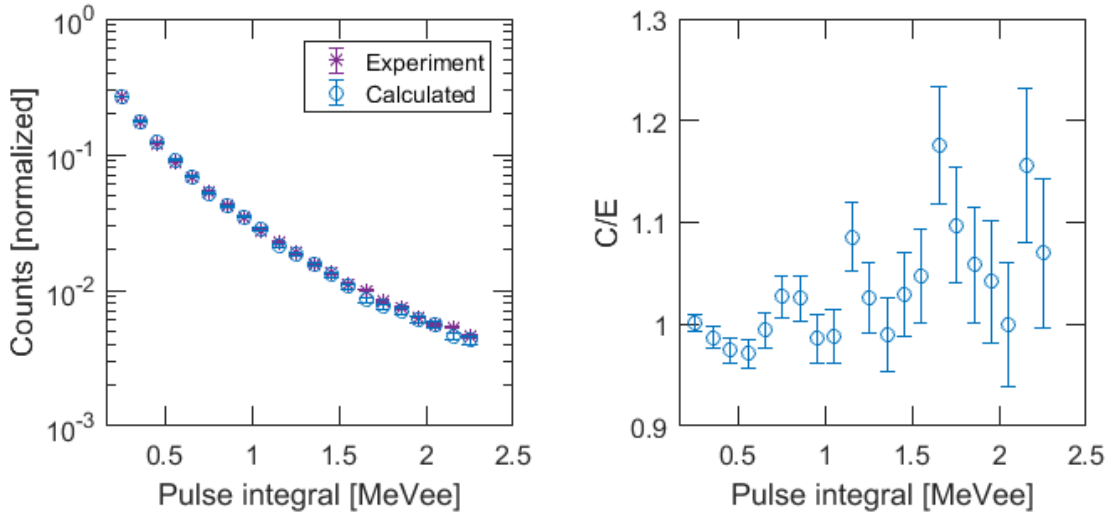

Figure 7.6: (left) Pulse integral distribution results and (right) calculated over experiment from a single detector experiment and simulation of ^{252}Cf(sf) neutrons. The uncertainties are smaller than the points in the integral distribution.

7.3 Results

Processed ^{240}Pu(sf) experiment and simulation results are shown in Figs. 7.7- **??**. Pulse integral distributions are shown to demonstrate a high fidelity model. The mean number of detected neutrons given a detected photon multiplicity are shown to evaluate multiplicity correlation in the experiment and fission models, and to evaluate the magnitude of competition in fission fragment deexcitation.

A histogram of the tail integral as a function of the total integral was used to apply a PSD line, which separates neutron and photon events. The total integral was over 200 ns of the waveform, and the tail was over 152 ns of the waveform. An algorithm based on that described in Polack et al. [22] was used to find the optimal discrimination line. Neutron events lie above the discrimination line because more scintillation light occurs in the tail relative to the total than for photons, due to a greater quantity of longer-lived triplet states produced by neutron events. The photon-to-neutron ratio is 59 for this plutonium sample, making for especially challenging PSD at low pulse integrals, where overlap of the two bands is significant.

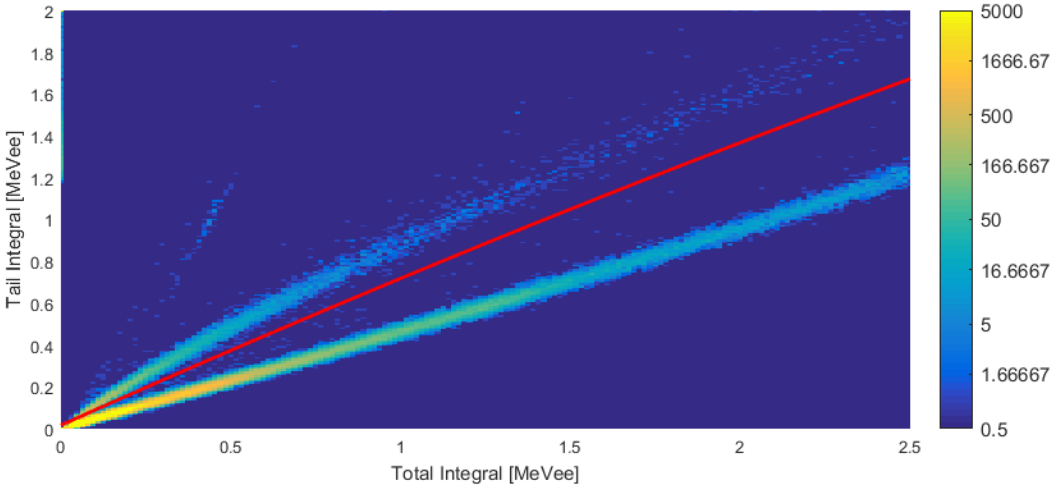

Figure 7.7: Experimental ^{240}Pu(sf) PSD histogram from 1.7 hrs of data on a single detector. Neutrons lie above the red line and photons lie below. Events at a total integral of 0.5 MeVee and tail of 1 MeVee are pile-up pulses.

7.3.1 Correlated fission model comparisons

In Figure 7.8(a), the simulated neutron pulse integral distributions agree well with the experiment data. Good agreement demonstrates that the neutron model is adequate for singles events. Both simulation results diverge from the experiment result above 0.75 MeVee, indicating that both simulated spectra are too hard. The overestimate at high pulse integrals could be partially due to the modeled (α, n) spectrum, which is harder than the ^{240}Pu(sf) spectrum. The (α, n) spectrum of this sample is not well characterized.

In Figure 7.8(b), the simulated photon pulse integral distributions underestimate the experiment data over the full range. The simulation result only includes fission photons and photons in coincidence with (α, n), whereas the experiment data also includes unmodeled α-decay gamma rays and other fission product decays. Significant Compton edges can be seen near 0.5 MeVee and 1.3 MeVee. The 0.5 MeV Compton edge is from various α-decay gamma rays including those from ^{240}Pu at 642 keV and from ^{241}Am at 653 and 662 keV [88]. The Compton edge at 1.3 MeVee is likely from the $\beta+$ decay of ^{19}Ne producing characteristic gamma rays of 1.357, 1.444, and 1.554 MeV [89]. Because this disagreement is largely due to single, uncorrelated photon events, it does not invalidate photon coincidence data from these simulations.

Figure 7.9 shows the photon pulse integral distribution when conditioned on another

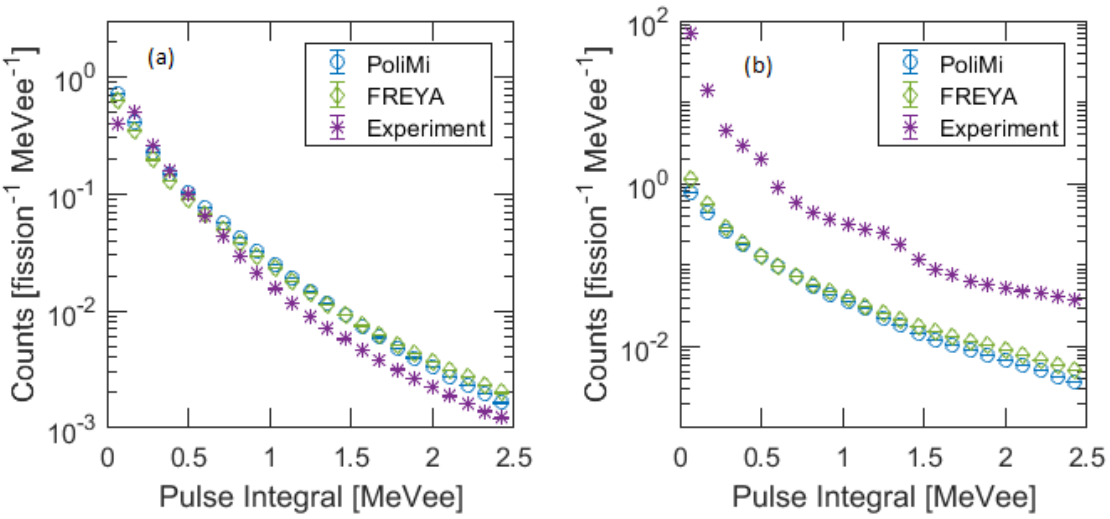

Figure 7.8: (a) Neutron and (b) photon experiment and simulation ^{240}Pu(sf) pulse integral distributions summed over all detectors and on a per fission basis. Pulse integrals for all coincidences are shown. The uncertainties are smaller than the points. For neutrons 1.6×10^7 and for photons 9.2×10^8 detections are shown for the experimental results.

detection. The coincidence condition significantly reduces the effect of α-decay gamma rays and the agreement with simulation distributions is good. Most of the coincidence photons are from fission rather than α decays, but small Compton edges are still visible near 0.5 and 1.3 MeV.

A two-dimensional histogram of neutron and photon coincidences from the plutonium sample and from background were made using a 300 ns coincidence window and signals from all included detectors. Background coincidences were removed from the plutonium sample coincidences. Figure 7.10 shows the detected neutron coincidence ν' count rates. The simulated results generally follow the experiment data, but diverge toward higher coincidences. The `FREYA` count rates are slightly less than the `PoliMi` data, likely due to differences in the neutron multiplicity distributions. The simulated neutron coincidences overpredict for the whole range of observed coincidences. The simulations overpredict because in the neutron pulse integral distributions in Fig. 7.8(a) both fission models also overpredict the experiment count rates.

Figure 7.11 shows the detected photon coincidence γ' count rates. The simulation data poorly model the experiment data at low coincidences, but agreement improves toward higher coincidences. Many α-decay gamma rays were present in the experiment

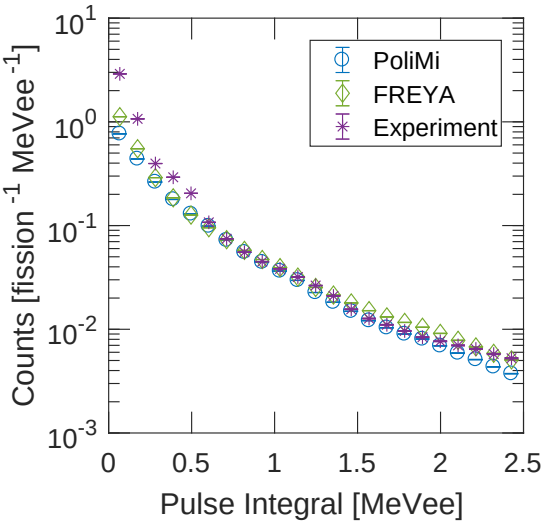

Figure 7.9: Photons in coincidence with another detection from experiment and simulation ^{240}Pu(sf) pulse integral distributions summed over all detectors and on a per fission basis. The uncertainties are smaller than the points.

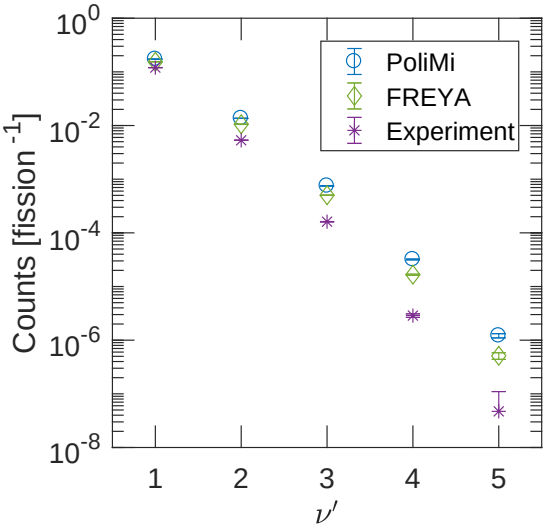

Figure 7.10: Background subtracted experiment and simulated ^{240}Pu(sf) neutron coincidence distributions. The uncertainties are smaller than most points and represent statistical uncertainty only.

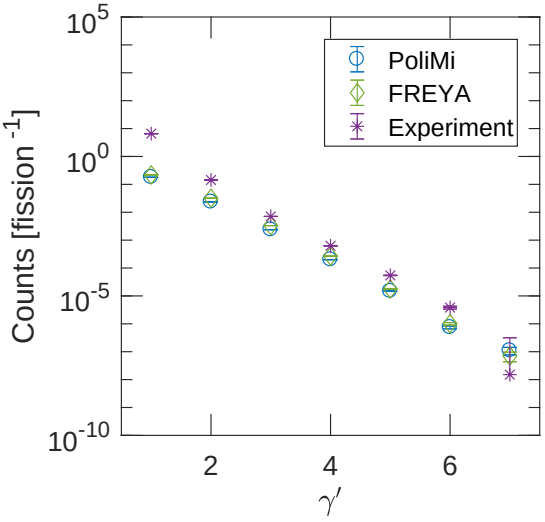

Figure 7.11: Background subtracted experiment and simulated ^{240}Pu(sf) photon coincidence distributions. The uncertainties are smaller than most points and error bars represent statistical uncertainty only.

data that were not modeled. These unmodeled gamma rays contributed most to low coincidences and would not occur with a correlated neutron. The fission model data are in good agreement.

7.3.2 Correlations between neutrons and photons

The mean number of photons detected with respect to the number of neutrons detected $E[\gamma'|\nu']$ is sensitive to neutron-photon multiplicity correlation. Figure 7.12(a) shows $E[\gamma'|\nu']$ increase for the experiment and `PoliMi` data, but decrease for the `FREYA` data. The `PoliMi` data increases at a greater rate than the experiment data. Neither of the simulation results agree well in magnitude, as we would expect, because the experiment includes unmodeled α-decay gamma rays. Figure 7.12(b) shows a positive slope in the `PoliMi` data, suggesting that the `PoliMi` fission model produces too many photons as neutron multiplicity increases. The slight positive trend in the `PoliMi` data is caused by induced fissions in the sample which increase the effective observed neutron multiplicity. The effect from induced fissions is also captured in the `FREYA` calculations, but competes with `FREYA`s negative neutron-photon multiplicity. The negative slope in the `FREYA` data suggests that the model produces too few photons as neutron multiplicity increases. In the `PoliMi` fission model, neutrons and photons are sampled independently, whereas in the

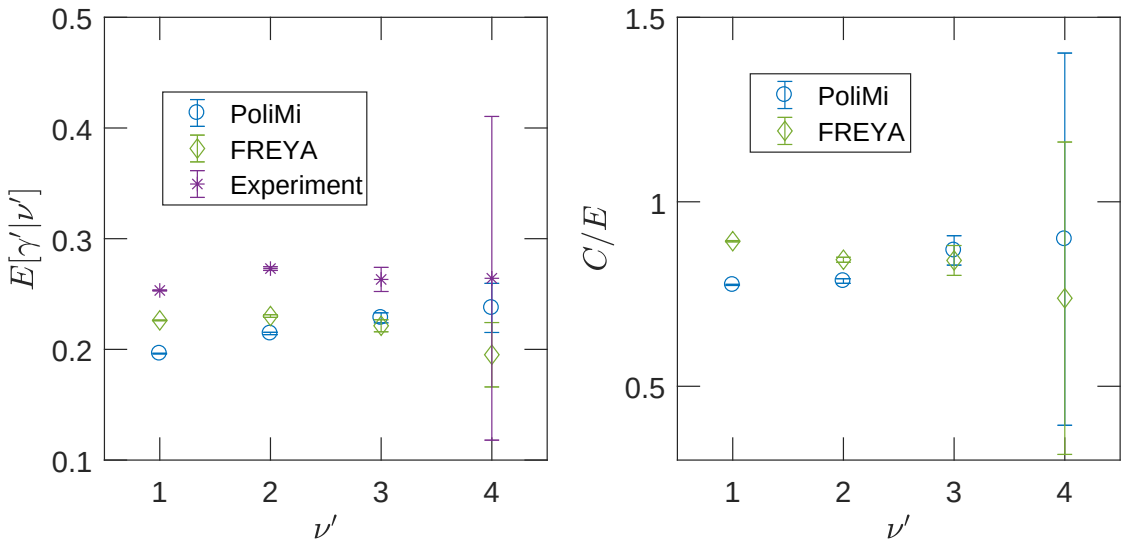

Figure 7.12: (a) Expected number of detected photons γ' given ν' neutrons detected in coincidence $E[\gamma'|\nu']$ and (b) calculation over experiment. Error bars represent statistical uncertainty only.

`FREYA` model neutrons and photons are negatively correlated. The data in Fig. 7.12(b) suggest that the true correlation, weak anti-correlation, lies between the `PoliMi` and `FREYA` model correlations. Weak anti-correlation in prompt neutron-photon multiplicity is consistent with previous findings of ^{252}Cf(sf) in Ref. [63].

Systematic uncertainties that could contribute to observed trends in $E[\gamma'|\nu']$ include strong spectral shifts outside of the sensitive range of the detectors due to energy-multiplicity correlations. The detectors are, however sensitive to most of the neutron spectrum and to the full photon spectrum. While the simulations include fission and (α, n) events, α-decay gamma rays are unmodeled. The effects of α-decay gamma rays are apparent in the data, where the pulse integral distributions are underpredicted and the γ' multiplicity results are also underpredicted. These α-decay gamma rays contribute equally to all ν' because they are uncorrelated with fission events and do not affect the conclusion of anti-correlation in neutron-photon multiplicity.

7.4 Conclusions

A dedicated experiment was performed to show, for the first time, anti-correlation in prompt ^{240}Pu(sf) neutron-photon multiplicity. Results from `MCNPX` – `PoliMi` simulations

with PoliMi and FREYA fission event generators were compared to the experiment data. The observed anti-correlation is weak and is bounded by the uncorrelated PoliMi model and the more strongly correlated FREYA model.

The simulated neutron pulse integral and multiplicity distributions agree well for both fission event generators. The photon pulse integral and multiplicity distributions do not agree well due to unmodeled gamma rays in the experimental data. The FREYA-generated events best explain the observed data because of their inherent negative correlation. The correlation in the FREYA result is stronger than observed in experiment, similar to previous findings for ^{252}Cf(sf) in Ref. [63].

Future work should include experiments with a plutonium sample in a fission ionization chamber or with some other method to trigger only on fission events. A fission triggered data set would reduce the effects of (α, n) and of α-decay gamma ray events. Additionally, future work should include simultaneous measurements of fragment properties and of their emissions.

Chapter 8

Summary, Conclusions, and Future Work

8.1 Summary

In Chapter 1, I discuss the motivation for this work in the context of nuclear safeguards and nonproliferation and in the context fission physics. This discussion highlights how detector technology and sensitivity has outpaced our ability to understand and reliably model fission emissions. I also discuss the specific contributions of this work.

In Chapter 2, I discuss the radiation detectors used in this work. I focus on key photon and neutron reactions in organic and inorganic scintillators. I also discuss the process for producing, converting, and reading out of scintillation light from these detectors.

In Chapter 3, I discuss how `MCNPX – PoliMi` is used to model particle transport in fission experiments to high fidelity. I also discuss how `MCNPX – PoliMi` outputs are used in `MPPost` to emulate detector response for scintillators. I describe how fission event generator outputs were coupled to `MCNPX – PoliMi`.

In Chapter 4 I show, for the first time, prompt neutron anisotropy from ^{240}Pu was observed and quantified in laboratory experiments. The ^{240}Pu(sf) prompt neutron angular distribution experiment and simulation showed that `MCNPX – PoliMi` simulations of the laboratory and detector system could be used to reliably estimate neutron cross talk and to ultimately remove the cross-talk contribution. Approximately 20% of small angle coincidences were from cross talk. ^{252}Cf spontaneous fission neutrons above 0.65 MeV (proton recoil) were observed to be significantly more anisotropic than ^{240}Pu spon-

taneous fission neutrons above that same energy. These experimental results were used to improve the FREYA fission event generator [48]. Results from this work helped to verify ^{240}Pu(sf) neutron-neutron angular distributions and thereby a fragment excitation energy sharing parameter in FREYA. With an improved excitation energy sharing parameter, FREYA can now be reliably used to predict experimental outcomes sensitive to the ^{240}Pu(sf) neutron angular distribution.

In Chapter 5, I show that the fission models PoliMi, CGMF, and FREYA generally captured key observed singles features from this experiment for ^{252}Cf(sf). Experiment data were compared to MCNPX − PoliMi simulations using correlated emission fission models. The results indicate that all models could improve neutron and photon energy and multiplicity distributions. PoliMi, however, agreed with experiment data the best for neutron and photon spectra, because PoliMi uses evaluated data for its models. No model result agreed perfectly well to experiment coincidence distributions. Neither experimental nor simulated neutron TOF energy data relative to neutron coincidences indicates a strong correlation in mean energy. A weak, positive trend in mean neutron energy relative to the number of photons in coincidence was observed. However, the trend could be biased because neutron energy is estimated by photon triggered TOF.

Chapter 6 describes a dedicated experiment to observe neutron-photon multiplicity correlations in ^{252}Cf(sf). Experimental data were compared to simulations using correlated emission fission models. The experimental data showed a weak negative neutron-photon multiplicity correlation on an event-by-event basis of -0.0016 ± 0.0096 $\overline{\nu}$ per emitted photon for ^{252}Cf(sf). This result suggests weak competition between neutron and photon emission. Results also suggest that the MCNPX − PoliMi with CGMF and FREYA generated events best explain the neutron-photon multiplicity correlation. CGMF and FREYA have inherent negative correlation, but the correlation in the models is stronger than observed in the experiment.

Chapter 7 describes another dedicated experiment to show, for the first time, anti-correlation in prompt ^{240}Pu(sf) neutron-photon multiplicity. Results from MCNPX − PoliMi simulations employing PoliMi and FREYA fission event generators were compared to the ex-

periment data. The observed anti-correlation was weak and was bounded by the uncorrelated `PoliMi` model and the more strongly correlated `FREYA` model. Again, `FREYA` generated events best explain the observed data because of their inherent negative correlation.

8.2 Conclusions

My fission experiments and simulations are useful and have already been used [90] to improve event-by-event fission models. Ongoing collaboration between DNNG and fission event generator developers will continue to refine fission models with these experiment data. Improved fission models are immensely useful to radiation detector system design and prediction, especially for novel nuclear safeguards and nonproliferation techniques [55, 58,91]. Work in this thesis ultimately contributes to global nuclear security and promoting the safe use of nuclear technology.

Efficient and cost-effective radiation detector system design relies heavily on accurate Monte Carlo particle transport codes, and these codes are only as accurate as the data that they use. Often in nuclear safeguards and nonproliferation detector systems are designed to be sensitive to fission emissions; consequently it is imperative that fission models used to inform design are accurate. ^{240}Pu(sf) is especially important in safeguards and nonproliferation because ^{240}Pu is present in all plutonium samples and is usually the driving source of induced fission chains. ^{252}Cf(sf) is a practical surrogate for fissile isotope emissions in the laboratory, therefore an accurate model is necessary for this isotope.

8.3 Future work

Future work should include experiments that simultaneously measure fragment properties and emissions with high efficiency. Higher neutron and photon efficiency would allow for a more sensitive measurement of the correlations. Event-by-event correlations measured with respect to fragment TKE would help to understand how excitation and spin impact emission competition. The `CGMF` and `FREYA` models start with fragment initial conditions before deexciting through emissions. Therefore, it would be useful to measure both the

starting condition (fragment properties) and the ending condition (neutron and photon emissions).

Appendix 1. Neutron Angular Distribution in ^{240}Pu(sf) from the Joint Research Centre Experiment in Ispra, Italy

The full `MCNPX – PoliMi` model is included.

```
c DNNG FNMC: PM2 with 1 cm Pb
c ~~~~~~~~~~~~~~~~~~~~~~~~~~~~~~~~~~~~
c
c  Cells
c ~~~~~~~~~~~~~~~~~~~~~~~~~~~~~~~~~~~~
c
c   EJ-309 Detectors
c ~~~~~~~~~~~~~~~~~~~~~~~~~~~~~~~~~~~~
c 1
  100 1 -0.935 -12 11 imp:n,p=1          $EJ-309 Liquid
  101 9 -2.51 -10 imp:n,p=1              $Optical Coupling
  102 9 -2.51 -11 imp:n,p=1              $Optical Window
  103 5 -2.6989  -13 12 imp:n,p=1        $Detector casing
  104 5 -2.6989  -14 15 imp:n,p=1        $Large Ring
  105 5 -2.6989  -16 17 imp:n,p=1        $Small Ring
c 2
  106 LIKE 100 BUT TRCL=1
  107 LIKE 101 BUT TRCL=1
  108 LIKE 102 BUT TRCL=1
  109 LIKE 103 BUT TRCL=1
  110 LIKE 104 BUT TRCL=1
  111 LIKE 105 BUT TRCL=1
c 3
  112 LIKE 100 BUT TRCL=2
  113 LIKE 101 BUT TRCL=2
  114 LIKE 102 BUT TRCL=2
  115 LIKE 103 BUT TRCL=2
  116 LIKE 104 BUT TRCL=2
  117 LIKE 105 BUT TRCL=2
c 4
  118 LIKE 100 BUT TRCL=3
  119 LIKE 101 BUT TRCL=3
  120 LIKE 102 BUT TRCL=3
```

```
  121 LIKE 103 BUT TRCL=3
  122 LIKE 104 BUT TRCL=3
  123 LIKE 105 BUT TRCL=3
c 5
  124 LIKE 100 BUT TRCL=4
  125 LIKE 101 BUT TRCL=4
  126 LIKE 102 BUT TRCL=4
  127 LIKE 103 BUT TRCL=4
  128 LIKE 104 BUT TRCL=4
  129 LIKE 105 BUT TRCL=4
c 6
  130 LIKE 100 BUT TRCL=5
  131 LIKE 101 BUT TRCL=5
  132 LIKE 102 BUT TRCL=5
  133 LIKE 103 BUT TRCL=5
  134 LIKE 104 BUT TRCL=5
  135 LIKE 105 BUT TRCL=5
c 7
  136 LIKE 100 BUT TRCL=6
  137 LIKE 101 BUT TRCL=6
  138 LIKE 102 BUT TRCL=6
  139 LIKE 103 BUT TRCL=6
  140 LIKE 104 BUT TRCL=6
  141 LIKE 105 BUT TRCL=6
c 8
  142 LIKE 100 BUT TRCL=7
  143 LIKE 101 BUT TRCL=7
  144 LIKE 102 BUT TRCL=7
  145 LIKE 103 BUT TRCL=7
  146 LIKE 104 BUT TRCL=7
  147 LIKE 105 BUT TRCL=7
c 9
  148 1 -0.935 -22 21 imp:n,p=1          $EJ-309 Liquid
  149 9 -2.51 -20 imp:n,p=1              $Optical Coupling
  150 9 -2.51 -21 imp:n,p=1              $Optical Window
  151 5 -2.6989  -23 22 imp:n,p=1        $Detector casing
  152 5 -2.6989  -24 25 imp:n,p=1        $Large Ring
  153 5 -2.6989  -26 27 imp:n,p=1        $Small Ring
c 10
  154 LIKE 148 BUT TRCL=1
  155 LIKE 149 BUT TRCL=1
  156 LIKE 150 BUT TRCL=1
  157 LIKE 151 BUT TRCL=1
  158 LIKE 152 BUT TRCL=1
  159 LIKE 153 BUT TRCL=1
c 11
  160 LIKE 148 BUT TRCL=2
  161 LIKE 149 BUT TRCL=2
```

```
  162 LIKE 150 BUT TRCL=2
  163 LIKE 151 BUT TRCL=2
  164 LIKE 152 BUT TRCL=2
  165 LIKE 153 BUT TRCL=2
c 12
  166 LIKE 148 BUT TRCL=3
  167 LIKE 149 BUT TRCL=3
  168 LIKE 150 BUT TRCL=3
  169 LIKE 151 BUT TRCL=3
  170 LIKE 152 BUT TRCL=3
  171 LIKE 153 BUT TRCL=3
c 13
  172 LIKE 148 BUT TRCL=4
  173 LIKE 149 BUT TRCL=4
  174 LIKE 150 BUT TRCL=4
  175 LIKE 151 BUT TRCL=4
  176 LIKE 152 BUT TRCL=4
  177 LIKE 153 BUT TRCL=4
c 14
  178 LIKE 148 BUT TRCL=5
  179 LIKE 149 BUT TRCL=5
  180 LIKE 150 BUT TRCL=5
  181 LIKE 151 BUT TRCL=5
  182 LIKE 152 BUT TRCL=5
  183 LIKE 153 BUT TRCL=5
c 15
  184 LIKE 148 BUT TRCL=6
  185 LIKE 149 BUT TRCL=6
  186 LIKE 150 BUT TRCL=6
  187 LIKE 151 BUT TRCL=6
  188 LIKE 152 BUT TRCL=6
  189 LIKE 153 BUT TRCL=6
c 16
  190 LIKE 148 BUT TRCL=7
  191 LIKE 149 BUT TRCL=7
  192 LIKE 150 BUT TRCL=7
  193 LIKE 151 BUT TRCL=7
  194 LIKE 152 BUT TRCL=7
  195 LIKE 153 BUT TRCL=7
c ~~~~~~~~~~~~~~~~~~~~~~~~~~~~~~~~~~~
c
c   Table
c ~~~~~~~~~~~~~~~~~~~~~~~~~~~~~~~~~~~
  201    5   -2.7        -31            imp:n,p=1    $ Surface
  206    5   -2.7        -32            imp:n,p=1    $ Support
  207    5   -2.7        -33            imp:n,p=1    $ Support
  208    5   -2.7        -34            imp:n,p=1    $ Support
  209    5   -2.7        -35            imp:n,p=1    $ Support
  215    5   -2.7        -36            imp:n,p=1    $ Leg
```

```
  216    5   -2.7       -37              imp:n,p=1    $ Leg
  218    5   -2.7       -38              imp:n,p=1    $ Leg
  219    5   -2.7       -39              imp:n,p=1    $ Leg
  220    5   -2.7       -40              imp:n,p=1    $ Leg
  221    5   -2.7       -41              imp:n,p=1    $ Leg
c  ~~~~~~~~~~~~~~~~~~~~~~~~~~~~~~~~~~~~
c    Detector Structure
c  ~~~~~~~~~~~~~~~~~~~~~~~~~~~~~~~~~~~~
  300    5   -2.7       -90 13 23        imp:N,P=1    $front plate
  301    5   -2.7       -91 13 23        imp:N,P=1    $back plate
  302    LIKE 300 BUT TRCL=1    $front plate
  303    LIKE 301 BUT TRCL=1    $back plate
  304    LIKE 300 BUT TRCL=2    $front plate
  305    LIKE 301 BUT TRCL=2    $back plate
  306    LIKE 300 BUT TRCL=3    $front plate
  307    LIKE 301 BUT TRCL=3    $back plate
  308    LIKE 300 BUT TRCL=4    $front plate
  309    LIKE 301 BUT TRCL=4    $back plate
  310    LIKE 300 BUT TRCL=5    $front plate
  311    LIKE 301 BUT TRCL=5    $back plate
  312    LIKE 300 BUT TRCL=6    $front plate
  313    LIKE 301 BUT TRCL=6    $back plate
  314    LIKE 300 BUT TRCL=7    $front plate
  315    LIKE 301 BUT TRCL=7    $back plate
  316    5   -2.7  -106:-108:-110:-112:
                   -114:-116:-118:-120 imp:N,P=1  $bottom bar
  317    5   -2.7  -107:-109:-111:-113:
                   -115:-117:-119:-121 imp:N,P=1  $top bar
c  ~~~~~~~~~~~~~~~~~~~~~~~~~~~~~~~~~~~~
c    Lead Shielding
c  ~~~~~~~~~~~~~~~~~~~~~~~~~~~~~~~~~~~~
  501    3 -11.34       -51 52 -53 54 imp:N,P=1    $lead shield
c  ~~~~~~~~~~~~~~~~~~~~~~~~~~~~~~~~~~~~
c  Ground
c  ~~~~~~~~~~~~~~~~~~~~~~~~~~~~~~~~~~~~
  601    6   -2.3       -500 -61         imp:N,P=1    $concrete floor
c  ~~~~~~~~~~~~~~~~~~~~~~~~~~~~~~~~~~~~
c    PM Source
c  ~~~~~~~~~~~~~~~~~~~~~~~~~~~~~~~~~~~~
  701    7   -19.7      -71              imp:n,p=1  $Pu Metal
  702    0              -72 71           imp:n,p=1  $Empty space
  703    5   -2.70      -73 72           imp:n,p=1  $Aluminum Casing
  706    8   -7.92      -77              imp:n,p=1  $Source stand
c  ~~~~~~~~~~~~~~~~~~~~~~~~~~~~~~~~~~~~
c   Environment
c  ~~~~~~~~~~~~~~~~~~~~~~~~~~~~~~~~~~~~
  901    2   -1.205E-3 -500 61 #100 #101 #102 #103 #104 #105 #106
     ↪ #107 #108 #109
```

```
                #110 #111 #112 #113 #114 #115 #116 #117 #118 #119
                   ↪ #120 #121 #122
                #123 #124 #125 #126 #127 #128 #129 #130 #131 #132
                   ↪ #133 #134 #135
                #136 #137 #138 #139 #140 #141 #142 #143 #144 #145
                   ↪ #146 #147
                #148 #149 #150 #151 #152 #153 #154 #155 #156 #157
                   ↪ #158 #159 #160
                #161 #162 #163 #164 #165 #166 #167 #168 #169 #170
                   ↪ #171 #172 #173
                #174 #175 #176 #177 #178 #179 #180 #181 #182 #183
                   ↪ #184 #185 #186
                #187 #188 #189 #190 #191 #192 #193 #194 #195
                31 32 33 34 35 36 37 38 39 40 41
                #300 #301 #302 #303 #304 #305 #306 #307 #308 #309
                   ↪ #310
                #311 #312 #313 #314 #315 73 77 #316 #317 #501 imp:
                   ↪ N,P=1
  999    0      500                    imp:N,P=0

c ~~~~~~~~~~~~~~~~~~~~~~~~~~~~~~~~~~
c
c  Surfaces
c ~~~~~~~~~~~~~~~~~~~~~~~~~~~~~~~~~~
c
c   EJ-309 Detectors
c ~~~~~~~~~~~~~~~~~~~~~~~~~~~~~~~~~~
  10  RCC 27.175 0 5.31    -0.635 0 0    3.9075       $Optical
     ↪ Coupling
  11  RCC 26.54 0 5.31    -1.6 0 0    3.25              $Optical
     ↪ Window
  12  RCC 26.54 0 5.31    -9.2 0 0    3.81              $3"
     ↪ Detector Cell
  13  RCC 26.54 0 5.31    -9.352 0 0    3.962           $Detector
     ↪ Casing
  14  RCC 26.54 0 5.31    1.54 0 0    5.08              $Large
     ↪ Ring Outside
  15  RCC 26.54 0 5.31    1.54 0 0    3.9075            $Large
     ↪ Ring Inside
  16  RCC 24.54 0 5.31   2 0 0    4.362                $Small Ring
     ↪ Outside
  17  RCC 24.54 0 5.31   2 0 0    3.962                $Small Ring
     ↪ Inside
  20  RCC 27.175 0 -5.31    -0.635 0 0    3.9075       $Optical
     ↪ Coupling
  21  RCC 26.54 0 -5.31    -1.6 0 0    3.25              $Optical
     ↪ Window
  22  RCC 26.54 0 -5.31    -9.2 0 0    3.81              $3"
     ↪ Detector Cell
  23  RCC 26.54 0 -5.31    -9.352 0 0    3.962           $Detector
```

```
    ↪  Casing
  24  RCC 26.54 0 -5.31   1.54 0 0   5.08              $Large
    ↪ Ring Outside
  25  RCC 26.54 0 -5.31   1.54 0 0   3.9075            $Large
    ↪ Ring Inside
  26  RCC 24.54 0 -5.31  2 0 0   4.362               $Small Ring
    ↪  Outside
  27  RCC 24.54 0 -5.31  2 0 0   3.962               $Small Ring
    ↪  Inside
c ~~~~~~~~~~~~~~~~~~~~~~~~~~~~~~~~~~
c
c   Table
c ~~~~~~~~~~~~~~~~~~~~~~~~~~~~~~~~~~
  31 8 BOX  -50   -100   -0.5   100   0 0   0 200   0   0 0
    ↪ 0.5   $ Surface
  32 8 BOX  -50   -100   -4.9     4.4 0 0   0 200   0   0 0
    ↪ 4.4   $ Support
  33 8 BOX   45.6 -100   -4.9     4.4 0 0   0 200   0   0 0
    ↪ 4.4   $ Support
  34 8 BOX  -45.6 -100   -4.9    91.2 0 0   0   4.4 0   0 0
    ↪ 4.4   $ Support
  35 8 BOX  -45.6   95.6 -4.9    91.2 0 0   0   4.4 0   0 0
    ↪ 4.4   $ Support
  36 8 BOX  -50     -2.2 -4.9     4.4 0 0   0   4.4 0   0 0
    ↪ -85.5   $ Leg
  37 8 BOX   45.6   -2.2 -4.9     4.4 0 0   0   4.4 0   0 0
    ↪ -85.5   $ Leg
  38 8 BOX  -50   -100   -4.9     4.4 0 0   0   4.4 0   0 0
    ↪ -85.5   $ Leg
  39 8 BOX   45.6 -100   -4.9     4.4 0 0   0   4.4 0   0 0
    ↪ -85.5   $ Leg
  40 8 BOX  -50     95.6 -4.9     4.4 0 0   0   4.4 0   0 0
    ↪ -85.5   $ Leg
  41 8 BOX   45.6   95.6 -4.9     4.4 0 0   0   4.4 0   0 0
    ↪ -85.5   $ Leg
c ~~~~~~~~~~~~~~~~~~~~~~~~~~~~~~~~~~
c
c   Lead Shielding
c ~~~~~~~~~~~~~~~~~~~~~~~~~~~~~~~~~~
  51   CZ   6.5        $outer cylinder
  52   CZ   5.5        $inner cylinder
  53   PZ   15.25      $top
  54   PZ  -16.25      $bottom
c ~~~~~~~~~~~~~~~~~~~~~~~~~~~~~~~~~~
c Ground
c ~~~~~~~~~~~~~~~~~~~~~~~~~~~~~~~~~~
  61 PZ     -108   $ Floor level
c ~~~~~~~~~~~~~~~~~~~~~~~~~~~~~~~~~~
c PM Material and Container
c ~~~~~~~~~~~~~~~~~~~~~~~~~~~~~~~~~~
```

```
  71   RCC   0 0 -4.02    0 0 1.32   0.5   $PM2
  72   RCC   0 0 -5.77    0 0 3.3    1.3   $Casing - inner
  73   RCC   0 0 -6.25    0 0 4.6    1.6   $Casing - outer
  77   RCC   0 0 -17.25   0 0 1      8.5
c ~~~~~~~~~~~~~~~~~~~~~~~~~~~~~~~~~~~~~~~~
c  Detector Structure
c ~~~~~~~~~~~~~~~~~~~~~~~~~~~~~~~~~~~~~~~~
  90    RPP  22       22.3175   -5.05      5.05    -17.25   13.35
     ↪ $front vertical plate
  91    RPP  24.2225 24.54      -5.05      5.05    -17.25   13.35
     ↪ $back vertical plate
 106    RPP  22.3176 24.2224    -10.0333 10.0333 -17.25 -15.345
    ↪ $bottom bar
 107    RPP  22.3176 24.2224    -10.0333 10.0333  11.445 13.35
    ↪ $top bar
 108 1  RPP  22.3176 24.2224    -10.0333 10.0333 -17.25 -15.345
    ↪ $bottom bar
 109 1  RPP  22.3176 24.2224    -10.0333 10.0333  11.445 13.35
    ↪ $top bar
 110 2  RPP  22.3176 24.2224    -10.0333 10.0333 -17.25 -15.345
    ↪ $bottom bar
 111 2  RPP  22.3176 24.2224    -10.0333 10.0333  11.445 13.35
    ↪ $top bar
 112 3  RPP  22.3176 24.2224    -10.0333 10.0333 -17.25 -15.345
    ↪ $bottom bar
 113 3  RPP  22.3176 24.2224    -10.0333 10.0333  11.445 13.35
    ↪ $top bar
 114 4  RPP  22.3176 24.2224    -10.0333 10.0333 -17.25 -15.345
    ↪ $bottom bar
 115 4  RPP  22.3176 24.2224    -10.0333 10.0333  11.445 13.35
    ↪ $top bar
 116 5  RPP  22.3176 24.2224    -10.0333 10.0333 -17.25 -15.345
    ↪ $bottom bar
 117 5  RPP  22.3176 24.2224    -10.0333 10.0333  11.445 13.35
    ↪ $top bar
 118 6  RPP  22.3176 24.2224    -10.0333 10.0333 -17.25 -15.345
    ↪ $bottom bar
 119 6  RPP  22.3176 24.2224    -10.0333 10.0333  11.445 13.35
    ↪ $top bar
 120 7  RPP  22.3176 24.2224    -10.0333 10.0333 -17.25 -15.345
    ↪ $bottom bar
 121 7  RPP  22.3176 24.2224    -10.0333 10.0333  11.445 13.35
    ↪ $top bar
c ~~~~~~~~~~~~~~~~~~~~~~~~~~~~~~~~~~~~~~~~
c  Environment
c ~~~~~~~~~~~~~~~~~~~~~~~~~~~~~~~~~~~~~~~~
 500 RPP -500 500    -500 500    -500 500
```

```
c ~~~~~~~~~~~~~~~~~~~~~~~~~~~~~~~~~~
c Data
c ~~~~~~~~~~~~~~~~~~~~~~~~~~~~~~~~~~
c Translations
c ~~~~~~~~~~~~~~~~~~~~~~~~~~~~~~~~~~
  TR1  0 0 0    0.7071   0.7071  0    -0.7071   0.7071  0    0  0  1
  TR2  0 0 0    0        1       0    -1        0       0    0  0  1
  TR3  0 0 0   -0.7071   0.7071  0    -0.7071  -0.7071  0    0  0  1
  TR4  0 0 0   -1        0       0     0       -1       0    0  0  1
  TR5  0 0 0   -0.7071  -0.7071  0     0.7071  -0.7071  0    0  0  1
  TR6  0 0 0    0       -1       0     1        0       0    0  0  1
  TR7  0 0 0    0.7071  -0.7071  0     0.7071   0.7071  0    0  0  1
  TR8  0 0 -17.25
  TR9  16.92 0 5.31
c ~~~~~~~~~~~~~~~~~~~~~~~~~~~~~~~~~~
c Physics
c ~~~~~~~~~~~~~~~~~~~~~~~~~~~~~~~~~~
  MODE n p
  PHYS:N J 20
  PHYS:P 0 1 1
  CUT:P 2J 0
c ~~~~~~~~~~~~~~~~~~~~~~~~~~~~~~~~~~
c Source
c ~~~~~~~~~~~~~~~~~~~~~~~~~~~~~~~~~~
  SDEF cel=701 pos=0 0 -4.02 axs=0 0 1 rad=d1 ext=d2 erg=d3
  SC1  Source radius (inner outer)
  SI1  0 0.5
  SC2  Source height
  SI2  0 1.32
  SI3  L 3 4
  SP3  0.9945 0.0055
  IPOL  99 1 2 1 J 1 16 100 106 112 118 124 130 136 142
                        148 154 160 166 172 178 184 190
  NPS 715403 $ 1430805 = Number of reactions in 3600 sec (aged
     ↪ PM src)
  FILES 21 DUMN1
  DBCN
  PRDMP 2J 1
c ~~~~~~~~~~~~~~~~~~~~~~~~~~~~~~~~~~
c Materials
c ~~~~~~~~~~~~~~~~~~~~~~~~~~~~~~~~~~
c  EJ-309 liquid scintillator d=-0.916
c (Eljen Technologies, EJ-309 Fact Sheet)
c ~~~~~~~~~~~~~~~~~~~~~~~~~~~~~~~~~~
  m1    NLIB=70c PLIB=04p
        1001         0.555443    $ H
        6012.50c     0.444557    $ C
c ~~~~~~~~~~~~~~~~~~~~~~~~~~~~~~~~~~
```

```
c Air, Dry (near sea level) d=-1.205E-3
c (Mat. Compendium PNNL)
c ~~~~~~~~~~~~~~~~~~~~~~~~~~~~~~~~~~
  m2  NLIB=70c PLIB=04p
       7014   -0.755636    $ N
       8016   -0.231475    $ O
      18040  -0.012838 $ Ar-40 at 99.6035 percent of natural Ar
      18036  -0.000043 $ Ar-36 at 0.3336 percent of natural Ar
      18038  -0.000008 $ Ar-38 at 0.00629 percent of natural Ar
c ~~~~~~~~~~~~~~~~~~~~~~~~~~~~~~~~~~
c  Lead Shielding d=-11.34
c
c ~~~~~~~~~~~~~~~~~~~~~~~~~~~~~~~~~~
  m3  82000.42c 1
c ~~~~~~~~~~~~~~~~~~~~~~~~~~~~~~~~~~
c Polyethylene d=-0.9300
c (Mat. Compendium PNNL)
c ~~~~~~~~~~~~~~~~~~~~~~~~~~~~~~~~~~
  m4  nlib=60c  plib=04p
       1001  -0.143716
       6000  -0.856284
c ~~~~~~~~~~~~~~~~~~~~~~~~~~~~~~~~~~
c Aluminum table d=-2.70
c ~~~~~~~~~~~~~~~~~~~~~~~~~~~~~~~~~~
  m5  nlib=60c  plib=04p
     13027      -1
c ~~~~~~~~~~~~~~~~~~~~~~~~~~~~~~~~~~
c Concrete (Mat. Compendium PNNL) d=-2.3
c (Mat. Compendium PNNL)
c ~~~~~~~~~~~~~~~~~~~~~~~~~~~~~~~~~~
  m6  nlib=60c  plib=04p
       1001       -0.022100
       6000       -0.002484
       8016       -0.574930
      11023       -0.015208
      12000       -0.001266
      13027       -0.019953
      14000       -0.304627
      19000       -0.010045
      20000       -0.042951
      26000.42c  -0.006435
c ~~~~~~~~~~~~~~~~~~~~~~~~~~~~~~~~~~
c  Pu Metal Sample d=-19.7
c (PM2)
c ~~~~~~~~~~~~~~~~~~~~~~~~~~~~~~~~~~
  m7  94238.42c    -0.00004
       94239.60c    -0.87367
       94240.60c    -0.04076
```

```
      94241.60c    -0.00028
      94242.60c    -0.00013
      95241.61c    -0.00234
      28058.60c    -0.03466
      28060.60c    -0.01335
      28061.60c    -0.00058
      28062.60c    -0.00185
      29063.60c    -0.02209
      29065.60c    -0.00985
c  ~~~~~~~~~~~~~~~~~~~~~~~~~~~~~~~~~~
c
c  Steel d=-7.92
c  (Mat. Compendium PNNL)
c  ~~~~~~~~~~~~~~~~~~~~~~~~~~~~~~~~~~
c
  m8   26000.55c  -0.6950
       24000.50c  -0.1900
       28000.50c  -0.0950
       25055.51c  -0.0200
c  ~~~~~~~~~~~~~~~~~~~~~~~~~~~~~~~~~~
c
c  BK7
c  ~~~~~~~~~~~~~~~~~~~~~~~~~~~~~~~~~~
c
  m9 NLIB=70c  PLIB=04p
       14028  -0.323138999
       8016   -0.483882614
       5011   -0.033384805
       56138  -0.027496631
       11023  -0.077153875
       19039  -0.052216449
       33075  -0.002726626
c  ~~~~~~~~~~~~~~~~~~~~~~~~~~~~~~~~~~
c
c   Tallies
c  ~~~~~~~~~~~~~~~~~~~~~~~~~~~~~~~~~~
c
c  detectors
c  ~~~~~~~~~~~~~~~~~~~~~~~~~~~~~~~~~~
c   F31:n 11.3 12.3 13.3 14.3 15.3 16.3 17.3 18.3 19.3
c   E31 0 0.5 0.7 29i 1 899i 10 100
c   C31 0 1
c   F41:p 11.3
c   E41 0 999i 10
c   C41 0 1
c  ~~~~~~~~~~~~~~~~~~~~~~~~~~~~~~~~~~
```

Appendix 2. Neutron and Photon Correlations from the University of Michigan ^{252}Cf(sf) Experiment

The full `MCNPX – PoliMi` model is included.

```
c nps = 1e7 over a 100 cores seems legit
c runs about 2e4 f/s
c June 2014 32 Detector Cf-252 Measurement
c
c Version: Detectors with PMTs, fully commented.  8/7/14
c
c This model reflects the detector set up used in June 2014
c using the double horizontal rings rig previously used at
   ↪ LANSCE
c in 2013 by Andreas Enquist and Brian Wieger.  Model was used
c in 2014 by Matt Marcath and Steve Ward.
c ~~~~~~~~~~~~~~~~~~~~~~~~~~~~~~~~~~~
c
c The 3x2 detectors are in a checkerboard pattern with the NaIs
c on one half ring, with the first 3x2 on the leftmost side (
   ↪ from the
c perspective of the source) being in the upper spot on the pole
   ↪ .
c Refer to the translation section for more details on how these
c are arranged.
c
c Source was at the center of the ring with the upper detectors
c 10 cm above the source height and the lower ring 10 cm below
   ↪ the
c source height.  Detectors were facing straight with respect to
c the horizon, i.e., not angled up/down to face the source more
c directly.  Distance from source to detector face was a radius
c of about 55 cm, equal in all directions.  Source is at the
c origin as discussed later.
c
c ~~~~~~~~~~~~~~~~~~~~~~~~~~~~~~~~~~~~~~~~~~~~~~~~~~~
c ~~~~~~~~~~~ 3x2 1 ~~~~~~~~~~~~~~
```

```
1 5 -2.70    10 -11 -22      imp:n,p=1 TRCL=20   $ Al cap front
2 5 -2.70    11 -22  23 -12 imp:n,p=1 TRCL=20   $ Al cap sides
3 2 -0.965   11 -23 -13   imp:n,p=1 TRCL=20    $ detector
4 5 -2.70    12 -13 -26  23 imp:n,p=1 TRCL=20   $ Al step
5 5 -2.70    13 -14 -27  23 imp:n,p=1 TRCL=20   $ Al ring
6 7 -8.747   14 -15 -25  24 imp:n,p=1 TRCL=20   $ large PMT
7 7 -8.747   17 -20 -28  30 imp:n,p=1 TRCL=20   $ skinny PMT
  ↪ front, mu metal
8 5 -2.70    20 -19 -28  29 imp:n,p=1 TRCL=20   $ skinny PMT
  ↪ middle
9 5 -2.70    19 -21 -28     imp:n,p=1 TRCL=20   $ skinny PMT cap
10 7 -8.747 -25 30 -17  15 imp:n,p=1 TRCL=20   $ cone
11 11 -2.5   -31            imp:n,p=1 TRCL=20   $ pyrex optical
  ↪ window
c ~~~~~~~~~~~ 3x2 2 ~~~~~~~~~~~~~~
c
12         LIKE 1 BUT TRCL=23          $ Al cap front
13         LIKE 2 BUT TRCL=23          $ Al cap sides
14         LIKE 3 BUT TRCL=23          $ detector
15         LIKE 4 BUT TRCL=23          $ Al step
16         LIKE 5 BUT TRCL=23          $ Al ring
17         LIKE 6 BUT TRCL=23          $ large PMT
18         LIKE 7 BUT TRCL=23          $ skinny PMT front, mu
  ↪ metal
19         LIKE 8 BUT TRCL=23          $ skinny PMT middle
20         LIKE 9 BUT TRCL=23          $ skinny PMT cap
21         LIKE 10 BUT TRCL=23         $ cone
22         LIKE 11 BUT TRCL=23         $ pyrex optical window
c ~~~~~~~~~~~ 3x2 3 ~~~~~~~~~~~~~~
23         LIKE 1 BUT TRCL=24          $ Al cap front
24         LIKE 2 BUT TRCL=24          $ Al cap sides
25         LIKE 3 BUT TRCL=24          $ detector
26         LIKE 4 BUT TRCL=24          $ Al step
27         LIKE 5 BUT TRCL=24          $ Al ring
28         LIKE 6 BUT TRCL=24          $ large PMT
29         LIKE 7 BUT TRCL=24          $ skinny PMT front, mu
  ↪ metal
30         LIKE 8 BUT TRCL=24          $ skinny PMT middle
31         LIKE 9 BUT TRCL=24          $ skinny PMT cap
32         LIKE 10 BUT TRCL=24         $ cone
33         LIKE 11 BUT TRCL=24         $ pyrex optical window
c ~~~~~~~~~~~ 3x2 4 ~~~~~~~~~~~~~~
34         LIKE 1 BUT TRCL=27          $ Al cap front
35         LIKE 2 BUT TRCL=27          $ Al cap sides
36         LIKE 3 BUT TRCL=27          $ detector
37         LIKE 4 BUT TRCL=27          $ Al step
38         LIKE 5 BUT TRCL=27          $ Al ring
39         LIKE 6 BUT TRCL=27          $ large PMT
```

```
40          LIKE 7 BUT TRCL=27          $ skinny PMT front, mu
   ↪ metal
41          LIKE 8 BUT TRCL=27          $ skinny PMT middle
42          LIKE 9 BUT TRCL=27          $ skinny PMT cap
43          LIKE 10 BUT TRCL=27         $ cone
44          LIKE 11 BUT TRCL=27         $ pyrex optical window
c ~~~~~~~~~~~~ 3x2 5 ~~~~~~~~~~~~~~~
45          LIKE 1 BUT TRCL=28          $ Al cap front
46          LIKE 2 BUT TRCL=28          $ Al cap sides
47          LIKE 3 BUT TRCL=28          $ detector
48          LIKE 4 BUT TRCL=28          $ Al step
49          LIKE 5 BUT TRCL=28          $ Al ring
50          LIKE 6 BUT TRCL=28          $ large PMT
51          LIKE 7 BUT TRCL=28          $ skinny PMT front, mu
   ↪ metal
52          LIKE 8 BUT TRCL=28          $ skinny PMT middle
53          LIKE 9 BUT TRCL=28          $ skinny PMT cap
54          LIKE 10 BUT TRCL=28         $ cone
55          LIKE 11 BUT TRCL=28         $ pyrex optical window
c ~~~~~~~~~~~~ 3x2 6 ~~~~~~~~~~~~~~~
56         LIKE 1 BUT TRCL=31          $ Al cap front
57         LIKE 2 BUT TRCL=31          $ Al cap sides
58         LIKE 3 BUT TRCL=31          $ detector
59         LIKE 4 BUT TRCL=31          $ Al step
60         LIKE 5 BUT TRCL=31          $ Al ring
61         LIKE 6 BUT TRCL=31          $ large PMT
62         LIKE 7 BUT TRCL=31          $ skinny PMT front, mu metal
63         LIKE 8 BUT TRCL=31          $ skinny PMT middle
64         LIKE 9 BUT TRCL=31          $ skinny PMT cap
65         LIKE 10 BUT TRCL=31         $ cone
66         LIKE 11 BUT TRCL=31         $ pyrex optical window
c ~~~~~~~~~~~~ 3x2 7 ~~~~~~~~~~~~~~~
67         LIKE 1 BUT TRCL=32          $ Al cap front
68         LIKE 2 BUT TRCL=32          $ Al cap sides
69         LIKE 3 BUT TRCL=32          $ detector
70         LIKE 4 BUT TRCL=32          $ Al step
71         LIKE 5 BUT TRCL=32          $ Al ring
72         LIKE 6 BUT TRCL=32          $ large PMT
73         LIKE 7 BUT TRCL=32          $ skinny PMT front, mu metal
74         LIKE 8 BUT TRCL=32          $ skinny PMT middle
75         LIKE 9 BUT TRCL=32          $ skinny PMT cap
76         LIKE 10 BUT TRCL=32         $ cone
77         LIKE 11 BUT TRCL=32         $ pyrex optical window
c ~~~~~~~~~~~~ 3x2 8 ~~~~~~~~~~~~~~~
78         LIKE 1 BUT TRCL=35          $ Al cap front
79         LIKE 2 BUT TRCL=35          $ Al cap sides
80         LIKE 3 BUT TRCL=35          $ detector
81         LIKE 4 BUT TRCL=35          $ Al step
```

```
82          LIKE 5 BUT TRCL=35          $ Al ring
83          LIKE 6 BUT TRCL=35          $ large PMT
84          LIKE 7 BUT TRCL=35          $ skinny PMT front, mu metal
85          LIKE 8 BUT TRCL=35          $ skinny PMT middle
86          LIKE 9 BUT TRCL=35          $ skinny PMT cap
87          LIKE 10 BUT TRCL=35         $ cone
88          LIKE 11 BUT TRCL=35         $ pyrex optical window
c ~~~~~~~~~~~~~~~~~~~~~~~~~~~~~~~~~~~~
c ~~~~~~~~~~~~~~~~~~~~~~~~~~~~~~~~~~~~
c The NaI detectors are in a checkerboard pattern with the 3x2s
c on one ring, with the first NaI on the leftmost side (from the
c perspective of the source) being in the lower spot on the pole
   ↪ .
c ~~~~~~~~~~~~~~~~~~~~~~~~~~~~~~~~~~~~~~~~~~~~~~~~~~~~~~~~~~~~~
c ~~~~~~~~~~~~ NaI 1 ~~~~~~~~~~~~~~
91 5 -2.70    70 -71 -52      imp:n,p=1 TRCL=21    $ Al cap front
92 5 -2.70    71 -52  53 -74 imp:n,p=1 TRCL=21    $ Al cap sides
93 21 -3.67   71 -53 -73      imp:n,p=1 TRCL=21    $ detector
94 7 -8.747   74 -75 -55 54   imp:n,p=1 TRCL=21    $ large PMT
95 7 -8.747   77 -80 -58 60   imp:n,p=1 TRCL=21    $ skinny PMT
   ↪ front, mu metal
96 5 -2.70    80 -79 -58 59   imp:n,p=1 TRCL=21    $ skinny PMT
   ↪ middle
97 7 -8.747   -55 60 -77 75   imp:n,p=1 TRCL=21    $ cone
98 5 -2.70    79 -78 -58  imp:n,p=1 TRCL=21    $ skinny PMT cap
c ~~~~~~~~~~~~ NaI 2 ~~~~~~~~~~~~~~
99          LIKE 91 BUT TRCL=22          $ Al cap front
100         LIKE 92 BUT TRCL=22          $ Al cap sides
101         LIKE 93 BUT TRCL=22          $ detector
102         LIKE 94 BUT TRCL=22          $ large PMT
103         LIKE 95 BUT TRCL=22          $ skinny PMT front
104         LIKE 96 BUT TRCL=22          $ skinny PMT middle
105         LIKE 97 BUT TRCL=22          $ cone
106         LIKE 98 BUT TRCL=22          $ skinny PMT cap
c ~~~~~~~~~~~~ NaI 3 ~~~~~~~~~~~~~~
107         LIKE 91 BUT TRCL=25          $ Al cap front
108         LIKE 92 BUT TRCL=25          $ Al cap sides
109         LIKE 93 BUT TRCL=25          $ detector
110         LIKE 94 BUT TRCL=25          $ large PMT
111         LIKE 95 BUT TRCL=25          $ skinny PMT front
112         LIKE 96 BUT TRCL=25          $ skinny PMT middle
113         LIKE 97 BUT TRCL=25          $ cone
114         LIKE 98 BUT TRCL=25          $ skinny PMT cap
c ~~~~~~~~~~~~ NaI 4 ~~~~~~~~~~~~~~
115         LIKE 91 BUT TRCL=26          $ Al cap front
116         LIKE 92 BUT TRCL=26          $ Al cap sides
117         LIKE 93 BUT TRCL=26          $ detector
118         LIKE 94 BUT TRCL=26          $ large PMT
```

```
119         LIKE 95 BUT TRCL=26          $ skinny PMT front
120         LIKE 96 BUT TRCL=26          $ skinny PMT middle
121         LIKE 97 BUT TRCL=26          $ cone
122         LIKE 98 BUT TRCL=26          $ skinny PMT cap
c ~~~~~~~~~~~ NaI 5 ~~~~~~~~~~~~~~
123         LIKE 91 BUT TRCL=29          $ Al cap front
124         LIKE 92 BUT TRCL=29          $ Al cap sides
125         LIKE 93 BUT TRCL=29          $ detector
126         LIKE 94 BUT TRCL=29          $ large PMT
127         LIKE 95 BUT TRCL=29          $ skinny PMT front
128         LIKE 96 BUT TRCL=29          $ skinny PMT middle
129         LIKE 97 BUT TRCL=29          $ cone
130         LIKE 98 BUT TRCL=29          $ skinny PMT cap
c ~~~~~~~~~~~ NaI 6 ~~~~~~~~~~~~~~
131         LIKE 91 BUT TRCL=30          $ Al cap front
132         LIKE 92 BUT TRCL=30          $ Al cap sides
133         LIKE 93 BUT TRCL=30          $ detector
134         LIKE 94 BUT TRCL=30          $ large PMT
135         LIKE 95 BUT TRCL=30          $ skinny PMT front
136         LIKE 96 BUT TRCL=30          $ skinny PMT middle
137         LIKE 97 BUT TRCL=30          $ cone
138         LIKE 98 BUT TRCL=30          $ skinny PMT cap
c ~~~~~~~~~~~ NaI 7 ~~~~~~~~~~~~~~
139         LIKE 91 BUT TRCL=33          $ Al cap front
140         LIKE 92 BUT TRCL=33          $ Al cap sides
141         LIKE 93 BUT TRCL=33          $ detector
142         LIKE 94 BUT TRCL=33          $ large PMT
143         LIKE 95 BUT TRCL=33          $ skinny PMT front
144         LIKE 96 BUT TRCL=33          $ skinny PMT middle
145         LIKE 97 BUT TRCL=33          $ cone
146         LIKE 98 BUT TRCL=33          $ skinny PMT cap
c ~~~~~~~~~~~ NaI 8 ~~~~~~~~~~~~~~
147         LIKE 91 BUT TRCL=34          $ Al cap front
148         LIKE 92 BUT TRCL=34          $ Al cap sides
149         LIKE 93 BUT TRCL=34          $ detector
150         LIKE 94 BUT TRCL=34          $ large PMT
151         LIKE 95 BUT TRCL=34          $ skinny PMT front
152         LIKE 96 BUT TRCL=34          $ skinny PMT middle
153         LIKE 97 BUT TRCL=34          $ cone
154         LIKE 98 BUT TRCL=34          $ skinny PMT cap
c ~~~~~~~~~~~~~~~~~~~~~~~~~~~~~~~~~~~~~~~~~~~~~~~~~~~~~~~~~~~~~~~~~~~~~~~~~~~~~~~~
c The 3x3s are all on the same ring, the ring sized for them.
c See the translation section for which translation goes with
   ↪ which spot.
c ~~~~~~~~~~~~~~~~~~~~~~~~~~~~~~~~~~~~~~~~~~~~~~~~~~~~~~~~~~~~~~~~~~~~~~~~~~~~~~~~
c ~~~~~~~~~~~ 3x3 1 ~~~~~~~~~~~~~~
155 5 -2.70    40 -41 -52      imp:n,p=1 TRCL=36    $ Al cap front
156 5 -2.70    41 -52  53 -42  imp:n,p=1 TRCL=36    $ Al cap sides
```

```
157 2 -0.965   41 -53 -43     imp:n,p=1 TRCL=36    $ detector
158 5 -2.70    42 -43 -56   53 imp:n,p=1 TRCL=36    $ Al step
159 5 -2.70    43 -44 -57   53 imp:n,p=1 TRCL=36    $ Al ring
160 7 -8.747   44 -45 -55   54 imp:n,p=1 TRCL=36    $ large PMT
161 7 -8.747   47 -50 -58   60 imp:n,p=1 TRCL=36    $ skinny PMT
   ↪ front, mu metal
162 5 -2.70    50 -49 -58   59 imp:n,p=1 TRCL=36    $ skinny PMT
   ↪ middle
163 5 -2.70    49 -51 -58    imp:n,p=1 TRCL=36    $ skinny PMT cap
164 7 -8.747   -55 60 -47   45 imp:n,p=1 TRCL=36    $ cone
165 11 -2.51    -61             imp:n,p=1 TRCL=36    $ pyrex
   ↪ optical window
c ~~~~~~~~~~~ 3x3 2 ~~~~~~~~~~~~~~
166         LIKE 155 BUT TRCL=37          $ Al cap front
167         LIKE 156 BUT TRCL=37          $ Al cap sides
168         LIKE 157 BUT TRCL=37          $ detector
169         LIKE 158 BUT TRCL=37          $ Al step
170         LIKE 159 BUT TRCL=37          $ Al ring
171         LIKE 160 BUT TRCL=37          $ large PMT
172         LIKE 161 BUT TRCL=37          $ skinny PMT front, mu
   ↪ metal
173         LIKE 162 BUT TRCL=37          $ skinny PMT middle
174         LIKE 163 BUT TRCL=37          $ skinny PMT cap
175         LIKE 164 BUT TRCL=37          $ cone
176         LIKE 165 BUT TRCL=37          $ pyrex optical window
c ~~~~~~~~~~~ 3x3 3 ~~~~~~~~~~~~~~
177         LIKE 155 BUT TRCL=38          $ Al cap front
178         LIKE 156 BUT TRCL=38          $ Al cap sides
179         LIKE 157 BUT TRCL=38          $ detector
180         LIKE 158 BUT TRCL=38          $ Al step
181         LIKE 159 BUT TRCL=38          $ Al ring
182         LIKE 160 BUT TRCL=38          $ large PMT
183         LIKE 161 BUT TRCL=38          $ skinny PMT front, mu
   ↪ metal
184         LIKE 162 BUT TRCL=38          $ skinny PMT middle
185         LIKE 163 BUT TRCL=38          $ skinny PMT cap
186         LIKE 164 BUT TRCL=38          $ cone
187         LIKE 165 BUT TRCL=38          $ pyrex optical window
c ~~~~~~~~~~~ 3x3 4 ~~~~~~~~~~~~~~
188         LIKE 155 BUT TRCL=39          $ Al cap front
189         LIKE 156 BUT TRCL=39          $ Al cap sides
190         LIKE 157 BUT TRCL=39          $ detector
191         LIKE 158 BUT TRCL=39          $ Al step
192         LIKE 159 BUT TRCL=39          $ Al ring
193         LIKE 160 BUT TRCL=39          $ large PMT
194         LIKE 161 BUT TRCL=39          $ skinny PMT front, mu
   ↪ metal
195         LIKE 162 BUT TRCL=39          $ skinny PMT middle
```

```
196         LIKE 163 BUT TRCL=39          $ skinny PMT cap
197         LIKE 164 BUT TRCL=39          $ cone
198         LIKE 165 BUT TRCL=39          $ pyrex optical window
c ~~~~~~~~~~~ 3x3 5 ~~~~~~~~~~~~~~
199         LIKE 155 BUT TRCL=40          $ Al cap front
200         LIKE 156 BUT TRCL=40          $ Al cap sides
201         LIKE 157 BUT TRCL=40          $ detector
202         LIKE 158 BUT TRCL=40          $ Al step
203         LIKE 159 BUT TRCL=40          $ Al ring
204         LIKE 160 BUT TRCL=40          $ large PMT
205         LIKE 161 BUT TRCL=40          $ skinny PMT front, mu
   ↪ metal
206         LIKE 162 BUT TRCL=40          $ skinny PMT middle
207         LIKE 163 BUT TRCL=40          $ skinny PMT cap
208         LIKE 164 BUT TRCL=40          $ cone
209         LIKE 165 BUT TRCL=40          $ pyrex optical window
c ~~~~~~~~~~~ 3x3 6 ~~~~~~~~~~~~~~
210         LIKE 155 BUT TRCL=41          $ Al cap front
211         LIKE 156 BUT TRCL=41          $ Al cap sides
212         LIKE 157 BUT TRCL=41          $ detector
213         LIKE 158 BUT TRCL=41          $ Al step
214         LIKE 159 BUT TRCL=41          $ Al ring
215         LIKE 160 BUT TRCL=41          $ large PMT
216         LIKE 161 BUT TRCL=41          $ skinny PMT front, mu
   ↪ metal
217         LIKE 162 BUT TRCL=41          $ skinny PMT middle
218         LIKE 163 BUT TRCL=41          $ skinny PMT cap
219         LIKE 164 BUT TRCL=41          $ cone
220         LIKE 165 BUT TRCL=41          $ pyrex optical window
c ~~~~~~~~~~~ 3x3 7 ~~~~~~~~~~~~~~
221         LIKE 155 BUT TRCL=42          $ Al cap front
222         LIKE 156 BUT TRCL=42          $ Al cap sides
223         LIKE 157 BUT TRCL=42          $ detector
224         LIKE 158 BUT TRCL=42          $ Al step
225         LIKE 159 BUT TRCL=42          $ Al ring
226         LIKE 160 BUT TRCL=42          $ large PMT
227         LIKE 161 BUT TRCL=42          $ skinny PMT front, mu
   ↪ metal
228         LIKE 162 BUT TRCL=42          $ skinny PMT middle
229         LIKE 163 BUT TRCL=42          $ skinny PMT cap
230         LIKE 164 BUT TRCL=42          $ cone
231         LIKE 165 BUT TRCL=42          $ pyrex optical window
c ~~~~~~~~~~~ 3x3 8 ~~~~~~~~~~~~~~
232         LIKE 155 BUT TRCL=43          $ Al cap front
233         LIKE 156 BUT TRCL=43          $ Al cap sides
234         LIKE 157 BUT TRCL=43          $ detector
235         LIKE 158 BUT TRCL=43          $ Al step
236         LIKE 159 BUT TRCL=43          $ Al ring
```

```
237         LIKE 160 BUT TRCL=43          $ large PMT
238         LIKE 161 BUT TRCL=43          $ skinny PMT front, mu
   ↪ metal
239         LIKE 162 BUT TRCL=43          $ skinny PMT middle
240         LIKE 163 BUT TRCL=43          $ skinny PMT cap
241         LIKE 164 BUT TRCL=43          $ cone
242         LIKE 165 BUT TRCL=43          $ pyrex optical window
c ~~~~~~~~~~~ 3x3 9 ~~~~~~~~~~~~~~
243         LIKE 155 BUT TRCL=44          $ Al cap front
244         LIKE 156 BUT TRCL=44          $ Al cap sides
245         LIKE 157 BUT TRCL=44          $ detector
246         LIKE 158 BUT TRCL=44          $ Al step
247         LIKE 159 BUT TRCL=44          $ Al ring
248         LIKE 160 BUT TRCL=44          $ large PMT
249         LIKE 161 BUT TRCL=44          $ skinny PMT front, mu
   ↪ metal
250         LIKE 162 BUT TRCL=44          $ skinny PMT middle
251         LIKE 163 BUT TRCL=44          $ skinny PMT cap
252         LIKE 164 BUT TRCL=44          $ cone
253         LIKE 165 BUT TRCL=44          $ pyrex optical window
c ~~~~~~~~~~~ 3x3 10 ~~~~~~~~~~~~~
254         LIKE 155 BUT TRCL=45          $ Al cap front
255         LIKE 156 BUT TRCL=45          $ Al cap sides
256         LIKE 157 BUT TRCL=45          $ detector
257         LIKE 158 BUT TRCL=45          $ Al step
258         LIKE 159 BUT TRCL=45          $ Al ring
259         LIKE 160 BUT TRCL=45          $ large PMT
260         LIKE 161 BUT TRCL=45          $ skinny PMT front, mu
   ↪ metal
261         LIKE 162 BUT TRCL=45          $ skinny PMT middle
262         LIKE 163 BUT TRCL=45          $ skinny PMT cap
263         LIKE 164 BUT TRCL=45          $ cone
264         LIKE 165 BUT TRCL=45          $ pyrex optical window
c ~~~~~~~~~~~ 3x3 11 ~~~~~~~~~~~~~~
265         LIKE 155 BUT TRCL=46          $ Al cap front
266         LIKE 156 BUT TRCL=46          $ Al cap sides
267         LIKE 157 BUT TRCL=46          $ detector
268         LIKE 158 BUT TRCL=46          $ Al step
269         LIKE 159 BUT TRCL=46          $ Al ring
270         LIKE 160 BUT TRCL=46          $ large PMT
271         LIKE 161 BUT TRCL=46          $ skinny PMT front, mu
   ↪ metal
272         LIKE 162 BUT TRCL=46          $ skinny PMT middle
273         LIKE 163 BUT TRCL=46          $ skinny PMT cap
274         LIKE 164 BUT TRCL=46          $ cone
275         LIKE 165 BUT TRCL=46          $ pyrex optical window
c ~~~~~~~~~~~ 3x3 12 ~~~~~~~~~~~~~~
276         LIKE 155 BUT TRCL=47          $ Al cap front
```

```
277         LIKE 156 BUT TRCL=47          $ Al cap sides
278         LIKE 157 BUT TRCL=47          $ detector
279         LIKE 158 BUT TRCL=47          $ Al step
280         LIKE 159 BUT TRCL=47          $ Al ring
281         LIKE 160 BUT TRCL=47          $ large PMT
282         LIKE 161 BUT TRCL=47          $ skinny PMT front, mu
   ↪ metal
283         LIKE 162 BUT TRCL=47          $ skinny PMT middle
284         LIKE 163 BUT TRCL=47          $ skinny PMT cap
285         LIKE 164 BUT TRCL=47          $ cone
286         LIKE 165 BUT TRCL=47          $ pyrex optical window
c ~~~~~~~~~~~ 3x3 13 ~~~~~~~~~~~~~~
287         LIKE 155 BUT TRCL=48          $ Al cap front
288         LIKE 156 BUT TRCL=48          $ Al cap sides
289         LIKE 157 BUT TRCL=48          $ detector
290         LIKE 158 BUT TRCL=48          $ Al step
291         LIKE 159 BUT TRCL=48          $ Al ring
292         LIKE 160 BUT TRCL=48          $ large PMT
293         LIKE 161 BUT TRCL=48          $ skinny PMT front, mu
   ↪ metal
294         LIKE 162 BUT TRCL=48          $ skinny PMT middle
295         LIKE 163 BUT TRCL=48          $ skinny PMT cap
296         LIKE 164 BUT TRCL=48          $ cone
297         LIKE 165 BUT TRCL=48          $ pyrex optical window
c ~~~~~~~~~~~ 3x3 14 ~~~~~~~~~~~~~
298         LIKE 155 BUT TRCL=49          $ Al cap front
299         LIKE 156 BUT TRCL=49          $ Al cap sides
300         LIKE 157 BUT TRCL=49          $ detector
301         LIKE 158 BUT TRCL=49          $ Al step
302         LIKE 159 BUT TRCL=49          $ Al ring
303         LIKE 160 BUT TRCL=49          $ large PMT
304         LIKE 161 BUT TRCL=49          $ skinny PMT front, mu
   ↪ metal
305         LIKE 162 BUT TRCL=49          $ skinny PMT middle
306         LIKE 163 BUT TRCL=49          $ skinny PMT cap
307         LIKE 164 BUT TRCL=49          $ cone
308         LIKE 165 BUT TRCL=49          $ pyrex optical window
c ~~~~~~~~~~~ 3x3 15 ~~~~~~~~~~~~~~
309         LIKE 155 BUT TRCL=50          $ Al cap front
310         LIKE 156 BUT TRCL=50          $ Al cap sides
311         LIKE 157 BUT TRCL=50          $ detector
312         LIKE 158 BUT TRCL=50          $ Al step
313         LIKE 159 BUT TRCL=50          $ Al ring
314         LIKE 160 BUT TRCL=50          $ large PMT
315         LIKE 161 BUT TRCL=50          $ skinny PMT front, mu
   ↪ metal
316         LIKE 162 BUT TRCL=50          $ skinny PMT middle
317         LIKE 163 BUT TRCL=50          $ skinny PMT cap
```

```
318         LIKE 164 BUT TRCL=50          $ cone
319         LIKE 165 BUT TRCL=50          $ pyrex optical window
c ~~~~~~~~~~~ 3x3 16 ~~~~~~~~~~~~~
320         LIKE 155 BUT TRCL=51          $ Al cap front
321         LIKE 156 BUT TRCL=51          $ Al cap sides
322         LIKE 157 BUT TRCL=51          $ detector
323         LIKE 158 BUT TRCL=51          $ Al step
324         LIKE 159 BUT TRCL=51          $ Al ring
325         LIKE 160 BUT TRCL=51          $ large PMT
326         LIKE 161 BUT TRCL=51          $ skinny PMT front, mu
   ↪ metal
327         LIKE 162 BUT TRCL=51          $ skinny PMT middle
328         LIKE 163 BUT TRCL=51          $ skinny PMT cap
329         LIKE 164 BUT TRCL=51          $ cone
330         LIKE 165 BUT TRCL=51          $ pyrex optical window
c ~~~~~~~~~~~~~~~~~~~~~~~~~~~~~~~~~~~~
c
c Space around all the detectors, divided into 4 sections by
c the x and y axis.  You can see this from the signs of the x
   ↪ and y
c coordinates in the translation cards.
c
c Why go to the trouble of dividing this into 4 sections?
c Because we learned the hard way that there is a limit on how
   ↪ many
c characters you enter in a single cell line.  It's about 2000,
   ↪ but that's
c characters (i.e., #100 is four characters plus the space
   ↪ before and
c after it) so when we were listing every single cell, we
   ↪ exceeded that
c limit.
c So this way you should be able to add all the cells you want
   ↪ in the
c model and not have that problem.
c
c Cell 996 is for stuff with the x and y coordinates > 0
904  9  -1.84 -90 91 -92 93 -94 95  IMP:N,P=1
914  9  -1.84  -97  IMP:N,P=1
c pvc with a lower desity to account for drawers
905  10  -1.1  -96  IMP:N,P=1
996 0 -999 901 902 #904
     #45 #46 #47 #48 #49 #50 #51 #52 #53 #54 #55
     #56 #57 #58 #59 #60 #61 #62 #63 #64 #65 #66
     #67 #68 #69 #70 #71 #72 #73 #74 #75 #76 #77
     #78 #79 #80 #81 #82 #83 #84 #85 #86 #87 #88
     #123 #124 #125 #126 #127 #128 #129 #130
     #131 #132 #133 #134 #135 #136 #137 #138
```

```
     #139 #140 #141 #142 #143 #144 #145 #146
     #147 #148 #149 #150 #151 #152 #153 #154
     #35 #66 #77 #88 #914
     IMP:N,P=1
c Cell 997 is for stuff with x > 0 and y < 0
997 0 -999 901 -902  #904
     #243 #244 #245 #246 #247 #248 #249 #250 #251 #252 #253
     #254 #255 #256 #257 #258 #259 #260 #261 #262 #263 #264
     #265 #266 #267 #268 #269 #270 #271 #272 #273 #274 #275
     #276 #277 #278 #279 #280 #281 #282 #283 #284 #285 #286
     #287 #288 #289 #290 #291 #292 #293 #294 #295 #296 #297
     #298 #299 #300 #301 #302 #303 #304 #305 #306 #307 #308
     #309 #310 #311 #312 #313 #314 #315 #316 #317 #318 #319
     #320 #321 #322 #323 #324 #325 #326 #327 #328 #329 #330
     #264 #319 #286 #297 #308 #275 #330 #253
     IMP:N,P=1
c Cell 998 is for stuff with x and y < 0
998 0 -999 -901 -902  #904
     #155 #156 #157 #158 #159 #160 #161 #162 #163 #164 #165
     #166 #167 #168 #169 #170 #171 #172 #173 #174 #175 #176
     #177 #178 #179 #180 #181 #182 #183 #184 #185 #186 #187
     #188 #189 #190 #191 #192 #193 #194 #195 #196 #197 #198
     #199 #200 #201 #202 #203 #204 #205 #206 #207 #208 #209
     #210 #211 #212 #213 #214 #215 #216 #217 #218 #219 #220
     #221 #222 #223 #224 #225 #226 #227 #228 #229 #230 #231
     #232 #233 #234 #235 #236 #237 #238 #239 #240 #241 #242 #905
      61 #176 #187 #198 #209 #220 #231 #242
     IMP:N,P=1
c Cell 999 is for stuff with x < 0 and y > 0
995 0 -999 -901 902  #904
     #1 #2 #3 #4 #5 #6 #7 #8 #9 #10 #11
     #12 #13 #14 #15 #16 #17 #18 #19 #20 #21 #22
     #23 #24 #25 #26 #27 #28 #29 #30 #31 #32 #33
     #34 #35 #36 #37 #38 #39 #40 #41 #42 #43 #44
     #91 #92 #93 #94 #95 #96 #97 #98
     #99 #100 #101 #102 #103 #104 #105 #106
     #107 #108 #109 #110 #111 #112 #113 #114
     #115 #116 #117 #118 #119 #120 #121 #122 #905
     #22 #11 #33 #44
     IMP:N,P=1
9999 0 999 IMP:N,P=0 $void outside space
c BLANK LINE FOLLOWS END OF CELL CARDS

c ~~~~~~~~~~~~~~~~~~~~~~~~~~~~~~~~~~~~~~~~~~~~~~~~~~~~
c ~~~~~~~~~~~~~~~~~~~~~~~~~~~~~~~~~~~~~~~~~~~~~~~~~~~~
c ~~~~~~~~~~~~~~~~~~Surfaces~~~~~~~~~~~~~~~~~~~~~~~~~
c ~~~~~~~~~~~~~~~~~~~~~~~~~~~~~~~~~~~~~~~~~~~~~~~~~~~~
c ~~~~~~~~~~~~~~~~~~~~~~~~~~~~~~~~~~~~~~~~~~~~~~~~~~~~
```

```
c Please note that the NaI detectors use surfaces from the 3x3s.
c So if you delete the 3x3 surfaces, the file will crash.
c
c ~~~~~~~~~~~~ EJ309 3x2~~~~~~~~~~~~~~
10 py 0.       $ front outer scint
11 py 0.152    $ front inner wall
12 py 4.55     $ scint step
13 py 5.232    $ ring front
14 py 8.17    $ large PMT start
15 py 13.53    $ large PMT end
17 py 13.6316
19 py 28.9475 $ skinny PMT end cap
20 py 24.5025 $ skinny PMT middle
21 py 29.90    $ PMT outer back
22 cy 3.9625   $ outer wall scint
23 cy 3.9473   $ inner wall scint  MODIFIED
24 cy 4.0584   $ inner large PMT
25 cy 4.16     $ outer large PMT
26 cy 4.52125 $ outer scint step
27 cy 5.08     $ outer ring
28 cy 2.94     $ outer skinny PMT
29 cy 2.74     $ inner skinny PMT middle
30 cy 2.8384   $ inner skinny PMT front, mu metal
31 RCC 0 5.232 0 0 1.5 0 3.3 $ PYREX Window
c ~~~~~~~~~~~~~~~~~~~~~~~~~~~~~~~~
c ~~~~~~~~~~~~ NaI ~~~~~~~~~~~~~~
c Note that the NaI cells use surfaces from the EJ309 3x3 below
70 py 0.       $ front outer scint
71 py 0.152    $ front inner wall
72 py 7.09     $ scint step
73 py 7.73     $ ring front
74 py 10.71    $ large PMT start
75 py 16.07    $ large PMT end
77 py 16.1716
78 py 32.44    $PMT outer back
79 py 31.4875 $ skinny PMT end cap
80 py 27.0425 $ skinny PMT middle
81 py 32.44    $ PMT outer back
c ~~~~~~~~~~~~~~~~~~~~~~~~~~~~~~~~
c
c Note the NaIs use some of the 3x3 surfaces so don't delete
c them all if you want the file to run for NaIs.
c ~~~~~~~~~~~~ EJ309 3x3~~~~~~~~~~~~~~
40 py 0.       $ front outer scint
41 py 0.152    $ front inner wall
42 py 7.09     $ scint step
43 py 7.772     $ ring front  $modified
44 py 10.71    $ large PMT start
45 py 16.07    $ large PMT end
```

```
47 py 16.1716
49 py 31.4875 $ skinny PMT end cap
50 py 27.0425 $ skinny PMT middle
51 py 32.44   $ PMT outer back
52 cy 3.9625  $ outer wall scint
53 cy 3.9473   $ inner wall scint MODIFIED
54 cy 4.0584  $ inner large PMT
55 cy 4.16    $ outer large PMT
56 cy 4.52125 $ outer scint step
57 cy 5.08    $ outer ring
58 cy 2.94    $ outer skinny PMT
59 cy 2.74    $ inner skinny PMT middle
60 cy 2.8384  $ inner skinny PMT front, mu metal
61 RCC 0 7.772 0 0 1.2 0 3.25 $ PYREX Window/modified
c ~~~~~~~~~~~~~~~~~~~~~~~~~~~~~~~~
c
c ~~~~~~~~~~~~ Other Surfaces ~~~~~~~~~~~~~~~~~~
c
c Planes to separate the space around detectors
c into 4 quadrants
c
90  pz  -120   $concrete floor 90-95
91  pz  -150
92  px  500
93  px  -500
94  py  500
95  py  -500
901 px 0.001
902 py 0.001
96  rpp  -190 -150 -60 60 -120 -20
97  rpp  60 300 140 170 -120 200
c
c Sphere around everything to define void
999 SO 1000.
c BLANK LINE FOLLOWS END OF SURFACE CARDS

c ~~~~~~~~~~~~~~~~~~~~~~~~~~~~~~~~~~~~~~~~~~~~~~~~~~~~
c ~~~~~~~~~~~~~~~~~~~~~~~~~~~~~~~~~~~~~~~~~~~~~~~~~~~~
c ~~~~~~~~~~~~~~~ The Rest ~~~~~~~~~~~~~~~~~~~~~~~~
c ~~~~~~~~~~~~~~~~~~~~~~~~~~~~~~~~~~~~~~~~~~~~~~~~~~~~
c ~~~~~~~~~~~~~~~~~~~~~~~~~~~~~~~~~~~~~~~~~~~~~~~~~~~~
mode n p
c ~~~~~~~~~~~~~~ TRANSLATIONS ~~~~~~~~~~~~~~
c Translations for the double ring holder set work as
c follows (you should read this if you need to move anything):
c
c If you are standing where your source is and
c facing the shorter diameter ring where 3x2s go,
```

```
c TR20 is the top spot furthest to the left and TR 21 is
c the lower spot on that same pole.  TRs 22 and 23 are the
c spots on the second pole from the left, and so on. Thus,
c the top and bottom spots on the right-most pole of that ring
c are TRs 34 and 35.
c
c If you turn around so you're facing the other ring for the 3
   ↪ x3s,
c the system is reversed.  TR36 is the upper spot on the RIGHT-
   ↪ most
c pole (again assuming you are standing in the center of the
   ↪ rings).
c So TR36 is the upper detector and TR37 is the lower detector
   ↪ on
c the pole furthest to your right.  The numbers continue towards
   ↪  your left
c until you hit TR50 and TR51 being the top and bottom spots on
   ↪ the final
c pole.
c
c Note that in this orientation set-up, the pole with Slots TR20
   ↪  and TR21
c is next to the pole with slots TR36 and TR37.  Similarly, the
   ↪ pole for
c TR34 and TR35 is next to the pole for TR50 and TR51.
c
c If you move a pole for some reason both translations on that
   ↪ pole
c will need to be changed to reflect the new location.
c
c This geometry assumes the detectors are pointed straight level
   ↪  with the
c horizontal or z-axis, i.e., how high the detector sits.  If
   ↪ you want the
c detectors angled toward the source, you'll have to redo the
   ↪ translations.
c Because of this imperfect orientation, we kept the detectors
   ↪ fairly close
c to the height of the source as noted below.
c
c Also, the vertical orientation assumes your source is at 0
   ↪ height on
c the z-axis.  Then your detector rings are 10 cm above and 10
   ↪ cm below
c this plane.  All detectors are at one of these two heights.
c
c Every cell that makes up a single detector uses the same
   ↪ translation,
```

```
c i.e., all 8 cells for a single NaI should be moved by the same
c translation number.
c
c Essentially, one of each detector is built in basically the
   ↪ same spot
c and then they have been translated to where they should be.
   ↪ Without a
c translation, all detectors would be on top of one another.
c
c Also, the vertical orientation assumes your source is at 0
   ↪ height on
c the z-axis.  Then your detector rings are 10 cm above and 10
   ↪ cm below
c this plane.  All detectors are at one of these two heights.
c
c Detector faces are 50 cm from the source which is at the
   ↪ origin.
c
*TR20 -46.35919 18.73033 10       68 -22 90  3J  90 90 0
*TR21 -46.35919 18.73033 -10      68 -22 90  3J  90 90 0
*TR22 -37.15724 33.45653 10       48 -42 90 3J 90 90 0
*TR23 -37.15724 33.45653 -10       48 -42 90 3J 90 90 0
*TR24 -23.47358 44.14738 10       28 -62 90 3J 90 90 0
*TR25 -23.47358 44.14738 -10      28 -62 90 3J 90 90 0
*TR26 -6.958655 49.5134 10        8  -82 90 3J 90 90 0
*TR27 -6.958655 49.5134 -10       8 -82 90 3J 90 90 0
*TR28 10.3956 48.90738 10          -12  -102 90 3J 90 90 0
*TR29 10.3956 48.90738 -10        -12 -102 90 3J 90 90 0
*TR30 26.496 42.4024 10           -32  -122 90 3J 90 90 0
*TR31 26.496 42.4024 -10          -32   -122 90 3J 90 90 0
*TR32 39.4005 30.78307 10         -52  -142 90 3J 90 90 0
*TR33 39.4005 30.78307 -10        -52  -142 90 3J 90 90 0
*TR34 47.5528 15.45085 10         -72 -162 90 3J 90 90 0
*TR35 47.5528 15.45085 -10        -72 -162 90 3J 90 90 0
*TR36 -46.35919 -18.73033 10      112 22 90  3J  90 90 0
*TR37 -46.35919 -18.73033 -10     112 22 90  3J  90 90 0
*TR38 -37.15724 -33.45653 10     132 42 90  3J  90 90 0
*TR39 -37.15724 -33.45653 -10    132 42 90  3J  90 90 0
*TR40 -23.47358 -44.14738 10     152 62 90  3J  90 90 0
*TR41 -23.47358 -44.14738 -10   152 62 90  3J  90 90 0
*TR42 -6.958655 -49.5134 10       172 82 90  3J  90 90 0
*TR43 -6.958655 -49.5134 -10    172 82 90  3J  90 90 0
*TR44 10.3956 -48.90738 10       192 102 90  3J  90 90 0
*TR45 10.3956 -48.90738 -10     192 102 90  3J  90 90 0
*TR46 26.496 -42.4024 10       212   122 90  3J  90 90 0
*TR47 26.496 -42.4024 -10       212 122 90  3J  90 90 0
*TR48 39.4005 -30.78307 10      232 142 90  3J  90 90 0
*TR49 39.4005 -30.78307 -10     232 142 90  3J  90 90 0
```

```
*TR50 47.5528 -15.4508 10      252 162 90  3J  90 90 0
*TR51 47.5528 -15.4508 -10     252 162 90  3J  90 90 0
c ~~~~~~~~~~~~~~ END TRANSLATIONS ~~~~~~~~~~~~~~~~~~~~
c
c ~~~~~~~~~~~~~~ General MCNP Stuff ~~~~~~~~~~~~~~~~~~
c
c The detectors are arranged for the source to be at the origin
c in all three axis.  If you move the source location and want
   ↪ the
c detectors evenly spaced around the source, you'll have to redo
   ↪  the
c translations to accommodate that.
c
SDEF
c
PRINT 10 40 100 110 126 128 140 160 117
c void
nps 10000000
c CTME 10.0 $ Stop time in minutes for debugging
c ~~~~~~~~~~~~~~~ PHYSICS ~~~~~~~~~~~~~~~
PHYS:N J 20
PHYS:P 0 1 1
CUT:P 2J 0
c ~~~~~~~~~~~~~~~~~~~~~~~~~~~~~~~~~~~~~~
c
c ~~~~~~~~~~~~~~~ MATERIALS ~~~~~~~~~~~~~~~
c m1     nlib=60c                                  $ Air, rho=.00093
c       6000                -0.000124
c       7014                -0.755268
c       8016                -0.231781
c       18000.42c           -.012827
m2      nlib=60c                                  $ EJ309 Liquid
        1001                .5556
        6000                .4444
m5      13027.60c 1                               $ al  2.7
m6        5011   -0.040064          nlib = 60c     $ pyrex
          8016   -0.539562          nlib = 60c
         11023   -0.028191          nlib = 60c
         13027   -0.011644          nlib = 60c
         14000   -0.377220          nlib = 60c
         19000   -0.003321          nlib = 60c
m7       28000.50c 0.8                            $ mu-metal
         42000.60c     0.05
         14000.60c     0.005
         29063       0.0002          nlib = 60c
         26056       0.1448          nlib = 70c
m21      11023.60c      0.5                         $ NaI detector,
   ↪ rho=3.67
```

```
        53127.60c      0.5
m9      1001.60c    -0.03       $concrete
        8016.60c    -0.63
        14028.60c    -0.24
        20040.60c    -0.1
m10     1001.60c      -0.048382   $ PVC
        6000.60c    -0.384361
        17000.60c    -0.567257
c BK7
m11     NLIB=70c PLIB=04p
       14028  -0.323138999
       8016   -0.483882614
       5011   -0.033384805
       56138  -0.027496631
       11023  -0.077153875
       19039  -0.052216449
       33075  -0.002726626
c
c  ~~~~~~~~~~~~~~~~~~~~~~~~~~~~~~~~~~~
c
c  ~~~~~~~~~~~~~~~ TALLIES ~~~~~~~~~~~~~~~
c  ~~~~~~~~~~~~~~~~~~~~~~~~~~~~~~~~~~~
c  ~~~~~~~~~~~~~~~ POLIMI ~~~~~~~~~~~~~~~
c Detector cells are tagged for tallies.  Each row as written
c below reflects a different group of 8 detectors, so we have
   ↪ the
c 3x2s, NaIs, then the 16 3x3s.
c
F8:n  223
IPOL 1 0 1 0 J 1 32 3 14 25 36 47 58 69 80
     93 101 109 117 125 133 141 149
     157 168 179 190 201 212 223 234
     245 256 267 278 289 300 311 322
c
RPOL 0.001 0.001
c  ~~~~~~~~~~~~~~~~~~~~~~~~~~~~~~~~~~~
FILES 21 DUMN1
  DBCN 1010123
PRDMP 2J 1
c END OF FILE
```

Appendix 3. ^{252}Cf(sf) Neutron-Photon Competition Experiment at LANL

A partial MCNPX – PoliMi model is included. A single detector specification is kept to keep the length of the appendix reasonable. The original input was 10,870 lines.

```
c cells
c ~~~~~~~~~~~~~~~~~~~~~~~~~~~~~~~~~~
c
c   Cf ionization chamber
c ~~~~~~~~~~~~~~~~~~~~~~~~~~~~~~~~~~
c
  80 08 -8.00       -5  4  $can cylinder
c  81 08 -8.00       -4  6 -7      $can front face
  82 08 -8.00       -4  -9 10      $back of FC
  83 06 -9.15E-4    -4 -10      $inside back cylinder
  84 06 -9.15E-4    -4  3 9    $front air space
  85 08 -8.00       -3  2 9      $hemi shell
  86 0              -2  1 8      $electrode gap
  87 08 -8.00       -1 8           $button
  88 0              -2  -8 9      $space behind button
c
 99 0             -22 23 -21            $CCC for source
c
c detector frame
c
c ring L1
c 270  6 -9.15E-4  410 -409 412 -411 -413
c 271  1 -2.699    406 -405 408 -407 -413 (-410:409:-412:411:
   ↪ 413)
c ring L2
c 272  6 -9.15E-4  420 -419 422 -421 -423
c 273  1 -2.699    416 -415 418 -417 -423 (-420:419:-422:421:
   ↪ 423)
c ring L3
c 274  6 -9.15E-4  430 -429 432 -431 -433
c 275  1 -2.699    426 -425 428 -427 -433 (-430:429:-432:431:
   ↪ 433)
c ring R1
```

```
c 276  6 -9.15E-4  410 -409 412 -411  414
c 277  1 -2.699    406 -405 408 -407  414
   ↪ (-410:409:-412:411:-414)
c ring R2
c 278  6 -9.15E-4  440 -439 442 -441  444
c 279  1 -2.699    436 -435 438 -437  444
   ↪ (-440:439:-442:441:-444)
c ring R3
c 280  6 -9.15E-4  450 -449 452 -451  454
c 281  1 -2.699    446 -445 448 -447  454
   ↪ (-450:449:-452:451:-454)
c
c support brackets
c
282  1 -2.699  -455
283  1 -2.699  -456
284  1 -2.699  -457
285  1 -2.699  -458
286  1 -2.699  -459
287  1 -2.699  -460
288  1 -2.699  -461
289  1 -2.699  -462
c
c legs
c
294  6 -9.15E-4 -465
295  1 -2.699    465 -466
296  1 -2.699    466 -468
297  1 -2.699    466 -467
298  1 -2.699   -469
299  1 -2.699   -470
c
300  6 -9.15E-4 -471
301  1 -2.699    471 -472
302  1 -2.699    472 -474
303  1 -2.699    472 -473
304  1 -2.699   -475
305  1 -2.699   -476
c
306  6 -9.15E-4 -477
307  1 -2.699    477 -478
308  1 -2.699    478 -480
309  1 -2.699    478 -479
310  1 -2.699   -481
311  1 -2.699   -482
c
312  6 -9.15E-4 -483
313  1 -2.699    483 -484
```

```
314   1  -2.699     484  -486
315   1  -2.699     484  -485
316   1  -2.699    -487
317   1  -2.699    -488
c ------
318   6  -9.15E-4  -489
319   1  -2.699     489  -490
320   1  -2.699     490  -492
321   1  -2.699     490  -491
322   1  -2.699    -493
323   1  -2.699    -494
c
324   6  -9.15E-4  -495
325   1  -2.699     495  -496
326   1  -2.699     496  -498
327   1  -2.699     496  -497
328   1  -2.699    -499
329   1  -2.699    -500
c
330   6  -9.15E-4  -501
331   1  -2.699     501  -502
332   1  -2.699     502  -504
333   1  -2.699     502  -503
334   1  -2.699    -505
335   1  -2.699    -506
c
336   6  -9.15E-4  -507
337   1  -2.699     507  -508
338   1  -2.699     508  -510
339   1  -2.699     508  -509
340   1  -2.699    -511
341   1  -2.699    -512
c
c air space
491  06  -9.15E-4   7999   -8000
   ↪ $detector space
                  (1195) 1295 1395 1495 1595 1695 1795 1895 (1995)
                  (2095) 2195 2295 2395 2495 2595 2695 2795 (2895)
                   2995       3095 3195 3295 3395 3495 3595 3695
                      ↪ 3795
                  (3895) 3995 4095 4195 4295 4395 4495 4595 (4695)
                  (4795) 4895 4995 5095 5195 5295 5395 5495 (5595)
                         5695 5795 5895 5995 6095 6195 6295 6395
                            ↪ 6495
c                          (405:-406:407:-408: 413)
   ↪                             $ring L1
c                          (415:-416:417:-418: 423)
   ↪                             $ring L2
```

```
c                          (425:-426:427:-428: 433)
   ↪                             $ring L3
c                          (405:-406:407:-408:-414)
   ↪                             $ring R1
c                          (435:-436:437:-438:-444)
   ↪                             $ring R2
c                          (445:-446:447:-448:-454)
   ↪                             $ring R3
                          455  456 457  458  459  460  461 462
                             ↪              $support brackets
                          466  467 468  469  470
                             ↪                          $legs
                          472  473 474  475  476
                          478  479 480  481  482
                          484  485 486  487  488
                          490  491 492  493  494
                          496  497 498  499  500
                          502  503 504  505  506
                          508  509 510  511  512
                          5
c
c det#1 (liquid)
c
1101 23  -2.23    1107  1115 -1102 -1116   $PMT front window
1102 0           -1115 -1116 -1102         $concave vacuum
1103 0            1116 -1117 -1102         $front section vacuum
1104 0            1117 -1108  1118 -1102   $outside focusing
   ↪ cone
1105 26  -8.96    1117 -1108 -1118  1119   $focusing cone
1106 0            1117 -1108 -1119         $inside focusing cone
1107 23  -2.23    1107 -1108 -1101  1102   $PMT front section
   ↪ wall
1108 23  -2.23    1108 -1109 -1101  1104
1109 0            1108 -1110 -1104  1120   $PMT mid section
   ↪ vacuum
1110 26  -8.96    1108 -1113 -1120  1121   $mid section tube
1111 26  -1.394   1108 -1113 -1121         $dynode space
1112 23  -2.23    1109 -1110 -1103  1104   $PMT mid section wall
1113 23  -2.23    1110 -1111 -1103  1106
1114 0            1110 -1113 -1106  1120   $PMT tail section
   ↪ vacuum
1117 23  -2.23    1111 -1113 -1105  1106   $PMT tail section
   ↪ wall
1118 24  -1.303   1113 -1114 -1105         $PMT tail solid
   ↪ section
c
1130 25 -8.74    -1130  1131  1107 -1109   $mu metal
1131 25 -8.74    -1134  1135  1109 -1136
```

```
1132 25 -8.74     -1132  1133  1136 -1114
1133 06 -9.15E-4 -1131  1101  1107 -1109
1134 06 -9.15E-4 -1135  1103  1109 -1111
1135 06 -9.15E-4 -1135  1105  1111 -1136
1136 06 -9.15E-4 -1133  1105  1136 -1114
c
1140 01 -2.699     1114 -1142 -1137  1138    $base cylinder
1141 06 -9.15E-4  1114 -1139 -1138          $base front well
1142 01 -2.699     1139 -1140 -1138          $base connector
1143 27 -0.35      1140 -1141 -1138          $base interior
1144 01 -2.699     1141 -1142 -1138          $base endplate
c
1145 23 -2.23      1144 -1165 -1143          $pyrex window
1146 01 -2.699     1156 -1146  1150 -1151    $front Al flange
1147 01 -2.699     1186 -1159  1130 -1158    $third collar
c
1148 19 -0.964    (1145 -1146 -1150):(1146 -1144 -1143)      $EJ
   ↪ -309
c
1149 01 -2.699     1146 -1166 -1151  1143    1184
   ↪ $middle Al flange
1150 01 -2.699     1147 -1145 -1150          $front wall
1151 01 -2.699     1147 -1156 -1155  1150    $side wall
1152 01 -2.699     1185 -1169 -1168  1158    $third flange
c
1153 01 -2.699     1151 -1177  1146 -1166    $ears
1154 01 -2.699     1151 -1178  1146 -1166
1155 01 -2.699     1151 -1179  1146 -1166
1156 01 -2.699     1151 -1180  1146 -1166
1157 01 -2.699     1151 -1181  1146 -1166
1158 01 -2.699     1151 -1182  1146 -1166
c
1160 01 -2.699     1151 -1173 -1183  1184  -1195    $transfer tube
1161 19 -0.964    -1184 -1195
c
1162 28 -1.230     1166 -1185  1143 -1169    $gasket 1
1163 28 -1.230     1107 -1186  1130 -1158    $gasket 2
1164 01 -2.699     1187 -1107  1130 -1143
c
1165 01 -2.699     1114 -1160 -1161  1137    $inner collar
1167 01 -2.699     1163 -1114 -1161  1132    $front collar plate
1168 01 -2.699     1143  1185 -1158 -1107    $light guide section
   ↪ wall
1169 06 -9.15E-4  1165 -1107 -1143  1167    $light guide space
                (-1130:-1187)
1170 22 -1.18      1165 -1107 -1167          $light guide
c
c 1171 01 -2.699     1173 -1170  1176 -1175    $exp chamber wall
```

```
c 1172 01 -2.699     1171 -1170 -1176          $top lid
c 1173 06 -9.15E-4   1174 -1171 -1176          $air bubble
c 1174 19 -0.964     1172 -1174 -1176          $liquid
c 1175 01 -2.699     1173 -1172 -1176  1184    $bot lid
c
1176 01 -2.699    -1188  1169                  $mount bracket up
   ↪ face
1177 01 -2.699    -1189                        $mount bracket bot
   ↪ face
c
1180 06 -9.15E-4 -1195 2095 $ -418                $air space with
   ↪  src and det
                (-1147: 1155: 1156)
                (-1156: 1151: 1166)
                (-1166: 1169: 1168)
                (-1168: 1158: 1159)
                (-1159: 1130: 1109)
                (-1109: 1134: 1136)
                (-1136: 1132: 1163)
                (-1163: 1161: 1160)
                (-1160: 1132: 1142)
c               (-1173: 1170: 1175)          $expansion chamber
                ( 1177:-1146: 1166)
                ( 1178:-1146: 1166)
                ( 1179:-1146: 1166)
                ( 1180:-1146: 1166)
                ( 1181:-1146: 1166)
                ( 1182:-1146: 1166)
                  1183                      $transfer tube
                ( 1188:-1169) 1189           $mount bracket
c
c Cell cards for detectors #2 through 54 (liquid) were removed
   ↪ for printing purposes only. Double space left in their
   ↪ place.
c



c
9998 18 -2.25     -7999 -8000
9999 0 8000

c surfaces
c
c ~~~~~~~~~~~~~~~~~~~~~~~~~~~~~~~~~
c
c   Cf fission chamber
c ~~~~~~~~~~~~~~~~~~~~~~~~~~~~~~~~~
  1 01 so 0.9271    $button surface 0.365"
 11 01 so 0.9273    $button surface++ PoliMi sources fail when
```

```
    ↪ sampled on a boundary...
  2 01 so 1.0541    $inner hemi 0.415"
  3 01 so 1.1786    $outer hemi 0.464"
c
  4 01 rcc 0 0 1.181   0 0 -6.4678   1.1811
  5 01 rcc 0 0 1.211   0 0 -6.574   1.27
c
  8 01 pz 0.4801   $back of button
  9 01 pz  0        $front wall of chamber
  10 01 pz  -0.076    $back wall of chamber
c CCC surfaces:
  21 01 cz 0.5000    $1-cm diam deposit
  22 01 pz 1.040
  23 01 pz 0.770
c detector frame rings
c L1,R1:
405      cx  112.8395
406      cx  107.7595
407      px  -12.70
408      px  -17.78
409      cx  112.522
410      cx  108.077
411      px  -13.0175
412      px  -17.4625
413      py  -22.93
414      py   22.93
c L2:
415   02 cx  112.8395
416   02 cx  107.7595
417   02 px  -12.70
418   02 px  -17.78
419   02 cx  112.522
420   02 cx  108.077
421   02 px  -13.0175
422   02 px  -17.4625
423   02 py  -22.93
424   02 py   22.93
c L3:
425   03 cx  112.8395
426   03 cx  107.7595
427   03 px  -12.70
428   03 px  -17.78
429   03 cx  112.522
430   03 cx  108.077
431   03 px  -13.0175
432   03 px  -17.4625
433   03 py  -22.93
434   03 py   22.93
```

```
c R2:
435  04 cx  112.8395
436  04 cx  107.7595
437  04 px  -12.70
438  04 px  -17.78
439  04 cx  112.522
440  04 cx  108.077
441  04 px  -13.0175
442  04 px  -17.4625
443  04 py  -22.93
444  04 py   22.93
c R3:
445  05 cx  112.8395
446  05 cx  107.7595
447  05 px  -12.70
448  05 px  -17.78
449  05 cx  112.522
450  05 cx  108.077
451  05 px  -13.0175
452  05 px  -17.4625
453  05 py  -22.93
454  05 py   22.93
c
c frame supports
c
455  06 box  -24.5     0.0    41.0
              49       0       0
               0       3.810   0
               0       0       1.164
c
456  06 box  -24.5     0.0   -41.0
              49       0       0
               0       3.810   0
               0       0      -1.164
457  07 box  -24.5     0.0    41.0
              49       0       0
               0      -3.810   0
               0       0       1.164
c
458  07 box  -24.5     0.0   -41.0
              49       0       0
               0      -3.810   0
               0       0      -1.164
c
459  08 box  -24.5     0.0    41.0
              49       0       0
               0       3.810   0
               0       0       1.164
```

```
c
460   08 box   -24.5      0.0   -41.0
                49         0        0
                 0         3.810    0
                 0         0       -1.164
c
461   09 box   -24.5      0.0    41.0
                49         0        0
                 0        -3.810    0
                 0         0        1.164
c
462   09 box   -24.5      0.0   -41.0
                49         0        0
                 0        -3.810    0
                 0         0       -1.164
c
c detector frame legs
c
465     rcc  -97.155   -30.4767 105.5782 79.375 0 0 2.2225
466     rcc  -97.155   -30.4767 105.5782 79.375 0 0 2.54
467     rcc  -97.155   -30.4767 105.5782 0.9525 0 0 5.7150
468     box  -18.7325  -35.2392 102.7207 0.9525 0 0 0 9.525 0 0 0
   ↪ 5.715
469     box  -98.4250  -39.3667  99.2282 1.2700 0 0 0 17.78 0 0 0
   ↪ 12.700
470     box  -104.50  -44.4467  99.2282 1.2700 0 0 0 27.94 0 0 0
   ↪ 12.700
c
471     rcc  -97.155    30.4767 105.5782 79.375 0 0 2.2225
472     rcc  -97.155    30.4767 105.5782 79.375 0 0 2.54
473     rcc  -97.155    30.4767 105.5782 0.9525 0 0 5.7150
474     box  -18.7325   35.2392 102.7207 0.9525 0 0 0 -9.525 0 0 0
   ↪ 5.715
475     box  -98.4250   39.3667  99.2282 1.2700 0 0 0 -17.78 0 0 0
   ↪ 12.700
476     box  -104.50   44.4467  99.2282 1.2700 0 0 0 -27.94 0 0 0
   ↪ 12.700
c
477     rcc  -97.155   -30.4767 -105.5782 79.375 0 0 2.2225
478     rcc  -97.155   -30.4767 -105.5782 79.375 0 0 2.54
479     rcc  -97.155   -30.4767 -105.5782 0.9525 0 0 5.7150
480     box  -18.7325  -35.2392 -102.7207 0.9525 0 0 0 9.525 0 0 0
   ↪ -5.715
481     box  -98.4250  -39.3667  -99.2282 1.2700 0 0 0 17.78 0 0 0
   ↪ -12.700
482     box  -104.50  -44.4467  -99.2282 1.2700 0 0 0 27.94 0 0 0
   ↪ -12.700
c
```

```
483     rcc  -97.155    30.4767  -105.5782 79.375 0 0 2.2225
484     rcc  -97.155    30.4767  -105.5782 79.375 0 0 2.54
485     rcc  -97.155    30.4767  -105.5782 0.9525 0 0 5.7150
486     box  -18.7325   35.2392  -102.7207 0.9525 0 0 0 -9.525 0 0 0
   ↪    -5.715
487     box  -98.4250   39.3667   -99.2282 1.2700 0 0 0 -17.78 0 0 0
   ↪    -12.700
488     box  -104.50   44.4467   -99.2282 1.2700 0 0 0 -27.94 0 0 0
   ↪  -12.700
c ---------
489     rcc   -97.155   -101.9035   42.2098 79.375 0 0 2.2225
490     rcc   -97.155   -101.9035   42.2098 79.375 0 0 2.54
491     rcc   -97.155   -101.9035   42.2098 0.9525 0 0 5.7150
492     box   -18.7325  -106.6660   39.3523 0.9525 0 0 0 9.525 0 0 0
   ↪   5.715
493     box   -98.4250  -110.7935   35.8598 1.2700 0 0 0 17.78 0 0 0
   ↪   12.700
494     box  -104.50   -115.8735   35.8598 1.2700 0 0 0 27.94 0 0 0
   ↪  12.700
c
495     rcc   -97.155    101.9035   42.2098 79.375 0 0 2.2225
496     rcc   -97.155    101.9035   42.2098 79.375 0 0 2.54
497     rcc   -97.155    101.9035   42.2098 0.9525 0 0 5.7150
498     box   -18.7325   106.6660   39.3523 0.9525 0 0 0 -9.525 0 0
   ↪  0  5.715
499     box   -98.4250   110.7935   35.8598 1.2700 0 0 0 -17.78 0 0
   ↪  0  12.700
500     box  -104.50    115.8735   35.8598 1.2700 0 0 0 -27.94 0 0 0
   ↪   12.700
c
501     rcc   -97.155   -101.9035  -42.2098 79.375 0 0 2.2225
502     rcc   -97.155   -101.9035  -42.2098 79.375 0 0 2.54
503     rcc   -97.155   -101.9035  -42.2098 0.9525 0 0 5.7150
504     box   -18.7325  -106.6660  -39.3523 0.9525 0 0 0 9.525 0 0 0
   ↪    -5.715
505     box   -98.4250  -110.7935  -35.8598 1.2700 0 0 0 17.78 0 0 0
   ↪   -12.700
506     box  -104.50   -115.8735  -35.8598 1.2700 0 0 0 27.94 0 0 0
   ↪  -12.700
c
507     rcc   -97.155    101.9035  -42.2098 79.375 0 0 2.2225
508     rcc   -97.155    101.9035  -42.2098 79.375 0 0 2.54
509     rcc   -97.155    101.9035  -42.2098 0.9525 0 0 5.7150
510     box   -18.7325   106.6660  -39.3523 0.9525 0 0 0 -9.525 0 0
   ↪  0   -5.715
511     box   -98.4250   110.7935  -35.8598 1.2700 0 0 0 -17.78 0 0
   ↪  0  -12.700
512     box  -104.50    115.8735  -35.8598 1.2700 0 0 0 -27.94 0 0 0
```

```
   ↪  -12.700
c
c
c  detector #01 (liquid scint)
c
1101 21 cz   6.65   $PMT front section od
1102 21 cz   6.35   $PMT front section id
1103 21 cz   3.84   $PMT middle section od
1104 21 cz   3.54   $PMT middle section id
1105 21 cz   2.72   $PMT end section od
1106 21 cz   2.42   $PMT end section id
c    s
1107 21 pz   0      $PMT front face
1108 21 pz   13.8
1109 21 pz   14.0   $end front section
1110 21 pz   17.9
1111 21 pz   18.1   $end mid section
1113 21 pz   22.8   $end glass tail section
1114 21 pz   25.9   $end bakelite tail
1115 21 sz   12.8 12.32 $spherical photocathode surface
1116 21 pz   2.05
c
1117 21 pz   7.5
1118 21 SQ 1 1 -0.1759 4J 0 0 21.9021
1119 21 SQ 1 1 -0.1759 4J 0 0 21.7021
c
1120 21 cz   2.32
1121 21 cz   2.22
1128 21 pz   13.8
c
1130 21 cz 7.10     $front mu-metal
1131 21 cz 7.02
1132 21 cz 3.85     $tail mu-meta
1133 21 cz 3.77
1134 21 SQ 1 1 -0.3368 4J 0 0 26.2338
1135 21 SQ 1 1 -0.3368 4J 0 0 26.0838
1136 21 pz 19.6
c
1137 21 cz 3.850    $base outer wall
1138 21 cz 3.557
1139 21 pz 26.5
1140 21 pz 27.135
1141 21 pz 35.265
1142 21 pz 35.9     $base end plate
c
1143 21 cz  7.925   $quartz window
1144 21 pz -3.635   $begin quartz window
1145 21 pz -9.0325 $begin liquid
```

```
1146 21 pz -3.9525 $2-in depth
1147 21 pz -9.2357 $begin front wall            $front face of
   ↪ detector
c
1150 21 cz 8.890   $Al can id
1151 21 cz 10.16   $Al flange od
1155 21 cz 9.0424  $Al can od
c
1156 21 pz -4.9525 $front flange begin
1158 21 cz 8.25    $third collar od
1159 21 pz 1.27    $third collar end
c
1160 21 pz 26.8525 $inner collar start
1161 21 cz 5.3975  $inner collar diam
c
1163 21 pz 25.265  $front plate start
c
1165 21 pz -3.00   $back of quartz window
1166 21 pz -2.6825 $back of big flange
1167 21 SQ 1 1 -0.89934 4J 0 0 5.3567          $light guide
   ↪ cone
1168 21 pz -2.0475 $back of third flange
1169 21 cz 9.345   $radius of third flange
c
1170 21 px  18.5928 $top of exp chamber
1171 21 px  17.9578 $inner top
1172 21 px  12.8628 $inner bot
1173 21 px  11.5928 $bot of exp chamber
1174 21 px  15.4    $liquid level
1175 21 c/x 0 -3.3175  2.54    $od
1176 21 c/x 0 -3.3175  2.2225  $id
c
1177 21 c/z  8.7988   5.08 1.00  $mounting tabs
1178 21 c/z  8.7988  -5.08 1.00
1179 21 c/z  0       10.16 1.40
1180 21 c/z  0      -10.16 1.40
1181 21 c/z -8.7988   5.08 1.40
1182 21 c/z -8.7988  -5.08 1.40
c
1183 21 rcc  10.0 0 -3.3175 1.5928 0 0 0.4763 $transfer tube
1184 21 rcc  8.25 0 -3.3175 4.6128 0 0 0.3175
c
1185 21 pz -2.5325  $end of gasket 1
1186 21 pz  0.1500  $end of gasket 2
1187 21 pz -0.6350
c
1188 21 box -12.700 -6.8326 -2.6825  6.350 0 0  0 13.6652 0  0 0
   ↪   0.6350
```

```
1189 21 box -12.700 -6.8326 -2.0475  0.635 0 0  0 13.6652 0  0 0
   ↪   5.715
c
1195 21 box -12.700 -12.000 -9.2357  23.0 0 0  0 24.00 0  0 0
   ↪ 45.1457
c
c  Surface cards for detectors #02 through 54 (liquid scint)
   ↪ were removed for printing. Double space left in their
   ↪ place.
c


c
7999 px -104.50 $ top floor
8000 rcc -154.50 0 0 310 0 0 250 $detector space boundary

c        dx         dy         dz        xx'  yx'  zx' xy' yy' zy'
   ↪ xz' yz' zz'
*TR01    -0.300          0          0.9271         $ Cf ionization
   ↪ chamber
c
*TR02    -0.01      0          0        33   57   90   J   J  90
   ↪ J   J   0   $det frame L2
*TR03    -0.01      0          0        66   24   90   J   J  90
   ↪ J   J   0   $det frame L3
*TR04    -0.01      0          0        33  123   90   J   J  90
   ↪ J   J   0   $det frame R2
*TR05    -0.01      0          0        66  156   90   J   J  90
   ↪ J   J   0   $det frame R3
*TR06     14.29  -102.00       0       5.5  84.5 90   J   J  90
   ↪ J   J   0
*TR07     14.29   102.00       0       5.5  95.5 90   J   J  90
   ↪ J   J   0
*TR08     67.6    -77.5        0      38.5  51.5 90   J   J  90
   ↪ J   J   0
*TR09     67.6     77.5        0      38.5 128.5 90   J   J  90
   ↪ J   J   0
c
*TR10     -7.1124    0          0        45   135   90  45  45  90
   ↪ 90  90   0
*TR11     -8.0104    0          0        45   135   90  45  45  90
   ↪ 90  90   0
*TR12     -7.1124    0          0        45    45   90 135  45  90
   ↪ 90  90   0
*TR13     -8.0104    0          0        45    45   90 135  45  90
   ↪ 90  90   0
c
*TR21      0   -52.1679   -90.3573    0   90   90    J   J  60    J
```

```
    ↪ J 150     $detectors
*TR22     0   −72.7865   −72.7865    0   90   90     J    J  45     J    J
    ↪  135
*TR23     0   −88.0191   −50.8179    0   90   90     J    J  30     J    J
    ↪  120
*TR24     0   −97.3998   −26.0982    0   90   90     J    J  15     J    J
    ↪  105
*TR25     0  −100.3357          0    0   90   90     J    J   0     J    J
    ↪   90
*TR26     0   −97.3032    26.0723    0   90   90     J    J  15     J    J
    ↪   75
*TR27     0   −88.6253    51.1679    0   90   90     J    J  30     J    J
    ↪   60
*TR28     0   −73.7058    73.7058    0   90   90     J    J  45     J    J
    ↪   45
*TR29     0   −52.6995    92.2431    0   90   90     J    J  60     J    J
    ↪   30
c
*TR30    28.6305   −44.0871   −91.0502   33   57   90     J    J  60
    ↪ J    J 150
*TR31    39.8349   −61.3404   −73.1401   33   57   90     J    J  45
    ↪ J    J 135
*TR32    48.1273   −74.1096   −51.0179   33   57   90     J    J  30
    ↪ J    J 120
*TR33    53.5738   −82.4964   −26.3570   33   57   90     J    J  15
    ↪ J    J 105
*TR34    55.3547   −85.2389          0   33   57   90     J    J   0
    ↪ J    J  90
*TR35    53.7316   −82.7395    26.4347   33   57   90     J    J  15
    ↪ J    J  75
*TR36    48.5518   −74.7632    51.4679   33   57   90     J    J  30
    ↪ J    J  60
*TR37    40.2971   −62.0521    73.9886   33   57   90     J    J  45
    ↪ J    J  45
*TR38    28.9028   −44.5065    91.9162   33   57   90     J    J  60
    ↪ J    J  30
c
*TR39    48.6626   −21.6660   −92.2626   66   24   90     J    J  60
    ↪ J    J 150
*TR40    67.5919   −30.0939   −73.9886   66   24   90     J    J  45
    ↪ J    J 135
*TR41    82.7829   −36.8573   −52.3179   66   24   90     J    J  30
    ↪ J    J 120
*TR42    92.3324   −41.1090   −27.0817   66   24   90     J    J  15
    ↪ J    J 105
*TR43    95.5895   −42.5592          0   66   24   90     J    J   0
    ↪ J    J  90
*TR44    92.3324   −41.1090    27.0817   66   24   90     J    J  15
```

```
    ↪ J    J   75
*TR45    84.2070   −37.4913    53.2179   66   24   90     J    J   30
    ↪ J    J   60
*TR46    69.2069   −30.8129    75.7564   66   24   90     J    J   45
    ↪ J    J   45
*TR47    49.3934   −21.9914    93.6483   66   24   90     J    J   60
    ↪ J    J   30
c
*TR48     0    51.8179   −89.7511    0   90   90     J    J 120     J    J
    ↪  150
*TR49     0    72.5037   −72.5037    0   90   90     J    J 135     J    J
    ↪  135
*TR50     0    87.1531   −50.3179    0   90   90     J    J 150     J    J
    ↪  120
*TR51     0    96.9168   −25.9688    0   90   90     J    J 165     J    J
    ↪  105
*TR52     0    99.6357          0    0   90   90     J    J 180     J    J
    ↪   90
*TR53     0    97.1100    26.0206    0   90   90     J    J 165     J    J
    ↪   75
*TR54     0    88.4521    51.0679    0   90   90     J    J 150     J    J
    ↪   60
*TR55     0    73.1401    73.1401    0   90   90     J    J 135     J    J
    ↪   45
*TR56     0    53.1179    92.0028    0   90   90     J    J 120     J    J
    ↪   30
c
*TR57    28.4943    43.8775   −90.6172   33 123   90     J    J 120
    ↪ J    J 150
*TR58    39.7194    61.1625   −72.9280   33 123   90     J    J 135
    ↪ J    J 135
*TR59    47.9858    73.8917   −50.8679   33 123   90     J    J 150
    ↪ J    J 120
*TR60    53.1530    81.8484   −26.1500   33 123   90     J    J 165
    ↪ J    J 105
*TR61    54.9190    84.5680          0   33 123   90     J    J 180
    ↪ J    J   90
*TR62    53.7316    82.7395    26.4347   33 123   90     J    J 165
    ↪ J    J   75
*TR63    48.5046    74.6906    51.4179   33 123   90     J    J 150
    ↪ J    J   60
*TR64    40.1045    61.7556    73.6351   33 123   90     J    J 135
    ↪ J    J   45
*TR65    28.9300    44.5484    92.0028   33 123   90     J    J 120
    ↪ J    J   30
c
*TR66    49.8959    22.2151   −94.6009   66 156   90     J    J 120
    ↪ J    J 150
```

```
*TR67    70.5634    31.4169   -77.2413   66 156   90     J    J 135
   ↪ J    J 135
*TR68    86.4222   38.4776   -54.6179   66 156   90     J    J 150     J
   ↪      J 120
*TR69    96.3915   42.9162   -28.2723   66 156   90     J    J 165     J
   ↪      J 105
*TR70    99.7918   44.4302     0.0000   66 156   90     J    J 180     J
   ↪      J  90
*TR71    96.3915   42.9162    28.2723   66 156   90     J    J 165     J
   ↪      J  75
*TR72    86.4222   38.4776    54.6179   66 156   90     J    J 150     J
   ↪      J  60
*TR73    70.5634   31.4169    77.2413   66 156   90     J    J 135     J
   ↪      J  45
*TR74    49.8959   22.2151    94.6009   66 156   90     J    J 120     J
   ↪      J  30
c
c --- material cards ---
c
c Aluminum 6061
c
m1    12024 -0.00935
      12025 -0.00123
      12026 -0.00141
      13027 -0.98001
      14028 -0.00735
      14029 -0.00039
      14030 -0.00026
      NLIB=70c
c
c Ti+Al+Pu dens=7.51E-3  cell volume
c
m2    13027 -0.49140
      22046 -0.03269
      22047 -0.03012
      22048 -0.30484
      22049 -0.02284
      22050 -0.02231
      94239 -0.09580
      NLIB=70c
c
c Pt+Al dens=0.3913  end foils
c
m3    13027.70c -0.0365
      78000     -0.9635
c
c Pt+Al dens=0.1045   inner foils
c
```

```
m4    13027.70c -0.0702
      78000     -0.9298
c
c nylon dens=0.712 (threaded rod)
c
m5    1001 -0.097976
      6000 -0.636856
      7014 -0.123779
      8016 -0.141389
      NLIB=70c
c
c air dens= 9.293E-4 @ 20C 6980ft
c air from PNNL-15870Rev1
c
m6    6000  -0.000124
      7014  -0.755268
      8016  -0.231781
      18040 -0.012827
      NLIB=70c
c
c  anodized Al + Teflon posts dens=2.213
c
m7    12024 -0.00436
      12025 -0.00057
      12026 -0.00066
      13027 -0.46474
      14028 -0.00343
      14029 -0.00018
      14030 -0.00012
      1001  -0.00027
      8016  -0.00876
      6000  -0.12406
      9019  -0.39285
      NLIB=70c
c
c 304L stainless steel dens=8.000 from PNNL-15870Rev1
c
m8     6000  -0.000150
      14028  -0.005000
      15031  -0.000230
      16032  -0.000150
      24050  -0.007931  $-0.190000
      24052  -0.159028
      24053  -0.018381
      24054  -0.004661
      25055  -0.010000
      26054  -0.039210  $-0.694480
      26056  -0.638234
```

```
      26057   -0.015001
      26058   -0.002035
      28058   -0.067198   $-0.100000
      28060   -0.026776
      28061   -0.001183
      28062   -0.003834
      28064   -0.001009
      NLIB=70c
c
c brass + teflon
c
m9    6000   -0.0266
      9019   -0.0843
      29063  -0.4089
      29065  -0.1880
      30000  -0.2922
      NLIB=70c
c
c kapton dens=1.42
c
m10   1001   -0.026362
      6000   -0.691133
      7014   -0.073270
      8016   -0.209235
      NLIB=70c
c
c buta-N dens=1.24
c
m11   1001  -0.0841
      6000  -0.7850
      9019  -0.1309
      NLIB=70c
c
c wires: RG-316
c
m12   6000    -0.1015
      9019    -0.3214
      29063   -0.3992
      29065   -0.1779
      NLIB=70c
c
c G10 no Cu dens=1.895
c
m14   1001   -0.03160
      5010   -0.00200
      5011   -0.00893
      6000   -0.31630
      8016   -0.34723
```

```
      12024 -0.01017
      12025 -0.00134
      12026 -0.00154
      13027 -0.03915
      14028 -0.12150
      14029 -0.00639
      14030 -0.00436
      17035 -0.03322
      17037 -0.01124
      20040 -0.06352
      20044 -0.00151
      NLIB=70c
c
c PE CH2 dens=0.91
c
m15   1001 -0.1429
      6000 -0.8571
      NLIB=70c
c
c low carbon steel
c
m16   6000  -0.00200
      25055 -0.00900
      26054 -0.05610
      26056 -0.90864
      26057 -0.02137
      26058 -0.00289
      NLIB=70c
c
c RG-223 dens=2.40
c
m17   1001  0.0254
      6000  0.1719
      17035 0.0911
      17037 0.0308
      29063 0.4664
      29065 0.2144
      NLIB=70c
c
c   concrete LANL MCNP mix dens=2.25
c
m18   01001 -0.00453
      08016 -0.5126
      14028 -0.36036
      13027 -0.03555
      11023 -0.01527
      20040 -0.05791
      26056 -0.01378
```

```
      NLIB=70c
c
c EJ-309 liquid dens= -0.964 g/cm^3
m19     nlib=60c                                  $ EJ309 Liquid
       1001                .5556
       6000                .4444
c
c  6Li-silicate glass 96% detailed spec  dens = 2.5
c
m20   3006   -0.073954
      3007   -0.003594
      8016   -0.507151
      12024  -0.018803
      12025  -0.002480
      12026  -0.002839
      13027  -0.095265
      14028  -0.240492
      14029  -0.012647
      14030  -0.008624
      58140  -0.030290
      58142  -0.003861
      NLIB=70c
c
c  7Li-silicate glass 96% detailed spec  dens = 2.5
c
m21   3006   -0.000007
      3007   -0.077541
      8016   -0.507151
      12024  -0.018803
      12025  -0.002480
      12026  -0.002839
      13027  -0.095265
      14028  -0.240492
      14029  -0.012647
      14030  -0.008624
      58140  -0.030290
      58142  -0.003861
      NLIB=70c
c
c lucite dens = 1.19
c
m22   1001   -0.080538
      6000   -0.599848
      8016   -0.319614
      NLIB=70c
c
c  borosilicate glass   dens = 2.23
c
```

```
m23   5010   −0.00738
      5011   −0.03268
      13027  −0.01164
      11023  −0.02819
      08016  −0.53957
      14028  −0.37722
      19039  −0.00310
      19041  −0.00022
      NLIB=70c
c
c   PVC dens=1.303
c
m24   6000   −0.3844
      1001   −0.0484
      17035  −0.4298
      17037  −0.1374
      NLIB=70c
c
c mu metal dens=8.74
c
m25   28058  −0.52478
      28060  −0.20184
      28062  −0.02772
      28061  −0.00851
      28064  −0.00690
      26056  −0.14680
      26054  −0.00931
      26057  −0.00350
      26058  −0.00050
      29063  −0.03462
      29065  −0.01541
      24052  −0.01681
      24053  −0.00190
      24050  −0.00090
      24054  −0.00050
      NLIB=70c
c
c Copper
c
m26   29063  −0.6850
      29065  −0.3150
      NLIB=70c
c
c Cu–C foam (simulate base electronics)
c
m27   6000   −0.5000
      29063  −0.3425
      29065  −0.1575
```

```
      NLIB=70c
c
c Neoprene dens=1.23
c
m28   1001   -0.056920
      6000   -0.542646
      17035  -0.303432
      17037  -0.097002
      NLIB=70c
c
c brass dens=8.7
c
m29   29063  -0.4599
      29065  -0.2114
      30000  -0.3287
      NLIB=70c
c  ~~~~~~~~~~~~~~~~~~~~~~~~~~~~~~~~~~
c Physics
c  ~~~~~~~~~~~~~~~~~~~~~~~~~~~~~~~~~~
  MODE n p
  PHYS:N J 20
  PHYS:P 0 1 1
  CUT:P 30 J 0
  CUT:N 30
  IMP:N 1 3246R 0
  IMP:P 1 3246R 0
c  ~~~~~~~~~~~~~~~~~~~~~~~~~~~~~~~~~~
c Source
c  ~~~~~~~~~~~~~~~~~~~~~~~~~~~~~~~~~~
  sdef sur=11
       ccc=99
       dir=d1
       vec=1 0 0
  si1 -1 1
  sp1 0 1
  IPOL 1 1 2 1 J 2 45 1148 1248 1348 1448 1548 1648 1748 1848
     ↪ 1948
                      2048 2148 2248 2348 2448 2548 2648 2748 2848
                      2948 3048 3148 3248 3348 3448 3548 3648 3748
                      3848 3948 4048 4148 4248 4348 4448 4548 4648
                      4748 4848 4948 5048 5148 5248 5348 5448 5548
c                      5648 5748 5848 5948 6048 6148 6248 6348
   ↪ 6448
  RPOL 0.001 0.001
  NPS 1e7
  FILES 21 DUMN1
  DBCN 19034044545681
  PRDMP 2J 1
```

Appendix 4. Measured and Simulated ^{240}Pu(sf) Prompt Neutron-Photon Competition Experiment at LANL

The full `MCNPX – PoliMi` model is included.

```
MJM FNMC
c *** CELLS ***
   ↪ ------------------------------------------------------------------------
   ↪
c
   ↪ ------------------------------------------------------------------------
   ↪
810   2   -1.205E-3 -1 101              IMP:N,P=1                $
   ↪ innermost cavity
811   8   -8.00       1 -2              IMP:N,P=1                $
   ↪ innermost can
812   2   -1.205E-3   2 -3              IMP:N,P=1                $
   ↪ second can interior
813   8   -8.00       3 -4              IMP:N,P=1                $
   ↪ second can
814   2   -1.205e-3   4 -5              IMP:N,P=1                $
   ↪ third can interior
815   8   -8.00       5 -6              IMP:N,P=1                $
   ↪ third can
816   2   -1.205e-3   6 -7              IMP:N,P=1                $
   ↪ fourth can interior
817   8   -8.00       7 -8              IMP:N,P=1                $
   ↪ fourth can
818   5   -2.6989     -9                IMP:N,P=1                $
   ↪ stage plate
819   21  -16.5    -101 -1           IMP:N,P=1                $ PuO2 (
   ↪ sort of)
c  ~~~~~~~~~~~~~~~~~~~~~~~~~~~~~~~~~~~~~~~~~~~~~~~~~~~~~~~~~~~~~~~~~~~~~~~~
c
c     STILBENE Detectors
c  ~~~~~~~~~~~~~~~~~~~~~~~~~~~~~~~~~~~~~~~~~~~~~~~~~~~~~~~~~~~~~~~~~~~~~~~~
c
c    Det #01
```

```
10   13  -1.160   -15                    TRCL=1   IMP:N,P=1
   ↪                    $ Stilbene
11    5  -2.6989  -12    13              TRCL=1   IMP:N,P=1
   ↪                    $ Aluminum case
12   19  -1.05    (-10    11):(11 -17 18):(-19 20 -21)
                                          TRCL=1   IMP:N,P=1
                                             ↪                  $ Plastic
                                             ↪ case
13   15  -2.32    -14                    TRCL=1   IMP:N,P=1
   ↪                    $ fused silica window
14   11  -2.25     14    16   -13    15 TRCL=1   IMP:N,P=1
   ↪                    $ PTFE
15   16  -0.021   -16   -13              TRCL=1   IMP:N,P=1
   ↪                    $ open cell foam
16   17  -2.23   -22 23                  TRCL=1   IMP:N,P=1
   ↪                    $ PMT Glass
17    0          -23                    TRCL=1   IMP:N,P=1
   ↪                    $ Inside PMT
18   10  -8.747   22 -24                 TRCL=1   IMP:N,P=1
   ↪                    $ Mu-metal
19   18  -1.19   -25                    TRCL=1   IMP:N,P=1
   ↪                    $ Bakelite base
20    0           (-11:-18) 12 24 25 TRCL=1   IMP:N,P=1
   ↪                    $ Void around PMT
c  ~~~~~~~~~~~~~~~~~~~~~~~~~~~~~~~~~~~~~~~~~~~~~~~~~~~~~~~~~~~~~~~~~~~~~~~~
c
c    Det #02
30   LIKE 10 BUT TRCL=2
31   LIKE 11 BUT TRCL=2
32   LIKE 12 BUT TRCL=2
33   LIKE 13 BUT TRCL=2
34   LIKE 14 BUT TRCL=2
35   LIKE 15 BUT TRCL=2
36   LIKE 16 BUT TRCL=2
37   LIKE 17 BUT TRCL=2
38   LIKE 18 BUT TRCL=2
39   LIKE 19 BUT TRCL=2
40   LIKE 20 BUT TRCL=2
c    Det #03
50   LIKE 10 BUT TRCL=3
51   LIKE 11 BUT TRCL=3
52   LIKE 12 BUT TRCL=3
53   LIKE 13 BUT TRCL=3
54   LIKE 14 BUT TRCL=3
55   LIKE 15 BUT TRCL=3
56   LIKE 16 BUT TRCL=3
57   LIKE 17 BUT TRCL=3
58   LIKE 18 BUT TRCL=3
59   LIKE 19 BUT TRCL=3
```

```
60   LIKE 20 BUT TRCL=3
c    Det #04
70   LIKE 10 BUT TRCL=4
71   LIKE 11 BUT TRCL=4
72   LIKE 12 BUT TRCL=4
73   LIKE 13 BUT TRCL=4
74   LIKE 14 BUT TRCL=4
75   LIKE 15 BUT TRCL=4
76   LIKE 16 BUT TRCL=4
77   LIKE 17 BUT TRCL=4
78   LIKE 18 BUT TRCL=4
79   LIKE 19 BUT TRCL=4
80   LIKE 20 BUT TRCL=4
c    Det #05
90   LIKE 10 BUT TRCL=5
91   LIKE 11 BUT TRCL=5
92   LIKE 12 BUT TRCL=5
93   LIKE 13 BUT TRCL=5
94   LIKE 14 BUT TRCL=5
95   LIKE 15 BUT TRCL=5
96   LIKE 16 BUT TRCL=5
97   LIKE 17 BUT TRCL=5
98   LIKE 18 BUT TRCL=5
99   LIKE 19 BUT TRCL=5
100   LIKE 20 BUT TRCL=5
c    Det #06
110   LIKE 10 BUT TRCL=6
111   LIKE 11 BUT TRCL=6
112   LIKE 12 BUT TRCL=6
113   LIKE 13 BUT TRCL=6
114   LIKE 14 BUT TRCL=6
115   LIKE 15 BUT TRCL=6
116   LIKE 16 BUT TRCL=6
117   LIKE 17 BUT TRCL=6
118   LIKE 18 BUT TRCL=6
119   LIKE 19 BUT TRCL=6
120   LIKE 20 BUT TRCL=6
c    Det #07
130   LIKE 10 BUT TRCL=7
131   LIKE 11 BUT TRCL=7
132   LIKE 12 BUT TRCL=7
133   LIKE 13 BUT TRCL=7
134   LIKE 14 BUT TRCL=7
135   LIKE 15 BUT TRCL=7
136   LIKE 16 BUT TRCL=7
137   LIKE 17 BUT TRCL=7
138   LIKE 18 BUT TRCL=7
139   LIKE 19 BUT TRCL=7
```

```
140   LIKE 20 BUT TRCL=7
c     Det #08
150   LIKE 10 BUT TRCL=8
151   LIKE 11 BUT TRCL=8
152   LIKE 12 BUT TRCL=8
153   LIKE 13 BUT TRCL=8
154   LIKE 14 BUT TRCL=8
155   LIKE 15 BUT TRCL=8
156   LIKE 16 BUT TRCL=8
157   LIKE 17 BUT TRCL=8
158   LIKE 18 BUT TRCL=8
159   LIKE 19 BUT TRCL=8
160   LIKE 20 BUT TRCL=8
c     Det #09
170   LIKE 10 BUT TRCL=9
171   LIKE 11 BUT TRCL=9
172   LIKE 12 BUT TRCL=9
173   LIKE 13 BUT TRCL=9
174   LIKE 14 BUT TRCL=9
175   LIKE 15 BUT TRCL=9
176   LIKE 16 BUT TRCL=9
177   LIKE 17 BUT TRCL=9
178   LIKE 18 BUT TRCL=9
179   LIKE 19 BUT TRCL=9
180   LIKE 20 BUT TRCL=9
c     Det #10
190   LIKE 10 BUT TRCL=10
191   LIKE 11 BUT TRCL=10
192   LIKE 12 BUT TRCL=10
193   LIKE 13 BUT TRCL=10
194   LIKE 14 BUT TRCL=10
195   LIKE 15 BUT TRCL=10
196   LIKE 16 BUT TRCL=10
197   LIKE 17 BUT TRCL=10
198   LIKE 18 BUT TRCL=10
199   LIKE 19 BUT TRCL=10
200   LIKE 20 BUT TRCL=10
c     Det #11
210   LIKE 10 BUT TRCL=11
211   LIKE 11 BUT TRCL=11
212   LIKE 12 BUT TRCL=11
213   LIKE 13 BUT TRCL=11
214   LIKE 14 BUT TRCL=11
215   LIKE 15 BUT TRCL=11
216   LIKE 16 BUT TRCL=11
217   LIKE 17 BUT TRCL=11
218   LIKE 18 BUT TRCL=11
219   LIKE 19 BUT TRCL=11
```

```
220   LIKE 20 BUT TRCL=11
c     Det #12
230   LIKE 10 BUT TRCL=12
231   LIKE 11 BUT TRCL=12
232   LIKE 12 BUT TRCL=12
233   LIKE 13 BUT TRCL=12
234   LIKE 14 BUT TRCL=12
235   LIKE 15 BUT TRCL=12
236   LIKE 16 BUT TRCL=12
237   LIKE 17 BUT TRCL=12
238   LIKE 18 BUT TRCL=12
239   LIKE 19 BUT TRCL=12
240   LIKE 20 BUT TRCL=12
c     Det #13
250   LIKE 10 BUT TRCL=13
251   LIKE 11 BUT TRCL=13
252   LIKE 12 BUT TRCL=13
253   LIKE 13 BUT TRCL=13
254   LIKE 14 BUT TRCL=13
255   LIKE 15 BUT TRCL=13
256   LIKE 16 BUT TRCL=13
257   LIKE 17 BUT TRCL=13
258   LIKE 18 BUT TRCL=13
259   LIKE 19 BUT TRCL=13
260   LIKE 20 BUT TRCL=13
c     Det #14
270   LIKE 10 BUT TRCL=14
271   LIKE 11 BUT TRCL=14
272   LIKE 12 BUT TRCL=14
273   LIKE 13 BUT TRCL=14
274   LIKE 14 BUT TRCL=14
275   LIKE 15 BUT TRCL=14
276   LIKE 16 BUT TRCL=14
277   LIKE 17 BUT TRCL=14
278   LIKE 18 BUT TRCL=14
279   LIKE 19 BUT TRCL=14
280   LIKE 20 BUT TRCL=14
c     Det #15
290   LIKE 10 BUT TRCL=15
291   LIKE 11 BUT TRCL=15
292   LIKE 12 BUT TRCL=15
293   LIKE 13 BUT TRCL=15
294   LIKE 14 BUT TRCL=15
295   LIKE 15 BUT TRCL=15
296   LIKE 16 BUT TRCL=15
297   LIKE 17 BUT TRCL=15
298   LIKE 18 BUT TRCL=15
299   LIKE 19 BUT TRCL=15
```

```
300   LIKE 20 BUT TRCL=15
c     Det #16
310   LIKE 10 BUT TRCL=16
311   LIKE 11 BUT TRCL=16
312   LIKE 12 BUT TRCL=16
313   LIKE 13 BUT TRCL=16
314   LIKE 14 BUT TRCL=16
315   LIKE 15 BUT TRCL=16
316   LIKE 16 BUT TRCL=16
317   LIKE 17 BUT TRCL=16
318   LIKE 18 BUT TRCL=16
319   LIKE 19 BUT TRCL=16
320   LIKE 20 BUT TRCL=16
c     Det #17
330   LIKE 10 BUT TRCL=17
331   LIKE 11 BUT TRCL=17
332   LIKE 12 BUT TRCL=17
333   LIKE 13 BUT TRCL=17
334   LIKE 14 BUT TRCL=17
335   LIKE 15 BUT TRCL=17
336   LIKE 16 BUT TRCL=17
337   LIKE 17 BUT TRCL=17
338   LIKE 18 BUT TRCL=17
339   LIKE 19 BUT TRCL=17
340   LIKE 20 BUT TRCL=17
c     Det #18
350   LIKE 10 BUT TRCL=18
351   LIKE 11 BUT TRCL=18
352   LIKE 12 BUT TRCL=18
353   LIKE 13 BUT TRCL=18
354   LIKE 14 BUT TRCL=18
355   LIKE 15 BUT TRCL=18
356   LIKE 16 BUT TRCL=18
357   LIKE 17 BUT TRCL=18
358   LIKE 18 BUT TRCL=18
359   LIKE 19 BUT TRCL=18
360   LIKE 20 BUT TRCL=18
c     Det #19
370   LIKE 10 BUT TRCL=19
371   LIKE 11 BUT TRCL=19
372   LIKE 12 BUT TRCL=19
373   LIKE 13 BUT TRCL=19
374   LIKE 14 BUT TRCL=19
375   LIKE 15 BUT TRCL=19
376   LIKE 16 BUT TRCL=19
377   LIKE 17 BUT TRCL=19
378   LIKE 18 BUT TRCL=19
379   LIKE 19 BUT TRCL=19
```

```
380   LIKE 20 BUT TRCL=19
c     Det #20
390   LIKE 10 BUT TRCL=20
391   LIKE 11 BUT TRCL=20
392   LIKE 12 BUT TRCL=20
393   LIKE 13 BUT TRCL=20
394   LIKE 14 BUT TRCL=20
395   LIKE 15 BUT TRCL=20
396   LIKE 16 BUT TRCL=20
397   LIKE 17 BUT TRCL=20
398   LIKE 18 BUT TRCL=20
399   LIKE 19 BUT TRCL=20
400   LIKE 20 BUT TRCL=20
c     Det #21
410   LIKE 10 BUT TRCL=21
411   LIKE 11 BUT TRCL=21
412   LIKE 12 BUT TRCL=21
413   LIKE 13 BUT TRCL=21
414   LIKE 14 BUT TRCL=21
415   LIKE 15 BUT TRCL=21
416   LIKE 16 BUT TRCL=21
417   LIKE 17 BUT TRCL=21
418   LIKE 18 BUT TRCL=21
419   LIKE 19 BUT TRCL=21
420   LIKE 20 BUT TRCL=21
c     Det #22
430   LIKE 10 BUT TRCL=22
431   LIKE 11 BUT TRCL=22
432   LIKE 12 BUT TRCL=22
433   LIKE 13 BUT TRCL=22
434   LIKE 14 BUT TRCL=22
435   LIKE 15 BUT TRCL=22
436   LIKE 16 BUT TRCL=22
437   LIKE 17 BUT TRCL=22
438   LIKE 18 BUT TRCL=22
439   LIKE 19 BUT TRCL=22
440   LIKE 20 BUT TRCL=22
c     Det #23
450   LIKE 10 BUT TRCL=23
451   LIKE 11 BUT TRCL=23
452   LIKE 12 BUT TRCL=23
453   LIKE 13 BUT TRCL=23
454   LIKE 14 BUT TRCL=23
455   LIKE 15 BUT TRCL=23
456   LIKE 16 BUT TRCL=23
457   LIKE 17 BUT TRCL=23
458   LIKE 18 BUT TRCL=23
459   LIKE 19 BUT TRCL=23
```

```
460  LIKE 20 BUT TRCL=23
c    Det #24
470  LIKE 10 BUT TRCL=24
471  LIKE 11 BUT TRCL=24
472  LIKE 12 BUT TRCL=24
473  LIKE 13 BUT TRCL=24
474  LIKE 14 BUT TRCL=24
475  LIKE 15 BUT TRCL=24
476  LIKE 16 BUT TRCL=24
477  LIKE 17 BUT TRCL=24
478  LIKE 18 BUT TRCL=24
479  LIKE 19 BUT TRCL=24
480  LIKE 20 BUT TRCL=24
c  ~~~~~~~~~~~~~~~~~~~~~~~~~~~~~~~~~~~~~~~~~~~~~~~~~~~~~~~~~~~~~~~~~~~
c     Aluminum plates
c  ~~~~~~~~~~~~~~~~~~~~~~~~~~~~~~~~~~~~~~~~~~~~~~~~~~~~~~~~~~~~~~~~~~~
500 5 -2.6989 -130  131 132 133 TRCL=30      IMP:N,P=1
501 LIKE 500 BUT TRCL=31
c 502 LIKE 500 BUT TRCL=32
502 5 -2.6989 -134 135 136 137   IMP:N,P=1
c 503 LIKE 500 BUT TRCL=33
503 5 -2.6989 -138 135 136 137   IMP:N,P=1
504 LIKE 500 BUT TRCL=34
505 LIKE 500 BUT TRCL=35
c 506 LIKE 500 BUT TRCL=36
506 5 -2.6989 -143 144 145 146   IMP:N,P=1
c 507 LIKE 500 BUT TRCL=37
507 5 -2.6989 -147 144 145 146   IMP:N,P=1
508 LIKE 500 BUT TRCL=38
509 LIKE 500 BUT TRCL=39
c 510 LIKE 500 BUT TRCL=40
510 5 -2.6989 -148 149 150 151   IMP:N,P=1
c 511 LIKE 500 BUT TRCL=41
511 5 -2.6989 -152 149 150 151   IMP:N,P=1
512 LIKE 500 BUT TRCL=42
513 LIKE 500 BUT TRCL=43
c 514 LIKE 500 BUT TRCL=44
514 5 -2.6989 -153 154 155 156   IMP:N,P=1
c 515 LIKE 500 BUT TRCL=45
515 5 -2.6989 -157 154 155 156   IMP:N,P=1
c  1" box tube frame
520 5 -2.6989 (-50 54 -40 41 42 43):(51 -55 -40 41 42 43):
        (-40 44 -50 51 42 43):(41 -45 -50 51 42 43)
        TRCL=46 IMP:N,P=1
521 LIKE 520 BUT TRCL=47
522 LIKE 520 BUT TRCL=48
523 LIKE 520 BUT TRCL=49
524 LIKE 520 BUT TRCL=50
```

```
525 LIKE 520 BUT TRCL=51
526 LIKE 520 BUT TRCL=52
527 LIKE 520 BUT TRCL=53
530 5 -2.6989 (52 -56 -40 41 42 43):(-53 57 -40 41 42 43):
        (-40 44 52 -53 42 43):(41 -45 52 -53 42 43)
        TRCL=46 IMP:N,P=1
531 LIKE 530 BUT TRCL=47
532 LIKE 530 BUT TRCL=48
533 LIKE 530 BUT TRCL=49
534 LIKE 530 BUT TRCL=50
535 LIKE 530 BUT TRCL=51
536 LIKE 530 BUT TRCL=52
537 LIKE 530 BUT TRCL=53
c  ~~~~~~~~~~~~~~~~~~~~~~~~~~~~~~~~~~~~~~~~~~~~~~~~~~~~~~~~~~~~~~~~~~~~~~~
c     Table
c  ~~~~~~~~~~~~~~~~~~~~~~~~~~~~~~~~~~~~~~~~~~~~~~~~~~~~~~~~~~~~~~~~~~~~~~~
700   5 -2.6989   -60   61                    IMP:N,P=1
701  20 -8.65     -60 -61 62                 IMP:N,P=1
702   8 -8.00     -60 -62                    IMP:N,P=1
c  ~~~~~~~~~~~~~~~~~~~~~~~~~~~~~~~~~~~~~~~~~~~~~~~~~~~~~~~~~~~~~~~~~~~~~~~
c
c     Floor
c  ~~~~~~~~~~~~~~~~~~~~~~~~~~~~~~~~~~~~~~~~~~~~~~~~~~~~~~~~~~~~~~~~~~~~~~~
800    6   -2.3         -600 -70   IMP:N,P=1          $Floor
c     Environment
c  ~~~~~~~~~~~~~~~~~~~~~~~~~~~~~~~~~~~~~~~~~~~~~~~~~~~~~~~~~~~~~~~~~~~~~~~
600    2   -1.205E-3   -600 601 -602
             #10 #11 #12 #13 #14 #15 #16 #17 #18 #19 #20
             #30 #31 #32 #33 #34 #35 #36 #37 #38 #39 #40
             #50 #51 #52 #53 #54 #55 #56 #57 #58 #59 #60
             #70 #71 #72 #73 #74 #75 #76 #77 #78 #79 #80
             #90 #91 #92 #93 #94 #95 #96 #97 #98 #99 #100
             #110 #111 #112 #113 #114 #115 #116 #117 #118 #119
                ↪ #120
             #130 #131 #132 #133 #134 #135 #136 #137 #138 #139
                ↪ #140
             #150 #151 #152 #153 #154 #155 #156 #157 #158 #159
                ↪ #160
             #500 #501 #502 #503 #504 #505 #506 #507 #508 #509
             #510 #511 #512 #513 #514 #515
             8 9
             IMP:N,P=1
601    2   -1.205E-3 -600 -601
             #410 #411 #412 #413 #414 #415 #416 #417 #418 #419
                ↪ #420
             #430 #431 #432 #433 #434 #435 #436 #437 #438 #439
                ↪ #440
             #450 #451 #452 #453 #454 #455 #456 #457 #458 #459
                ↪ #460
```

```
                #470 #471 #472 #473 #474 #475 #476 #477 #478 #479
                    ↪ #480
                #500 #501 #502 #503 #504 #505 #506 #507 #508 #509
                #510 #511 #512 #513 #514 #515
                #530 #531 #532 #533 #534 #535 #536 #537
                60
                70
                IMP:N,P=1
602     2   -1.205E-3  -600   602  -603
                #170 #171 #172 #173 #174 #175 #176 #177 #178 #179
                    ↪ #180
                #190 #191 #192 #193 #194 #195 #196 #197 #198 #199
                    ↪ #200
                #210 #211 #212 #213 #214 #215 #216 #217 #218 #219
                    ↪ #220
                #230 #231 #232 #233 #234 #235 #236 #237 #238 #239
                    ↪ #240
                #250 #251 #252 #253 #254 #255 #256 #257 #258 #259
                    ↪ #260
                #270 #271 #272 #273 #274 #275 #276 #277 #278 #279
                    ↪ #280
                #290 #291 #292 #293 #294 #295 #296 #297 #298 #299
                    ↪ #300
                #310 #311 #312 #313 #314 #315 #316 #317 #318 #319
                    ↪ #320
                #500 #501 #502 #503 #504 #505 #506 #507 #508 #509
                #510 #511 #512 #513 #514 #515
                IMP:N,P=1
603     2   -1.205E-3  -600  603
                #330 #331 #332 #333 #334 #335 #336 #337 #338 #339
                    ↪ #340
                #350 #351 #352 #353 #354 #355 #356 #357 #358 #359
                    ↪ #360
                #370 #371 #372 #373 #374 #375 #376 #377 #378 #379
                    ↪ #380
                #390 #391 #392 #393 #394 #395 #396 #397 #398 #399
                    ↪ #400
                #500 #501 #502 #503 #504 #505 #506 #507 #508 #509
                #510 #511 #512 #513 #514 #515
                #520 #521 #522 #523 #524 #525 #526 #527
                IMP:N,P=1
c  ~~~~~~~~~~~~~~~~~~~~~~~~~~~~~~~~~~~~~~~~~~~~~~~~~~~~~~~~~~~~~~~~~~~~~~~~
c      Graveyard
c  ~~~~~~~~~~~~~~~~~~~~~~~~~~~~~~~~~~~~~~~~~~~~~~~~~~~~~~~~~~~~~~~~~~~~~~~~
999     0                   600                IMP:N,P=0
c
    ↪ ------------------------------------------------------------------------
    ↪
```

```
c *** END CELLS ***
   ↪ ------------------------------------------------------------------------

c *** SURFACES ***
   ↪ ------------------------------------------------------------------------
   ↪
c
   ↪ ------------------------------------------------------------------------
   ↪
c  ~~~~~~~~~~~~~~~~~~~~~~~~~~~~~~~~~~~~~~~~~~~~~~~~~~~~~~~~~~~~~~~~~~~~~~~~~~~
c
c     Source encasement
c  ~~~~~~~~~~~~~~~~~~~~~~~~~~~~~~~~~~~~~~~~~~~~~~~~~~~~~~~~~~~~~~~~~~~~~~~~~~~
c
  1    RCC 0 0  0        0 0 0.5976   1.0203        $ innermost
     ↪ cavity
  2    RCC 0 0 -0.1992   0 0 0.9549   1.3346        $ first can
     ↪ exterior
  3    RCC 0 0 -0.1992   0 0 1.2656   1.3946        $ second can
     ↪ interior
  4    RCC 0 0 -0.3632   0 0 1.5936   1.5538        $ second can
     ↪ exterior
  5    RCC 0 0 -0.3632   0 0 2.3117   2.58          $ third can
     ↪ interior
  6    RCC 0 0 -0.4337   0 0 2.4701   2.6892        $ third can
     ↪ exterior
  7    RCC 0 0 -0.4337   0 0 2.9433   2.7466        $ fourth/outer
     ↪ can interior
  8    RCC 0 0 -0.5039   0 0 3.1075   2.8287        $ fourth/outer
     ↪ can exterior
  9    BOX -5.08 -5.08 -0.5039  10.16 0 0  0 10.16 0  0 0 -0.3175
  101  PZ  0.127  $ can fill height
c  ~~~~~~~~~~~~~~~~~~~~~~~~~~~~~~~~~~~~~~~~~~~~~~~~~~~~~~~~~~~~~~~~~~~~~~~~~~~
c
c     STILBENE Detectors
c  ~~~~~~~~~~~~~~~~~~~~~~~~~~~~~~~~~~~~~~~~~~~~~~~~~~~~~~~~~~~~~~~~~~~~~~~~~~~
c
10     RCC  0 0 0      19.05 0 0     3.175     $ plastic case outer,
   ↪   guess 1mm thick
11     RCC  0.05 0 0   19.2 0 0      3.075     $ plastic case inner
12     RCC  0.05 0 0    6.35 0 0     2.9464    $ Aluminum case outer
   ↪   0.07" thick
13     RCC  0.2278 0 0 6.1722 0 0    2.7686    $ Aluminum case inner
14     RCC  6.4 0 0    -0.16 0 0     2.7686    $ fused silica window
   ↪   0.063"
15     RCC  6.24 0 0   -5.08 0 0     2.54      $ Stilbene cell
16     PX   1.1092                              $ plane for PTFE
   ↪ assumed front face thickness of 0.02"
17     RCC 19.05 0 0   10.0 0 0      3.575     $ Back plastic case
   ↪ outer
18     RCC 19.25 0 0    9.8 0 0      3.475     $ Back plastic case
   ↪ inner
```

```
19     PZ 3.575                                    $ plastic case flange
   ↪  cutout
20     PZ -3.575                                   $ plastic case flange
   ↪  cutout
21     RCC 29.05 0 0   0.4 0 0     4.575    $ plastic case flange
   ↪  base
22     RCC 6.4 0 0     13.3 0 0    2.575    $ PMT glass outer
   ↪ GUESS
23     RCC 6.6 0 0     12.9 0 0    2.275    $ PMT glass inner
   ↪ GUESS
24     RCC 6.4 0 0     13.3 0 0    2.625    $ Mu-metal
25     RCC 19.7 0 0    1.7 0 0     2.575    $ Bakelite PMT base
   ↪ GUESS
c  ~~~~~~~~~~~~~~~~~~~~~~~~~~~~~~~~~~~~~~~~~~~~~~~~~~~~~~~~~~~~~~~~~~~~~~~
c     Small Aluminum Plates
c  ~~~~~~~~~~~~~~~~~~~~~~~~~~~~~~~~~~~~~~~~~~~~~~~~~~~~~~~~~~~~~~~~~~~~~~~
130     BOX  0 -5.08 -15.24  0.3175 0 0  0 10.16 0  0 0 30.48
131     C/X  0 -7.151 3.18
132     C/X  0 0 3.18
133     C/X  0 7.151 3.18
134   32  BOX  0 -5.08 -15.24  0.3175 0 0  0 10.16 0  0 0 30.48
135   32  C/X  0 -7.151 3.18
136   32  C/X  0 0 3.18
137   32  C/X  0 7.151 3.18
138   33  BOX  0 -5.08 -15.24  0.3175 0 0  0 10.16 0  0 0 30.48
139   34  BOX  0 -5.08 -15.24  0.3175 0 0  0 10.16 0  0 0 30.48
140   34  C/X  0 -7.151 3.18
141   34  C/X  0 0 3.18
142   34  C/X  0 7.151 3.18
143   36  BOX  0 -5.08 -15.24  0.3175 0 0  0 10.16 0  0 0 30.48
144   36  C/X  0 -7.151 3.18
145   36  C/X  0 0 3.18
146   36  C/X  0 7.151 3.18
147   37  BOX  0 -5.08 -15.24  0.3175 0 0  0 10.16 0  0 0 30.48
148   40  BOX  0 -5.08 -15.24  0.3175 0 0  0 10.16 0  0 0 30.48
149   40  C/X  0 -7.151 3.18
150   40  C/X  0 0 3.18
151   40  C/X  0 7.151 3.18
152   41  BOX  0 -5.08 -15.24  0.3175 0 0  0 10.16 0  0 0 30.48
153   44  BOX  0 -5.08 -15.24  0.3175 0 0  0 10.16 0  0 0 30.48
154   44  C/X  0 -7.151 3.18
155   44  C/X  0 0 3.18
156   44  C/X  0 7.151 3.18
157   45  BOX  0 -5.08 -15.24  0.3175 0 0  0 10.16 0  0 0 30.48
c  ~~~~~~~~~~~~~~~~~~~~~~~~~~~~~~~~~~~~~~~~~~~~~~~~~~~~~~~~~~~~~~~~~~~~~~~
c     1" box tubing
c  ~~~~~~~~~~~~~~~~~~~~~~~~~~~~~~~~~~~~~~~~~~~~~~~~~~~~~~~~~~~~~~~~~~~~~~~
40     PX 24.765
```

```
41     PX 22.225
42     P 10.258 -24.765 0 0
43     P 10.258 24.765 0 0
44     PX 24.4475
45     PX 22.5425
50     PZ 15.24
51     PZ 12.70
52     PZ -15.24
53     PZ -12.70
54     PZ 14.9225
55     PZ 13.0175
56     PZ -14.9225
57     PZ -13.0175
c  ~~~~~~~~~~~~~~~~~~~~~~~~~~~~~~~~~~~~~~~~~~~~~~~~~~~~~~~~~~~~~~~~
c     Table
c  ~~~~~~~~~~~~~~~~~~~~~~~~~~~~~~~~~~~~~~~~~~~~~~~~~~~~~~~~~~~~~~~~
60     BOX  -96.265 -44.765  -15.24  153.5 0 0  0 76.5 0  0 0
    ↪ -0.84455
61     PZ  -15.875
62     PZ  -15.9258
c  ~~~~~~~~~~~~~~~~~~~~~~~~~~~~~~~~~~~~~~~~~~~~~~~~~~~~~~~~~~~~~~~~
c     Floor
c  ~~~~~~~~~~~~~~~~~~~~~~~~~~~~~~~~~~~~~~~~~~~~~~~~~~~~~~~~~~~~~~~~
70     PZ   -105.04
    ↪ $Floor Level
c  ~~~~~~~~~~~~~~~~~~~~~~~~~~~~~~~~~~~~~~~~~~~~~~~~~~~~~~~~~~~~~~~~
c     Environment
c  ~~~~~~~~~~~~~~~~~~~~~~~~~~~~~~~~~~~~~~~~~~~~~~~~~~~~~~~~~~~~~~~~
600    RPP  -200 200      -200 200      -200 200
    ↪ $Environment
601    PZ   -3.5755
602    PZ    3.5755
603    PZ   10.7265
c  *** END SURFACES ***
    ↪ ------------------------------------------------------------------

c  *** DATA *** ------------------------------------------------------
c
    ↪ ------------------------------------------------------------------------------
    ↪
c  ~~~~~~~~~~~~~~~~~~~~~~~~~~~~~~~~~~~~~~~~~~~~~~~~~~~~~~~~~~~~~~~~
c     Translations
c  ~~~~~~~~~~~~~~~~~~~~~~~~~~~~~~~~~~~~~~~~~~~~~~~~~~~~~~~~~~~~~~~~
TR1      7.75 0 0
         1 0 0
         0 1 0
         0 0 1
TR2      5.48008 -5.48008 0
```

```
          0.707106781186548   -0.707106781186547
             ↪ 0
          0.707106781186547    0.707106781186548
             ↪ 0
                          0                    0    1.000000000000000
TR3       0  -7.75  0
          0.0000    -1.0000          0
          1.0000     0.0000     0.0000
          0.0000     0.0000     1.0000
TR4       -5.48008  -5.48008  0
          -0.707106781186547   -0.707106781186548
             ↪                    0
           0.707106781186548   -0.707106781186547
              ↪                    0
                          0                    0    1.000000000000000
TR5       -7.75  0  0
          -1.000000000000000   -0.000000000000000
             ↪                    0
           0.000000000000000   -1.000000000000000
              ↪                    0
                          0                    0    1.000000000000000
TR6       -5.48008  5.48008  0
          -0.707106781186548    0.707106781186547
             ↪                    0
          -0.707106781186547   -0.707106781186548
             ↪                    0
                          0                    0    1.000000000000000
TR7       0  7.75  0
          -0.000000000000000    1.000000000000000
             ↪                    0
          -1.000000000000000   -0.000000000000000
             ↪                    0
                          0                    0    1.000000000000000
TR8       5.48008  5.48008  0
          0.707106781186547    0.707106781186548
             ↪ 0
         -0.707106781186548    0.707106781186547
            ↪ 0
                          0                    0    1.000000000000000
TR9       7.75  0  7.151
          1  0  0
          0  1  0
          0  0  1
          1
TR10       5.48008  -5.48008  7.151
          0.707106781186548   -0.707106781186547
             ↪ 0
          0.707106781186547    0.707106781186548
```

```
    ↪ 0
                0                       0     1.000000000000000
    1
TR11    0  −7.75  7.151
    0.0000    −1.0000         0
    1.0000     0.0000    0.0000
    0.0000     0.0000    1.0000
    1
TR12    −5.48008  −5.48008  7.151
    −0.707106781186547   −0.707106781186548
    ↪                       0
    0.707106781186548   −0.707106781186547
    ↪                       0
                0                       0     1.000000000000000
    1
TR13    −7.75  0  7.151
    −1.0000    −0.0000         0
    −0.0000     1.0000    −0.0000
    0.0000    −0.0000    −1.0000
    1
TR14    −5.48008  5.48008  7.151
    −0.707106781186548    0.707106781186547
    ↪                       0
    −0.707106781186547   −0.707106781186548
    ↪                       0
                0                       0     1.000000000000000
    1
TR15    0  7.75  7.151
    −0.000000000000000    1.000000000000000
    ↪                       0
    −1.000000000000000   −0.000000000000000
    ↪                       0
                0                       0     1.000000000000000
    1
TR16    5.48008  5.48008  7.151
    0.707106781186547    0.707106781186548
    ↪ 0
    −0.707106781186548    0.707106781186547
    ↪ 0
                0                       0     1.000000000000000
TR17    4.60  3.89  11.467
    0  0  1
    1  0  0
    0  1  0
TR18    4.60  −3.89  11.467
    0  0  1
    1  0  0
    0  1  0
```

```
TR19      −4.60  −3.89  11.467
          0  0  1
          1  0  0
          0  1  0
TR20      −4.60  3.89  11.467
          0  0  1
          1  0  0
          0  1  0
TR21      0  0  −7.151
TR22      0  −3.175  −7.151
          0.0000    −1.0000          0
          1.0000     0.0000    0.0000
          0.0000     0.0000    1.0000
TR23      0  0  −7.151
          −1.0000    −0.0000          0
          −0.0000     1.0000   −0.0000
          0.0000    −0.0000   −1.0000
TR24      0  3.175  −7.151
          −0.000000000000000   1.000000000000000
             ↪                      0
          −1.000000000000000   −0.000000000000000
             ↪                      0
                       0                      0   1.000000000000000
TR30      18.165  0  0
TR31      15.625  0  0
TR32      15.4517  −15.4517  0
          0.707106781186548   −0.707106781186547
             ↪ 0
          0.707106781186547    0.707106781186548
             ↪ 0
                       0                      0   1.000000000000000
TR33      11.9996  −11.9996  0
          0.707106781186548   −0.707106781186547
             ↪ 0
          0.707106781186547    0.707106781186548
             ↪ 0
                       0                      0   1.000000000000000
TR34      0  −21.85  0
          0.0000    −1.0000          0
          1.0000     0.0000    0.0000
          0.0000     0.0000    1.0000
TR35      0  −16.97  0
          0.0000    −1.0000          0
          1.0000     0.0000    0.0000
          0.0000     0.0000    1.0000
TR36      −15.4517  −15.4517  0
          −0.707106781186547   −0.707106781186548
             ↪                      0
```

```
          0.707106781186548   −0.707106781186547
            ↪                   0
                    0                   0    1.000000000000000
TR37    −11.9996  −11.9996  0
          −0.707106781186547  −0.707106781186548
            ↪                   0
          0.707106781186548   −0.707106781186547
            ↪                   0
                    0                   0    1.000000000000000
TR38    −18.165  0  0
TR39    −15.625  0  0
TR40     −15.4517  15.4517  0
          −0.707106781186548   0.707106781186547
            ↪                   0
          −0.707106781186547  −0.707106781186548
            ↪                   0
                    0                   0    1.000000000000000
TR41      −11.9996  11.9996  0
          −0.707106781186548   0.707106781186547
            ↪                   0
          −0.707106781186547  −0.707106781186548
            ↪                   0
                    0                   0    1.000000000000000
TR42     0  21.85  0
          −0.000000000000000   1.000000000000000
            ↪                   0
          −1.000000000000000  −0.000000000000000
            ↪                   0
                    0                   0    1.000000000000000
TR43      0  16.97  0
          −0.000000000000000   1.000000000000000
            ↪                   0
          −1.000000000000000  −0.000000000000000
            ↪                   0
                    0                   0    1.000000000000000
TR44      15.4517  15.4517  0
         0.707106781186547   0.707106781186548
            ↪ 0
         −0.707106781186548   0.707106781186547
           ↪ 0
                    0                   0    1.000000000000000
TR45      11.9996  11.9996  0
         0.707106781186547   0.707106781186548
            ↪ 0
         −0.707106781186548   0.707106781186547
           ↪ 0
                    0                   0    1.000000000000000
TR46     0.01  0  0
```

```
TR47   0.01  -0.01  0
         0.707106781186548   -0.707106781186547
           ↪ 0
         0.707106781186547    0.707106781186548
           ↪ 0
                  0                    0    1.000000000000000
TR48     0  0.01  0
         0.0000    -1.0000          0
         1.0000     0.0000     0.0000
         0.0000     0.0000     1.0000
TR49     -0.01  -0.01  0
         -0.707106781186547   -0.707106781186548
           ↪                     0
          0.707106781186548   -0.707106781186547
            ↪                    0
                  0                    0    1.000000000000000
TR50     -0.01  0  0
         -1.000000000000000   -0.000000000000000
           ↪                     0
          0.000000000000000   -1.000000000000000
            ↪                    0
                  0                    0    1.000000000000000
TR51     -0.01  0.01  0
         -0.707106781186548    0.707106781186547
           ↪                     0
         -0.707106781186547   -0.707106781186548
           ↪                     0
                  0                    0    1.000000000000000
TR52     0  0.01  0
         -0.000000000000000    1.000000000000000
           ↪                     0
         -1.000000000000000   -0.000000000000000
           ↪                     0
                  0                    0    1.000000000000000
TR53     0.01  0.01  0
         0.707106781186547    0.707106781186548
           ↪ 0
        -0.707106781186548    0.707106781186547
          ↪ 0
                  0                    0    1.000000000000000
c  ~~~~~~~~~~~~~~~~~~~~~~~~~~~~~~~~~~~~~~~~~~~~~~~~~~~~~~~~~~~~
c
c     Physics
c  ~~~~~~~~~~~~~~~~~~~~~~~~~~~~~~~~~~~~~~~~~~~~~~~~~~~~~~~~~~~~
   MODE n P
   PHYS:N  J  20
   PHYS:P  0  1  1
   CUT:P  2J  0
c  ~~~~~~~~~~~~~~~~~~~~~~~~~~~~~~~~~~~~~~~~~~~~~~~~~~~~~~~~~~~~
```

```
c     Source
c ~~~~~~~~~~~~~~~~~~~~~~~~~~~~~~~~~~~~~~~~~~~~~~~~~~~~~~~~~~~~~~~~~~~~~~~
c
c  VOID
  SDEF POS=0 0 0.06359  CEL=819  RAD=D2 EXT=D3 AXS=0 0 1
  SI2 0 1.02
  SI3 0.06359
c SDEF POS=0 0 0.06359
  IPOL 3 1 2 0 J 1 24 10  30  50  70  90 110 130 150
                     170 190 210 230 250 270 290 310
                     330 350 370 390 410 430 450 470
  RPOL 0.0002 0.0002
  NPS 1e6
  FILES 21 DUMN1
  DBCN
  PRDMP 2J 1
c ~~~~~~~~~~~~~~~~~~~~~~~~~~~~~~~~~~~~~~~~~~~~~~~~~~~~~~~~~~~~~~~~~~~~~~~
c
c     Materials
c ~~~~~~~~~~~~~~~~~~~~~~~~~~~~~~~~~~~~~~~~~~~~~~~~~~~~~~~~~~~~~~~~~~~~~~~
c
c  EJ-309 liquid scintillator d=-0.916
c (Eljen Technologies, EJ-309 Fact Sheet)
c ~~~~~~~~~~~~~~~~~~~~~~~~~~~~~~~~~~~~
     m1    nlib=70c   plib=04p
         1001       0.548
         6000       0.452
c ~~~~~~~~~~~~~~~~~~~~~~~~~~~~~~~~~~~~
c
c Air, Dry (near sea level) d=-1.205E-3
c (Mat. Compendium PNNL)
c ~~~~~~~~~~~~~~~~~~~~~~~~~~~~~~~~~~~~
c
  m2  NLIB=70c PLIB=04p
       7014   -0.755636    $ N
       8016   -0.231475    $ O
       18040.60c -0.012838 $ Ar-40 at 99.6035 percent of natural
          ↪ Ar
       18036.60c -0.000043 $ Ar-36 at 0.3336 percent of natural
          ↪ Ar
       18038.60c -0.000008 $ Ar-38 at 0.00629 percent of natural
          ↪ Ar
c ~~~~~~~~~~~~~~~~~~~~~~~~~~~~~~~~~~~~
c
c  Lead Shielding d=-11.34
c
c ~~~~~~~~~~~~~~~~~~~~~~~~~~~~~~~~~~~~
c
  m3  82000.60c 1
c tungsten rho = 19.25
  m31 74000.60c 1
c ~~~~~~~~~~~~~~~~~~~~~~~~~~~~~~~~~~~~
c
c Polyethylene d=-0.9300
c (Mat. Compendium PNNL)
c ~~~~~~~~~~~~~~~~~~~~~~~~~~~~~~~~~~~~
c
```

```
  m4   nlib=70c   plib=04p
       1001  -0.143716
       6000  -0.856284
c  ~~~~~~~~~~~~~~~~~~~~~~~~~~~~~~~~~~
c
c Aluminum table d=-2.70
c  ~~~~~~~~~~~~~~~~~~~~~~~~~~~~~~~~~~
  m5   nlib=60c   plib=04p
      13027      -1
c  ~~~~~~~~~~~~~~~~~~~~~~~~~~~~~~~~~~
c
c Concrete (Mat. Compendium PNNL) d=-2.3
c (Mat. Compendium PNNL)
c  ~~~~~~~~~~~~~~~~~~~~~~~~~~~~~~~~~~
c
  m6   nlib=70c   plib=04p
       1001       -0.022100
       6000       -0.002484
       8016       -0.574930
      11023       -0.015208
      12000       -0.001266
      13027       -0.019953
      14000       -0.304627
      19000       -0.010045
      20000       -0.042951
      26000.42c  -0.006435
c  ~~~~~~~~~~~~~~~~~~~~~~~~~~~~~~~~~~
c
c 304L stainless steel dens=8.000 from PNNL-15870Rev1
c  ~~~~~~~~~~~~~~~~~~~~~~~~~~~~~~~~~~
 m8     6000   -0.000150
       14028   -0.005000
       15031   -0.000230
       16032   -0.000150
       24050   -0.007931   $-0.190000
       24052   -0.159028
       24053   -0.018381
       24054   -0.004661
       25055   -0.010000
       26054   -0.039210   $-0.694480
       26056   -0.638234
       26057   -0.015001
       26058   -0.002035
       28058   -0.067198   $-0.100000
       28060   -0.026776
       28061   -0.001183
       28062   -0.003834
       28064   -0.001009
      NLIB=70c
c  ~~~~~~~~~~~~~~~~~~~~~~~~~~~~~~~~~~
c
c BK7
c  ~~~~~~~~~~~~~~~~~~~~~~~~~~~~~~~~~~
c
```

```
  m9 NLIB=70c PLIB=04p
       14028  -0.323138999
       8016   -0.483882614
       5011   -0.033384805
       56138.60c  -0.027496631
       11023  -0.077153875
       19039  -0.052216449
       33075  -0.002726626
c  ~~~~~~~~~~~~~~~~~~~~~~~~~~~~~~~~~~
c
c mumetal
c  ~~~~~~~~~~~~~~~~~~~~~~~~~~~~~~~~~~
c
   m10 28000.50c 0.8
       42000.60c     0.05
       14000.60c     0.005
       29063      0.0002          nlib = 60c
       26056      0.1448          nlib = 70c
c  ~~~~~~~~~~~~~~~~~~~~~~~~~~~~~~~~~~
c
c PTFE  rho = 2.25 g/cm3
c  ~~~~~~~~~~~~~~~~~~~~~~~~~~~~~~~~~~
c
   m11 6000.70c  0.333339
       9019.70c  0.666661
c  ~~~~~~~~~~~~~~~~~~~~~~~~~~~~~~~~~~
c
c vinyl  rho = 1.19
c  ~~~~~~~~~~~~~~~~~~~~~~~~~~~~~~~~~~
c
   m12  1001.70c  .07
        6000.70c  .559
        8016.60c  .371
c  ~~~~~~~~~~~~~~~~~~~~~~~~~~~~~~~~~~
c
c stilbene  rho = 1.16
c  ~~~~~~~~~~~~~~~~~~~~~~~~~~~~~~~~~~
c
   m13  1001.70c  .4615
        6000.70c  .5385
c  ~~~~~~~~~~~~~~~~~~~~~~~~~~~~~~~~~~
c
c wood  rho = 0.64
c  ~~~~~~~~~~~~~~~~~~~~~~~~~~~~~~~~~~
c
   m14  1001.70c   -0.059642
        6000.60c   -0.497018
        7014.70c   -0.004970
        8016.70c   -0.427435
       12000.60c   -0.001988
       16000.60c   -0.004970
       19000.60c   -0.001988
       20000.60c   -0.001988
c  ~~~~~~~~~~~~~~~~~~~~~~~~~~~~~~~~~~
c
c fused silica (silicon dioxide)  rho = 2.32 g/cm3
c  ~~~~~~~~~~~~~~~~~~~~~~~~~~~~~~~~~~
c
   m15  8016.70c    0.666667
       14000.70c    0.333333
```

```
c  ~~~~~~~~~~~~~~~~~~~~~~~~~~~~~~~~~~~
c Polyurethane Foam  rho = 0.021 g/cm3
c  ~~~~~~~~~~~~~~~~~~~~~~~~~~~~~~~~~~~
c
   m16  1001.70c     0.360023
        6000.70c     0.400878
        7014.70c     0.076459
        8016.70c     0.162639
c  ~~~~~~~~~~~~~~~~~~~~~~~~~~~~~~~~~~~
c
c  PYREX Glass Corning 7740
c  (NIST p = -2.23)
c  ~~~~~~~~~~~~~~~~~~~~~~~~~~~~~~~~~~~
c
  m17  nlib=60c  plib=04p
       5011   -0.040064
       8016   -0.539562
      11023   -0.028191
      13027   -0.011644
      14000   -0.377220
      19000   -0.003321
c  ~~~~~~~~~~~~~~~~~~~~~~~~~~~~~~~~~~~
c
c lucite dens = 1.19
c  ~~~~~~~~~~~~~~~~~~~~~~~~~~~~~~~~~~~
c
   m18  nlib=60c  plib=04p
      1001   -0.080538
      6000   -0.599848
      8016   -0.319614
c  ~~~~~~~~~~~~~~~~~~~~~~~~~~~~~~~~~~~
c
c ABS plastic dens = 1.05
c  ~~~~~~~~~~~~~~~~~~~~~~~~~~~~~~~~~~~
c
   m19  nlib=60c  plib=04p
      1001    0.5151515
      6000    0.4545455
      7014    0.0303030
c  ~~~~~~~~~~~~~~~~~~~~~~~~~~~~~~~~~~~
c
c Cadmium  dens = 8.65 g/cm3
c  ~~~~~~~~~~~~~~~~~~~~~~~~~~~~~~~~~~~
c
   m20  nlib=60c  plib=04p
      48000 1
c  ~~~~~~~~~~~~~~~~~~~~~~~~~~~~~~~~~~~
c
c PuO2  dens = 11.5 g/cm3 or 16.5
c  ~~~~~~~~~~~~~~~~~~~~~~~~~~~~~~~~~~~
c
  m21  nlib=60c plib=04p
      94238     -0.013
      94239     -0.954
      94240   -93.51
      94241     -0.193
      94242     -4.56
      95241     -0.4862
        8016     -0.01
```

```
c        8016     -0.134
c  ~~~~~~~~~~~~~~~~~~~~~~~~~~~~~~~~~~~~~~~~~~~~~~~~~~~~~~~~~~~~~~~~~~~~~~~
c
c     Tallies
c  ~~~~~~~~~~~~~~~~~~~~~~~~~~~~~~~~~~~~~~~~~~~~~~~~~~~~~~~~~~~~~~~~~~~~~~~
c
 FC11  Source case neutron flux tally
 F11:N 8.1 8.2 8.3
 C11 0 1
 E11 0.0 99i 10
 FC21  Source case photon flux tally
 F21:P 8.1 8.2 8.3
 C21 0 1
 E21 0.0 99i 10
 FC31  Stilbene surface neutron flux tally
 F31:N 10015.2 15.1 10015.3
 C31 0 1
 E31 0.0 99i 10
 FC41  Stilbene surface photon flux tally
 F41:P 10015.2 15.1 10015.3
 C41 0 1
 E41 0.0 99i 10
c *** END DATA ***
   ↪ ------------------------------------------------------------------------
c ********** END OF FILE **********
```

References

[1] O. Hahn and F. Strassmann, "Über den Nachweis und das Verhalten der bei der Bestrahlung des Urans mittels Neutronen entstehenden Erdalkalimetalle," *Naturwissenschaften*, vol. 27, no. 1, pp. 11–15, jan 1939. [Online]. Available: http://link.springer.com/10.1007/BF01488241

[2] L. Meitner and O. R. Frisch, "Products of the fission of the uranium nucleus," *Nature*, vol. 143, no. 3620, pp. 471–472, 1939.

[3] A. Einstein, "Letter to President Roosevelt," *URL http//hypertextbook. com/eworld/einstein. shtml*, 1939.

[4] "Comprehensive Nuclear-Test-Ban Treaty," 2008. [Online]. Available: https://www.un.org/disarmament/wmd/nuclear/ctbt/

[5] "Treaty on the Non-Proliferation of Nuclear Weapons - Treaties database home," pp. 1–7, 2016. [Online]. Available: http://disarmament.un.org/treaties/t/npt

[6] "Special Nuclear Material," 2017. [Online]. Available: https://www.nrc.gov/materials/sp-nucmaterials.html

[7] L. S. Waters, G. W. McKinney, J. W. Durkee, M. L. Fensin, J. S. Hendricks, M. R. James, R. C. Johns, and D. B. Pelowitz, "The MCNPX Monte Carlo radiation transport code," *AIP Conf. Proc.*, vol. 896, no. 2007, pp. 81–90, 2007.

[8] S. Pozzi, E. Padovani, and M. Marseguerra, "MCNP-PoliMi: A Monte-Carlo code for correlation measurements," *Nucl. Instrum. Methods Phys. Res., Sect A*, vol. 513, no. 3, 2003.

[9] P. Talou, R. Vogt, J. Randrup, M. E. Rising, J. Verbeke, M. T. Andrews, S. D. Clarke, P. Jaffke, M. Jandel, T. Kawano, M. J. Marcath, K. Meierbachtol, G. Rusev, A. Sood, I. Stetcu, and C. Walker, "Correlated Prompt Fission Data in Transport Simulations," *Eur. J. Phys. (to be published)*, 2017. [Online]. Available: http://arxiv.org/abs/1710.00107

[10] S. Pozzi, E. Larsen, B. Wieger, A. Enqvist, S. Clarke, M. Flaska, M. Marcath, R. Haight, and E. Padovani, "Correlated Neutron Emissions from 252Cf," *Nucl. Sci. Eng.*, vol. 178, no. 2, pp. 250–260, 2014. [Online]. Available: http://www.ans.org/pubs/journals/nse/a{_}36216

[11] P. Talou, T. Kawano, and I. Stetcu, "Monte Carlo Hauser-Feshbach Calculations of Prompt Fission Neutrons and Gamma Rays: Application to Thermal Neutron-Induced Fission Reactions on U-235 and Pu-239," Los Alamos National Laboratory, Los Alamos, NM (United States), Tech. Rep. LA-UR-12-25059, 2012.

[12] R. Vogt and J. Randrup, "Event-by-event study of neutron observables in spontaneous and thermal fission," *Phys. Rev. C*, vol. 87, no. 4, p. 044602, 2013.

[13] R. C. Haight, H. Y. Lee, T. N. Taddeucci, J. M. O'Donnell, B. A. Perdue, N. Fotiades, M. Devlin, J. L. Ullmann, A. Laptev, T. Bredeweg, M. Jandel, R. O. Nelson, S. A. Wender, M. C. White, C. Y. Wu, E. Kwan, A. Chyzh, R. Henderson, and J. Gostic, "The Prompt Fission Neutron Spectrum (PFNS) Measurement Program at LANSCE," *Nucl. Data Sheets*, vol. 119, pp. 205–208, 2014. [Online]. Available: http://www.sciencedirect.com/science/article/pii/S0090375214005912

[14] M. A. Norsworthy, A. Poitrasson-Rivière, M. L. Ruch, S. D. Clarke, and S. A. Pozzi, "Evaluation of neutron light output response functions in EJ-309 organic scintillators," *Nucl. Instrum. Methods Phys. Res., Sect A*, vol. 842, no. October 2016, pp. 20–27, jan 2017. [Online]. Available: http://dx.doi.org/10.1016/j.nima.2016.10.035http://linkinghub.elsevier.com/retrieve/pii/S0168900216310737

[15] N. Zaitseva, A. Glenn, L. Carman, H. Paul Martinez, R. Hatarik, H. Klapper, and S. Payne, "Scintillation properties of solution-grown trans-stilbene single crystals," *Nucl. Instrum. Methods Phys. Res., Sect A*, vol. 789, pp. 8–15, 2015. [Online]. Available: http://dx.doi.org/10.1016/j.nima.2015.03.090

[16] F. D. Brooks, R. W. Pringle, and B. L. Funt, "Pulse Shape Discrimination in a Plastic Scintillator," *IRE Trans. Nucl. Sci.*, vol. 7, no. 2-3, pp. 35–38, jun 1960. [Online]. Available: http://ieeexplore.ieee.org/stamp/stamp.jsp?tp={&}arnumber=4315733{&}tag=1http://ieeexplore.ieee.org/document/4315733/

[17] M. Berger, J. Hubbell, S. Seltzer, J. Chang, J. Coursey, R. Sukumar, D. Zucker, and K. Olsen, "XCOM: Photon Cross Sections Database," 2018. [Online]. Available: https://physics.nist.gov/cgi-bin/Xcom/xcom2

[18] D. Brown, B. Pritychenko, and A. A. Sonzogni, "Evaluated Nuclear Data File (ENDF) Retrieval & Plotting," 2018. [Online]. Available: https://www.nndc.bnl.gov/sigma/

[19] P. Schuster, P. Feng, and E. Brubaker, "On the Relationship Between Scintillation Anisotropy and Crystal Structure in Pure Crystalline Organic Scintillator Materials," *IEEE Trans. Nucl. Sci.*, vol. 65, no. 6, pp. 1292–1306, 2018.

[20] G. F. Knoll, *Radiation Detection and Measurement*, 4th ed. John Wiley & Sons, Hoboken, 2010.

[21] P. Schuster and E. Brubaker, "Investigating the Anisotropic Scintillation Response in Anthracene through Neutron, Gamma-Ray, and Muon Measurements," *IEEE Trans. Nucl. Sci.*, vol. 63, no. 3, pp. 1942–1954, jun 2016. [Online]. Available: http://arxiv.org/abs/1511.00081http://dx.doi.org/10.1109/TNS.2016.2542589http://ieeexplore.ieee.org/document/7465791/

[22] J. K. Polack, M. Flaska, A. Enqvist, C. S. Sosa, C. C. Lawrence, and S. A. Pozzi, "An algorithm for charge-integration, pulse-shape discrimination and estimation of neutron/photon misclassification in organic scintillators," *Nucl. Instrum. Methods Phys. Res., Sect A*, vol. 795, pp. 253–267, sep 2015. [Online]. Available: http://www.sciencedirect.com/science/article/pii/S0168900215006889

[23] L. F. Miller, J. Preston, S. Pozzi, M. Flaska, and J. Neal, "Digital pulse shape discrimination," *Radiat. Prot. Dosimetry*, vol. 126, no. 1-4, pp. 253–255, 2007.

[24] C. Wagemans, *The Nuclear Fission Process.* Boca Raton, Florida: CRC Press, 1991, pp. 498–501.

[25] T. Ichikawa, A. Iwamoto, P. Möller, and A. J. Sierk, "Contrasting fission potential-energy structure of actinides and mercury isotopes," *Phys. Rev. C - Nucl. Phys.*, vol. 86, no. 2, 2012.

[26] W. M. Gibson, T. D. Thomas, and G. L. Miller, "Structure in the Kinetic Energy Spectrum of Fragments from Thermal-Neutron-Induced Fission of U-235," *Phys. Rev. Lett.*, vol. 7, no. 2, pp. 65–66, jul 1961. [Online]. Available: http://arxiv.org/abs/1010.2381https://link.aps.org/doi/10.1103/PhysRevLett.7.65

[27] H. R. Bowman, J. Milton, S. G. Thompson, and W. J. Swiatecki, "Further Studies of the Prompt Neutrons from the Spontaneous Fission of Cf-252," *Phys. Rev.*, vol. 129, no. 5, pp. 2133–2147, 1963.

[28] H. Nifenecker, C. Signarbieux, M. Ribrag, J. Poitou, and J. Matuszek, "Gamma-Neutron Competition in the De-excitation Mechanism of the Fission Fragments of Cf-252," *Nucl. Phys.*, vol. A189, pp. 285–304, 1972.

[29] P. Talou, T. Kawano, and I. Stetcu, "Prompt Fission Neutrons and Gamma Rays in a Monte Carlo Hauser-Feshbach Formalism," *Phys. Procedia*, vol. 47, no. November 2012, pp. 39–46, 2013. [Online]. Available: http://linkinghub.elsevier.com/retrieve/pii/S1875389213004367

[30] J. R. Grover and J. Gilat, "De-Excitation of Highly Excited Nuclei," *Phys. Rev.*, vol. 157, no. 4, pp. 802–813, may 1967. [Online]. Available: https://link.aps.org/doi/10.1103/PhysRev.157.802

[31] O. Litaize and O. Serot, "Investigation of phenomenological models for the Monte Carlo simulation of the prompt fission neutron and γ emission," *Phys. Rev. C - Nucl. Phys.*, vol. 82, no. 5, pp. 1–11, 2010.

[32] C. Budtz-Jorgensen and H. H. Knitter, "Simultaneous investigation of fission fragments and neutrons in 252Cf (SF)," *Nucl. Physics, Sect. A*, 1988.

[33] S. A. E. Johansson, "Gamma de-excitation of fission fragments (I). Prompt Radiation," *Nucl. Phys.*, vol. 60, pp. 378–400, 1964.

[34] ——, "Gamma de-excitation of fission fragments (II). Delayed Radiation," *Nucl. Phys.*, vol. 64, pp. 147–160, 1965.

[35] M. M. Hoffman, "Directional correlation of fission fragments and prompt gamma rays associated with thermal neutron fission," *Phys. Rev.*, vol. 133, no. 3B, 1964.

[36] H. Van Der Ploeg, R. Postma, J. C. Bacelar, T. Van Den Berg, V. Iacob, J. Jongman, and A. Van Der Woude, "Large gamma anisotropy observed in the Cf252 spontaneous-fission process," *Phys. Rev. Lett.*, vol. 68, no. 21, pp. 3145–3147, may 1992. [Online]. Available: https://link.aps.org/doi/10.1103/PhysRevLett.68.3145

[37] H. Schölermann and H. Klein, "Optimizing the energy resolution of scintillation counters at high energies," *Nucl. Instruments Methods*, vol. 169, no. 1, pp. 25–31, 1980.

[38] A. Enqvist, C. C. Lawrence, B. M. Wieger, S. A. Pozzi, and T. N. Massey, "Neutron light output response and resolution functions in EJ-309 liquid scintillation detectors," *Nucl. Instrum. Methods Phys. Res., Sect A*, vol. 715, pp. 79–86, 2013.

[39] M. A. Norsworthy, A. Poitrasson-Rivière, M. L. Ruch, S. D. Clarke, and S. A. Pozzi, "Evaluation of neutron light output response functions in EJ-309 organic scintillators," *Nucl. Instrum. Methods Phys. Res., Sect A*, vol. 842, no. October, pp. 20–27, jan 2017. [Online]. Available: http://dx.doi.org/10.1016/j.nima.2016.10.035http://linkinghub.elsevier.com/retrieve/pii/S0168900216310737

[40] S. A. Pozzi, S. D. Clarke, W. J. Walsh, E. C. Miller, J. L. Dolan, M. Flaska, B. M. Wieger, A. Enqvist, E. Padovani, J. K. Mattingly, D. L. Chichester, and P. Peerani, "MCNPX-PoliMi for nuclear nonproliferation applications," *Nucl. Instrum. Methods Phys. Res., Sect A*, vol. 694, pp. 119–125, 2012. [Online]. Available: http://dx.doi.org/10.1016/j.nima.2012.07.040

[41] P. Talou, I. Stetcu, and T. Kawano, "Modeling the Emission of Prompt Fission γ Rays for Fundamental Physics and Applications," *Phys. Procedia*, vol. 59, pp. 83–88, 2014. [Online]. Available: http://linkinghub.elsevier.com/retrieve/pii/S187538921400488X

[42] P. Talou, T. Kawano, I. Stetcu, J. P. Lestone, E. McKigney, and M. B. Chadwick, "Late-time emission of prompt fission γ rays," *Phys. Rev. C*, vol. 94, no. 6, p. 064613, 2016.

[43] J. Randrup and R. Vogt, "Calculation of fission observables through event-by-event simulation," *Phys. Rev. C*, vol. 80, no. 2, p. 024601, 2009. [Online]. Available: n

[44] R. Vogt and J. Randrup, "Event-by-event study of neutron observables in spontaneous and thermal fission," *Phys. Rev. C*, vol. 84, no. 4, p. 044621, sep 2011. [Online]. Available: http://arxiv.org/abs/1109.3788http://dx.doi.org/10.1103/PhysRevC.84.044621

[45] ——, "Neutron angular correlations in spontaneous and neutron-induced fission," *Phys. Rev. C*, vol. 90, no. 6, p. 064623, 2014.

[46] J. Randrup and R. Vogt, "Refined treatment of angular momentum in the event-by-event fission model freya," *Phys. Rev. C*, vol. 89, no. 4, p. 044601, 2014. [Online]. Available: http://link.aps.org/doi/10.1103/PhysRevC.89.044601

[47] R. Vogt and J. Randrup, "Improved modeling of photon observables with FREYA," *Phys. Rev. C*, vol. 96, p. 064620, aug 2017. [Online]. Available: http://arxiv.org/abs/1708.07312http://dx.doi.org/10.1103/PhysRevC.96.064620

[48] J. M. Verbeke, J. Randrup, and R. Vogt, "Fission Reaction Event Yield Algorithm FREYA 2.0.2," *Comput. Phys. Commun.*, vol. 222, pp. 263–266, 2018.

[49] W. Mannhart, "Evaluation of the Cf-252 fission neutron spectrum between 0 MeV and 20 MeV," in *Proc. an Advis. Gr. Meet. Prop. neutron sources*, Leningrad, USSR, 1987, pp. 158–171.

[50] R. Billnert, F. J. Hambsch, A. Oberstedt, and S. Oberstedt, "New prompt spectral γ-ray data from the reaction 252Cf(sf) and its implication on present evaluated nuclear data files," *Phys. Rev. C*, vol. 87, no. 2, p. 024601, 2013.

[51] T. E. Valentine and J. T. Mihalczo, "MCNP-DSP: A neutron and gamma ray Monte Carlo calculation of source-driven noise-measured parameters," *Ann. Nucl. Energy*, vol. 23, no. 16, pp. 1271–1287, 1996.

[52] P. Santi and M. Miller, "Reevaluation of Prompt Neutron Emission Multiplicity Distributions for Spontaneous Fission," *Nucl. Sci. Eng.*, vol. 160, no. 2, pp. 190–199, oct 2008. [Online]. Available: https://www.tandfonline.com/doi/full/10.13182/NSE07-85

[53] T. E. Valentine, "Evaluation of prompt fission gamma rays for use in simulating nuclear safeguard measurements," *Ann. Nucl. Energy*, vol. 28, no. 3, pp. 191–201, 2001.

[54] M. Marcath, T. Shin, S. Clarke, P. Peerani, and S. Pozzi, "Neutron angular distribution in plutonium-240 spontaneous fission," *Nucl. Instrum. Methods Phys. Res., Sect A*, vol. 830, pp. 163–169, 2016.

[55] J. L. Dolan, M. Flaska, A. Poitrasson-Riviere, A. Enqvist, P. Peerani, D. L. Chichester, and S. a. Pozzi, "Plutonium measurements with a fast-neutron multiplicity counter for nuclear safeguards applications," *Nucl. Instrum. Methods Phys. Res., Sect A*, vol. 763, pp. 565–574, 2014. [Online]. Available: http://linkinghub.elsevier.com/retrieve/pii/S0168900214007359

[56] N. Ensslin, W. C. Harker, M. S. Krick, D. G. Langner, M. M. Pickrell, and J. E. Stewart, "LA-13422-M Application Guide to Neutron Multiplicity Counting," Los Alamos National Laboratory, Tech. Rep., 1998.

[57] J. L. Dolan, M. Flaska, S. A. Pozzi, and D. L. Chichester, "Passive measurements of mixed-oxide fuel for nuclear nonproliferation," *Nucl. Instrum. Methods Phys. Res., Sect A*, vol. 703, pp. 102–106, 2013. [Online]. Available: http://dx.doi.org/10.1016/j.nima.2012.11.092

[58] L. Holewa, W. Charlton, E. Miller, and S. Pozzi, "Using neutron angular anisotropy information to dynamically determine the ratio of the (??,n) rate to spontaneous fission rate for coincidence counting applications," *Nucl. Instrum. Methods Phys. Res., Sect A*, vol. 701, pp. 249–253, 2013.

[59] J. S. Fraser, "The angular distribution of prompt neutrons emitted in fission," *Phys. Rev.*, vol. 88, no. 3, pp. 536–541, 1952. [Online]. Available: http://journals.aps.org/pr/pdf/10.1103/PhysRev.88.536

[60] C. Wagemans, E. Allaert, A. Deruytter, R. Barthelemy, and P. Schillebeeckx, "Comparison of the energy and mass characteristics of the Pu-239(n-th, f) and the Pu-240(sf) fragments," *Phys. Rev. C*, vol. 30, no. 1, pp. 218–223, 1984.

[61] S. Pozzi, M. Bourne, J. Dolan, K. Polack, C. Lawrence, M. Flaska, S. Clarke, a. Tomanin, and P. Peerani, "Plutonium metal vs. oxide determination with the pulse-shape-discrimination-capable plastic scintillator EJ-299-33," *Nucl. Instrum. Methods Phys. Res., Sect A*, vol. 767, pp. 1–5, 2014. [Online]. Available: http://linkinghub.elsevier.com/retrieve/pii/S016890021400922X

[62] G. A. Petrov, A. S. Vorobyev, V. E. Sokolov, A. M. Gagarski, I. S. Guseva, O. A. Shcherbakov, V. I. Petrova, T. A. Zavarukhina, G. V. Val'ski, Y. S. Pleva, and T. E. Kuzmina, "Search for scission neutrons emitted in low energy fission of heavy nucleus," in *AIP Conf. Proc.*, vol. 1175, 2009, pp. 289–296.

[63] M. J. Marcath, R. C. Haight, R. Vogt, M. Devlin, P. Talou, I. Stetcu, J. Randrup, P. F. Schuster, S. D. Clarke, and S. A. Pozzi, "Measured and simulated 252Cf(sf) prompt neutron-photon competition," *Phys. Rev. C*, vol. 97, no. 4, pp. 1–15, apr 2018. [Online]. Available: https://journals.aps.org/prc/abstract/10.1103/PhysRevC.97.044622https://link.aps.org/doi/10.1103/PhysRevC.97.044622

[64] K. Skarsvag, "Time distribution of gamma-rays from spontaneous fission of Cf-252," *Nucl. Phys. A*, vol. 153, pp. 82–96, 1970. [Online]. Available: https://doi.org/10.1016/0375-9474(70)90757-8

[65] H. R. Bowman, S. G. Thompson, J. C. D. Milton, and W. J. Swiatecki, "Velocity and Angular Distributions of Prompt Neutrons from Spontaneous Fission of Cf-252," *Phys. Rev.*, vol. 126, no. 6, pp. 2120–2136, jun 1962. [Online]. Available: https://link.aps.org/doi/10.1103/PhysRev.126.2120

[66] A. Vorobyev, O. Shcherbakov, A. Gagarski, G. Val'ski, and G. Petrov, "Investigation of the prompt neutron emission mechanism in low energy fission of ^{235,233}U(n_{th}, f) and ^{252}Cf(sf)," *EPJ Web Conf.*, vol. 8, p. 03004, 2010.

[67] J. L. Ullmann, E. M. Bond, T. A. Bredeweg, A. Couture, R. C. Haight, M. Jandel, T. Kawano, H. Y. Lee, J. M. O'Donnell, A. C. Hayes, I. Stetcu, T. N. Taddeucci, P. Talou, D. J. Vieira, J. B. Wilhelmy, J. A. Becker, A. Chyzh, J. Gostic, R. Henderson, E. Kwan, and C. Y. Wu, "Prompt γ-ray production in neutron-induced fission of ^{239}Pu," *Phys. Rev. C*, vol. 87, no. 4, p. 044607, apr 2013. [Online]. Available: https://link.aps.org/doi/10.1103/PhysRevC.87.044607

[68] E. Kwan, C. Wu, R. Haight, H. Lee, T. Bredeweg, A. Chyzh, M. Devlin, N. Fotiades, J. Gostic, R. Henderson, M. Jandel, A. Laptev, R. Nelson, J. O'Donnell, B. Perdue, T. Taddeucci, J. Ullmann, and S. Wender, "Prompt Fission γ-rays Measured Using Liquid Scintillators," *Nucl. Data Sheets*, vol. 119, pp. 221–224, 2014. [Online]. Available: http://www.sciencedirect.com/science/article/pii/S009037521400595X

[69] V. N. Dushin, F. J. Hambsch, V. A. Jakovlev, V. A. Kalinin, I. S. Kraev, A. B. Laptev, D. V. Nikolaev, B. F. Petrov, G. A. Petrov, V. I. Petrova, Y. S. Pleva, O. A. Shcherbakov, V. I. Shpakov, V. E. Sokolov, A. S. Vorobyev, and T. A. Zavarukhina, "Facility for neutron multiplicity measurements in fission," *Nucl. Instrum. Methods Phys. Res., Sect. A*, vol. 516, no. 2-3, pp. 539–553, 2004.

[70] A. Göök, F.-J. Hambsch, and M. Vidali, "Prompt neutron multiplicity in correlation with fragments from spontaneous fission of ^{252}Cf," *Phys.*

Rev. C, vol. 90, no. 6, p. 064611, 2014. [Online]. Available: http://link.aps.org/doi/10.1103/PhysRevC.90.064611

[71] A. Oberstedt, R. Billnert, F. J. Hambsch, and S. Oberstedt, "Impact of low-energy photons on the characteristics of prompt fission γ -ray spectra," *Phys. Rev. C*, vol. 92, no. 92, p. 014618, 2015.

[72] T. Wang, G. Li, L. Zhu, Q. Meng, L. Wang, H. Han, W. Zhang, H. Xia, L. Hou, R. Vogt, and J. Randrup, "Correlations of neutron multiplicity and γ-ray multiplicity with fragment mass and total kinetic energy in spontaneous fission of 252 Cf," *Phys. Rev. C*, vol. 93, p. 014606, 2016.

[73] P. Glässel, R. Schmid-Fabian, D. Schwalm, D. Habs, and H. U. V. Helmolt, "^{252}Cf fission revisited - new insights into the fission process," *Nucl. Physics, Sect. A*, vol. 502, no. C, pp. 315–324, oct 1989. [Online]. Available: http://linkinghub.elsevier.com/retrieve/pii/0375947489906726

[74] D. Bleuel, L. Bernstein, J. Burke, J. Gibelin, M. Heffner, J. Mintz, E. Norman, L. Phair, N. Scielzo, S. Sheets, N. Snyderman, M. Stoyer, and M. Wiedeking, "Gamma-ray multiplicity measurement of the spontaneous fission of 252Cf in a segmented HPGe/BGO detector array," *Nucl. Instrum. Methods Phys. Res., Sect A*, vol. 624, no. 3, pp. 691–698, 2010. [Online]. Available: http://linkinghub.elsevier.com/retrieve/pii/S0168900210021790

[75] F. S. Dietrich, J. C. Browne, W. J. O'Connell, and M. J. Kay, "Spectrum of γ rays in the 8- to 20-MeV range from ^{252}Cf spontaneous fission," *Phys. Rev. C*, vol. 10, no. 2, pp. 795–802, aug 1974. [Online]. Available: https://link.aps.org/doi/10.1103/PhysRevC.10.795

[76] D. G. Madland and J. R. Nix, "New Calculation of Prompt Fission Neutron Spectra and Average Prompt Neutron Multiplicities," *Nucl. Sci. Eng.*, vol. 81, no. October, p. 213, 1982.

[77] O. Litaize, O. Serot, and L. Berge, "Fission modeling with FIFRELIN," *Eur. Phys. J. A*, vol. 51, no. 12, pp. 1–14, 2015.

[78] K. H. Schmidt, B. Jurado, C. Amouroux, and C. Schmitt, "General Description of Fission Observables: GEF Model Code," *Nucl. Data Sheets*, vol. 131, pp. 107–221, 2016. [Online]. Available: http://dx.doi.org/10.1016/j.nds.2015.12.009

[79] W. John, J. J. Wesolowski, and F. Guy, "Mass-dependent structure in the fission γ-ray yields from 252Cf," *Phys. Lett. B*, vol. 30, no. 5, pp. 340–341, oct 1969. [Online]. Available: http://linkinghub.elsevier.com/retrieve/pii/0370269369904997

[80] L. E. Kirsch, M. Devlin, S. M. Mosby, and J. A. Gomez, "A new measurement of the ^{6}Li(n, α)t cross section at MeV energies using a ^{252}Cf fission chamber and ^{6}Li scintillators," *Nucl. Instrum. Methods Phys. Res., Sect A*, vol. 874, no. September, pp. 57–65, 2017. [Online]. Available: http://linkinghub.elsevier.com/retrieve/pii/S0168900217309464

[81] R. B. Oberer, "Maximum Alpha To Minimum Fission Pulse Amplitude for a Parallel-Plate and Hemispherical Cf-252 Ion- Chamber Instrumented Neutron Source," Oak Ridge National Laboratory, Oak Ridge, TN, Tech. Rep. ORNL/TM-2000/290, 2000.

[82] N. J. Roberts and L. N. Jones, "The content of ^{250}Cf and ^{248}Cm in ^{252}Cf neutron sources and the effect on the neutron emission rate," *Radiat. Prot. Dosimetry*, vol. 126, no. 1-4, pp. 83–88, 2007.

[83] M. M. Bourne, S. D. Clarke, N. Adamowicz, S. A. Pozzi, N. Zaitseva, and L. Carman, "Neutron detection in a high-gamma field using solution-grown stilbene," *Nucl. Instrum. Methods Phys. Res., Sect A*, vol. 806, pp. 348–355, 2016. [Online]. Available: http://dx.doi.org/10.1016/j.nima.2015.10.025

[84] B. C. Diven, H. C. Martin, R. F. Taschek, and J. Terrell, "Multiplicities of Fission Neutrons," *Phys. Rev.*, vol. 101, no. 3, pp. 1012–1015, feb 1956. [Online]. Available: https://link.aps.org/doi/10.1103/PhysRev.101.1012

[85] H. Maier-Leibnitz, P. Armbruster, and H. J. Specht, "Prompt and delayed gamma-rays from fission," in *Phys. Chem. Fission*, Salzburg, Austria, 1965, pp. 113–123.

[86] I. Stetcu, P. Talou, T. Kawano, and M. Jandel, "Properties of prompt-fission γ rays," *Phys. Rev. C*, vol. 90, no. 2, p. 024617, aug 2014. [Online]. Available: https://link.aps.org/doi/10.1103/PhysRevC.90.024617

[87] H. O. Menlove, "Manual for the Portable Handheld Neutron Counter (PHNC) for Neutron Survey and the Measurement of Plutonium Samples," Los Alamos National Laboratory, Tech. Rep., 2005.

[88] D. Reilly, N. Ensslin, H. Smith Jr., and S. Kreiner, "LA-UR-90-732 Passive Nondestructive Assay of Nuclear Materials," Los Alamos National Laboratory, Tech. Rep., 1991. [Online]. Available: http://www.lanl.gov/orgs/n/n1/panda/

[89] D. R. Tilley, H. R. Weller, C. M. Cheves, and R. M. Chasteler, "Energy levels of light nuclei A = 18-19," *Nucl. Physics, Sect. A*, vol. 595, no. 1, pp. 1–170, 1995.

[90] J. M. Verbeke, L. F. Nakae, and R. Vogt, "Neutron-neutron angular correlations in spontaneous fission of ^{252}Cf and $_{240}$Pu," *Phys. Rev. C*, vol. 97, no. 4, p. 044601, apr 2018. [Online]. Available: https://link.aps.org/doi/10.1103/PhysRevC.97.044601

[91] J. Mueller and J. Mattingly, "Using anisotropies in prompt fission neutron coincidences to assess the neutron multiplication of highly multiplying subcritical plutonium assemblies," *Nucl. Instrum. Methods Phys. Res., Sect A*, vol. 825, pp. 87–92, jul 2016. [Online]. Available: http://linkinghub.elsevier.com/retrieve/pii/S0168900216301917